Nonlinear ionization of many-electron systems over a broad photon-energy range

Dissertation

zur Erlangung des Doktorgrades an der Fakultät für Mathematik, Informatik und Naturwissenschaften Fachbereich Physik der Universität Hamburg

vorgelegt von

Antonia Karamatskou

Hamburg
2015

Tag der Disputation: 16.11.2015

Folgende Gutachter empfehlen die Annahme der Dissertation:

Prof. Dr. Robin Santra

Prof. Dr. Daniela Pfannkuche

Prof. Dr. Uwe Thumm

meiner Familie

"We cannot solve our problems with the same thinking we used when we created them."

Albert Einstein (1879-1955)

Preface

In this thesis I present my doctoral work which I completed in a bit more than 3 years working in the Theory Division of the Center for Free-Electron Laser Science. Changing from mathematical and high-energy physics to atomic and many-body physics was challenging but I am very happy about my decision to switch to photon science. Already at this point I would like to thank my supervisor Prof. Dr. Robin Santra who supported me, challenged me to produce better and better scientific work and from whom I learned a lot about both theory and experiment related to ultrafast and strong-field physics.

During my PhD I was fortunate enough to be a member of the collaborative research center (SFB) 925: "Light induced dynamics and control of correlated quantum systems". This scientific structure not only facilitates communication but positively enforces collaboration between the members. Through this research center discussions with other doctoral students arose and a collaboration emerged with the group of Dr. Michael Meyer from the European XFEL GmbH about an experiment conducted at FLASH. For me, this close collaboration provided insight into the experimental setup and the conditions at a free-electron laser. It led to highly interesting and novel results in the collective excitation of atomic systems in the XUV photon energy regime. I am grateful to Dr. Michael Meyer who was also my second supervisor within the graduate school of the SFB 925.

I had the chance to benefit from the communicative and interdisciplinary environment that the Center for Free-Electron Laser Science (CFEL) provides. During my doctoral time I was given three chances to contribute actively to the scientific life at CFEL and to teaching: Together with Stefan Pabst and Jan Malte Slowik, at the time colleagues in our group, we organized an international workshop funded mainly by the Körber Foundation and supported by the SFB 925 and DESY. We invited young researchers and set the focus on discussions between the scientists. Furthermore, through the DAAD RISE program I had the opportunity to supervise a summer student, Matthew Tilley, with whom we investigated an interesting project about nonlinear atom-photon interaction in the x-ray regime. This supervision and collaboration was a great experience for me. Thirdly, I led the exercise groups belonging to the lecture "Theory of photon-matter interactions" given by Prof. Santra at the University of Hamburg.

My interest in light-induced phenomena in matter has been growing constantly over the last three years, and I hope that this work will stand only at the beginning of more exciting scientific studies and results to come.

Zusammenfassung

Die rasante Laserentwicklung und insbesondere die technologischen Fortschritte im Bereich der freien Elektronenlaser haben große Erfolge sowohl in der theoretischen als auch in der experimentellen Atom-, Molekül- und optischen Physik eingeleitet. Dank der hohen Intensitäten und gleichzeitig kurzen Pulsdauern kann Licht-Materie-Wechselwirkung unter extremen Bedingungen im nichtlinearen Regime im Hinblick auf die Dynamik und die Eigenschaften der Materie untersucht werden. Die neuen Möglichkeiten der freien Elektronenlaser im Röntgenbereich haben die Bedeutung der nichtlinearen Optik auch in den Bereich der Röntgenstrahlung erweitert. Ich zeige in meiner Arbeit, wie der Bereich des nichtlinearen Ansprechverhaltens ausgeschöpft werden kann, um verborgene Information über Resonanzstrukturen zu erhalten, die im linearen Bereich nicht aufgelöst werden kann. Dies eröffnet Aussichten für zukünftige Anwendung in der Untersuchung von diversen, komplexen Systemen mithilfe von freien Elektronenlasern.

Gegenstand der vorliegenden Arbeit ist die Wechselwirkung von atomaren Systemen mit einer abgeschlossenen äußeren Schale mit ultrakurzen und starken Laserpulsen. Das Hauptaugenmerk bei der Untersuchung der Eigenschaften der Atomhülle liegt auf dem nichtlinearen Antwortverhalten und den Korrelationen zwischen den Elektronen. Mehrere Erweiterungen des Softwarepakets XCID für Mehrelektronensysteme werden beschrieben und deren Anwendungen werden in verschiedenen Projekten demonstriert; neue Möglichkeiten der numerischen Methode wurden durch die Implementierung der Berechnung von Photoelektronenspektren und Eigenzuständen des Vielteilchen-Hamiltonoperators realisiert. Das hier behandelte Forschungsgebiet umfasst 1) den Starkfeldbereich, in dem das diabatische Verhalten in der Tunnelionisierung insbesondere für kürzere Pulsdauern als ein optischer Zyklus diskutiert wird; 2) das XUV Regime, in dem wir zum ersten Mal zeigen, dass kollektives Verhalten im nichtlinearen Regime bei resonanter Anregung neue Information preisgibt; und 3) den für freie Elektronenlaser-Experimente relevanten (harten) Röntgenbereich, in dem wir die Bedeutung der Mehrphotonenphysik im Hinblick auf angestrebte zukünftige Intensitäten verdeutlichen. Unsere Analyse des Experiments bei FLASH über die riesige Dipolresonanz der $4d$ Schale von Xenon im nichtlinearen XUV Regime enthüllt die Existenz von zwei unterliegenden Resonanzen. Zum ersten Mal rechtfertigen Messungen der Zweiphotonen-Absorption die Vorhersage von Unterstruktur und beweisen die Wichtigkeit der Korrelationseffekte im nichtlinearen Regime.

All diese Studien beschreiben Dynamik und Eigenschaften der Systeme nach der Wechselwirkung mit einem bestimmten Puls. Wir stellen auch die inverse Frage: Wie muss der Puls aussehen, um ein bestimmtes Photoelektronenspektrum zu erhalten? Das Ergebnis der Ionisierung soll optimiert werden, der Puls soll die Elektronen lenken. Zielsetzung der kohärenten Optimierung des Pulses ist, ein vorgegebenes Spektrum zu erhalten. Der Lichtpuls kann in Bandbreite, Amplitude und Pulsdauer beschränkt werden, um experimentelle Durchführbarkeit sicherzustellen. Wir runden so das Gebiet der Ionisierung von Mehrelektronensystemen ab und identifizieren Möglichkeiten für zukünftige Entwicklungen.

Abstract

Rapid developments in laser technology and, in particular, the advances in the realm of free-electron lasers have initiated tremendous progress in both theoretical and experimental atomic, molecular and optical physics. Owing to high intensities in combination with short pulse durations we can enter the utterly nonlinear regime of light-matter interaction and study the dynamics and features of matter under extreme conditions. The capabilities of x-ray free-electron laser sources have promoted the importance of nonlinear optics also in the x-ray regime. I will show in my thesis how we can exploit the nonlinear response regime to reveal hidden information about resonance structures that are not resolved in the weak-field regime. This prospect points to many applications for future investigations of various complex systems with free-electron lasers.

In the present thesis the interaction of atomic closed-shell systems with ultrashort and strong laser pulses is investigated. Over a broad photon-energy range the characteristics of the atomic shell are studied with a particular focus on the nonlinear response regime and on electron correlation effects. Several computational extensions of the XCID package for multi-electron dynamics are presented and their applications in various studies are demonstrated; a completely new capability of the numerical method is realized by implementing the calculation of photoelectron spectra and by calculating eigenstates of the many-electron Hamiltonian. The field of study within the present work encompasses 1) the strong-field regime, where the question of the adiabatic character in tunneling ionization is discussed and analyzed, especially for the case of few-cycle pulses; 2) the XUV regime, in which we show for the first time that the collectivity in resonant excitation reveals new information; and 3) the (hard) x-ray regime, which is highly relevant for x-ray free-electron laser experiments, and where we show how important two-photon absorption in this regime can be at the envisaged high intensities at future hard x-ray sources. Analyzing the experiment carried out at FLASH by physicists from the European XFEL, our study of the well-known giant dipole resonance of the $4d$ shell in atomic xenon in the nonlinear regime brings to light the existence of two underlying resonances. For the first time, the experimental measurements of two-photon absorption of xenon legitimate the theoretical prediction of its substructure and demonstrates that collective effects are essential to describe the electronic response in the two-photon regime.

All of these studies are concerned with the dynamics and the result upon irradiation with specific pulses. We address also the inverse question: How must the pulses be shaped in order to achieve a certain photoelectron spectrum? We wish to optimize the result of the ionization procedure and, thereby, to steer electrons. The coherent control objective is discussed by forcing the pulse to generate a predetermined photoelectron spectrum. The light pulses can be restricted in bandwidth, amplitude and duration so as to assure experimental feasibility. In this way, we complete the picture of ionization of multi-electron systems by strong and short laser pulses over a broad frequency range and identify possible directions for future developments.

List of publications

2015 *Quantum optimal control of photoelectron spectra and angular distributions*
R. Esteban Goetz, **Antonia Karamatskou**, Robin Santra, and Christiane Koch
submitted

2015 *Wave-packet propagation based calculation of above-threshold ionization in the x-ray regime*
Matthew Tilley, **Antonia Karamatskou**, and Robin Santra
Journal of Physics B: Atomic, Molecular and Physics **48** 124001

2015 *Sensitivity of nonlinear photoionization to previously unresolved resonance substructure in collective excitation*
Tommaso Mazza, **Antonia Karamatskou**, Markus Ilchen, Sadegh Bakhtiarzadeh, Amir Jones Rafipoor, Patrick O'Keeffe, Mossy Kelly, Nichola Walsh, John T. Costello, Michael Meyer, and Robin Santra
Nature Communications **6**, 6799

2015 *Theoretical characterization of the collective resonance states underlying the xenon giant dipole resonance*
Yi-Jen Chen, Stefan Pabst, **Antonia Karamatskou**, and Robin Santra
Physical Review A **91**, 032503

2014 *Calculation of photoelectron spectra within the time-dependent configuration interaction singles scheme*
Antonia Karamatskou, Stefan Pabst, Yi-Jen Chen, and Robin Santra
Physical Review A **89**, 033415; Physical Review A, **91**, 069907 (2015)

2013 *Adiabaticity and diabaticity in strong-field ionization*
Antonia Karamatskou, Stefan Pabst, and Robin Santra
Physical Review A **87**, 043422

Acronyms

ADK	Ammosov, Delone, and Krainov
APS	American Physical Society
ARPACK	Arnoldi package
ATI	Above-threshold ionization
CAP	Complex absorbing potential
CI	Configuration interaction
CIS	Configuration interaction singles
ECS	Exterior complex scaling
EOM	Equation of motion
FEL	Free-electron laser
FERMI	Free-electron Laser for Multidisciplinary Investigations, Trieste
FLASH	Free-electron Laser Hamburg
FWHM	Full width at half maximum
GDR	Giant dipole resonance
HFS	Hartree-Fock-Slater
HHG	High harmonic generation
LAPACK	Linear algebra package
LCLS	(Stanford) LINAC Coherent Light Source
MBES	Magnetic bottle electron spectrometer
OCT	Optimal control theory
PAD	Photoelectron angular distribution
PES	Photoelectron spectrum
RPAE	Random-phase approximation with exchange
SACLA	Spring-8 Ångström Compact Free Electron Laser
SAE	Single-active electron
SASE	Self-amplified spontaneous emission
SES	Smooth exterior scaling
SLAC	Stanford Linear Accelerator Center
SPring-8	Super Photon Ring 8 GeV
t-surff	Time-dependent surface flux
TDCIS	Time-dependent configuration interaction singles
UV	Ultraviolett
VUV	Vacuum Ultraviolet
XATOM	Integrated toolkit for x-ray atomic physics
XCID	Configuration interaction dynamics package for multichannel dynamics
XFEL	X-ray free-electron laser
XUV	Extreme Ultraviolet

Contents

1 Introduction

Remarkable progress in the realm of light-source development has shaped the physics of the 20^{th} and the beginning of the 21^{st} century. The power of producing coherent electromagnetic radiation of high intensity evolved simultaneously with the quest for ever increasing precision and for more information about the structure and dynamics of matter. Modern light sources developed from the maser and the first laser, and now lasers, synchrotron, terahertz and microwave sources span the frequency range from radio frequencies to the ultraviolet (UV) and extreme ultraviolet (XUV). With the extension of the laser to free-electron lasers the photon energy of the coherent laser light can lie even in the soft to hard x-ray regime. These light sources provided the ground for new tools and methods to study atoms and molecules interacting with light. On the one hand light is utilized to investigate the structure and dynamics of atoms; on the other hand it is also employed to control atomic degrees of freedom and to steer electrons, in turn also leading to the generation of new types of light sources. Light-matter interactions have been interesting to physicists, engineers and chemists for a long time now and their investigation has opened new fields of study in atomic, molecular, optical, and solid state physics, chemistry and engineering.

The present thesis deals with the theoretical investigation of atomic systems interacting with intense light pulses, spanning a broad frequency range from the infrared to the x-ray regime. In particular, the nonlinear response regime is investigated by studying the interaction of strong laser pulses with atoms. In undertaking this type of study one needs to employ a theoretical framework capable of efficiently describing the absorption, emission and scattering of photons by atoms. Thus, the essential ingredients of the theory are threefold: the description of the atomic/electronic structure, of the light field and of their interaction. To this end, in the present work the route of "first principles" or "ab initio" calculations is taken: the Schrödinger equation is solved numerically. A central guiding principle of our approach is the predictive character that our calculations shall have: we are not imperatively pursuing a high-precision ab-initio theory, but focus more strongly on the qualitative validity of our results. Regarding the light-field part it should be emphasized that the light is described semiclassically and as a function of time only. Due to the exclusive time dependence the electric field does not change over the spatial extent of the atom and, consequently, our description remains in the dipole approximation. Yet, as will be shown, regarding the photon-energy range the whole range of the spectrum can be considered without any difficulty.

One particularly important aspect of my thesis work regarding the electronic structure problem is the description of correlation effects between electrons and holes in the atomic shell, which are created by the light, and the phenomena to which the collective behavior leads. Whenever the dynamics are governed by significant quantum many-body interactions the physics becomes much richer; it is not sufficient to consider single electrons interacting with the light field. We start from the Hartree-Fock ground state and truncate the configuration interaction (CI) space after the space of one-particle–one-hole excitations: The full N-particle wave function for closed-shell atoms is expanded in the one-particle–one-hole basis and, thus, we obtain the configuration interaction singles (CIS) scheme. Therefore, the correlation between the electron and the hole created in the shell is inherently contained within the description of the wave function. In this way, an effective two-particle theory is constructed.

Specifically, if we open all channels that can partake in a certain ionization or excitation process and if we allow all the possible holes that can be created through this process to interact via Coulomb interaction with the leaving electron we obtain the "interchannel" coupling scheme, which will be of central importance within this thesis. It is also possible to constrain the Coulomb interaction between the ejected electron and the shell to the hole from which it initially originated. This scenario is known under the name "intrachannel" coupling scheme. The investigation of both schemes and the comparison of the results enables us to distinguish the impact of the particle–hole interaction, i.e., the electron correlation effects, onto a certain process. In order to avoid confusion we define here what correlation and/or collectiveness shall signify: Whenever it is not possible to write the wave function as a single particle–hole state, yet a superposition is required to describe the state of the system, there is entanglement between different particle-hole states. The Coulomb interaction leads to correlation between these particle–hole states and the wave function describes a collective system far beyond a single-particle state.

We expand the N-electron wave function in the CIS basis and solve the time-dependent Schrödinger equation through time propagation. Therefore, this computational method is called time-dependent configuration interaction singles or TDCIS. Since we obtain the full N-electron wave function we can analyze it to extract information about the process we want to describe: ionization probabilities, cross sections, high-harmonic generation spectra, etc.

My doctoral work led to the following publications: The study of adiabaticity in strong-field ionization is published in Ref. [1], the extension of the XCID package to the calculation of photoelectron spectra is summarized in Ref. [2] and complemented by the Erratum [3]. In the publication [4] the findings of our collaboration on the collective excitation of the giant dipole resonance in xenon are presented, the subsequent theoretical analysis is published in Ref. [5]. The work on x-ray above-threshold ionization (ATI) has been published in Ref. [6], and will appear in the Special Issue on Frontiers of Free-Electrons Laser Science Series II. The work on quantum optimal control of photoelectron distributions has been submitted [7].

In the following, I briefly present an introduction to the processes and methods that

are contemplated within my doctoral work, the theoretical basis of my calculations and the structure of this thesis.

1.1 Ionization of atoms

Photoionization is one of the most probable processes to happen when light interacts with matter. It has been studied extensively from the very beginning of the development of quantum theory [8–12], e.g. in argon or xenon [9, 13]. Since then, its theoretical description has been refined constantly [10–12], and both theoretically and experimentally the ionization of atoms and molecules has served as a tool to investigate the nature of the atomic shell and the molecular orbitals [9]. Especially nowadays with the development of new light sources such as free-electron lasers (FELs) and attosecond light sources, the realm of strong-field physics, multiphoton processes and the interaction of light with matter on an ultrashort timescale (femtoseconds to attoseconds) has become a focus of interest. These light sources provide the experimental means to control and image atomic and molecular systems and to test theoretical predictions of nonlinear processes [14–18].

The photon energies of FELs extend from the UV to the x-ray range, and the intensities are such that they permit the investigation and control of inner-shell processes, Auger decay or above-threshold ionization (ATI) [19, 20]. Typically, the duration of FEL pulses are as short as a few femtoseconds (10^{-15} s). The generation of high-order harmonics (HHG) [21] and the development of ultrashort light sources provide the tools for studying phenomena within atoms and molecules with a new quality in time resolution. The forces acting on the atoms become comparable to the intra-atomic forces, and the ultrashort pulse durations of the order of femtoseconds down to attoseconds (10^{-18} s) [22–24] reach the typical time scales involved in electronic excitations (roughly between 50 as and 50 fs). All of these processes are directly linked to the process of photo-excitation and -ionization.

With the mentioned pulse properties typical atomic timescales which extend from a few attoseconds to tens of femtoseconds can be accessed in order to study electronic dynamics in atoms, molecules and clusters [23, 25, 26]. In the strong-field regime, multiphoton processes play a significant role, especially if the photon energies lie in the UV to x-ray range [27–29]. In general, in this frequency range a diversity of processes must be faced. The removal of a deep inner-shell electron is followed by various processes depending on the atomic states and the photon energy [30]. If the laser pulse is strong enough, also multiphoton inner-shell ionization [31] as well as ATI processes can occur.

For relatively weak fields the light field can be treated as a perturbation and the light-matter interaction can be classified within a few low orders of perturbation theory. In this regime, which is commonly called the *perturbative multiphoton regime*, the order of the interaction or, equivalently, the number of photons that are absorbed is described by the corresponding order of perturbation theory.

However, the strong-field or *tunneling regime* requires a nonperturbative description because the potential resulting from the light field is of comparable magnitude as the intra-atomic potential and, thus, cannot be treated as a small perturbation. This leads to highly nonlinear processes, such as strong-field ATI, a process where the intensity of the peaks observed for a certain order of photoabsorption cannot be captured by the corresponding order of perturbation theory, and lowest-order perturbation theory breaks down.

1.1.1 Strong-field ionization

The realm of strong-field physics has become a focal point of interest in the atomic, molecular, and optical physics community over the last two decades. This was particularly supported by the rapid development of lasers so that the time-resolved investigation of electron dynamics in atoms and molecules has come into reach.

In particular, the process of tunneling ionization has been studied extensively. Ionization in this regime is described in the following picture: The electric field, which oscillates with a small frequency, bends the Coulomb potential in such a way that a barrier of finite width is created through which the electron can tunnel and leave the ion. This is shown schematically in the left panel of Fig. 1.1. Following the calculation of the tunneling ionization rate for the ground state of hydrogen in a static electric

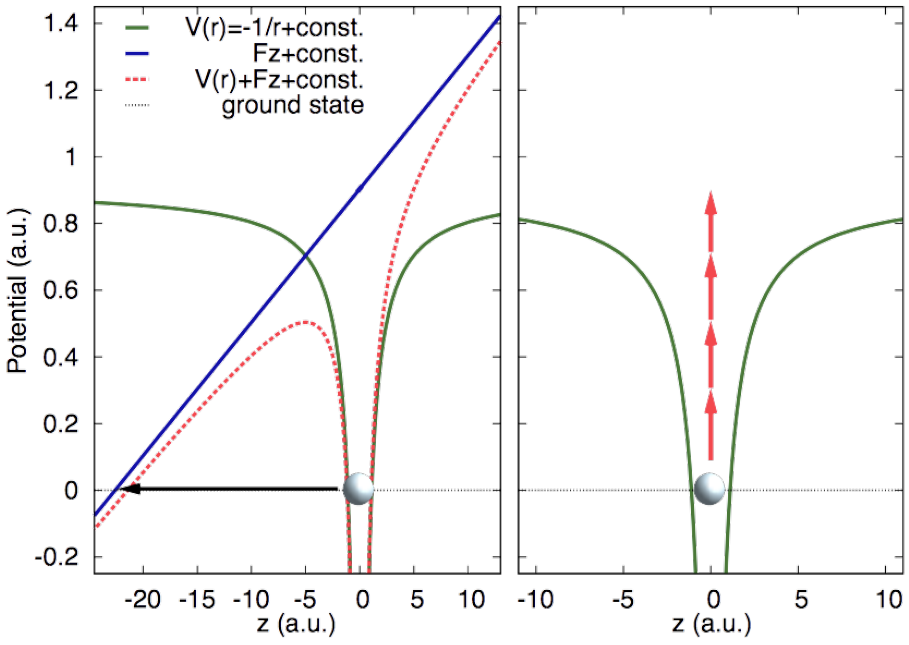

Figure 1.1: The two different ionization regimes depicted schematically for helium. Left panel: Tunneling ionization, $\gamma \ll 1$. The strong electric field (black-dashed line) tilts the Coulomb potential (green curve) so that a barrier of finite width is generated (red curve). The electron can tunnel through the barrier and leave the ionic core in the direction of the barrier suppression. Right panel: Multiphoton regime, $\gamma \gg 1$. Via the absorption of several photons the Coulomb barrier is overcome and the electron can be ionized.

field by Landau [32], Keldysh extended the theory to ionization by strong electromagnetic fields [33]. Later, Ammosov, Delone, and Krainov (ADK) generalized the results to slowly varying fields by introducing the quasistatic approximation and defining the tunneling ionization rate by averaging over one optical period (ADK theory) [34]. A self-contained derivation of the tunneling rate in this approximation is presented in Ref. [35]. In the original derivation [33] Keldysh introduced the parameter

$$\gamma = \sqrt{I_p/(2U_p)},$$

which is now known as the Keldysh parameter [36]. Here, I_p is the ionization potential and $U_p = I/(4\omega^2)$ is the ponderomotive potential, which corresponds to the average energy of a free electron oscillating in the electric field. Here, I is the intensity of the light field and ω is the central frequency. In this way, the Keldysh parameter sets into proportion the frequency of the light field and the field amplitude, $\gamma = 2\omega\sqrt{I_p/(2I)}$. According to Keldysh, γ divides the phenomenon of strong-field ionization into two regimes: for $\gamma \ll 1$ the ponderomotive potential is much larger than the ionization potential and ionization is governed by tunneling ionization [32], while for $\gamma \gg 1$ the process is governed by perturbative multiphoton ionization [37]. In the range of $\gamma \approx 1$ both effects compete with each other [38, 39]. In later publications the Keldysh parameter has been connected to the notion of adiabaticity of the ionization process [40, 41]. Far into the tunneling regime, the atomic response is considered to be purely adiabatic. Adiabatic means in this context that the ionization rate at a given time is solely defined by the instantaneous electric field. This classification will be analyzed in detail in Ch. 4.

1.1.2 Multiphoton ionization

Multiphoton ionization [37] is a process where the system absorbs simultaneously several photons to undergo ionization. This process was theoretically predicted very early [42] and then also verified experimentally with lasers that interact with single atoms [43, 44]. As long as the pulse intensities are not too high (for atomic systems $\ll 10^{16}\mathrm{Wcm}^{-2}$) the multiphoton process can be described successfully by perturbation theory where the light represents a small perturbation with respect to the inneratomic Coulomb potential. Of course, this approximation is invalid once the strength of the light field is comparable to the inneratomic electric fields. Multiphoton ionization has been studied extensively over the last decades [37, and references therein].

In the regime, where the Keldysh parameter is much larger than one, ionization can be understood as initiated by the absorption of multiple photons. This provides the energy necessary to overcome the Coulomb potential and to leave the ion, see Fig. 1.1, right panel. In the perturbative multiphoton regime cross sections can be defined [45] for the description of the absorption or scattering of photon by atoms. Cross sections link the transition matrix element for the particular transition from an initial state to a final state to the photon flux, $j = I/\omega_{\mathrm{photon}}$, which is the number of

incident photons per unit time and unit area. Here, I is the intensity and ω_{photon} the photon energy. For instance, the absorption of two photons is described in second-order perturbation theory. For this purpose, the transition matrix element associated with the transition induced by the interaction Hamiltonian $\hat{H}_{\text{int}}$ from an initial state of the coupled atom-light system I to a final state F is calculated. To this end, all possible pathways leading to this final state by absorbing two photons have to be taken into account. Through the absorption of one photon an intermediate state M_{res} is populated and a summation over all these possible intermediate states must be carried out

$$M^{(2)}_{F\leftarrow I} = \sum_{M_{\text{res}}} \frac{\langle F|\hat{H}_{\text{int}}|M_{\text{res}}\rangle\langle M_{\text{res}}|\hat{H}_{\text{int}}|I\rangle}{E - E_{M_{\text{res}}} + \frac{i}{2}\Gamma_{M_{\text{res}}} + E_I}, \tag{1.1}$$

where E is the energy of the photon, $E_{M_{\text{res}}}$ and $\Gamma_{M_{\text{res}}}$ are the energy and the width of the intermediate state, respectively, and E_I is the energy of the initial state. The two-photon cross section, $\sigma^{(2)}$, is derived from the quantity $|M^{(2)}_{F\leftarrow I}|^2$.

In general, for simplicity disregarding indirect channels, the rate equation for the population evolving due to an N-photon ionization process reads

$$\frac{\mathrm{d}P_N}{\mathrm{d}t} = [1 - P_N(t)]\sigma^{(N)} j^N, \tag{1.2}$$

thus involving the product of the generalized cross section for the N-photon process, $\sigma^{(N)}$, and the intensity to the power N. Solving this differential equation formally by integrating the ionization probability at time t is obtained

$$P_N(t) = 1 - \exp\left(-\int_{-\infty}^{t} \mathrm{d}\tau \sigma^{(N)} j^N\right). \tag{1.3}$$

From this relation it follows that as long as the saturation regime is not reached, i.e., as long as the intensity is low enough and the cross section does not depend on the intensity, the following relation holds: $\ln P_N = N \ln I + \ln \sigma^{(N)} + \text{const}$. This linear dependence results in a straight line on a double-logarithmic scale and allows to read off the order of the ionization process from the slope of the curve.

1.2 Photoelectron spectroscopy

Experimentally, photoelectron spectroscopy is a powerful tool to analyze and quantify the processes that happen within complex systems upon irradiation and understand the electronic structure [46, 47, 47–51]. One highly nonlinear process which was discovered with photoelectron spectroscopy and which I have studied extensively within my doctoral work is the ATI process. First observed in 1979 by P. Agostini *et al.* [52] ATI is a highly nonlinear process where an electron absorbs more photons than are necessary for ionization [53]. As a consequence a series of peaks can be observed in the photoelectron spectrum, where the separation between two consecutive peaks

corresponds to the energy of one photon. This phenomenon occurs in both regimes mentioned above if the light intensity is high enough, in the (infrared) strong-field regime and the perturbative multiphoton regime. Photoelectron spectroscopy was also employed in early experiments with intense light sources in the 1980s to measure the angular distribution in ATI of xenon [49] in order to better understand the ATI phenomenon. Synchrotron radiation was used to obtain high-quality angular distributions of electrons in the photoionization of atoms [50, 54]. Photoelectron spectra (PES) and photoelectron angular distributions (PAD) contain not only fingerprints of the interaction of the electrons with the electromagnetic fields, but also of their interaction and their correlations with each other [55]. In particular, PAD can be used to uncover electron interactions and correlations [56, 57]. Also, in recent experiments using short and intense pulses photoelectron spectroscopy has been used to reveal decay mechanisms and multiphoton excitations in deep shells of atoms [58] and to understand the origin of the low-energy structure in strong-field ionization [51, 59]. PES reveal important information about electron dynamics and time-dependent phenomena [14, 23, 60, 61].

On the theory side, photoelectron distributions can also help to extract information and predict fundamental processes occurring during the interaction with the light pulse. The applications of analyzing the photoelectron spectrum are manifold. Exemplarily, I simply list a few of them: the photoelectron spectrum has been employed to optimize attosecond pulse measurements [62], to steer electrons with light waves [63], which opened the way to attosecond streaking techniques [30, 64], to reveal the electronic structure of molecules [65], to study nonsequential and sequential double ionization in complex atoms [66], and to scrutinize multielectron ionization dynamics [67].

1.2.1 Calculation of photoelectron distributions

Generally, the calculation of the photoelectron spectrum can be done easily after the pulse has ceased by projecting the photoelectron wave packet onto the eigenstates of the field-free continuum. This corresponds to the Fourier transform of the wave packet. However, this approach requires large numerical grids in the cases where the electrons can travel a long distance while the pulse is still interacting with the system. The application of this approach is very limited even in the single-active electron (SAE) cases. For this reason, new methods were developed to calculate the spectrum using wave packet information in a fixed spatial volume much smaller than the volume that would be needed to fully encapsulate the wave packet at the end of the strong-field pulse. Especially for strong and long ionizing light pulses the detection of the photoelectron far away from the atom poses a computational challenge in numerical experiments because propagating the outgoing photoelectron wave packet requires large grid sizes.

In the weak-field limit, where the light-matter interaction can be treated perturbatively, the photoelectron spectrum has been calculated with methods that also

include correlation effects. Most prominent examples are post-Hartree-Fock methods that use reference states, e.g. correlation methods like the configuration interaction [9, 68], the coupled clusters method [69] and the random-phase approximation [70–72]. Furthermore, approaches constructing continuum wave functions, like R-matrix theory [73], have been applied to calculate photoionization cross sections [74] and photoelectron angular distributions [75]; taking into account the interaction of the liberated electron with other atomic orbitals has led to the explanation of the giant dipole resonance of the $4d$ subshell in xenon [9].

In the strong-field regime the description of the ionized wave packet is challenging due to the nonperturbative interaction between the electrons and the light pulse. Therefore, the calculation of photoelectron spectra is numerically more demanding than in the weak-field limit. Moreover, many-body processes are often neglected in the strong-field regime and SAE approaches have become a standard tool [76–79] where correlation effects are omitted. Nevertheless, recently, extensions to many-body dynamics have been presented, e.g., R-matrix theory [80–84], two-active electron [85–87] and time-dependent restricted-active-space configuration interaction theory [88, 89].

There exist several approaches to overcome the obstacle of large grids, e.g., by measuring the electronic flux through a sphere at a fixed radius [90] or splitting the wave function into an internal and an asymptotic part [91, 92] where the latter is then analyzed to yield the spectrum. The first implementation of the flux method in the strong-field case is the time-dependent surface flux (t-surff) method introduced by Tao and Scrinzi [93]. It has recently been extended to the description of dissociation in molecules [94]. Tong et al. [77] applied the splitting approach to strong-field scenarios. With both methods double-differential photoelectron spectra can be calculated, i.e., the electron distribution as a function of kinetic energy and ejection angle. We combine both the splitting and the t-surff methods with TDCIS in order to calculate the PES and the PAD.

1.2.2 Collaboration theory–experiment: ATI in the XUV at FLASH

While I was implementing the calculation of photo-electron spectra we organized discussions with other doctoral students from the collaborative research center 925 in order to foster collaborations within the project area “Ultrafast dynamics and correlations in small quantum systems”. We realized that in photoelectron spectroscopy experiments performed at the Free-Electron LASer in Hamburg (FLASH) the group of Dr. Michael Meyer had measured electron yields of argon and xenon, which we could model with our numerical methods. In the framework of this collaborative research center our proposition was embraced by the principal investigators, and we decided to start a collaboration on the photoelectron spectra and their interpretation. I immediately started work with Dr. Tommaso Mazza, first by understanding how the experiment had been conducted and what exactly had been measured. They were in the process of analyzing and processing their data so that I was involved from an early

stage on in the investigation of argon and xenon irradiated by strong XUV pulses. In the experiment, one- and two-photon electron yields were collected at three different photon energies as a function of pulse intensity over a broad intensity range. In fact, because one photon already suffices to ionize the atom, the two-photon ionization process that we studied at the photon energies used in the experiment is ATI. The absorption of the second photon due to the high pulse intensity promotes the electron to a kinetic energy which is larger by exactly the amount of energy of the absorbed photon. After exchanging parameters about the experimental setup with Dr. Mazza I performed iterations of calculations on argon by first determining the cross sections of the relevant processes and then calculating the electron yields as a function of pulse intensity along with the experimental specifications. Together we found a set of parameters regarding the pulse duration, beam geometry and optical setup for which we found nice agreement between theory and experiment. Using argon as a calibrating system we proceeded with the interpretation of the xenon data where we discovered surprising new information about the giant dipole resonance in xenon.

1.2.3 Collective phenomena

Obviously, the photon energies for the experiment were chosen in a manner that was everything but random: they lie exactly in the range of the giant dipole resonance of the $4d$ shell of xenon, which is the prime example of a collective atomic system. With the newly developed strong XUV radiation available at the free-electron laser we could investigate xenon in the nonlinear response regime. With the help of our theoretical tools we could – for the first time in direct comparison with experiment in this nonlinear regime – classify the impact of the collectiveness of the xenon shell on the photon absorption process and study the resonance structure in more detail. Collective phenomena have been under investigation for many decades now and the interest in collectivity has grown because interesting material properties arise, e.g., superfluidity and superconductivity.

Indeed, numerous phenomena and basic properties of matter including resonant behavior in nuclei, atoms, clusters and plasmas [95–97], interactions in electron gases [98, 99] and superconductivity and superfluidity [100, 101] can be described in terms of a collective many-body response to an external perturbation. Collective electronic behavior is well understood in the weak-field regime, consistent with linear response theory [95, 102]. Since it is a characteristic feature in many-body systems, important for developments in fields such as magnetism, superconductivity, photonics and electronics there has been recently also increasing interest in the optically nonlinear response of collective excitations. Significant advancements in photonics [103–105], especially in electric field enhancement [97, 106] and harmonic generation [107], have been mostly triggered by the recent development in tailoring materials on the nanometer scale exploiting their resonant collective response to radiation [108]. In order to optimize the coupling between the nanostructure and the electromagnetic field a detailed understanding of the underlying resonant response is essential. To this

end, atomic samples provide a valuable benchmark for understanding more complex systems, because they can be investigated more easily both from a theoretical and an experimental perspective. In this sense, our choice of xenon, an atomic system exhibiting strong collective behavior in the XUV, can be viewed as a case study or model system for the understanding of more complex systems. The investigation of larger systems with regard to their resonance behavior could be studied also in other frequency regimes in the nonlinear response regime. Possibly revealed interesting properties could be then exploited in material science or nanotechnology.

Of course collective effects or correlation phenomena are also abundant in atomic and molecular systems: examples are autoionization, Auger decay, Fano resonances, as mentioned above the giant dipole resonance in xenon, and interatomic Coulombic decay [102, 109–111].

1.3 Quantum optimal control

In collaboration with Prof. Dr. Christiane Koch and Esteban Goetz from the Universität Kassel, experts in optimal control theory, we elaborated a method combining TDCIS and its capability to evaluate photoelectron distributions with a monotonically convergent optimal-control algorithm to achieve specific PESs or PADs.

The controllability of quantum systems is an interesting topic of study [112]. While it is natural to ask how the electron dynamics is reflected in the experimental observables, PES and PAD [113–117], it is intriguing to see whether one can control or manipulate directly these observables by tailoring the light pulse. In other words, we want to control the atomic system in such a way that we steer electrons and produce photoelectrons of a specified energy and angular distribution. This type of problem is known as the optimal control problem and has been theoretically tackled by optimal control theory (OCT) [112]. With our capability to calculate photoelectron distributions the opportunity arises to utilize them as observables for the optimal control problem and thereby control the signature that the electron dynamics imprint onto the PES. By tailoring the pulsed electric field in its amplitude, phase or polarization [113–117] the electron dynamics can be controlled with their corresponding signatures in the photoelectron spectrum. While OCT has been employed to study the quantum control of electron dynamics before, in the framework of TDCIS [118] as well as the multi-configurational time-dependent Hartree-Fock (MCTDHF) method [119] or density functional theory (TDDFT) [120, 121], the PES and PAD have not been tackled as control targets before. In fact, most previous studies did not even account for the presence of the ionization continuum which of course for our purposes is indispensable and whose description within grid methods has been studied extensively [122–127].

We employed optimal control theory (OCT), adapting it to the specific task of realizing photoelectron spectra with the given desired features. Optimal control of the underlying quantum dynamics can be used to enhance certain desired features in

the photoelectron spectra and the angular distributions.

1.4 Structure of this thesis

Within my doctoral work not only methodological developments were achieved, but also the new capabilities that I contributed to the computational toolbox of our group were employed immediately to study interesting and nontrivial problems. These tools enabled us to tackle new questions regarding the ionization of many-electron systems. My thesis work spans the broad photon-energy range from the infrared to the x-ray regime. Different photon-atom interaction regimes are studied, from the infrared strong-field regime to the perturbative multiphoton regime.

The first extension of the software package XCID, which was developed in our group for the investigation of light-atom interactions including many-body effects, deals with the calculation of eigenstates of the Hamiltonian. After introducing the implementation of the Arnoldi algorithm, first in my own implementation of the Lanczos algorithm in Sec. 3.1, then within the framework of ARPACK in Sec. 3.2, I present its application to the strong-field ionization of helium in Ch. 4. My thesis starts with a study in the infrared photon energy range. Using the instantaneous eigenstates of the Hamiltonian I analyzed whether tunneling ionization can be understood as an adiabatic process. In the strong-field literature the tunneling regime is always viewed as the adiabatic regime. However, we found that there is a single *diabatic* state, in contrast to the *adiabatic* states, that is taken by the electron during tunneling ionization. Therefore, already the tunneling regime should be interpreted as a non-adiabatic phenomenon. In particular, I studied the highly interesting few-cycle pulse case, where the ionization is always viewed as non-adiabatic. A single *diabatic* state is identified, which is constructed in a diabatization procedure from the field-free ground state that describes the ionization by a few-cycle pulse. Especially in this case, the ionization depends greatly on the form of the pulse because the field amplitude changes dramatically from one field oscillation to the next. It is not the short pulse duration that seems to make a difference but rather this immense change of the field between two successive oscillations.

Next I present the implementation of the calculation of photoelectron distributions within TDCIS in Ch. 5. The methods we employ are applicable to all types of ionization, from the infrared strong-field regime to XUV and x-ray ionization. We follow two approaches to calculate the spectrum without the need for huge grid sizes. The first method employs the scheme of Tong et al. [77] where the photoelectron wave function is absorbed by a real splitting function. The second method after Tao and Scrinzi [93] measures the flux of the electron wave packet through a surface at a fixed radius. With both methods the full angle- and energy-resolved photoelectron distribution is obtained. Combined with the TDCIS scheme it is possible to analyze the dynamics of the outgoing electron in a channel-resolved way and, additionally, to study the dynamics of the bound electrons in the parent ion, i.e., to describe the correlation

between the ejected electron and the remaining hole. As proof-of-principle applications I show the one- and two-photon (ATI) ionization spectra of argon in the XUV energy regime and the strong-field phenomenon of Rabi splitting due to Rabi oscillations in the positive ion during the ionization process. It should be emphasized that with this computational extension of the code it is now possible to directly analyze the ejected electron, which, of course, carries also information about the remaining ion. Previously, quantities linked to the remaining ion were calculated to infer characteristics of the ionization or excitation process. In the case of ionization the study of the spectrum of the emitted electrons is an obvious observable to understand the underlying processes which can be directly compared to experimental measurements.

The next two chapters, Ch. 6 and Ch. 7, are devoted to our collaboration with the group of Dr. Michael Meyer and our analysis of the two-photon ionization of argon and xenon in the XUV. Apart from comparing our theoretical data to the experimental measurements and calibrating the comparison using argon I theoretically analyzed the two-photon cross section of xenon over a broad photon-energy range. I found that the width of the curve and its shape reveal significant substructure which we could analyze in detail owing to the TDCIS framework and the calculation of eigenstates using ARPACK. Our investigation of the nonlinear response of xenon to XUV irradiation in the range of the famous giant dipole resonance led for the first time to a substantiated prediction of two resonances underlying the giant dipole resonance. Our results pave the way towards a deeper understanding of collective behavior in atoms, molecules and solid-state systems using nonlinear spectroscopic techniques enabled by modern short-wavelength light sources. This insight opens up a whole new field considering the importance that nonlinear effects and resonance phenomena have in technological applications.

In the case of the optimal control problem in combination with TDCIS, presented in Ch. 8, we encountered numerical problems when propagating the wave function in the backward direction, which I analyzed and solved directly by implementing the Lanczos propagation scheme (see Ch. 3). In order to steer electrons and to be able to control certain features of the PES and PAD we combined an optimal control algorithm with our TDCIS formalism using the wave-function splitting method (see Ch. 5) to calculate photoelectron spectra and angular distributions. The optimization target can be formulated to include specific desired properties in the PAD, in the PES, or in both. The capabilities of our approach are demonstrated in test examples for hydrogen under strong XUV radiation, maximizing the difference of emission in the upper and lower hemispheres, in order to realize directed electron emission in the multiphoton regime. Further studies on argon are currently being carried out and a manuscript for submission to a peer-reviewed journal is being prepared. For the first time, we employ a multichannel approach together with optimal control theory to test the controllability of ionizing atoms. Our study illustrates that we will be facing experimental challenges, as far as the pulse shaping and the intensities are concerned. Nevertheless, due to its broad applicability this kind of control problem will certainly receive a lot of attention once the technical and experimental capabilities

that currently exist will have been developed even further.

Ending with the largest photon energies or the shortest wavelength, namely the x-ray regime, in Ch. 9, I present our study of how x-ray ATI might be significant for future experiments at hard x-ray free-electron lasers. In the quest of understanding the structure of biologically significant molecules coherent diffraction imaging has become an integral tool of structural biology and biophysics. Of course, high-intensity signals are desirable in the measurements and for this reason the intensity of the FEL pulses will also be increased in the future. In view of real-space image retrieval we pose, therefore, the question to what extent the absorption of multiple photons in the hard x-ray regime has to be taken into account. We find that at intensities around 10^{24} Wcm^{-2} ATI of the core electrons becomes as probable as single-photon ionization of the valence shells.

Finally, a short conclusion and outlook completes my thesis. I will use atomic units, which are the natural units for processes occurring on atomic time and length scales throughout this thesis, except when otherwise indicated. In atomic units the mass, as well as the charge of the electron are set to unity, i.e., $m_e = 1$, and $|e| = 1$. Furthermore, the reduced Planck constant is set to one, $\hbar = 1$. It follows that the fine-structure constant $\alpha = \frac{e^2}{\hbar c} = \frac{1}{c} \approx \frac{1}{137}$, where c is the speed of light. The Bohr radius, or bohr, is the atomic unit of length, $a_0 = \frac{1}{\alpha}\frac{\hbar}{m_e c} = 0.53\,\text{Å}$ and the Hartree energy, or hartree, is the atomic unit of energy, $E_h = \frac{\hbar^2}{m_e a_0^2} = 27.21\,\text{eV}$. The atomic unit of time corresponds to the classical orbital period of the electron in atomic hydrogen, $t_0 = \frac{1}{\alpha^2}\frac{\hbar}{m_e c^2} = 24\,\text{as}$.

2 Theory

As already alluded to in the introductory chapter we follow an *ab-initio* or *first-principles* strategy for solving the light-atom interaction problem. No fitting procedure is performed or any other additional information is added, rather the nonrelativistic Schrödinger equation is solved numerically. For the purpose of a qualitative and effective description of the atomic system one relies heavily on the convenient and numerically feasible representation of the Hilbert space of the system under investigation. Depending on the problem the choice of the basis set can be very different from others. In our case we want to be able to describe electronic dynamics in an atom, in particular ionization and excitation initiated by the absorption of a photon. For this reason a high-quality representation of the continuum states is needed. In this chapter I will present the theoretical background of our numerical method and the time propagation employed to solve the differential equation.

2.1 Theoretical framework: configuration interaction

In general, the field-free N-electron Hamiltonian for an atomic system has the form

$$\hat{H} = \underbrace{\sum_{n=1}^{N}\left(\frac{\hat{\mathbf{p}}_n^2}{2} - \frac{Z}{|\hat{\mathbf{r}}_n|} + \hat{V}_{\mathrm{MF}}(\hat{\mathbf{r}}_n)\right)}_{\hat{H}_0} + \underbrace{\frac{1}{2}\sum_{n\neq n'}^{N}\frac{1}{|\hat{\mathbf{r}}_n - \hat{\mathbf{r}}_{n'}|} - \sum_{n=1}^{N}\hat{V}_{\mathrm{MF}}(\hat{\mathbf{r}}_n)}_{\hat{H}_1}, \tag{2.1}$$

where the single-electron part of the Hamiltonian, in the following denoted by $\hat{H}_0$, contains the kinetic energy $\hat{T} \equiv \sum_n \hat{\mathbf{p}}_n^2/2$, the nuclear potential $\hat{V}_{\mathrm{nuc}} \equiv -\sum_n Z/|\hat{\mathbf{r}}_n|$ and the potential at the mean-field level $\hat{V}_{\mathrm{MF}}$. The electron-electron Coulomb interaction $\hat{V}_{\mathrm{e-e}} \equiv \frac{1}{2}\sum_{n\neq n'} 1/|\hat{\mathbf{r}}_n - \hat{\mathbf{r}}_{n'}|$ completes the many-electron part of the Hamiltonian $\hat{H}_1 \equiv \hat{V}_{\mathrm{e-e}} - \hat{V}_{\mathrm{MF}}$.

In order to solve the electronic structure problem a convenient basis set must be found in which the wave function can be expanded. In quantum chemistry a widely-used scheme is the configuration interaction [68, 128]: Starting from the Hartree-Fock ground state $|\Phi_0^{\mathrm{HF}}\rangle$ the configuration space is built up by exciting electrons from the occupied orbital and promoting them to an orbital which was previously unoccupied (this is called a virtual orbital). This yields a one-particle–one-hole state $|\Phi_i^a\rangle$ for the N-electron system. Exciting a second electron and letting it occupy another

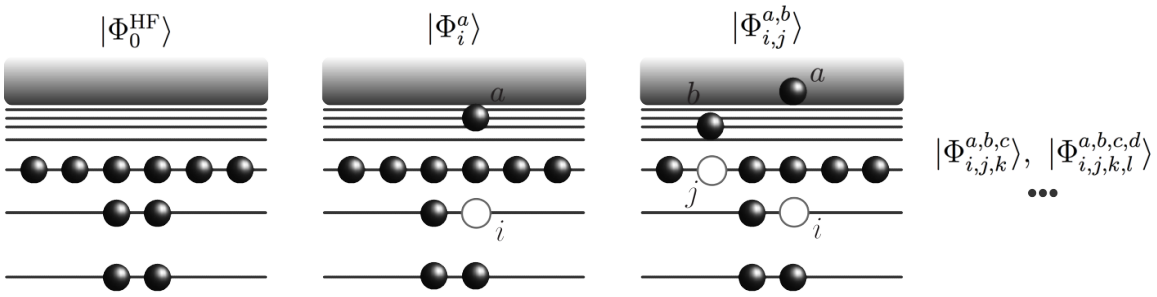

Figure 2.1: Schematic term scheme of an atomic shell. The spheres symbolize electrons and the open circles holes; the lines denote energy levels and the grey shaded area at the top symbolizes the electronic continuum. Starting from the (closed-shell) Hartree-Fock ground state $|\Phi_0\rangle$ through repeated one-particle–one-hole excitations the full CI space is built up: one-particle–one-hole states $|\Phi_i^a\rangle$, two-particle–two-hole states $|\Phi_{i,j}^{a,b}\rangle$, etc. The indices $i, j, ...$ symbolize occupied orbitals, $a, b, ...$ denote virtual (i.e. initially unoccupied) orbitals.

previously unoccupied orbital yields a two-particle–two-hole state $|\Phi_{i,j}^{a,b}\rangle$, promoting a third electron from an initially occupied orbital to a virtual orbital represents a three-particle–three-hole state $|\Phi_{i,j,k}^{a,b,c}\rangle$, and so forth. This is visualized schematically in Fig. 2.1, where $i, j, k, \ldots$ always denote the initially occupied orbitals and $a, b, c, \ldots$ denote the virtual orbitals. Of course, this strategy works well only for closed-shell (atomic) systems where the ground state can be represented by a single Slater determinant.

It is clear that in order to describe multiply ionized systems one needs to include the description of multiple holes and more than one ionized electron in the system, and also the description of multiple, simultaneous excitations requires the inclusion of multiple holes and multiple electrons occupying bound states within the system. These phenomena are beyond the scope and the possibilities of the present work because, for computational reasons that will become obvious below, we are going to restrict the configuration space to the one-particle–one-hole basis, allowing only a single electron at a time to be excited or ionized.

2.2 Time-dependent configuration interaction singles (TDCIS) scheme

The configuration interaction basis set mentioned above and shown in Fig. 2.1 is complete if all possible particle–hole excitations are taken into account. However, for our purposes it is impossible to follow this logic and build up all excitations in an atom. This is because, as mentioned above, we not only want to obtain the bound ground states but also describe the electronic continuum. For this reason, the space of virtual orbitals becomes very large, and with higher excitations this space grows immensely. Therefore, our method for treating the electron dynamics within atoms relies on a truncated CI method; it is based on the time-dependent configuration interaction

singles TDCIS scheme [129]. Neglecting higher order excitations $|\Phi_{i,j}^{a,b}\rangle, |\Phi_{i,j,k}^{a,b,c}\rangle, \ldots$, we restrict the configuration space to states where one electron is excited to a previously unoccupied state. Within the CIS framework the electron dynamics in atoms shall be investigated during irradiation by laser pulses that interact with the shell. For this purpose, the time-dependent Schrödinger equation is solved numerically by wave-packet propagation while expanding the N-electron wave function in the configuration interaction singles (CIS) basis. The TDCIS approach, implemented within the XCID package [129, 130], allows for investigating the wave-packet dynamics and, in particular, the impact of correlation effects between the photoelectron wave packet and the remaining ion. This is done as discussed in this thesis and e.g. in Refs. [131–134]. It is versatile with respect to the electric field properties, and it has proven especially successful for previous strong-field studies [132, 133, 135] and for the projects within this dissertation.

2.2.1 Length and velocity form of the light-matter interaction

The time dependent Schrödinger equation of an N-electron system is given by

$$i\frac{\partial}{\partial t}|\Psi^N(t)\rangle = \hat{H}(t)|\Psi^N(t)\rangle. \tag{2.2}$$

Here, $\hat{H}(t)$ is the full N-electron Hamiltonian of Eq. (2.1) and $|\Psi^N(t)\rangle$ is the full N-electron wave function. As far as the light field is concerned, the Coulomb gauge for the vector potential $\mathbf{A}$, $\mathrm{div}\mathbf{A}=0$, is often chosen in the context of atomic physics. As a consequence, the vector potential is divergence-free and purely transverse. Furthermore, adopting the dipole approximation, the vector potential is only time-dependent, and higher order multipole effects are neglected.

There are two ways to describe the light-matter interaction with a Hamiltonian, the length form and the velocity form. The former involves the electric field, $\mathcal{E}$, and the latter the vector potential, $\mathbf{A}$. The relation between the two fields is given by

$$\mathbf{A}(t) = -\int_{-\infty}^{t} \mathcal{E}(\tau)\mathrm{d}\tau, \tag{2.3a}$$

$$\mathcal{E}(t) = -\frac{\mathrm{d}}{\mathrm{d}t}\mathbf{A}(t). \tag{2.3b}$$

The two descriptions are equivalent as long as no approximations are introduced. For the length form the multipolar Hamiltonian as described in Ref. [136] enters the Schrödinger equation, where the interaction with the light occurs through the dipole, $\mathbf{r}\cdot\mathcal{E}(t)$, and higher orders of multipoles. As an example the Schrödinger equation for a hydrogen atom is presented in dipole approximation, which in the length form

reads

$$i\frac{\partial}{\partial t}\Psi_l = \left[-\frac{\Delta}{2} - \frac{1}{r} - \mathbf{r}\cdot\mathcal{E}(t)\right]\Psi_l, \tag{2.4}$$

where Ψ_l denotes the wave function in length form.

In the case of the velocity form in the Coulomb gauge the interaction Hamiltonian, which contains the coupling between the light and the atomic system, is obtained through the minimal coupling prescription, where the momentum $\mathbf{p}$ is replaced by $\mathbf{p}+\mathbf{A}$. Consequently, the terms resulting from the kinetic energy in the field $(\mathbf{p}+\mathbf{A})^2$ are $\mathbf{p}^2/2$, $\mathbf{p}\cdot\mathbf{A}$, and $\mathbf{A}^2$. Thus, the Schrödinger equation in velocity form reads

$$i\frac{\partial}{\partial t}\Psi_v = \left[\frac{\mathbf{p}^2}{2} + \mathbf{p}\cdot\mathbf{A}(t) + \mathbf{A}^2(t) - \frac{1}{r}\right]\Psi_v, \tag{2.5}$$

where Ψ_v is the wave function in velocity form. The first term describes the kinetic energy of the single electron, cf. the term $\hat{H}_0$ in expression (2.1). Again, the dipole approximation has been used, so that the vector potential depends only on time and not on the spatial coordinates.

To show that the two descriptions are equivalent we perform a unitary transformation of the wave function in length form in Eq. (2.4) with the prescription

$$\Psi_l = e^{i\mathbf{A}\cdot\mathbf{r}}\Psi_v. \tag{2.6}$$

Inserting the right-hand side into the Schrödinger equation and exploiting the relations (2.3) leads indeed to the equation in velocity form

$$i\frac{\partial}{\partial t}\Psi_v = \left\{\frac{1}{2}\left[i\nabla - \mathbf{A}(t)\right]^2 - \frac{1}{r}\right\}\Psi_v = \left\{\frac{1}{2}[\mathbf{p} + \mathbf{A}(t)]^2 - \frac{1}{r}\right\}\Psi_v. \tag{2.7}$$

In this case, where $\mathbf{A}$ depends only on time, the Schrödinger equation can be transformed in such a way that the term proportional to $\mathbf{A}^2$ vanishes. This is because it contributes only a time-dependent but space-independent phase $\exp\left[-i/2\int d\tau\mathbf{A}^2(\tau)\right]$ on the wave function which has no effect on the observables. Now, the light-matter interaction is described by the term $\mathbf{p}\cdot\mathbf{A}(t)$.

The Hamiltonian including the light-matter interaction takes on the form

$$\hat{H}(t) = \hat{H}_0 + \hat{H}_1 + \hat{\mathbf{p}}\cdot\mathbf{A}(t), \tag{2.8}$$

where $\hat{\mathbf{p}}$ is the momentum operator and $\mathbf{A}$ is the vector potential. Unlike in previous work on the TDCIS method [129, 134], we use the velocity form in this thesis except in Ch. 4, where the electric field will be directly employed as variable and, therefore, the dipole approximation will be used in the length form. Furthermore, the charge of the electron is negative, $q_e = -1$, so that $|q_e| = 1$. Only linearly polarized light will be considered in this thesis.

Since the light-matter interaction is present in a non-perturbative manner in Eq. (2.2) all orders of the interaction are automatically included in our calculations. Also, the interaction of closed-shell atoms with different photon energies or, alternatively, field frequencies can be studied without any difficulty. Thus, this approach can cover all frequency ranges from the infrared to x-rays in a non-perturbative way making it quite versatile. In combination with the extension I built into TDCIS, namely the calculation of photoelectron spectra, our numerical toolbox enables us to study phenomena in vastly different regimes of the light-matter interaction – from the weak-field to the strong-field regime. This versatility will be exploited in all chapters of this thesis. Especially in Chaps. 6 and 7 the comparison with experimental data will lie at the focus of interest; our theoretical calculations in the x-ray regime presented in Ch. 9 and the photoelectron distributions in the XUV used as observables in Ch. 8 shall render predictive power and stimulate future experiments.

2.2.2 Configuration interaction singles (CIS)

The Hartree-Fock ground state $|\Phi_0^N\rangle$ of an N-electron closed-shell system is constructed from the vacuum state $|0\rangle$ by applying the spin-orbital creation operators $\hat{c}_{p\sigma}^\dagger$, which create the spin orbitals $|\varphi_{p\sigma}\rangle$, i.e., $\hat{c}_{p\sigma}^\dagger|0\rangle = |\varphi_{p\sigma}\rangle$:

$$|\Phi_0^N\rangle = \prod_{p=1}^{N/2} \hat{c}_{p+}^\dagger \hat{c}_{p-}^\dagger |0\rangle. \tag{2.9}$$

The field-free one-particle Hamiltonian $\hat{H}_0$ has the form $\hat{H}_0 = \sum_p \varepsilon_p \sum_\sigma \hat{c}_{p\sigma}^\dagger \hat{c}_{p\sigma}$, so that $\hat{H}_0|\varphi_{p\sigma}\rangle = \varepsilon_p|\varphi_{p\sigma}\rangle$, where ε_p denotes the energy of the orbital $|\varphi_{p\sigma}\rangle$. Within the CIS approach only one-particle–one-hole excitations $|\Phi_i^a\rangle$ with respect to the Hartree-Fock ground state $|\Phi_0^N\rangle$ are considered. Therefore, the N-electron wave function (now omitting the superscript N for better legibility) is expanded in the CIS basis as

$$|\Psi(t)\rangle = \alpha_0(t)|\Phi_0^N\rangle + \sum_{i,a} \alpha_i^a(t)|\Phi_i^a\rangle, \tag{2.10}$$

where the index i symbolizes an initially occupied orbital and a denotes an unoccupied (or virtual) orbital to which the electron can be excited in the sense described previously. Writing this in operator notation one obtains the configurations

$$|\Phi_i^a\rangle = \frac{1}{\sqrt{2}} \left(\hat{c}_{a+}^\dagger \hat{c}_{i+} + \hat{c}_{a-}^\dagger \hat{c}_{i-} \right) |\Phi_0\rangle, \tag{2.11}$$

from the Hartree-Fock ground state . The anticommuting operators $\hat{c}_{p\sigma}^\dagger$ and $\hat{c}_{p\sigma}$ are creation and annihilation operators, which create and electron in the spin orbital $|\varphi_{p\sigma}\rangle$ or annihilate an electron from this orbital, respectively. Since we aim at describing closed-shell atoms in the Hartree-Fock ground state the total spin is not altered in

the considered processes ($S = 0$, and there is no magnetic field involved), so that only spin singlets occur. Therefore, and for the sake of readability, we hereforth drop the spin index from now on and only treat the spatial part of the orbitals $|\varphi_p\rangle$.

Inserting the wave function expansion (2.10) into the Schrödinger equation (2.2) and projecting it onto the states $|\Phi_0\rangle$ and $|\Phi_i^a\rangle$ yields the following equations of motion for the expansion coefficients $\alpha_i^a(t)$:

$$i\dot{\alpha}_0(t) = \mathbf{A}(t) \cdot \sum_{i,a} \langle \Phi_0 | \, \hat{\mathbf{p}} \, | \Phi_i^a \rangle \alpha_i^a(t), \tag{2.12a}$$

$$\begin{aligned} i\dot{\alpha}_i^a(t) = {} & (\varepsilon_a - \varepsilon_i)\alpha_i^a(t) + \sum_{j,b} \langle \Phi_i^a | \hat{H}_1 | \Phi_j^b \rangle \alpha_j^b(t) \\ & + \mathbf{A}(t) \cdot \left(\langle \Phi_i^a | \, \hat{\mathbf{p}} \, | \Phi_0 \rangle \alpha_0(t) + \sum_{j,b} \langle \Phi_i^a | \, \hat{\mathbf{p}} \, | \Phi_j^b \rangle \alpha_j^b(t) \right). \end{aligned} \tag{2.12b}$$

In this form the equations involve information about the configurations. In the following we assume that the electric field is polarized along the z-axis, such that the light-atom interaction term simplifies to the projection of the momentum on the direction of the vector potential, $\hat{p}_z A_z$. Using the Slater-Condon rules [128] and writing the one- and two-body matrix elements explicitly in terms of the spatial orbitals the Eqs. (2.12) read [134]:

$$i\dot{\alpha}_0 = 2A(t) \sum_{i,a} \alpha_i^a \, p_{ia}, \tag{2.13a}$$

$$\begin{aligned} i\dot{\alpha}_i^a = {} & (\varepsilon_a - \varepsilon_i)\alpha_i^a + \sum_{i'b} \alpha_{i'}^b (2v_{ai'ib} - v_{ai'bi}) + \sqrt{2}A(t) \, \alpha_0 \, p_{ai} + A(t) \sum_b p_{ab} \, \alpha_i^b \\ & - A(t) \sum_{i'} p_{i'i} \, \alpha_{i'}^a, \end{aligned} \tag{2.13b}$$

where the two-body matrix elements are given by

$$v_{pqrs} = \int \mathrm{d}^3x \, \mathrm{d}^3x' \, \varphi_p^\dagger(\mathbf{x}) \varphi_q^\dagger(\mathbf{x}') \frac{1}{|\mathbf{x} - \mathbf{x}'|} \varphi_r(\mathbf{x}) \varphi_s(\mathbf{x}'), \tag{2.14}$$

and the matrix elements of the dipole operator, which is a one-body operator, are of the form

$$p_{ab} = \langle \varphi_a | \hat{p}_z | \varphi_b \rangle. \tag{2.15}$$

The differential equations (2.13) are solved by numerical time propagation either using the Runge-Kutta algorithm of order four or the Lanczos propagation, which will be discussed in the next chapter. Thus, the coefficients $\alpha_i^a(t)$ can be used to analyze ionization and excitation processes in a channel-resolved manner. In this way, quantities that can be inferred from the N-electron wave function, such as the ionization probability, cross sections, and other quantities can be calculated. A special quantity that can be calculated is the ion density matrix [129, 131].

Now it becomes clear what the computational challenge is. Numerically heavy computations reside in the Coulomb matrix elements $\langle\Phi_i^a|\hat{H}_1|\Phi_j^b\rangle$, which must be calculated for all active occupied orbitals symbolized by the index i and j, all virtual orbitals indicated by a and b. In order to determine all the virtual orbitals that must be included in our calculation, we define a cut-off energy E_{cut} up to which the virtual orbitals are calculated. Of course, one needs to assure that all physical states of interest are included in the calculation in a manner that depends on the problem.

The self-consistent Hartree-Fock method to obtain the Hartree-Fock ground state $|\Phi_0\rangle$ is performed by constructing the orbitals on a grid with non-uniformly distributed grid points [129]. Consecutively, the one-particle–one-hole states are built, the Coulomb matrix elements are calculated and the Schrödinger equation is solved through time propagation. In order to prevent reflections at the end of the grid different methods can be used. Some of them will be used and discussed within this work: The complex-absorbing potential method (Chs. 4, 5, and 7), the smooth exterior complex scaling (Chs. 4 and 7) and the wave-function splitting method (Chs. 5, 6, 8, and 9).

2.3 Multichannel physics and electron correlation effects

One particular strength of the CIS approach is that it encapsulates many-body interactions beyond mean-field physics by the effective two-particle description of both electron and hole. By activating the i^{th} orbital the electron there can participate in the dynamics. The set of active occupied orbitals i builds the space of channels through which excitation and ionization can occur. Therefore, the CI approach automatically allows for the distinction and analysis of multichannel physics.

Within CIS the matrix elements that lead to two-body interaction are the Coulomb matrix elements $\langle\Phi_i^a|\hat{V}_{\text{e-e}}|\Phi_j^b\rangle$. If we manually allow only for the matrix elements with hole indices $i = j$ to be nonzero, we obtain the intrachannel picture, which is visualized in Fig. 2.2 a). Physically, this means that the excited electron, although interacting with the hole, cannot modify the ionic hole state (depicted by open circles) in the remaining parent ion. In contrast to this restricted picture, there can be non-vanishing matrix elements for two configurations whose hole indices are different from one another, additionally to a different index of the excited electron, $i = j$ *and* $i \neq j$. This is called interchannel coupling and means that a simultaneous change of the excited electron state and the ionic hole state through electron-electron correlation is permitted. Fig. 2.2 b) depicts this situation, which couples states with $i \neq j$ and $a \neq b$, is depicted. In this way a correlated particle-hole pair is created. We will refer to the electron interaction and the entangled states to which it leads as *electron correlation effects*: As a result of electron correlations collective states are formed,

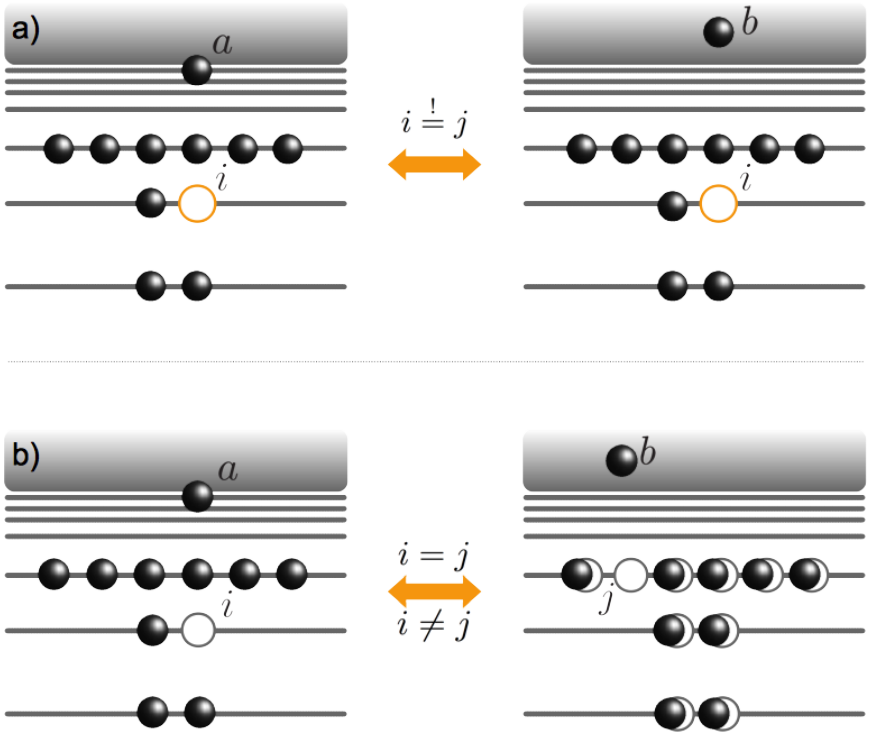

Figure 2.2: Schematic representation of the intrachannel (a) and the interchannel (b) coupling in the atomic shell. The operator $\hat{V}_{\mathrm{e-e}}$ (see. Eq. 2.1) couples different electronic configurations. In the intrachannel coupling case the particle-hole interaction is confined to states $|\Phi_i^a\rangle, |\Phi_j^b\rangle$ whose hole indices (symbolized by open circles) are equal, $i = j$. In contrast, the interchannel coupling leads to non-zero Coulomb matrix elements for all pairs of hole indices and virtual state indices, the cases $i = j$ as well as $i \neq j$ are taken into account.

and the wave function cannot be written as a single particle-hole state – rather, it must be described by a superposition of different particle-hole states.

In theory it is easy to switch interactions on and off artificially and to tailor the Hamiltonian and the interaction matrix elements in such ways as to isolate the origin of an effect from other possible sources. For example, by setting the matrix elements $\langle\Phi_i^a|\hat{V}_{\mathrm{e-e}}|\Phi_j^b\rangle = 0$ if $i \neq j$, i.e., employing the intrachannel scenario, we obtain results that cannot describe electron-hole correlation except for the hole where the electron came from. In contrast, activating the full interchannel coupling $\langle\Phi_i^a|\hat{V}_{\mathrm{e-e}}|\Phi_j^b\rangle \neq 0$ for all combinations of indices will produce other results. Comparing the results produced with the two different schemes enables us to evaluate the impact of electron correlation effects. This will be exploited in particular in Ch. 7, where correlation effects in xenon are studied.

Furthermore, the Hartree-Fock-Slater (HFS) mean-field approach [137, 138] can be used within TDCIS by utilizing the HFS potential instead of the calculated Coulomb integrals to simulate a one-particle picture. The HFS approach is used in the software package XATOM, an integrated toolkit [139, 140] for the description of x-ray ionization of atoms, which was developed by Sang-Kil Son in our group. Briefly, in the HFS

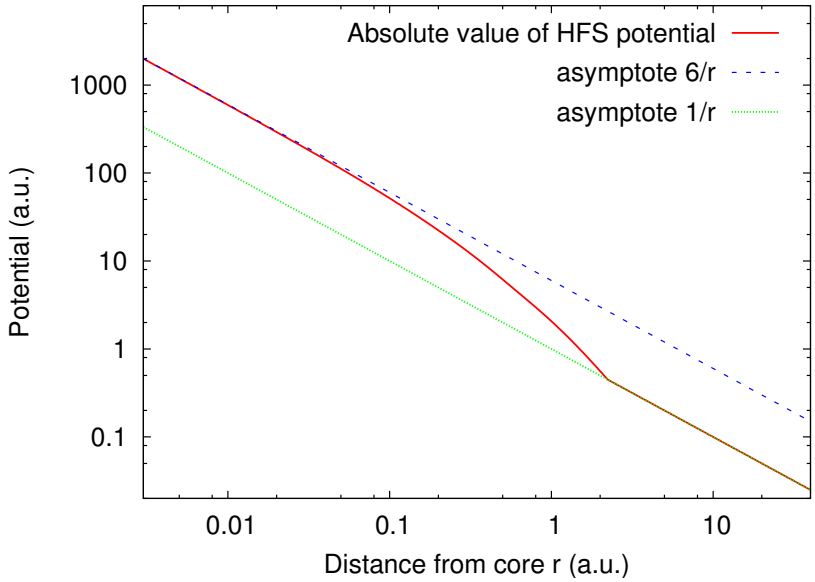

Figure 2.3: Abolute value of the HFS potential for carbon in a double-logarithmic plot. Also shown are the two asymptotic potentials for small (Z/r) and large $(1/r)$ distances from the core.

picture the exchange interaction between the electrons is modeled by the local density approximation. This results in an effective one-particle picture where the electron experiences a mean-field potential $V(\mathbf{r})$ created by all the electrons in the shell:

$$V(\mathbf{r}) = -\frac{Z}{r} + \int \mathrm{d}^3 r' \frac{\rho(\mathbf{r})}{|\mathbf{r} - \mathbf{r}'|} + V_{\mathbf{ex}}(\mathbf{r}). \tag{2.16}$$

Here Z is the nuclear charge, and ρ is the electronic density of the N_{elec} electrons. The Slater exchange potential is given by

$$V_{\mathbf{ex}}(\mathbf{r}) = -\frac{3}{2}\left[\frac{3}{\pi}\rho(\mathbf{r})\right]^{1/3}. \tag{2.17}$$

For the case of large distances from the origin the Latter tail correction [141] can be used to obtain the proper asymptotic potential for both occupied and unoccupied orbitals:

$$V(\mathbf{r}) = -(Z'+1)/r, \text{ if } -Z/r + \int \mathrm{d}^3 r' \frac{\rho(\mathbf{r})}{|\mathbf{r} - \mathbf{r}'|} + V_{\mathbf{ex}}(\mathbf{r}) < -(Z'+1)/r,$$

with the effective charge $Z' = Z - N_{\mathrm{elec}}$. In this way, we obtain the asymptotic behavior of Z/r for small radii from the ion (the electron can feel the nucleus as a whole as a Coulomb attractor). Also, another asymptote of $1/r$ for large distances is obtained (from afar, the $N_{\mathrm{elec}} - 1$ positive nuclear charges are screened by the other electrons and the electron experiences an effective Coulomb potential equivalent to one unscreened charge).

The strategy of comparing HFS results with full TDCIS results will be pursued in Ch. 9. The HFS potential is calculated utilizing XATOM. In Fig. 2.3 the HFS potential for carbon (nuclear charge $Z = 6$) which will be used for the x-ray ATI study is shown together with the asymptotes $6/r$ and $1/r$ for small and large distances from the ion, respectively.

3 Additional features within TDCIS

New propagation method and diagonalization of the Hamiltonian

As mentioned in the introduction the XCID package was extended by adding new capabilities and by implementing new features, while adapting the software package to the issues we encountered in the various projects. In this chapter I summarize two additional computational methods: the first section deals with a stable propagation scheme for forward *and* backward propagation and the second section with a method for the calculation and analysis of eigenstates of the Hamiltonian.

3.1 Lanczos propagation

In Ch. 2 I alluded to the fact that time propagation is employed for the numerical time integration of the Schrödinger equation (2.2). Common propagation schemes for wave propagation in media and, in particular, for wave function propagation are the split operator method [142, 143], the Chebyshev expansion method [144], and Runge-Kutta algorithms of fourth order [145]. The latter are known to be stable if the time step is chosen to be sufficiently small (in our cases a time step that usually leads to convergence for moderate field strengths is, e.g., 0.05 a.u.).

In all projects presented in this work, except for the optimal control problem discussed in Ch. 8, the Runge-Kutta algorithm of fourth order was used and led to converged results. The reason why the symmetry in time is of less importance and why the precision of the Runge-Kutta propagation usually suffices is the following: In standard atomic physics problems mere propagation of the Schrödinger equation in the forward direction is performed in order to obtain the relevant observables and dynamics, e.g. ionization yields, cross sections, electron spectra, etc. In contrast, the optimization algorithm employed in Ch. 8, the Krotov algorithm, involves in addition backward propagation which entails the need for further accuracy in propagation. It is known, that the Runge-Kutta algorithm is not symmetric in time which obviously leads to problems if the backward propagation is an essential ingredient of an iterative method. For this reason, the Lanczos algorithm for Hermitian matrices was implemented. The Arnoldi iteration or algorithm, which is called Lanczos algorithm

in the case of Hermitian matrices, belongs to the Krylov subspace methods [146] and has been used for atomic and molecular physics problems before [147, 148]. With this development we are able to employ a stable propagation scheme for forward *and* backward propagation of the wave function. In the following I give a brief overview of the Lanczos algorithm as implemented within TDCIS.

3.1.1 Lanczos algorithm

Suppose that some of the eigenvalues of a large and sparse matrix $A \in \mathbb{K}^{n\times n}$, over a field $\mathbb{K}$, shall be calculated, which is either symmetric, if $A \in \mathbb{R}$, or Hermitian, if $A \in \mathbb{C}$. If the matrix is large, full diagonalization is not the method of choice to obtain the spectrum and the eigenvectors. Instead, the eigenvalues and eigenvectors shall be approximated in an iterative manner such that the full diagonalization of A is circumvented. Let $\lambda_1, \ldots, \lambda_n$ be the n eigenvalues of A, ordered by their magnitude. The Rayleigh quotient

$$R(\mathbf{x}) = \frac{\mathbf{x}^* A \mathbf{x}}{\mathbf{x}^* \mathbf{x}} \tag{3.1}$$

gives us the smallest and the largest eigenvalues by the relations $\lambda_1 = \max_{\mathbf{x}\neq\mathbf{0}} R(\mathbf{x})$ and $\lambda_n = \min_{\mathbf{x}\neq\mathbf{0}} R(\mathbf{x})$ [146]. Let $\mathcal{V}_k$ be a subspace of $\mathbb{K}^{n\times n}$ and let $\{\mathbf{q}\}_1^k = \{\mathbf{q}_1, \mathbf{q}_2, \ldots, \mathbf{q}_k\}$ be an orthonormal basis of $\mathcal{V}_k$. Arranging the vectors $\mathbf{q}_k$ as columns in a matrix, let us call it Q_k the eigenvalues of $Q_k^T A Q_k$ shall approximate the eigenvalues of A. The Lanczos method generates the vectors $\mathbf{q}_k$ iteratively, such that the eigenvalues of the matrices $Q_k^T A Q_k = T_k \in \mathbb{K}^{k\times k}$, with $k < n$, are, with $k \to k+1$, progressively better approximations to the eigenvalues of A. To understand how the Lanczos algorithm determines increasingly better eigenvalues consider the Rayleigh quotient of the matrix T_k

$$\lambda_1 \geq \max_{\mathbf{y}\neq\mathbf{0}} R(Q_k\mathbf{y}) = R(\mathbf{u}_k) \equiv M_k, \tag{3.2a}$$

$$\lambda_n \leq \min_{\mathbf{y}\neq\mathbf{0}} R(Q_k\mathbf{y}) = R(\mathbf{v}_k) \equiv m_k. \tag{3.2b}$$

with vectors $\mathbf{u}_k, \mathbf{v}_k \in \operatorname{span}\{\mathbf{q}_1, \mathbf{q}_2, \ldots, \mathbf{q}_k\}$. $R(\mathbf{x})$ increases most rapidly in the direction of the gradient

$$\nabla R(\mathbf{x}) = \frac{2}{\mathbf{x}^*\mathbf{x}} \left[A\mathbf{x} - R(\mathbf{x})\mathbf{x}\right], \tag{3.3}$$

from which it follows that $\nabla R(\mathbf{x}) \in \operatorname{span}\{\mathbf{x}, A\mathbf{x}\}$. The largest eigenvalue of the next iteration step M_{k+1} will be larger than M_k, and therefore approach the "real" eigenvalue of the original matrix A, if the next vector $\mathbf{q}_{k+1}$ is determined such that $\nabla R(\mathbf{x}) \in \operatorname{span}\{\mathbf{q}_1, \mathbf{q}_2, \ldots, \mathbf{q}_{k+1}\}$. Following the same argument for the eigenvalue of minimal magnitude, if also $\nabla r(\mathbf{v}_k) \in \operatorname{span}\{\mathbf{q}^1, \mathbf{q}^2, \ldots, \mathbf{q}^{k+1}\}$ then $m_{k+1} < m_k$, because $R(\mathbf{x})$ decreases most rapidly in the direction of the negative gradient $-\nabla R(\mathbf{x})$.

Therefore, both requirements can be satisfied if $\mathbf{q}_{k+1}$ is chosen such that

$$\text{span}\left\{\mathbf{q}_1, \ldots, \mathbf{q}_{k+1}\right\} = \text{span}\left\{\mathbf{q}_1, A\mathbf{q}_1, A^2\mathbf{q}_1, \ldots, A^k\mathbf{q}_1\right\}. \tag{3.4}$$

This space, which results by applying successively higher powers of the matrix A, is called Krylov space. Thus, now the problem is reformulated and the new objective is to calculate efficiently orthonormal bases of these Krylov subspaces. In the following the Lanczos algorithm is developed explicitly and applied to the time propagation of the wave function.

3.1.2 Application to the Schrödinger equation and implementation

In our case we wish to solve the time-dependent Schrödinger equation in the interaction picture

$$i\partial_t|\Psi(t)\rangle = \hat{H}(t)|\Psi(t)\rangle. \tag{3.5}$$

Formally this equation has the solution

$$|\Psi(t)\rangle = \hat{U}(t,0)|\Psi(0)\rangle, \tag{3.6}$$

where

$$\hat{U}(t,0) = \mathcal{T}\exp\left[-i\int_0^t \mathrm{d}\tau \hat{H}(\tau)\right] \tag{3.7}$$

is the time evolution operator. Here, $\mathcal{T}$ denotes the time-ordering operator

$$\mathcal{T}[\hat{H}(t_1)\hat{H}(t_2)] = \begin{cases} \hat{H}(t_1)\hat{H}(t_2) & \text{if } t_1 < t_2 \\ \hat{H}(t_2)\hat{H}(t_1) & \text{if } t_1 > t_2. \end{cases} \tag{3.8}$$

Therefore, in an approximation we can write the wave function at the next time step $t + \mathrm{d}t$ as

$$|\Psi(t+\mathrm{d}t)\rangle = \mathrm{e}^{-i\hat{H}\left(t+\frac{\mathrm{d}t}{2}\right)\mathrm{d}t}|\Psi(t)\rangle + \mathcal{O}(\mathrm{d}t^3). \tag{3.9}$$

Since the Hamiltonian matrix can be very large, we do not aim at diagonalizing it directly. Instead, the right hand side shall be approximated numerically, i.e., we want to find an expression for the exponential operator acting on the wave function $|\Psi(t)\rangle$ which requires only matrix-vector or matrix-matrix multiplications for small and/or sparse matrices. For this purpose, we make use of the fact that the Hamiltonian is a Hermitian and even a real and symmetric matrix in the case where the splitting method is used for the absorption of the wave function at the end of the grid, see Ch. 5). We build up the Krylov space by acting on the starting vector $|\Psi(0)\rangle$ with increasingly higher powers of the Hamiltonian operator

$$\hat{H}^n|\Psi(0)\rangle = \mathbf{v}^n, \tag{3.10}$$

where the set of N vectors $\mathbf{v}_n$, $n = 0, 1, \ldots N-1$, is the Krylov basis. N is, therefore, the dimension of the Krylov space. The smaller the dimension N the more efficient and numerically cheap this algorithm will be. The aim is to orthonormalize this basis set. If we have a tridiagonal matrix

$$T = Q^T \hat{H} Q, \tag{3.11}$$

with Q being orthogonal, we can find an orthogonal matrix U ($U^T U = \mathbb{1}$) that diagonalizes T. Let us call the diagonal matrix $D = U^T T U$. Then from $D = U^T Q^T \hat{H} Q U$ it follows that

$$Q^T \hat{H} Q = U D U^T. \tag{3.12}$$

From the properties of diagonal matrices it follows that

$$U\, \mathrm{e}^{-iD\mathrm{d}t}\, U^T = \mathrm{e}^{-iQ^T \hat{H} Q \mathrm{d}t} \Rightarrow \tag{3.13}$$

$$\mathrm{e}^{-i\hat{H}\mathrm{d}t}\, |\Psi\rangle \approx Q U\, \mathrm{e}^{-iD\mathrm{d}t}\, U^T Q^T |\Psi\rangle. \tag{3.14}$$

Orthonormalizing the N vectors $\{\mathbf{v}_n\}$ we obtain an orthonormal set of vectors $\{\mathbf{q}_n\}$. If we arrange them as columns in a matrix Q we know that the matrix $Q^T \hat{H} Q = T$ is tridiagonal (QR factorization) [146]:

$$T = \begin{pmatrix} \alpha_0 & \beta_1 & & & & & \\ \beta_1 & \alpha_1 & \beta_2 & & & & \\ & \beta_2 & \alpha_2 & \beta_3 & & 0 & \\ & & \ddots & \ddots & & & \\ & & & & \ddots & & \\ & 0 & & & & & \beta_{N-1} \\ & & & & \beta_{N-1} & & \alpha_N \end{pmatrix} \tag{3.15}$$

Thus, we wish to directly compute the elements of this tridiagonal matrix, $\{\alpha_k\}_{k=1}^{N}$, $\{\beta_k\}_{k=1}^{N-1}$, in an iterative way. Since $\hat{H} Q = Q T$ we find

$$\hat{H} \mathbf{q}_k = \beta_{k-1} \mathbf{q}_{k-1} + \alpha_k \mathbf{q}_k + \beta_k \mathbf{q}_{k+1}, \tag{3.16}$$

while $\beta_0 \mathbf{q}_0 \equiv 0$. Solving this equation for $\mathbf{q}_{k+1}$, if

$$\mathbf{r}_k = \left(\hat{H} - \alpha_k \mathbb{1}\right) - \beta_{k-1} \mathbf{q}_{k-1} \neq 0,$$

then $\mathbf{q}_{k+1} = \mathbf{r}_k / \beta_k$, where $\beta_k = |\mathbf{r}_k|$. The vectors $\mathbf{q}_k$ are called Lanczos vectors. We see that we need three vectors to store the necessary quantities for the calculation of the Lanczos vectors – the previous vector $\mathbf{v}_k$, the current vector $\mathbf{q}_k$, and the next vector $\mathbf{r}_k$ – and two more vectors to store the α and β coefficients. In this way the

Lanczos algorithm is obtained, where the starting vector is denoted by $\mathbf{q}_0$:

$$
\begin{aligned}
&k = 0;\ \mathbf{r}_k = \mathbf{q}_0/|\mathbf{q}_0|;\ \beta_0 = 1;\ \mathbf{r}_1 = \hat{H}\mathbf{q}_0;\ Q(:,1) = \mathbf{r}_1 \\
&\text{do while } (\beta_k \neq 0)^{1} \\
&\quad k = k + 1 \\
&\quad \mathbf{v}_k = \mathbf{q}_{k-1};\ \mathbf{q}_k = \mathbf{r}_{k-1}/\beta_{k-1};\ Q(:,k) = \mathbf{q}_k; \\
&\quad \mathbf{r}_k = \hat{H}\mathbf{q}_k;\ \alpha_k = \mathbf{q}_k \cdot \mathbf{r}_k \\
&\quad \mathbf{r}_k = \mathbf{r}_k - \beta_{k-1}\mathbf{v}_k - \alpha_k\mathbf{q}_k;\ \beta_k = |\mathbf{r}_k| \\
&\text{end do}
\end{aligned}
\tag{3.17}
$$

The tridiagonal matrix T is built up and is then diagonalized using the LAPACK [149] routine for a sparse, general, symmetric matrix to yield the eigenvalues that form the matrix D. Then the matrix product $P \equiv QU$ is calculated. Hence, we arrive at the following expression for the time-propagated wave function:

$$
\mathrm{e}^{-i\hat{H}\mathrm{d}t}\,|\Psi(t)\rangle = P\,\mathrm{e}^{-iD\mathrm{d}t}\,P^T|\Psi(t)\rangle \tag{3.18}
$$

In practice, the algorithm which is implemented within TDCIS works as follows:

- At time step t the time $t + \mathrm{d}t/2$ is defined at which the Hamiltonian shall be evaluated. The parameters N and the propagation time step $\mathrm{d}t$ are read in from the input file (specified by the user), common sizes of N are on the order of five to twenty vectors in order to obtain converged results. The starting vector is created from the coefficients of the wave function at time t (at the very beginning this is the Hartree-Fock ground state).
- The subroutine performing the Lanczos iteration step described above is called.
- It returns the matrix P and the eigenvalues of the tridiagonal matrix in the matrix D. The matrix-vector multiplication $P\,\mathrm{e}^{-iD\mathrm{d}t}\,P^T|\Psi(t)\rangle$ is performed. Exploiting the diagonal nature of D the operations result in vector-vector multiplications for all N columns, the dimension of the Krylov space.
- The propagated wave function at time step $t + \mathrm{d}t$ is returned: $|\Psi(t + \mathrm{d}t)\rangle$.

Compared to the Runge-Kutta algorithm, when using the same time step $\mathrm{d}t = 0.05$ a.u. the propagation consumes about 3/2 the time duration when using a Krylov space dimension of $N = 6$.

The Lanczos-Arnoldi propagation method was tested for various propagation settings and it was found that it yields the same results as the Runge-Kutta algorithm with the additional feature of a higher precision of about 6 orders of magnitude when used in the backward direction. This precision will be of great importance for the stability of the optimization algorithm utilized in Ch. 8.

[1] Numerically, this is solved by a cut-off parameter: For instance, $|\beta_k| > 10^{-18}$.

3.2 ARPACK - Arnoldi algorithm for the diagonalization of the Hamiltonian

The diagonalization of large matrices is one of the most common procedures that are treated numerically. In this respect the versatility of the software package ARPACK is remarkable. It enables the user to solve eigenvalue problems of huge dimensions providing many options. Therefore, we chose to implement ARPACK within XCID and use the diagonalization strategy in combination with TDCIS in order to obtain the eigenstates of the atomic systems under investigation. So far, within our group the explicit Hamiltonian eigenvalue problem had not been in the focus of interest but the investigations using TDCIS concentrated rather on ionization probabilities, hole populations, the ion density matrix elements, the HHG yield or cross sections. Therefore, the possibilities that ARPACK provides presented new features for our computational approach.

Very large Hamiltonian eigenvalue problems can involve matrices with a rank on the order of 10^6. For example, when high energies are involved and strong fields are considered, the necessary maximum angular momentum can be on the order of $l_{\max} = 100$. In combination with many active channels and around 1000 states in total the rank of a million is easily achieved. Typically, these matrices are sparse, but nevertheless an efficient diagonalization algorithm is indispensable. There are LAPACK routines, a package for the numerical solution of linear algebra problems, that can handle various types of sparse matrices, however the full diagonalization of the whole matrix is often not required. For this reason, the iterative Arnoldi algorithm was implemented in FORTRAN 77. The freely available package which received the name ARPACK consists now of a collection of efficient subroutines for solving large-scale eigenvalue problems, which partly also use LAPACK subroutines, and it contains interfaces for the communication with the various subroutines [150, 151]. It requires an inner product to be defined by the user and performs the matrix-vector operations within the Arnoldi algorithm to solve a general eigenvalue problem

$$A\mathbf{x} = \lambda B\mathbf{x}.$$

Similarly to the Lanczos-Arnoldi algorithm described below the Arnoldi algorithm employs Krylov techniques to construct subspaces of the eigenvector-space and obtain good approximations to the exact space of eigenvectors. Again, the structure is very closely related to the QR algorithm, where a matrix is decomposed into an orthogonal matrix Q and an upper triangular matrix R.

Depending on the request of the user it returns, eigenvalues, eigenvectors at either end of the spectrum: eigenvalues with the smallest or largest magnitude, largest or smallest real part etc. The package includes interfaces where the corresponding parameters that have to be defined by the user can be handed over to the subroutines of ARPACK. More details can be found in the ARPACK Users' Guide [150]. The main

difficulty of the programming task within TDCIS was to understand the structure of ARPACK, the order of the subroutines necessary for the diagonalization and the connection to the quantities of TDCIS. Assigning starting vectors and appropriate dimensions of the eigenvalue problem as well as convergence studies posed a challenge because of the large size and the partly excessive (for our needs) overhead that is created by this powerful software package. This is also the reason why the Lanczos-Arnoldi algorithm, discussed in the previous section, was implemented anew instead of accessing the ARPACK routines.

For our purposes the use of ARPACK is interesting because we want to be able to compute the eigenstates and the eigenvalues of the Hamiltonian. Our eigenproblem has the following form:

$$\left[\hat{H} + F(t)\hat{z}\right] |\Psi_n(t)\rangle = E_n(t)|\Psi_n(t)\rangle, \tag{3.19}$$

where $\hat{H}$ is the field-free Hamiltonian, $F(t)$ is the electric field and $\hat{z}$ is the position operator, so that $F(t)\hat{z}$ is the dipole interaction between field and electron for a light field which is polarized in the z-direction. E_n are the eigenenergies belonging to the eigenvector $|\Psi_n\rangle$ of the system. For each time t the field has a certain value and there is an instantaneous eigenvalue problem to be solved. The diagonalization of the many-body Hamiltonian including an electric field will be applied directly in the next chapter, Ch. 4, to a strong-field problem in helium. Through the diagonalization the instantaneous eigenstates are obtained from which the diabatic states can be constructed.

This diagonalization method is also very useful in a different context within the present work. By diagonalizing the Hamiltonian for the xenon atom we performed a more detailed characterization of the one-photon resonances in the XUV, which can be performed by imposing an overlap criterion between the ground state and the resonance state coupled by a dipole step. In this way, the relevant eigenstates that form temporarily trapped resonances can be identified (see Ch. 7).

4 Adiabaticity and diabaticity in strong-field ionization

Physical Review A **87**, 043422 (2013)

This chapter deals with the infrared end of the spectrum: the photon energy is very small compared to the electron binding energy of the atoms, i.e. we apply (strong) infrared pulses in order to study the dynamics of atoms. More precisely, in this chapter the nature of electronic states is studied in the tunneling regime. This regime is characterized by a quasistatic situation, which means that the oscillation of the applied field is so slow that the electron encounters a superposition of the potential associated with the instantaneous electric component of the optical field and the atomic potential. In this case, ionization of an atom by a strong optical field is often described in terms of electron tunneling through the potential barrier resulting from this superposition of the atomic potential and the potential of the external electric field. In the quasistatic scenario it is legitimate to calculate and analyze the instantaneous eigenstates to the Hamiltonian that contains the instantaneous electric field coupled to the atomic system. This will be done using ARPACK for the diagonalization.

In the strict tunneling regime, where the Keldysh parameter is smaller than one, $\gamma \ll 1$ (cf. Ch. 1), the electron response to the optical field is said to be adiabatic, and nonadiabatic effects are assumed to be negligible. Here, it is investigated to what degree this terminology is consistent with a language based on the so-called adiabatic representation. It is desirable to employ a well-defined language and utilize it in a precise way in order to understand phenomena in related fields and make progress across the disciplines.

4.1 Adiabatic representation

The adiabatic representation is commonly used in various fields of physics. For electronically bound states, the adiabatic representation yields discrete potential energy curves that are connected by nonadiabatic transitions. When applying the adiabatic representation to optical strong-field ionization, a conceptual challenge is that the eigenstates of the instantaneous Hamiltonian form a continuum; i.e., there are no

discrete adiabatic states. This difficulty can be overcome by applying an analytic-continuation technique. In this way, we obtain a rigorous classification of adiabatic states and a clear characterization of (non)adiabatic and (non)diabatic ionization dynamics which we will define in the following and distinguish them clearly. Moreover, we distinguish two different regimes within tunneling ionization and explain the dependence of the ionization probability on the pulse envelope.

Generally, when a time-dependent process is adiabatic, the state of the system at any given time is always an eigenstate of the instantaneous Hamiltonian, which depends on one or more external parameters (like the electric field). Consequently, the energy eigenstates and their corresponding eigenenergies become parametrized and lead to energy curves (or energy hyperplanes depending on the number of external parameters). Nonadiabatic dynamics occur when transitions between adiabatic curves start to appear. This is, particularly, the case when two adiabatic curves are energetically close to each other and the external parameters are changed relatively fast such that the system has no time to "instantaneously" respond to the change. As a result, the system is not in one defined adiabatic state anymore but rather in a superposition of several adiabatic eigenstates. In various fields of physics and chemistry the adiabatic representation has been used to study adiabatic and nonadiabatic effects. Its application includes fields like Rydberg atoms [152, 153], molecular dynamics [154–156], atomic and molecular collisions [157–159], and ultracold gases and trapped ions [160–162].

An important aspect in the adiabatic representation is the discreteness of eigenstates which is essential to obtain a discrete set of energy curves. In the case of strong-field ionization, however, the instantaneous eigenstates of the Hamiltonian form a continuum. Therefore, the identification of a nonadiabatic effect happens rather indirectly [163, 164]: either the spectrum of the photoelectron after the pulse or the field dependence of the ionization rate is analyzed. Various results on nonadiabatic behavior in strong-field ionization have been presented in the literature [165–167] and there are many different usages of the terms "adiabatic" and "nonadiabatic". By introducing an analytic continuation in the complex plane the instantaneous Hamiltonian becomes non-Hermitian and tunneling states appear as *discrete* eigenstates. These discrete states can be now used to apply the adiabatic representation to strong-field ionization dynamics.

In the following, the adiabatic representation is strictly applied to strong-field ionization and it is found that in the tunneling regime the ionization dynamics is defined by a *diabatic* rather than an adiabatic behavior. Diabatic dynamics means that the response of the system follows one specific diabatic state. Here, the diabatic states are defined by the overlap with the field-free eigenstates. In this formulation we find that the ionization dynamics can be divided into two regimes. Furthermore, with increasing frequency we observe a transition from the *diabatic* to the *nondiabatic* regime. In particular, we study the few-cycle limit and find a non-constant population as a function of the optical frequency which has been interpreted in the literature as a sign of a nonadiabatic process [41, 164]. I will show for a few-cycle pulse with a Keldysh

parameter $\gamma \ll 1$ that this effect rather represents a dependence on the form of the pulse and can be fully explained by a diabatic picture depending on a single diabatic state connected to the field-free ground state.

4.2 Adiabatic eigenstates

Whenever a system is given time to adjust to the parameters on which it depends, the response is called adiabatic. In the following, we derive the quantum-mechanical equations of motion in the adiabatic basis, which is given by the states that are eigensolutions to the Hamiltonian of the system for a set of instantaneous parameters.

Let us study a system where the Hamiltonian depends on an external time-dependent parameter $\epsilon(t)$. The time-dependent Schrödinger equation has the form

$$i\partial_t|\Psi(t)\rangle = \hat{H}(t)|\Psi(t)\rangle = \left\{\hat{H}_0 + \hat{U}[\epsilon(t)]\right\}|\Psi(t)\rangle. \tag{4.1}$$

$\hat{H}_0$ describes the atomic Hamiltonian, whereas $\hat{U}$ includes all external potentials and is dependent on the parameter $\epsilon(t)$. At a given time t, the instantaneous eigenstates, which constitute the adiabatic basis, are defined by[1]

$$\left[\hat{H}_0 + \hat{U}(t)\right]|\Psi_n(t)\rangle = E_n(t)|\Psi_n(t)\rangle. \tag{4.2}$$

To analyze adiabatic and nonadiabatic effects we expand the electronic wavefunction in terms of the adiabatic eigenstates, $|\Psi(t)\rangle = \sum_n \alpha_n(t)|\Psi_n(t)\rangle$. Upon inserting this expression into Eq. (4.1) and projecting onto the eigenstate $|\Psi_m(t)\rangle$, the equation of motion for the coefficient $\alpha_m(t)$ reads

$$i\dot{\alpha}_m(t) + i\sum_n \alpha_n(t)\langle\Psi_m(t)|\partial_t|\Psi_n(t)\rangle = \alpha_m(t)E_m(t). \tag{4.3}$$

The off-diagonal matrix elements $\langle\Psi_m(t)|\partial_t|\Psi_n(t)\rangle$ introduce couplings between different adiabatic eigenstates, thus making the dynamics nonadiabatic [168]. In the adiabatic approximation, where these couplings are considered to be very small, Eq. (4.3) becomes

$$i\dot{\alpha}_m(t) + i\alpha_m(t)\langle\Psi_m(t)|\dot{\Psi}_m(t)\rangle = \alpha_m(t)E_m(t), \tag{4.4}$$

which is solved with the initial condition $\alpha_m(0) = 1$ by

$$\alpha_m(t) = \exp\left[-i\int_0^t \mathrm{d}t' E_m(t')\right]\exp[i\gamma_m(t)], \tag{4.5}$$

where $\gamma_m(t) = i\int_0^t \mathrm{d}t'\langle\Psi_m(t')|\dot{\Psi}_m(t')\rangle$, so that the system evolves in a specific adia-

[1] The time dependence is implicit via the parameter $\epsilon(t)$.

batic eigenstate with a phase. If, on the other hand, $\langle\Psi_m(t)|\dot{\Psi}_n(t)\rangle$ cannot be neglected, the whole sum in Eq. (4.3) has to be considered, so that different adiabatic eigenstates get coupled and nonadiabatic motion emerges. We can use $\partial_t = \frac{\partial\epsilon}{\partial t}\partial_\epsilon$ and express the off-diagonal coupling elements also in terms of the change in ϵ:

$$\langle\Psi_m|\dot{\Psi}_n\rangle = \langle\Psi_m|\partial_\epsilon\Psi_n\rangle\frac{\partial\epsilon}{\partial t}. \tag{4.6}$$

Considering a two-level system with an external perturbation proportional to ϵ, the Hamiltonian of the system takes the form

$$\hat{H} = \underbrace{\begin{pmatrix}-1 & 0\\ 0 & 1\end{pmatrix} + \frac{\Delta}{2}\begin{pmatrix}0 & 1\\ 1 & 0\end{pmatrix}}_{\hat{H}_0} + \underbrace{\frac{\epsilon}{2}\begin{pmatrix}1 & 0\\ 0 & -1\end{pmatrix}}_{\hat{U}}, \tag{4.7}$$

where Δ is an internal coupling parameter. In Fig. 4.1 the energy curves of the two adiabatic states $|\Psi_1\rangle$ and $|\Psi_2\rangle$ of this system are shown as a function of the external parameter ϵ, assuming $\Delta = 1$. The internal coupling between the diabatic states $|1\rangle = (1,0)^T$ and $|2\rangle = (0,1)^T$ results in the effect that the two adiabatic curves do not cross. This phenomenon is known as an "avoided crossing". We see that Δ is the energy splitting between $|\Psi_1\rangle$ and $|\Psi_2\rangle$ at the degeneracy point of the states $|1\rangle$ and $|2\rangle$. If the parameter ϵ is changed sufficiently slowly, the system will remain in a given adiabatic state $|\Psi_i\rangle$ if, for $\epsilon \ll 1$ or $\epsilon \gg 1$, the system was in the state $|\Psi_i\rangle$. Note that in the vicinity of $\epsilon = 1$ the character of the adiabatic states changes from $|1\rangle$ to $|2\rangle$ and vice versa. If ϵ changes rapidly in the vicinity of $\epsilon = 1$, the system has no time to change the character of its state; it makes a transition from one adiabatic state to the other and follows the diabatic states $|1\rangle$ and $|2\rangle$, respectively. These jumps between adiabatic curves make the resulting dynamics nonadiabatic. For a given value of the external parameter, we can obtain the diabatic states also by choosing the adiabatic eigenstates with the maximal overlap with the free states ($\epsilon = 0$). For $\epsilon < 1$, the diabatic state $|1\rangle$ has the maximal overlap with the adiabatic state $|\Psi_1\rangle$, while for $\epsilon > 1$ the overlap of state $|1\rangle$ with the adiabatic state $|\Psi_2\rangle$ is maximal, and vice versa for the diabatic state $|2\rangle$. Asymptotically, the states $|1\rangle$ and $|2\rangle$ correspond to the states $|\Psi_1\rangle$ and $|\Psi_2\rangle$ before the avoided crossing, and vice versa after the crossing. Near the crossing an interpolation is performed in order to obtain a continuous and smooth state.

A system's dynamics can of course also be formulated in other representations, e.g., in a diabatic basis [169], where the diabatic states do cross (see the states $|1\rangle$ and $|2\rangle$ in Fig. 4.1). Usually the basis is chosen such, that the off-diagonal couplings in Eq. (4.6) vanish or are at least small [158, 170]. However, the diabatic basis, which is derived from the adiabatic basis by a unitary transformation, is not unique and there are many different approaches for reaching a diabatic representation [171–173]. One practicable method of diabatization is a local diabatization method, which

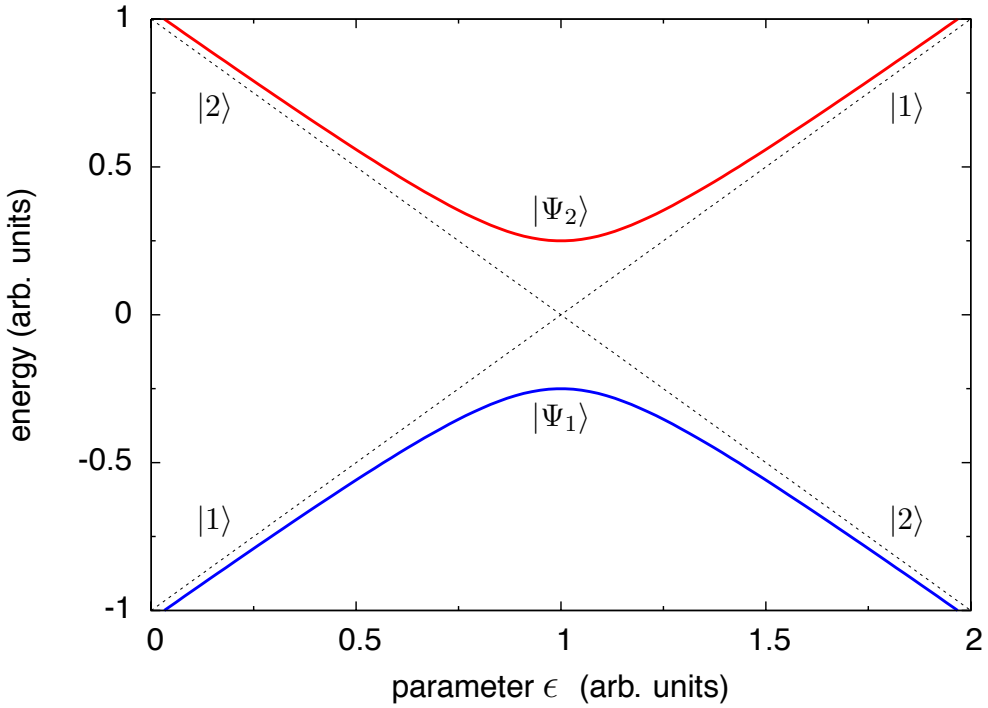

Figure 4.1: The energy curves of the two adiabatic states $|\Psi_1\rangle$ and $|\Psi_2\rangle$ are shown as functions of the parameter ϵ. Through the off-diagonal matrix element $\Delta/2$ a nonadiabatic transition is possible, whereupon the system follows the diabatic states $|1\rangle$ and $|2\rangle$, respectively. © 2013 APS.

means that the diabatic state is constructed piecewise in a two-level model: At each avoided crossing between two adiabatic states the diabatic state is followed. To this end, the size of the overlap with the corresponding field-free state can be used as a criterion. This method turns out to be fruitful for the description of diabatic and nondiabatic strong-field ionization (see Sec. 4.4). Once a diabatic representation has been found, one can ask with which rate transitions between diabatic states occur. These transitions will be called nondiabatic.

In the following section we will make use of the fact that for weak perturbations the adiabatic eigenstates can be approximated through the field-free eigenstates. Therefore, the diabatic states exhibiting the maximal overlap with the field-free states are also the adiabatic states. In this case, the nondiabatic transitions are exactly the nonadiabatic transitions described above.

4.3 One-photon absorption

First, we analyze the case of one-photon absorption within the adiabatic representation. If the system is exposed to a weak electric field of the form $F(t) = F_0 \cos(\omega t)$ (in the dipole approximation, see Sec. 4.4), with a frequency ω, the system Hamiltonian

is perturbed by the term $F(t)\,\hat{z}$ [174], where $\hat{z}$ is pointing in the direction of the field (which is assumed to be linearly polarized). The Hamiltonian in Eq. (4.1) takes the form

$$\hat{H}(t) = \hat{H}_0 + F(t)\hat{z}, \tag{4.8}$$

where $\hat{H}_0$ is the atomic Hamiltonian and the electric field $F(t)$ is coupled classically to the dipole operator $\hat{z}$ of the electron. The field $F(t)$ corresponds to the parameter ϵ of Sec. 4.2.

In the following, we show that in the adiabatic representation the off-diagonal coupling elements in Eq. (4.3) are crucial for introducing transitions. Let $\{|\Psi_n^{(0)}\rangle\}_{n=0}^{\infty}$ be the eigenstates of the field-free Hamiltonian, $H_0\,|\Psi_n^{(0)}\rangle = \omega_n|\Psi_n^{(0)}\rangle$. For simplicity, we assume that the initial and final states of interest in the one-photon transition are nondegenerate. Performing static perturbation theory to first order, the adiabatic eigenstates read [175]

$$|\Psi_n^{(1)}\rangle = |\Psi_n^{(0)}\rangle + \sum_{k\neq n} \frac{\langle\Psi_k^{(0)}|F\hat{z}|\Psi_n^{(0)}\rangle}{\omega_n - \omega_k}|\Psi_k^{(0)}\rangle. \tag{4.9}$$

Inserting Eq. (4.9) in Eq. (4.6) with ϵ being the field F, we obtain the nonadiabatic coupling elements to first order in F:

$$\frac{\partial F}{\partial t}\langle\Psi_m^{(0)}|\sum_{k\neq n}\frac{\langle\Psi_k^{(0)}|\hat{z}|\Psi_n^{(0)}\rangle}{\omega_n-\omega_k}|\Psi_k^{(0)}\rangle = \frac{\partial F}{\partial t}\frac{\langle\Psi_m^{(0)}|\hat{z}|\Psi_n^{(0)}\rangle}{\omega_n-\omega_m}. \tag{4.10}$$

We are now ready to solve Eq. (4.3) including nonadiabatic coupling. We may treat the operator $\hat{V}_F = \frac{\partial F}{\partial t}\,\partial_F$ as a perturbing time-dependent operator and, hence, analyze the states with time-dependent perturbation theory [175]. The first-order correction to the zeroth-order coefficient [Eq. (4.5)] is given by

$$\alpha_f^{(1)}(t) = -i\int_0^t \mathrm{d}t' e^{i(\omega_f-\omega_i)t'}\frac{\partial F}{\partial t'}\frac{\langle\Psi_f^{(0)}|\hat{z}|\Psi_i^{(0)}\rangle}{\omega_f-\omega_i}. \tag{4.11}$$

Assuming $\omega_f > \omega_i$, we obtain the total transition probability per unit time

$$w_i = \sum_f \frac{|\alpha_f^{(1)}|^2}{t} = 2\pi\sum_f\left|\langle\Psi_f^{(0)}|\frac{F_0\hat{z}}{2}|\Psi_i^{(0)}\rangle\right|^2\delta(\omega_f-\omega_i-\omega). \tag{4.12}$$

This equation is exactly Fermi's golden rule [176]. In the present approach it is the nonadiabatic coupling that induces one-photon transitions between the field-free eigenstates. Viewed in this way, the phenomenon of one-photon absorption is entirely nonadiabatic. In the one-photon case, the states are well separated by a large energy gap and there is no avoided crossing due to the weak field, which is only a perturbation to the field-free states. Note that the adiabatic states coincide with the diabatic states in the weak-field limit.

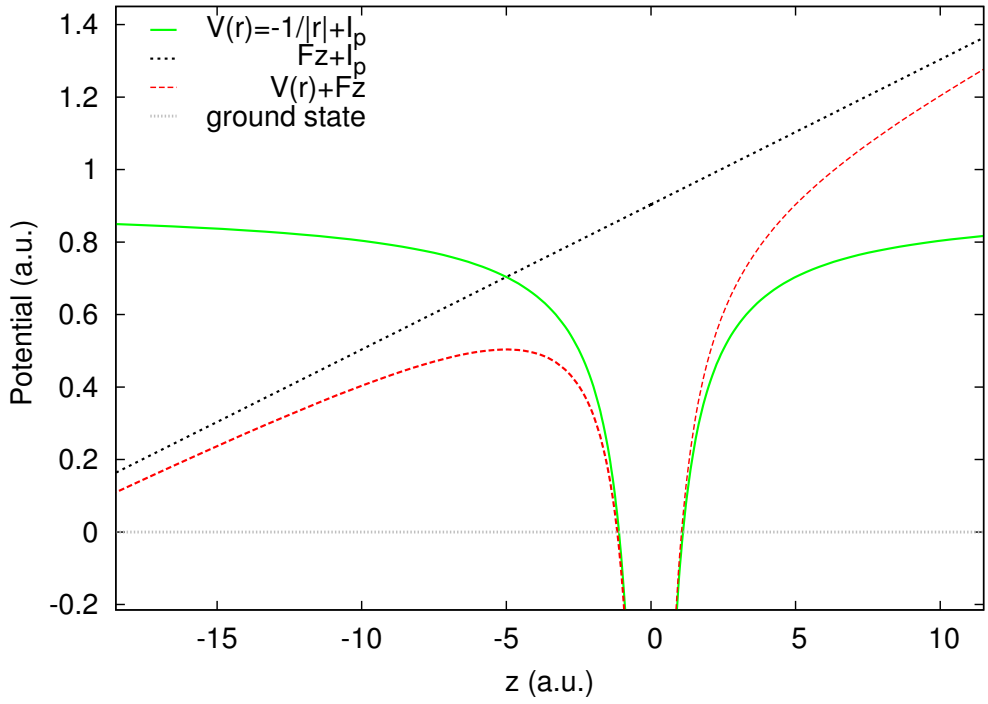

Figure 4.2: The pure Coulomb potential of the helium atom (solid green curve, shifted by the ionization potential I_p) is tilted in the presence of the electric field (dotted black line) and a barrier of finite width in z-direction is created (dashed red line). The dotted grey line denotes the field-free ground-state energy.

4.4 Strong-field ionization of atoms

While in the case of one-photon ionization the photon energy necessarily exceeds the ionization potential, we will now examine the situation where the atomic system is irradiated by an intense electric field $F(t)$ with a low photon energy, i.e., many photons are needed to ionize the atom.

When applying a strong external field [see Eq. (4.8)] the effective potential seen by an electron gets tilted, see Fig. 4.2. Therefore, a barrier of finite height is created through which the electron can tunnel. If the electric field is so strong that the electron's energy lies above the barrier, the electron can just leave the atom without tunneling. This effect is called above-barrier ionization [177, 178]. This tunneling picture of a tilted potential relies on the length form of the light-matter interaction, i.e., $F(t)\,\hat{z}$. Furthermore, the form of the Hamiltonian [cf. Eq. (4.8)] is a result of the dipole approximation, which holds in our case, because the size of the system of interest (a few Å) is much smaller than the wavelength of the light pulse (≈ 1 μm) [136, 179].

In order to describe strong-field ionization dynamics, the Schrödinger equation of the atom exposed to the field has to be solved nonperturbatively because perturbation theory fails for these high field strengths. As shown in Sec. 4.2 in the adiabatic case the system will follow a given adiabatic state without making any transition.

However, in the presence of a static electric field, electronically bound states become tunneling states, which means that there is ionization via tunneling.

In the following, we study helium as a concrete example to illustrate tunneling ionization within the framework of the adiabatic representation.

4.4.1 Constructing adiabatic and diabatic states for helium

As already discussed (see Sec. 4.1), in strong-field ionization the spectrum forms a continuum where a direct application of the adiabatic representation is inconvenient. To overcome this problem, a rigorous analytical continuation of the Hamiltonian can be performed by rotating the electron coordinates about an angle into the complex plane; this procedure is called complex scaling [180]. Another way to generate discrete eigenstates is to add a CAP to the Hamiltonian [181]. It can be shown that the latter method, which is conceptually easier, is closely connected to the complex scaling approach [182]. The key idea here is that for every tunneling state, i.e., every adiabatic atomic state that allows the electron to tunnel through the field-induced barrier, there exists a discrete eigenstate — a so-called Gamow vector [183] or Siegert state [184] — of the instantaneous Hamiltonian. A Siegert state is associated with a complex energy and lies outside the Hermitian domain of the Hamiltonian. In fact, the associated wave function is exponentially divergent for large distances from the atom. Complex scaling or the use of a CAP eliminates the divergent behavior and renders the tunneling wavefunction square integrable. Thus, by making the Hamiltonian non-Hermitian, it becomes possible to calculate, within Hilbert space, the complex Siegert energies of tunneling states. The imaginary part of the Siegert energy E provides the tunneling rate Γ of each Siegert state by the relation $\Gamma = -2\ \mathrm{Im}(E)$ [185, 186].

In order to obtain the instantaneous eigenstates we solve Eq. (4.2) with the Hamiltonian in Eq. (4.8) including a CAP. This yields the adiabatic eigenstates and corresponding eigenenergies of the atom shown in Fig. 4.3. A more detailed description of the methods used is given in Sec. 3.2. We observe many avoided crossings among the higher adiabatic eigenstates for field strengths in the range below 0.01 a.u. (1 a.u.$= 5.14 \times 10^9$ V/cm), while the ground state energy does not change significantly. One might wonder whether for sufficiently slow ramping of the electric field the atom follows the adiabatic ground state. Indeed, for field strengths up to 0.02 a.u. the adiabatic ground-state energy seems to remain constant. But we know that the electric field can mix a whole manifold of excited states into the field-free states. When this happens, the adiabatic ground state loses the character of the field-free ground state (cf. Fig. 4.1). Analyzing the avoided crossings involving the adiabatic ground state around the field strength of 0.02 a.u., we find that the ramping of the field has to be so slow that it lies in the radio frequency regime. Therefore, the system does not follow the adiabatic ground state for the frequency range of light usually employed in experiments (typically around 800 nm, corresponding to 4×10^{14} Hz).

The electronic state follows the instantaneous eigenstate that has the maximal over-

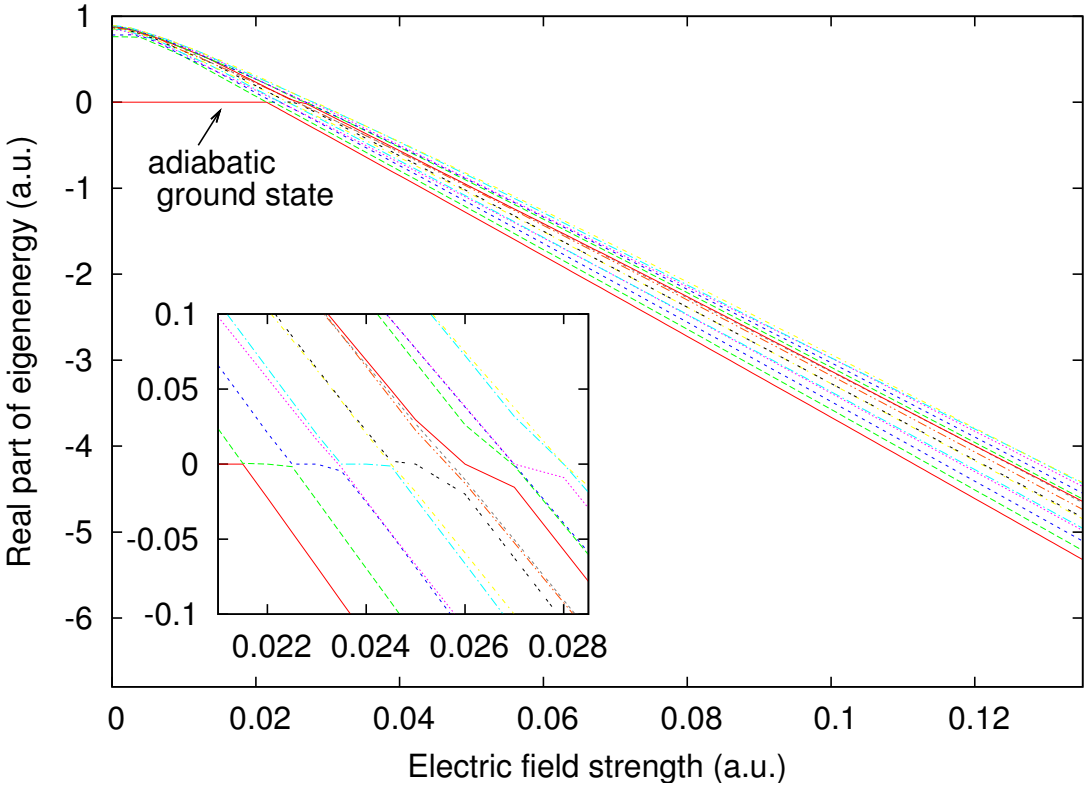

Figure 4.3: The real part of the energy of the first adiabatic eigenstates as a function of a static electric field. The inset magnifies avoided crossings for small electric fields. © 2013 APS

lap with the field-free ground state. This is exactly the diabatic behavior described in Sec. 4.2, where the electronic state jumps from one adiabatic state to the other, keeping its field-free character. Here, we employ the diabatization method already alluded to in Sec. 4.2, where we construct the diabatic state $|\Psi_i^{(d)}(t)\rangle$ from the adiabatic basis $\{|\Psi_n(t)\rangle\}$ using the criterion of maximal overlap with the field-free state $|\Psi_i^{(0)}\rangle$, i.e.,

$$|\Psi_i^{(d)}(t)\rangle = |\Psi_n(t)\rangle, \text{ where} \qquad (4.13)$$
$$|\langle\Psi_n(t)|\Psi_i^{(0)}\rangle| > |\langle\Psi_m(t)|\Psi_i^{(0)}\rangle|, \ \forall m \neq n.$$

This can be done as long as there is one distinct adiabatic state with a prominent character of the corresponding field-free state, so that the (orthogonal) complement of adiabatic states which are mixed in is small and can be ignored. The procedure works in principle also for excited states. However, for excited states the condition of a small admixture breaks down already at low field strengths, such that this construction method works best for the field-free ground state. The overlap of the corresponding diabatic state $|\Psi_0^{(d)}\rangle$ with the field-free ground state $|\Psi_0^{(0)}\rangle$ is always larger than 90% for field strengths considered here (see Fig. 4.4 c). Figures 4.4 a) and 4.4 b) show the real part of the energy and the tunneling rate of $|\Psi_0^{(d)}\rangle$ as a function of the electric

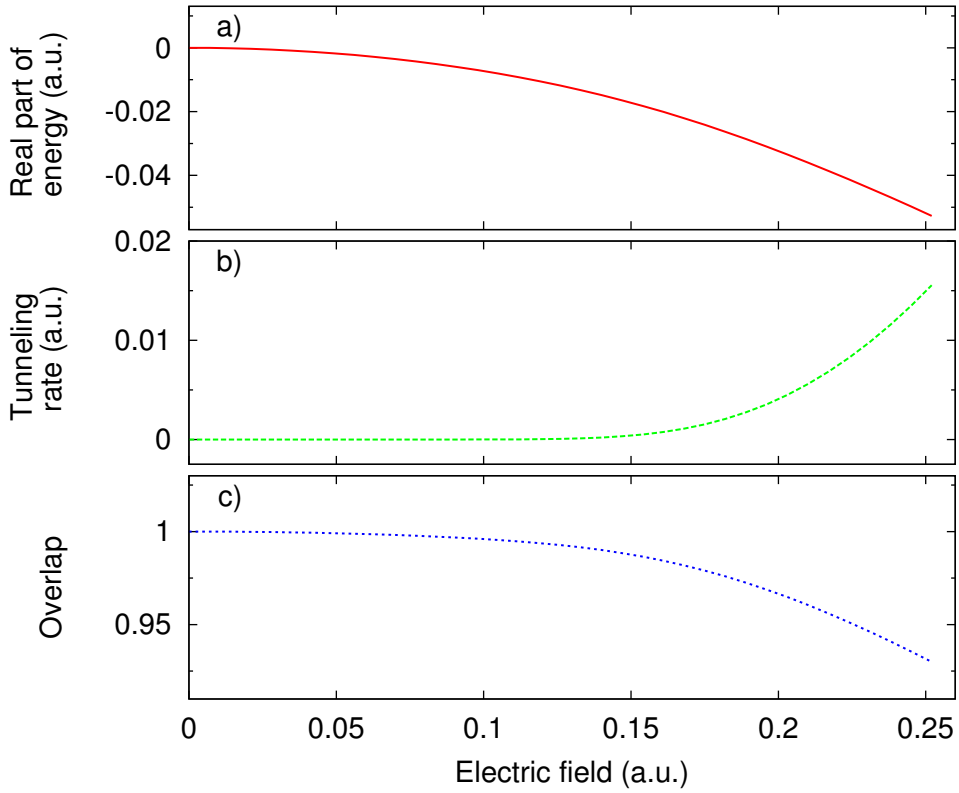

Figure 4.4: (a) The real part of the energy of the diabatic state $|\Psi_0^{(d)}\rangle$, and (b) its tunneling rate, $\Gamma = -2\,\mathrm{Im}(E)$, are shown as a function of the electric field. (c) The overlap of $|\Psi_0^{(d)}\rangle$ with the field-free ground state. © 2013 APS

field. The shift of the real part of the energy is well approximated by a quadratic behavior; for low field strengths below 0.1 a.u. the prefactor is in accordance with the literature value of the polarizability of the helium ground state [187, 188]. As expected, the tunneling rate increases considerably for sufficiently high field strengths. For field strengths larger than 0.07 a.u. the ionization rate is well captured by the analytic expression derived in the tunneling limit of the strong-field approximation [36].

Studying the adiabatic eigenstates and the avoided crossings reveals the suitability of the diabatic state constructed as shown above for the description of strong-field ionization. The advantage of the diabatic basis is that the system follows one single diabatic state, which gives a clear and intuitive picture for the explanation of the physics in the tunneling regime.

4.4.2 Ionization dynamics

So far, the analysis was performed for the spectrum of adiabatic eigenstates, i.e., for static electric fields. Now we introduce dynamics by considering a Gaussian pulse of the form

$$F(t) = f(t)\,\cos(\omega t) = F_0\, e^{-t^2/2\tau^2}\,\cos(\omega t), \tag{4.14}$$

where F_0 is the peak strength of the electric field, τ is connected to the full width of the pulse at half maximum by $\tau^2 = \mathrm{FWHM}^2/(2\ln 2)$, and ω is the field frequency.

We want to calculate the ionization probability out of the diabatic state $|\Psi_0^{(d)}\rangle$ when applying this pulse. Let us assume that we have found a diabatic basis in which this particular diabatic state can be described by a coefficient $\alpha_0^{(d)}$. Then the exact wavefunction reads $\Psi(t) = \sum_i \alpha_i^{(d)}(t)\Psi_i^{(d)}(t)$. In analogy to the case of the adiabatic representation, equations of motion can be obtained for the coefficients in the diabatic basis where now coupling elements between the diabatic states imply nondiabatic transitions [cf. Eq. (4.3)]. If, in a "diabatic approximation", the nondiabatic transitions are neglected we obtain the following equation of motion for the coefficients:

$$i\dot{\alpha}_i^{(d)}(t) = \left[E_i^{(d)} - i\frac{\Gamma_i^{(d)}}{2}\right]\alpha_i^{(d)}(t), \tag{4.15}$$

where $\Gamma_i^{(d)}$ is the ionization rate of the diabatic state i. From the ionization rate of our distinguished diabatic state its population evolution $P_0^{(d)}(t) = |\alpha_0^{(d)}(t)|^2$ during the pulse can be inferred. To this end, the equation of motion for the probability of remaining in this particular diabatic state is calculated (we omit indices for the sake of readability):

$$\frac{dP}{dt} = \frac{d}{dt}|\alpha(t)|^2 = \alpha^*(t)\dot{\alpha}(t) + \dot{\alpha}^*(t)\alpha(t). \tag{4.16}$$

Inserting Eq. (4.15) in this equation the following rate equation for the population is obtained (cf. Ref. [179]):

$$\dot{P}(t) = -\Gamma[F(t)]\ P(t), \tag{4.17}$$

which can be analytically solved by separation of variables:

$$P(t) = \exp\left\{-\int_{-\infty}^{t} \mathrm{d}t'\ \Gamma[F(t')]\right\}, \tag{4.18}$$

with the initial condition $P(t=-\infty)=1$. Note that the rate depends on the external field. Inserting the tunneling rate of the diabatic state in Eq. (4.18) we calculate the diabatic ionization dynamics. Thereby we observe how much is ionized out of $|\Psi_0^{(d)}\rangle$. Deviations from Eq. (4.18) in the population dynamics can be attributed to nondiabatic behavior, i.e., transitions to other diabatic states.

The results for four selected photon energies are shown in Fig. 4.5 for an electric field amplitude of $F_0 = 0.25$ a.u. The pulse duration is kept constant so that we can study the ionization regime from few- to multi-cycle pulses. The exact result refers to the numerical solution of the Schrödinger equation [see Eq. (4.1)], where all dynamics are included, while the calculation of the diabatic curve via Eq. (4.18) involves only the diabatic state $|\Psi_0^{(d)}\rangle$. The gray-shaded areas in the background indicate the pulse intensity. In the frequency range shown, the evolution of the ground state population is well described by considering only the single diabatic state. For $\omega = 0.3 - 0.8$ eV

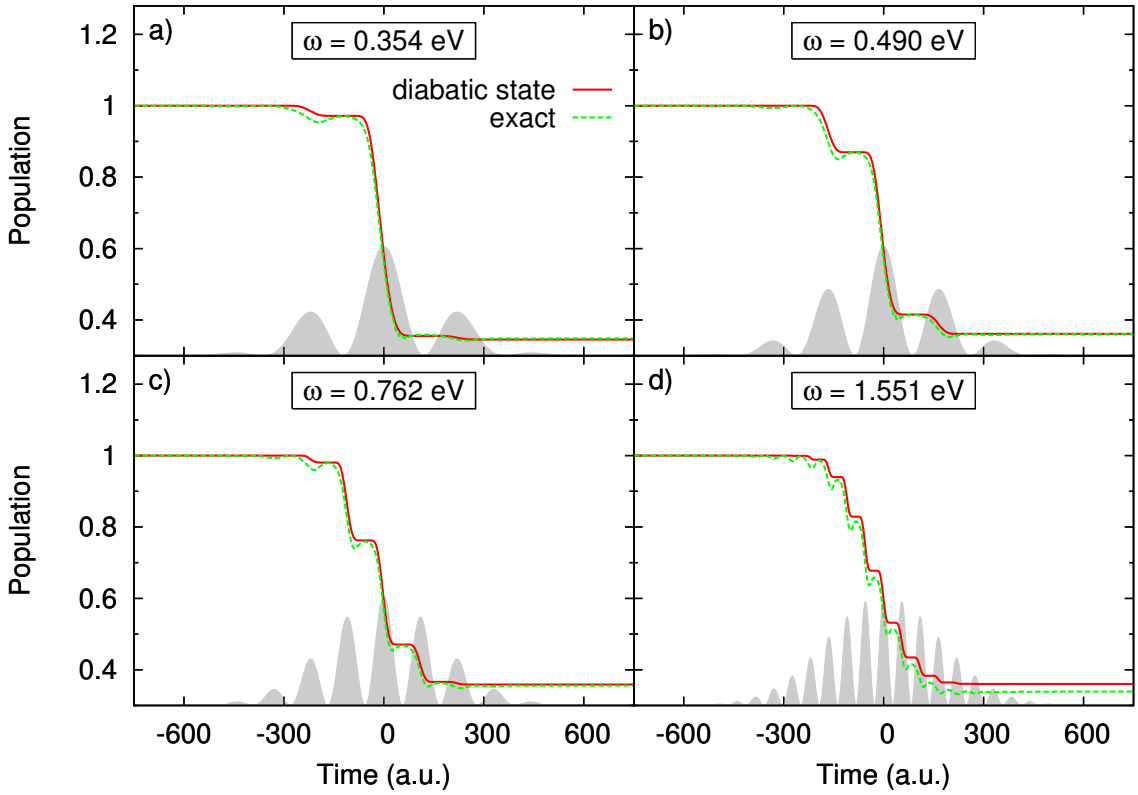

Figure 4.5: Comparison of the ground-state populations calculated via numerical solution of the Schrödinger equation and via the rate equation (4.18) for the distinguished diabatic state for four different photon energies. The pulse intensities are highlighted in the background: the pulse amplitude is $F_0 = 0.25$ a.u., and the pulse duration is 400 a.u. (≈ 10 fs).

[see Fig. 4.5 a) – c)] the difference between the numerically exact and the diabatic calculation is insignificant, while for $\omega = 1.5$ eV [see Fig. 4.5 d)] the discrepancy between the two methods becomes more noticeable. This is exactly the difference which gives us a measure of nondiabaticity. To clarify this further, a comparison between the two methods is shown in Fig. 4.6 for a peak field strength of 0.2 a.u. by depicting the populations [Fig. 4.6 a)] and the relative difference [Fig. 4.6 b)] between them after the end of the pulse. One can clearly see that for sufficiently low energies the total ionization probability is reproduced exactly by considering only the diabatic state (region I). For higher energies around 1 eV (region II), the difference increases significantly, indicating that nondiabatic effects start to become important.

4.5 Nondiabaticity and the special case of few-cycle pulses

In order to find a common way of speaking we incorporate the Keldysh parameter in our considerations, which has been used as an adiabaticity parameter. Following

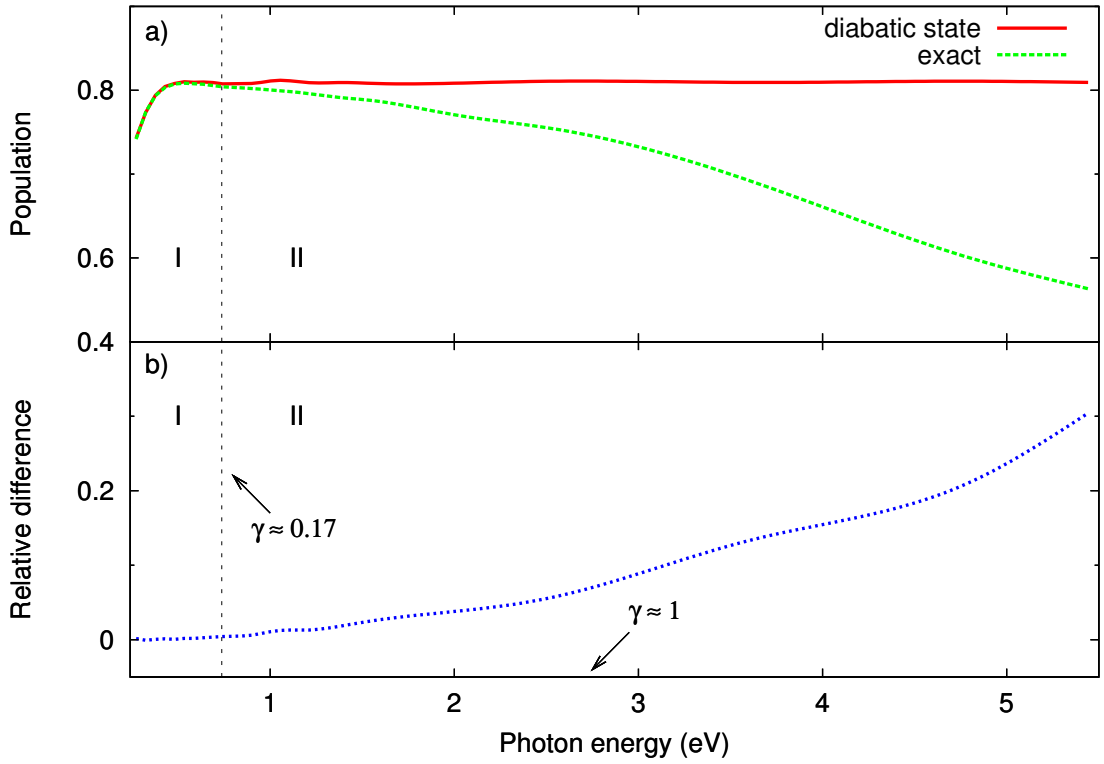

Figure 4.6: a) Ground-state population after the end of the pulse calculated via numerical solution of the Schrödinger equation and from the single diabatic ground state as a function of the photon energy, and b) relative difference between the two results, corresponding to the degree of nondiabaticity of the ionization. The peak field strength is $F_0 = 0.2$ a.u., and the pulse duration is 400 a.u. The corresponding Keldysh parameter γ is shown for different regions.

our language of the adiabatic representation, the ionization in the tunneling regime, $\gamma \ll 1$, is diabatic rather than adiabatic. We conclude from Fig. 4.6 that in the region where $\gamma \approx 1$ the relative difference between the results calculated from the diabatic ionization rate via Eq. (4.18) and from the solution of the Schrödinger equation is greater than 10%. This is a clear sign of *nondiabatic* behavior. Already for $\gamma \approx 0.17$ the diabatic ionization probability starts to differ slightly from the total ionization probability. For a fixed pulse duration we can also divide the frequency range according to the number of cycles in the pulse. Starting from the highest frequencies studied here we have multi-cycle pulses, until we reach few-cycle pulses at a photon energy of ≈ 0.8 eV.

The dynamics for few-cycle pulses is commonly considered to be nonadiabatic (in our language this translates to nondiabatic) [41, 164]. We find that even for few-cycle pulses the tunneling is completely diabatic. In the framework of ADK theory and other approaches [189] the ionization rate $\overline{\Gamma}(t)$ is obtained by integrating over

one period of the field [35]:

$$\overline{\Gamma}(t) = \frac{1}{2\pi} \int_0^{2\pi} \mathrm{d}\varphi \; \Gamma[f(t) \; \cos\varphi], \tag{4.19}$$

where $\Gamma[F]$ is the instantaneous ionization rate. Hence, the fact that the ADK theory of tunneling ionization and similar approaches cannot reproduce the correct (diabatic) ionization rate for few-cycle pulses is not due to coupling to higher states [163, 164], but rather because the pulse envelope changes dramatically within one cycle. In this limit the rate cannot be averaged over one period as was done in Eq. (4.19), whereas for multi-cycle pulses it can be used in combination with Eq. (4.18) yielding

$$P(t) \approx \exp\left\{ - \int_{-\infty}^{t} \mathrm{d}t' \; \overline{\Gamma}[f(t')] \right\}. \tag{4.20}$$

Analyzing region I in Fig. 4.6 further, we observe that the ionization probability is not constant as a function of photon energy. But the population loss in region I is well described by the ionization out of $|\Psi_0^{(d)}\rangle$. According to our argument above, the apparent frequency dependence is rather a dependence on the form of the pulse or analogously on the relation between the cycles and the pulse envelope, which appears in a pronounced way for few-cycle pulses. Preferably, to avoid confusion, we propose that it could be called rather a form dependence. As we have seen, the ionization behavior for few-cycle pulses can be well understood from the dynamics of a single diabatic state.

We have studied the dynamics of tunneling ionization in atoms and have found that, within the framework of the adiabatic representation, it is diabatic rather than adiabatic. We have identified two distinct ionization regimes depending on their diabatic behavior. In particular we have characterized the transition from the diabatic to the nondiabatic regime.

In the low-frequency limit the total ionization probability is reproduced by the contribution of the tunneling probability of one single diabatic state. This means that in this regime there are no significant transitions to other diabatic states. For few-cycle pulses, the ionization probability depends on the frequency for a fixed pulse duration. However, this is not a nondiabatic effect, but the effect stems from the form dependence of the pulse, and the consequent fact that the rate cannot be averaged any longer over one period.

When nondiabatic transitions start to happen, the difference between the diabatic state ionization probability and the total probability increases dramatically. For frequencies in the range of the binding energy of the atom one-photon absorption can occur which is a completely nonadiabatic and even nondiabatic process. Already for parameters $\gamma \approx 0.17$ the diabatic ionization probability starts to differ noticeably from the total ionization probability, even though the perturbative multiphoton regime is not yet entered. From the perspective of the adiabatic representation, the Keldysh parameter is found to be an approximate measure of diabaticity.

In the present chapter we have seen that the analysis of the (instantaneous) eigenstates of a system reveals interesting information. The diagonalization of the many-electron Hamiltonian will be used again in Ch. 7 in a different context for the detailed characterization of relevant eigenstates of xenon in the XUV excitation regime. In the remainder of this thesis the calculation of photoelectron distributions will be of central interest. We will leave the infrared strong-field regime and study the characteristics of atomic systems interacting with strong laser pulses in the multiphoton regime in detail. In particular, the photon energy will span the range from the XUV to the x-ray regime.

5 Calculation of photoelectron spectra within the time-dependent configuration interaction singles scheme

Physical Review A, **89**, 033415 (2014), **91**, 069907 (2015)

The calculation of the angular and energy-resolved photoelectron distribution allows for a direct comparison with experimental data. In this chapter I present the extension of the time-dependent configuration interaction singles (TDCIS) method to the computation of the photoelectron energy spectrum (PES) and the photoelectron angular distribution (PAD) in photoionization processes. For this purpose, the calculation of the spectral components of the wave function of the outgoing electron was implemented following two different computational approaches. The two different methods which allow for the extraction of the asymptotic photoelectron momentum are compared regarding their methodological and computational performance.

In the following I present the theoretical details of how the photoelectron distribution is obtained within the TDCIS scheme: The wave-function splitting method [77] is described in Sec. 5.1.1 and the time-dependent surface flux method [93] in Sec. 5.1.2. In Sec. 5.2 the two methods are analyzed with respect to their efficiency within TDCIS and are compared briefly. As first *proof-of-principle* applications, first one-photon and above-threshold ionization (ATI) of argon following strong XUV irradiation are studied via energy- and angle-resolved photoelectron spectra in view of our studies on multiphoton ionization in the XUV, while the second application deals with the strong-field induced Rabi splitting in the photoelectron peaks due to the coupling of an atomic resonance.

5.1 Computational methods

The theoretical framework of Ch. 1 is employed to expand the wave function in the one-particle–one-hole basis

$$|\Psi(t)\rangle = \alpha_0(t)|\Phi_0\rangle + \sum_{i,a} \alpha_i^a(t)|\Phi_i^a\rangle. \tag{5.1}$$

The radial part of the spin orbitals is again denoted as $|\varphi_a\rangle$. As introduced in Ref. [134], for each ionization channel all single excitations from the occupied spin orbital $|\varphi_i\rangle$ may be collected in one "channel wave function":

$$|\chi_i(t)\rangle = \sum_a \alpha_i^a(t)|\varphi_a\rangle. \tag{5.2}$$

These channel wave functions may now be used to calculate all quantities in a channel-resolved manner. This means that the wave function for each particular ionization channel i are employed to obtain the spectral coefficients. In this way, effectively one-particle wave functions are obtained, which will be used in the following to derive the formulae for the photoelectron spectra.

During the time propagation, quantities that are needed for the calculation of the photoelectron distribution are prepared using the channel wave function coefficients. After the propagation, these quantities are then used in the subsequent analysis step to determine the spectral components of the channel wave functions. At the end, an incoherent summation over all ionization channels is performed to obtain the photoelectron spectrum. The two analysis methods are described in the following.

5.1.1 Wave-function splitting method

The concrete implementation of the splitting method, originally introduced by Tong et al. in Ref. [77], is described within our time-dependent propagation scheme. A real radial splitting function that has the shape of a smoothed-out step function

$$\hat{S} = \left[1 + e^{-(\hat{r}-r_c)/\Delta}\right]^{-1} \tag{5.3}$$

is used to smoothly split the channel wave function (5.2). The parameter r_c determines the radius where the splitting function is centered, and Δ is a "smoothing" parameter controlling the slope or smoothness of the function. At the first splitting time step t_0 the channel wave function is split into two parts (for each channel i):

$$|\chi_i(t_0)\rangle = (1-\hat{S})|\chi_i(t_0)\rangle + \hat{S}|\chi_i(t_0)\rangle \equiv |\chi_{i,\mathrm{in}}(t_0)\rangle + |\chi_{i,\mathrm{out}}(t_0)\rangle. \tag{5.4}$$

$|\chi_{i,\mathrm{in}}(t)\rangle$ is the wave function in the inner region $0 < r \lesssim r_c$ and $|\chi_{i,\mathrm{out}}(t)\rangle$ is the wave function in the outer region $r_c \lesssim r \leq r_{\max}$. Then, the following procedure is performed at t_0: The outer part of the wave function $|\chi_{i,\mathrm{out}}(t_0)\rangle$ is analytically propagated to a long time T after the laser pulse is over using the Volkov Hamiltonian $\hat{H}_V(\tau)$ with the time propagator

$$\hat{U}_V(t_2,t_1) = \exp\left(-i\int_{t_1}^{t_2}\hat{H}_V(\tau)\mathrm{d}\tau\right), \qquad \hat{H}_V(\tau) = \frac{1}{2}\left[\hat{\mathbf{p}} + \mathbf{A}(\tau)\right]^2, \tag{5.5}$$

under the assumption that far from the atom the electron experiences only the laser field and not the Coulomb field of the parent ion. It is also assumed that, at the

splitting radius, the electron is sufficiently far away to not return to the ion.

The inner part of the wave function $|\chi_{i,\mathrm{in}}(t_0)\rangle$ is propagated on a numerical grid using the full CIS Hamiltonian [see Eqs. (2.12a) and (2.12b)]. For the splitting function the ratio $r_c/\Delta \gg 1$ must be chosen such that the ground state $|\Phi_0\rangle$ is not affected by the splitting: $\hat{S}|\Phi_0\rangle = 0$.

At the next splitting time t_1 the inner part of the wave function which was propagated from t_0 to t_1 is split again. Thus, the following prescription is obtained:

$$|\chi_{i,\mathrm{in}}(t_j)\rangle \to |\tilde{\chi}_i(t_{j+1})\rangle = |\chi_{i,\mathrm{in}}(t_{j+1})\rangle + |\chi_{i,\mathrm{out}}(t_{j+1})\rangle. \tag{5.6}$$

This is now repeated for every splitting time t_j, until all parts of the electron wave packet that are of interest have reached the outer region. Each $|\chi_{i,\mathrm{out}}(t_{j+1})\rangle$ is again propagated analytically to $t = T$.

Computationally, $|\chi_{i,\mathrm{out}}(t_j)\rangle$ is initially expressed in the CIS basis. For this purpose, new expansion coefficients for the outer wave function are defined

$$\beta_i^a(t_j) = \langle\varphi_a|\hat{S}|\tilde{\chi}_i(t_j)\rangle, \tag{5.7}$$

and the wave function in the outer region is expressed as

$$|\chi_{i,\mathrm{out}}(t_j)\rangle = \sum_a \beta_i^a(t_j)|\varphi_a\rangle. \tag{5.8}$$

In our original publication [2] one term in the equation of motion (EOM) was omitted for the electron in the outer region. That term can only be neglected if the driving field cannot induce changes in the ionic wave function. This is, however, not always true. The EOM including the channel mixing in the ion is presented in the following. In the meantime, the addendum has been published as an erratum to our publication [3]. However, we have carefully verified that the results of our publications are not affected by this additional term in the EOM.

Employing the splitting method the Eq. (2.12b) reads as follows for the inner part and the outer part of the wave function, respectively:

$$\begin{aligned} i\dot{\alpha}_i^a = {} & (\varepsilon_a - \varepsilon_i)\alpha_i^a + \sum_{i'b} \alpha_{i'}^b (2v_{ai'ib} - v_{ai'bi}) + \sqrt{2}A(t)\alpha_0\, p_{ai} + A(t)\sum_b p_{ab}\,\alpha_i^b \\ & - A(t)\sum_{i'} p_{i'i}\,\alpha_{i'}^a, \end{aligned} \tag{5.9a}$$

$$i\dot{\beta}_i^a = (\varepsilon_a - \varepsilon_i)\beta_i^a + A(t)\sum_b p_{ab}\,\beta_i^b \underbrace{- A(t)\sum_{i'} p_{i'i}\,\beta_{i'}^a}_{\text{originally neglected}}, \tag{5.9b}$$

where $p_{ab} = \langle\varphi_a|\hat{p}|\varphi_b\rangle$. This form of Eq. (4) from Ref. [2] in terms of spatial orbitals, cf. Eq. (2.13), corresponds to Eq. (27) in Ref. [134]. The term involving $(2v_{ai'ib} - v_{ai'bi})$ in Eq. (5.9a) vanishes for large distances as $1/r$ and can, therefore, be neglected (cf.

Ref. [134]). This justifies the Volkov approximation for the outer part of the wave function. The last term of the EOM for the outgoing electron, Eq. (5.9b), which involves only hole indices, was neglected in Ref. [2]. The inner part in Eq. (5.9a) is unaffected because it is propagated with the full Hamiltonian [129]. The time evolutions of the ionic and the electronic part of the electron wave packet in the outer region are decoupled. Therefore, they can be propagated with two time evolution operators: The ionic part is propagated with $U^{\text{ion}}(T,t)$, while the electronic part is propagated with the Volkov time propagator $U^{\text{elec}}(T,t) = U_V(T,t)$, see Eq. (5.5). Thus, the time evolution for the coefficients split at time step t_n is

$$\beta_i^a(T;t_n) = \sum_{j,b} U_{ab;ij}(T,t_n)\beta_j^b(t_n) = \sum_b U_{ab}^{\text{elec}}(T,t_n) \sum_j U_{ij}^{\text{ion}}(T,t_n)\beta_j^b(t_n). \tag{5.10}$$

The EOM corresponding to the ionic time evolution reads:

$$i\partial_t U_{ij}^{\text{ion}}(t,t_n) = \left[-\varepsilon_i \delta_{ij} U_{ij}^{\text{ion}}(t,t_n) - A(t) \sum_{i'} \langle \varphi_{i'} | \hat{p} | \varphi_i \rangle U_{i'j}^{\text{ion}}(t,t_n) \right], \tag{5.11a}$$

$$U_{ij}^{\text{ion}}(t_n,t_n) = \delta_{ij}. \tag{5.11b}$$

This must be solved by numerical propagation in time to large times T. After having found the propagator the channel mixing for the β_i^a coefficients in Eq. (5.10) must be performed once before calculating the PES as described in Ref. [2]. This means that for each splitting time t_n the channel mixing must be carried out before coherently summing up the contributions $\beta_i^a(T;t_n)$ from all splitting time steps.

Algorithmically, the coupling is done in an extra routine which is called before the actual photoelectron distribution is calculated. Depending on the wave-function propagation scheme, either Runge-Kutta of order four or Lanczos propagation, Eq. (5.11) is solved by the Runge-Kutta algorithm or by direct diagonalization, respectively. The latter is feasible because the size of the channel matrix is usually small for all atomic species of interest. The matrix U_{ion} is propagated with the same propagation time step as in the wave-function propagation from the first splitting time step t_1 to a large time T. During this propagation, if a propagation time step t_n happens to be a splitting time step, the multiplication in Eq. (5.10) of the matrix onto the coefficients $\beta_i^a(T;t_n)$ is performed for all splitting contributions from times smaller than the current propagation time, $t_n < t$, and the initial condition is reset for the matrix U_{ion}. The full propagation of the matrix is performed by piecewise propagating between two adjacent splitting time steps and applying the channel coupling matrix directly on the coefficients. Through the consecutive multiplications on the fly no additional storage of matrix elements is necessary.

Computational challenges

During the time propagation, at every splitting time step t_j, which can be – and for computational efficiency should be – a multiple of the actual propagation time step,

the splitting function $\hat{S}$ is applied and the expansion coefficients β_i^a from (5.7) are calculated and stored. It is clear that the more splitting time steps are necessary, the more the amount of data grows that must be stored in order to be analyzed later on. This is in particular a problem if the propagation time step must be small (e.g., because of large field amplitudes or rapid field oscillations) or the total propagation time itself is long (e.g., for long fields). Therefore, the splitting time step should be chosen as large as possible. In fact, as will become obvious in Ch. 9 for the x-ray ATI, where both the field frequency and the field amplitude are very high, this numerical issue poses a real challenge and renders data analysis very demanding. Later, when the spectrum is calculated, the coefficients β_i^a are read in from the stored files, inserted and used for the analysis.

However, a great advantage of this method is the size of the numerical grid used for the calculations: Since the outer wave function is split from the inner part and treated analytically, the grid size needed for the description of the wave function is automatically reduced. One limiting factor for the grid size is the interplay of the parameters for smoothness Δ and for the center of the splitting function r_c as mentioned above, because it must be guaranteed that the ground state, which is well localized near the origin and cannot have any ionized contribution, is not affected by the splitting function. Practically, this means that the splitting function must be very small (on the order of $10^{-5} - 10^{-6}$) at the origin.

Analysis procedure

The next steps are now part of an additional analysis program. It is called after the propagation is finished and since all necessary data are stored as described above the analysis of the parts of the wave function that describes the ejected electron can be performed.

The Volkov states $|\Psi_{\mathbf{p}}^V\rangle \equiv |\mathbf{p}^V\rangle$ are eigenstates of the Volkov Hamiltonian given in Eq. (5.5) and form a basis set in which the channel wave packet at time T can be expanded:

$$|\chi_{i,\mathrm{out}}(T)\rangle = \int \mathrm{d}^3p \sum_{t_j} C_i(\mathbf{p}, t_j)\, |\mathbf{p}^V\rangle \equiv \int \mathrm{d}^3p\, \tilde{C}_i(\mathbf{p})\, |\mathbf{p}^V\rangle. \tag{5.12}$$

In the velocity form the Volkov states are nothing but plane waves

$$\Psi_{\mathbf{p}}^V(\mathbf{r}) = (2\pi)^{-3/2} e^{i\mathbf{p}\cdot\mathbf{r}}.$$

The photoelectron spectrum is obtained by calculating the spectral components of the outer wave function. For this purpose, the following coefficients are evaluated:

$$C_i(\mathbf{p}, t_j) = \int \mathrm{d}^3p' \langle \mathbf{p}^V | \hat{U}_V(T, t_j) | \mathbf{p}'^V \rangle \underbrace{\langle \mathbf{p}'^V | \chi_{i,\mathrm{out}}(t_j) \rangle}_{c_i(\mathbf{p}', t_j)}. \tag{5.13}$$

First, the $c_i(\mathbf{p}, t_j)$ are calculated for each splitting time t_j

$$c_i(\mathbf{p}, t_j) = (2\pi)^{-3/2} \sum_a \beta_i^a(t_j) \int \mathrm{d}^3 r e^{-i\mathbf{p}\cdot\mathbf{r}} \varphi_a(\mathbf{r}), \tag{5.14}$$

where the orbital is now explicitly given in the spatial representation by

$$\langle \mathbf{r}|\hat{c}_a^\dagger|0\rangle = \langle \mathbf{r}|\varphi_a\rangle = \varphi_a(\mathbf{r}) = \frac{u_{n_a,l_a}(r)}{r} Y_{l_a,m_a}(\Omega_\mathbf{r}), \tag{5.15}$$

and, thus, possesses a radial and an angular part. The multipole expansion for the exponential function reads

$$e^{i\mathbf{p}\cdot\mathbf{r}} = 4\pi \sum_{l=0}^{\infty} i^l j_l(pr) \sum_{m=-l}^{l} Y_{lm}^*(\Omega_\mathbf{p}) Y_{lm}(\Omega_\mathbf{r}), \tag{5.16}$$

where $j_l(pr)$ denotes the spherical Bessel function of order l. The orthonormality relations of the spherical harmonics reduce the three-dimensional integrals in Eq. (5.14) to one-dimensional radial integrals. Finally, propagating to a long time T after the pulse, the coefficients are obtained:

$$C_i(\mathbf{p}, t_j) = \langle \mathbf{p}^{\,V}|\hat{U}_V(T, t_j)|\chi_{i,\mathrm{out}}(t_j)\rangle \tag{5.17}$$

$$= \sqrt{\frac{2}{\pi}} \exp\left(-\frac{i}{2}\int_{t_j}^{T} \mathrm{d}\tau\, [\mathbf{p}+\mathbf{A}(\tau)]^2\right) \times \sum_a (-i)^{l_a} \beta_i^a(t_j) Y_{l_a,m_a}(\Omega_\mathbf{p}) \int \mathrm{d}r\, r\, u_{n_a,l_a}(r) j_{l_a}(pr). \tag{5.18}$$

These coefficients can be used to calculate the angle and energy distribution of the ejected electron because at time T the canonical momentum equals the kinetic momentum. One can choose now a homogeneous momentum grid and calculate these coefficients for each splitting time step. In order to obtain the full electron wave packet at time T all contributions from all splitting times t_j must be summed up coherently to yield the coefficients $\tilde{C}_i(\mathbf{p}\,)$ in Eq. (5.12) for each ionization channel i. Then, incoherent summation over all possible ionization channels yields the photoelectron spectrum as a function of the kinetic energy and the angle with respect to the light polarization axis:

$$\frac{d^2P(\mathbf{p})}{dE d\Omega} = p \sum_i \left|\tilde{C}_i(\mathbf{p}\,)\right|^2. \tag{5.19}$$

The extra factor of p results from the conversion from the momentum to the energy differential. As long as the time T is chosen to be after the pulse the result is T independent. Of course, one needs to choose a sufficiently large T such that the parts of the electron wave function that one wants to record have entered the outer region and can be analyzed.

5.1.2 Time-dependent surface flux method (t-surff)

The second method for the calculation of photoelectron spectra is based on the approach presented by Tao and Scrinzi in Ref. [93] where it was used to calculate strong-field infrared photoionization spectra in combination with infinite-range exterior complex scaling [190]. In this approach the electron wave function is analyzed during its evolution when crossing the surface of a sphere of a given radius r_c. Again, it is assumed that the wave function can be split into two parts: One part is bound to the atom and is a solution to the full Hamiltonian, the other part can be viewed as free from the parent ion and is a solution to the Volkov Hamiltonian. Therefore, the method also relies conceptually on a splitting procedure. Nevertheless, and in contrast to the splitting method, the wave function is not altered in this process. As above, the key idea is to obtain the spectral components of the wave function by projecting onto plane waves.

The surface radius r_c is chosen such that the electron can be considered to be free, and a sufficiently large time T after the pulse is over is picked by which the electron with the kinetic energy of interest has passed this surface. (For very low-energy electrons a correspondingly larger time has to be chosen.) At this time, the channel wave function $|\chi_i\rangle$ for each ionization channel i can be split into a bound part (corresponding to the inner wave function in the splitting method) and an asymptotic part, which describes the ionized contribution:

$$|\chi_i(T)\rangle = |\chi_{i,\mathrm{in}}(T)\rangle + |\chi_{i,\mathrm{out}}(T)\rangle. \tag{5.20}$$

As in Sec. 5.1.1, the system Hamiltonian for distances larger than r_c is approximated by the Volkov Hamiltonian. Using the Volkov states of Sec. 5.1.1 and the propagation to long times with the Volkov time propagator $|\Psi_{\mathbf{p}}^V(T)\rangle = \hat{U}_V(T,-\infty)|\Psi_{\mathbf{p}}^V\rangle$, the outer wave function is represented as follows:

$$|\chi_{i,\mathrm{out}}(T)\rangle = \int \mathrm{d}^3p\; b_i(\mathbf{p})\; |\Psi_{\mathbf{p}}^V(T)\rangle, \tag{5.21}$$

which vanishes for $r \leq r_c$. Thus, the photoelectron spectrum is the sum, over all channels, of the $|b_i(\mathbf{p})|^2$, where

$$|b_i(\mathbf{p})|^2 = \left| \int_{r>r_c} \mathrm{d}^3r\; \Psi_{\mathbf{p}}^{V*}(\mathbf{r},T)\; \chi_{i,\mathrm{out}}(\mathbf{r},T) \right|^2 =: \left| \langle \Psi_{\mathbf{p}}^V(T)|\theta(\hat{r}-r_c)|\chi_{i,\mathrm{out}}(T)\rangle \right|^2. \tag{5.22}$$

Here, the Heaviside step function θ enters (adopting the notation by Tao and Scrinzi [93]). In order to avoid the need for a representation of $\chi_{i,\mathrm{out}}(\mathbf{r},T)$ at large r (because T is large, a fast electron moves far out during this time), this $3D$-integral is converted into a time integral involving the wave function only at $r = r_c$. For that, the time evolution of the asymptotic part of the wave function has to be known after it has passed the surface. Inserting the Schrödinger equation where necessary and using the

Volkov solutions in the velocity form outside the sphere with radius r_c yields [93]

$$\langle \Psi_{\mathbf{p}}^V(T)|\theta(\hat{r}-r_c)|\chi_{i,\mathrm{out}}(T)\rangle = i\int_{-\infty}^{T}\mathrm{d}t\,\langle \Psi_{\mathbf{p}}^V(t)|\left[-\frac{1}{2}\Delta - i\mathbf{A}(t)\cdot\nabla, \theta(\hat{r}-r_c)\right]|\chi_{i,\mathrm{out}}(t)\rangle. \tag{5.23}$$

The commutator, which vanishes everywhere except at $r = r_c$, is easily evaluated in polar coordinates (assuming linear polarization) and we obtain

$$\left[-\frac{1}{2}\Delta - i\mathbf{A}(t)\cdot\nabla, \theta(\hat{r}-r_c)\right] = -\frac{1}{2r^2}\partial_r r^2\delta(r-r_c) - \frac{1}{2}\delta(r-r_c)\partial_r + iA(t)\cos(\theta)\delta(r-r_c). \tag{5.24}$$

More details can be found in Ref. [93] as well as in Ref. [191]. The derivative in the first operator term is shuffled to the left, via integration by parts, and the following operator is obtained

$$-\frac{1}{r}\delta(r-r_c) + \overleftarrow{\partial}_r\frac{1}{2}\delta(r-r_c) - \frac{1}{2}\delta(r-r_c)\partial_r + iA(t)\cos(\theta)\delta(r-r_c), \tag{5.25}$$

where "$\overleftarrow{\partial}$" means that the derivative acts to the left on the Volkov state and "∂" means that the derivative acts to the right on the channel wave function. In order to implement this operator acting on the channel wave functions also the first derivative of the wave functions with respect to r has to be calculated at the radius r_c. After the propagation, during which the coefficients of the channel wave functions $\chi_i(r_c,t)$ as well as of their first derivatives $[\partial_r\chi_i(r,t)|_{r=r_c}]$ have been calculated, the expression (5.23) can be computed. Since the multipole expansion is introduced [see Eq. (5.16)] for the Volkov states also derivatives of the spherical Bessel functions have to be calculated at the radius r_c. This calculation is performed during the analysis step for each angular momentum l. In the last term the cosine is expressed as a spherical harmonic and the identity for the integral over three spherical harmonics is used

$$\int \mathrm{d}\Omega\; Y^*_{l_3,m_3}(\Omega)Y_{l_2,m_2}(\Omega)Y_{l_1,m_1}(\Omega) = \frac{\sqrt{(2l_1+1)(2l_2+1)}}{4\pi(2l_3+1)}C^{l_3m_3}_{l_1m_1,l_2m_2}C^{l_30}_{l_10,l_20},$$

where the Clebsch-Gordan coefficients are given by $C^{l_3m_3}_{l_1m_1,l_2m_2} = \langle l_1m_1, l_2m_2|l_3m_3\rangle$. Thus, the spectral components in their final form are obtained:

$$\begin{aligned}\langle \Psi_{\mathbf{p}}^V(T)|\theta(\hat{r}-r_c)|\chi_{i,\mathrm{out}}(T)\rangle = {} & i\sqrt{\frac{2}{\pi}}\int_{-\infty}^{T}\mathrm{d}t\,\exp\left(-\frac{i}{2}\int_{-\infty}^{t}\mathrm{d}\tau\,[\mathbf{p}+\mathbf{A}(\tau)]^2\right) \\ & \times\sum_a\Bigg\{(-i)^{l_a}\left[-j_{l_a}(pr_c) + \frac{pr_c}{2}j'_{l_a}(pr_c) - \frac{1}{2}j_{l_a}(pr_c)\right]Y_{l_a,m_a}(\Omega_{\mathbf{p}})\,u_{n_a,l_a}(r_c)\,\alpha_i^a(t) \\ & -\frac{(-i)^{l_a}}{2}\,j_{l_a}(pr_c)\,Y_{l_a,m_a}(\Omega_{\mathbf{p}})\,u'_{n_a,l_a}(r_c)\,\alpha_i^a(t) \\ & +\frac{i}{2\sqrt{\pi}}\,r_c\,u_{n_a,l_a}(r_c)\,A(t)\,\alpha_i^a(t)\sum_{l=0}^{\infty}(-i)^l j_l(pr_c)\frac{\sqrt{2l_a+1}}{2l+1}\,C^{l,m_a}_{l_a,m_a;1,0}C^{l,0}_{l_a,0;1,0}Y_{l,m_a}(\Omega_{\mathbf{p}})\Bigg\}\,,\end{aligned} \tag{5.26}$$

where the prime denotes the first derivative: $j'_{l_a}(pr_c) = \partial_z j_{l_a}(z)\big|_{z=pr_c}$ and $u'_{n_a,l_a}(r_c) = \partial_r u_{n_a,l_a}(r)\big|_{r=r_c}$.

Also in the case of the t-surff method the ansatz in Eq. (5.9) can be made in order to account for the channel mixing according to the expression in Eq. (5.10), which must be taken into account for each time t before projecting onto the Volkov states in Eq. (5.26). This means that, again the mixing must be calculated

$$\alpha_i^a(T;t_n) = \sum_{j,b} U_{ab;ij}(T,t_n)\alpha_j^b(t_n) = \sum_b U_{ab}^{\text{elec}}(T,t_n) \sum_j U_{ij}^{\text{ion}}(T,t_n)\alpha_j^b(t_n), \tag{5.27}$$

before evaluating the expression (5.26).

Although the expression (5.26) may seem fairly complicated, it involves only quantities evaluated at one single radius $r = r_c$. The photoelectron spectrum is then obtained as

$$\frac{d^2P(\mathbf{p})}{dEd\Omega} = p\sum_i \left|\langle \Psi_{\mathbf{p}}^V(T)|\theta(\hat{r}-r_c)|\chi_{i,\text{out}}(T)\rangle\right|^2, \tag{5.28}$$

where, as in the splitting method, the incoherent sum over all ionization channels i is performed. In the present implementation, a CAP absorbs the wave function near the end of the numerical grid [181, 186, 192]. A CAP of the form $W(r) = \theta(r-r_{\text{CAP}})(r-r_{\text{CAP}})^2$ is utilized, where θ is again the Heaviside step function and r_{CAP} is the radius where the CAP starts absorbing. It is added to the Hamiltonian in Eq. (2.1) in the form $-i\,\eta\,\hat{W}$, where η is the CAP strength. As will be discussed in Sec. 5.2.2 the absorption via a CAP has to be optimized carefully, because reflections from the end of the numerical grid as well as from the CAP itself have to be minimized in order to obtain an accurate photoelectron spectrum.

5.2 Application: Argon under strong XUV radiation

With two methods for the calculation of photoelectron spectra implemented in TDCIS, one-photon and above-threshold ionization processes of argon in the XUV regime are investigated (nuclear charge $Z = 18$). Motivated by an experiment carried out at the free-electron laser facility FLASH in Hamburg [193] (for more details see Chapters 6 and 7) we assume a photon energy of 105 eV, which is far above the threshold for the ionization out of the 3p and 3s subshells. In the following we examine the functionality of the splitting and the surface flux methods by means of the specific example of ionization of argon in the XUV.

5.2.1 Wave-function splitting method

In the splitting method, three parameters have to be adjusted: the splitting radius, the smoothness of the splitting function and the rate at which the absorption is applied. A first criterion for verifying that the absorption through the masking function

	splitting	relative diff. to CAP
$dt_{spl} = 10$ a.u.	7.177×10^{-3}	2.8×10^{-3}
$dt_{spl} = 1$ a.u.	7.177×10^{-3}	2.8×10^{-3}
$dt_{spl} = 0.2$ a.u.	7.180×10^{-3}	2.4×10^{-3}

Table 5.1: The ionization probability of argon for a pulse at 105 eV photon energy, 9×10^{13} Wcm^{-2} peak intensity and 1.2 fs duration (FWHM) calculated via a CAP (converged calculation) is compared to the ionization probability calculated via the splitting function ($r_{max} = 150$ a.u., $r_c = 80$ a.u., $\Delta = 10$ a.u.) for different splitting times. The relative difference is of the order 10^{-3}.

is performed correctly is the comparison of the total ground state population obtained via splitting with the population obtained with the CAP. We use a Gaussian pulse with 9×10^{13} Wcm^{-2} peak intensity and 1.2 fs duration (full width at half maximum, FWHM) at a photon energy of 105 eV. For this pulse a converged result for the CAP strength $\eta = 1 \times 10^{-3}$, $r_{max} = 150$ a.u., and $r_{max} - r_{CAP} = 30$ a.u. gives an ionization probability of 7.197×10^{-3} after the pulse. In the studied parameter cases the agreement between the splitting results and that CAP result is better than 3×10^{-3} relative difference (choosing, e.g., $r_{max} = 150$ a.u., $r_c = 80$ a.u., $\Delta = 10$ a.u., and varying the splitting time step between 0.2 a.u. and 10 a.u.). With more frequent absorption the agreement gets slightly better. The results for three different splitting time steps, for a grid size of $r_{max} = 150$ a.u., a splitting radius of $r_c = 80$ a.u., and a smoothing parameter of $\Delta = 10$ a.u., are summarized in Table 5.1 where also the relative differences are given. The results are in agreement on the order of 10^{-3} relative difference.

Analyzing the splitting method, it is found that the splitting radius r_c and the smoothing parameter Δ can be varied rather freely without changing the (physical) spectrum. Although the total radial grid size can be chosen as small as 100 a.u. (cf. Fig. 5.1) also a larger radial grid extension with $r_{max} = 250$ a.u. is chosen and the splitting radius is varied in the wide range from 80 a.u. to 230 a.u. Exemplarily, results in the direction $\theta = 0$ (along the XUV polarization axis) when the radial grid size and splitting radius are varied are shown in Fig. 5.1(a). The spectrum shows the one-photon absorption peaks at the energy corresponding to the difference between photon energy and binding energy of the corresponding orbital ($3s$ and $3p$, respectively). The second part of the spectrum, in Fig. 5.1(b), is separated from the first part by the photon energy and is, therefore, attributed to above-threshold ionization. The width of the peaks corresponds to the Fourier-limited energy width according to $\tau\Delta\omega = 2.765$ (all quantities in atomic units), where τ is the duration of the pulse intensity envelope (FWHM) and $\Delta\omega$ is the bandwidth of the power spectrum (FWHM). The figure shows that the spectrum is independent of the splitting radius as long as around 30 a.u. are left to the end of the numerical grid for absorption. Reducing the difference $r_{max} - r_c$ to 20 a.u. produces artificial peaks near the physical peaks. To estimate how large the absorption range must be let us consider an electron with 200 eV kinetic energy. It covers a distance of roughly 4 a.u. per atomic unit

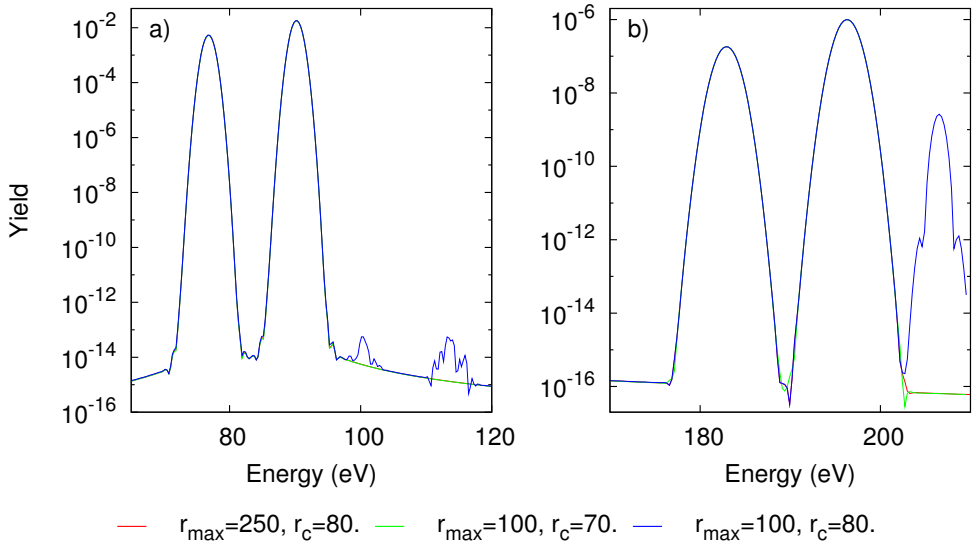

Figure 5.1: The photoelectron spectrum of argon for a pulse with 105 eV photon energy, 9×10^{13} Wcm^{-2} intensity and 1.2 fs duration is shown for different radial grid sizes $r_{\max}$ and splitting radii r_c. The smoothing parameter is $\Delta = 10$ a.u. and the splitting time step is $\mathrm{d}t_{\mathrm{spl}} = 0.2$ a.u. Panel a) shows the one-photon absorption lines, panel b) shows the energetically lowest ATI lines for different splitting radii. All radii are given in atomic units. The spectrum does not change under variation of the splitting radius as long as around 30 a.u. units are left for absorption.

of time. The numerical results show that the range over which the wave function is absorbed by the splitting function must be much larger than this distance (almost 10 times larger) in order to avoid reflections. This can be understood if one considers that the slope of the splitting function at a smoothing parameter of $\Delta = 10$ a.u. extends over a range of around 30 a.u. beyond the splitting radius to reach 95% absorption of the wave function.

Since the splitting radius is not very crucial for the spectrum we proceed to the variation of the other parameters. Spectra for various smoothing parameters Δ are shown in Fig. 5.2. Here, the radial grid size is kept fixed at $r_{\max} = 150$ a.u., the splitting radius is 80 a.u., and absorption is performed every 10 a.u. of time. The physical peaks are reproduced correctly for all Δ, the noise amplitude, however, is changing. A value of $\Delta = 10$ seems to be the optimum, for $\Delta = 15$ the amplitude of unphysical peaks is higher, while the steeper slope corresponding to $\Delta = 5$ a.u. produces higher oscillations near the physical peaks, which should be avoided.

The method is particularly sensitive to the splitting rate, i.e., how often the splitting is applied. The more frequently the splitting function is applied the less noise is obtained. This is shown in Fig. 5.3, where only the splitting time step is varied, while the radial grid size is kept constant at 150 a.u., the splitting radius is set to 80 a.u. and the smoothing parameter is 10 a.u. It is found that the unphysical peaks or artifacts do not contribute to the physical observables because they are orders

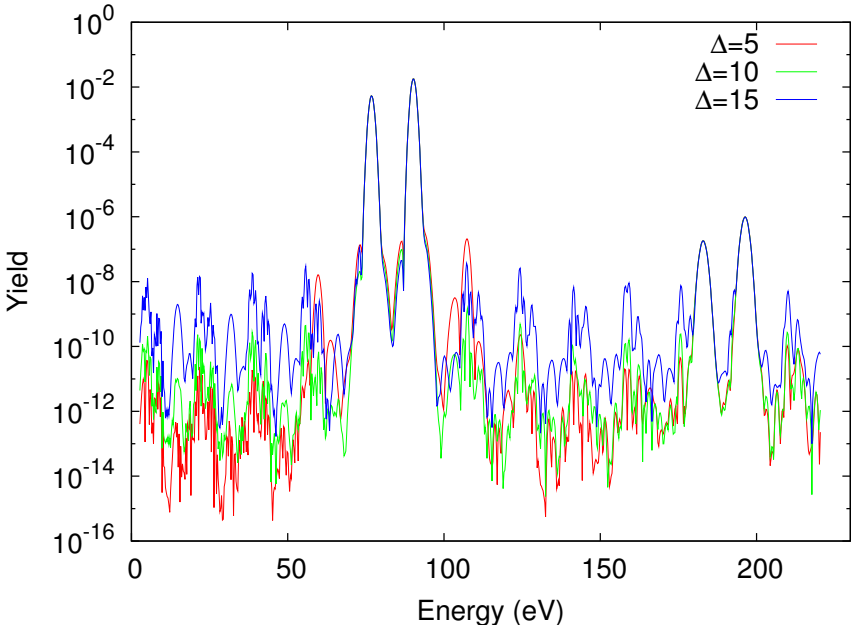

Figure 5.2: The argon photoelectron spectrum is shown for different smoothing parameters Δ. The pulse parameters are the same as for Fig. 5.1. The radial grid size is $r_{\max} = 150$ a.u., the splitting radius is 80 a.u., and the splitting is applied every 10 a.u. of time. The 3p and 3s peaks are not affected by the change of the slope of the splitting function, although the numerical noise resulting from reflections from the splitting function changes. © 2014 APS

of magnitude smaller. The noisy oscillations result from numerical issues, e.g., the higher the frequency of splitting the more reflections are accumulated from the slope of the splitting function. For this reason, the choice of the slope of the splitting function is coupled to the frequency of splitting. For more frequent absorption of the wave function the steepness should be reduced. Since for every splitting time step the new coefficients $\beta_i^a(t_j)$ have to be calculated and stored during the propagation and the quantities (5.17) have to be evaluated during the analysis step, it is not convenient to perform the splitting at every propagation time step as mentioned in Sec. 5.1.1. In the calculations shown the propagation time step is 0.05 a.u.

From the derivation of the splitting method in subsection 5.1.1 it can be seen that the electron spectrum is normalized to the total ionization probability (because only normalized wave functions are used). Therefore, the integrated spectrum represents a good measure of the quality of the spectrum; the fully integrated spectrum must agree with the total ionization probability. This can be verified for different parameter specifications. The relative difference to the CAP result is found to be smaller than 2% in all studied parameter cases.

In the following a strong XUV pulse centered at 105 eV with 0.7 eV bandwidth (FWHM) are applied, which corresponds to a Fourier-transform limited pulse with 108 a.u. (2.6 fs) duration. The peak intensity of the pulse is 1.0×10^{15} Wcm^{-2}. In Fig. 5.4a) the full angle- and energy-resolved photoelectron spectrum of argon

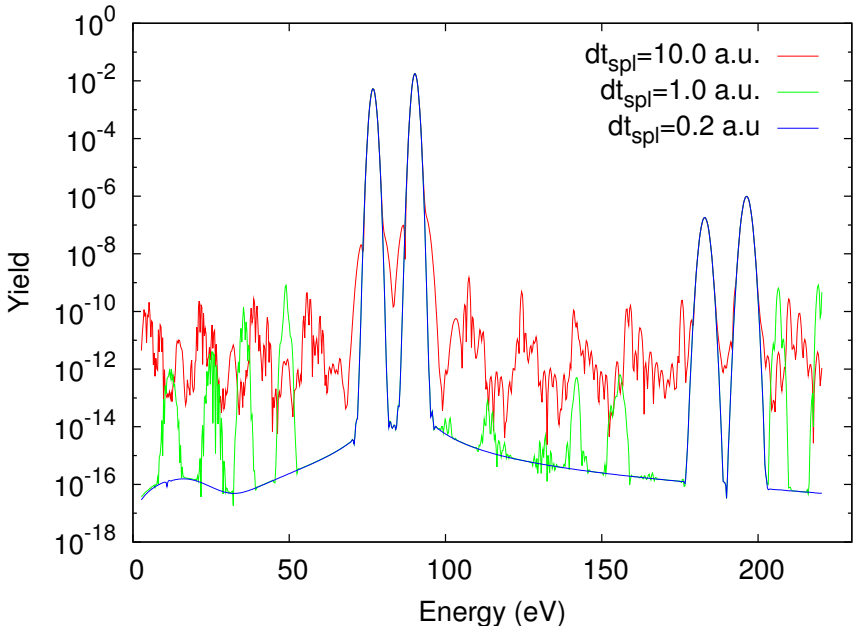

Figure 5.3: The argon photoelectron spectrum in the polarization direction is shown. The variation of the splitting time step results in significant changes in the (numerical) oscillations. The pulse parameters are the same as for Figs. 5.1 and 5.2. At a fixed smoothing parameter $\Delta = 10$ a.u., $r_{\max} = 150$ a.u., $r_c = 80$ a.u., the noise is suppressed by several orders of magnitude for more frequent splitting. The one-photon peaks and ATI peaks do not change significantly. © 2014 APS

after one-photon absorption is shown. Since only linearly polarized light is applied the system exhibits cylindrical symmetry about the polarization direction and is, therefore, symmetric in the azimuthal angle φ. For this reason only the polar angle θ needs to be considered as a variable together with the kinetic energy (or equivalently the photoelectron momentum). Then, the angle θ denotes the direction with respect to the polarization axis. The peaks arise from ionization out of the 3s and 3p shells, respectively. The lower panel of Fig. 5.4a shows the corresponding ATI spectrum. As expected, the angular distributions feature the corresponding contributions from the different channels, which can be seen in Fig. 5.4b in the four cuts along the fixed peak energies: The one-photon peak from the 3s shell shows a $\cos\theta$ behavior and, thus, a p-wave character, the 3p peak has both an s- and a d-wave contribution, compatible with a $\cos^2\theta - 1$ behavior. Analogously, the two-photon peak of 3s exhibits an s- and d-wave character and the 3p peak a p- and f-wave character, i.e., showing also an admixture of the third power of trigonometric functions, and exhibiting three minima.

In a nutshell, the splitting method is a well-working tool for the calculation of photoelectron spectra although the requirement to optimize three parameters (r_c, Δ, $\mathrm{d}t_{\mathrm{spl}}$) can render calculations time-consuming and the storage of the splitting-time wave-function components β_i^a can –depending on the problem– easily exceed several gigabytes of disk space.

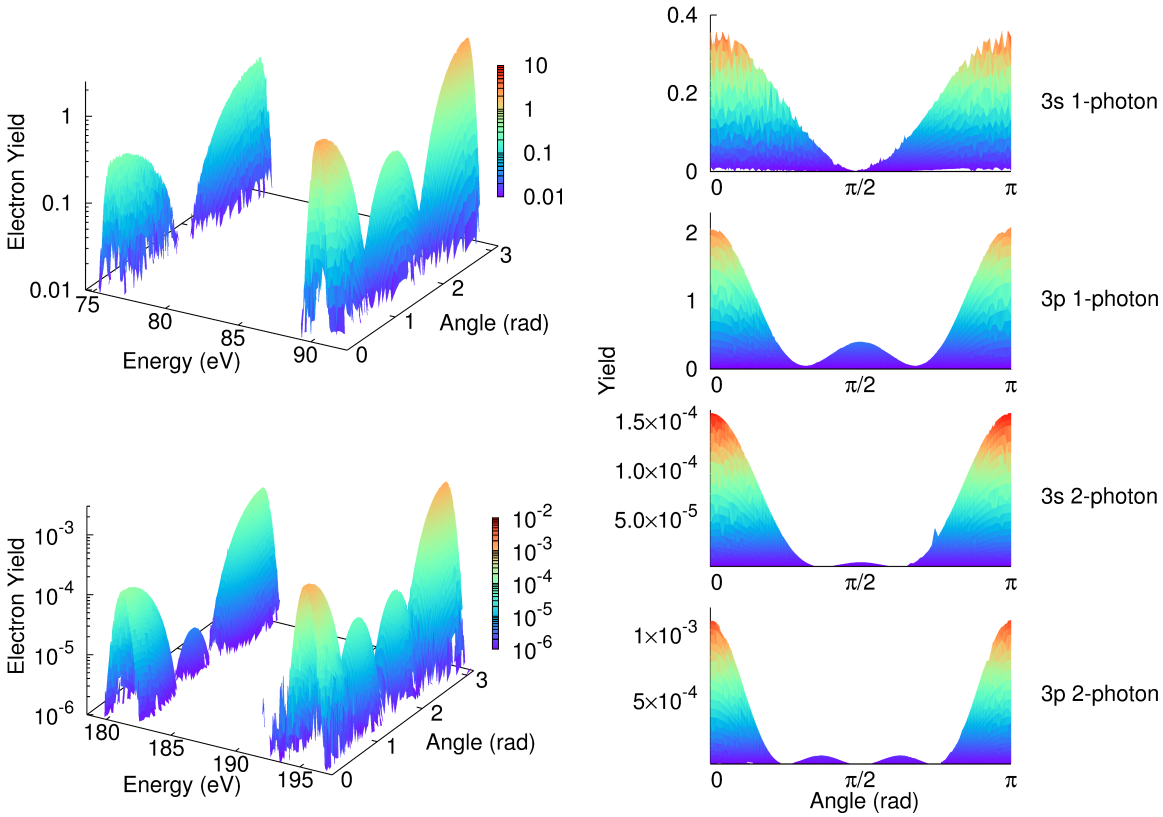

(a) Angle- and energy-resolved PES.

(b) Energy cuts along the peak energies as a function of angle.

Figure 5.4: The energy- and angle-resolved argon photoelectron distribution produced with the splitting method is shown for an XUV pulse at 105 eV photon energy, 1.0×10^{15} Wcm^{-2} intensity and 2.6 fs pulse duration. The grid size is $r_{\max} = 100$ a.u., $r_c = 20$ a.u., $\Delta = 5$ a.u., and $\mathrm{d}t_{\mathrm{spl}} = 10$ a.u. The angle denotes the direction with respect to the polarization axis of the pulse. The angular distribution reflects the change in angular momentum by multiphoton absorption. © 2014 APS

5.2.2 Time-dependent surface flux method (t-surff)

Let us turn now to the t-surff method. The method depends on the radius r_c where the surface measuring the flux is placed and on the parameters of the absorption method. As already mentioned in Sec. 5.1.2, in the present work the absorption is performed with a CAP, which depends on two parameters: the CAP strength η and the radius r_{CAP} where the CAP starts absorbing. For t-surff also the total propagation time plays an important role. While the splitting method is not affected by a variation of the propagation time (as long as it is longer than the pulse and long enough for the electronic wave packet of interest to enter the absorption region), t-surff requires a long propagation. This is shown in Fig. 5.5. The noise level decreases dramatically with longer time propagation. On the other hand, the calculation of the spectrum itself can be performed faster than with the splitting method, because no radial integrals are involved. Instead, all quantities are evaluated at the radius $r = r_c$.

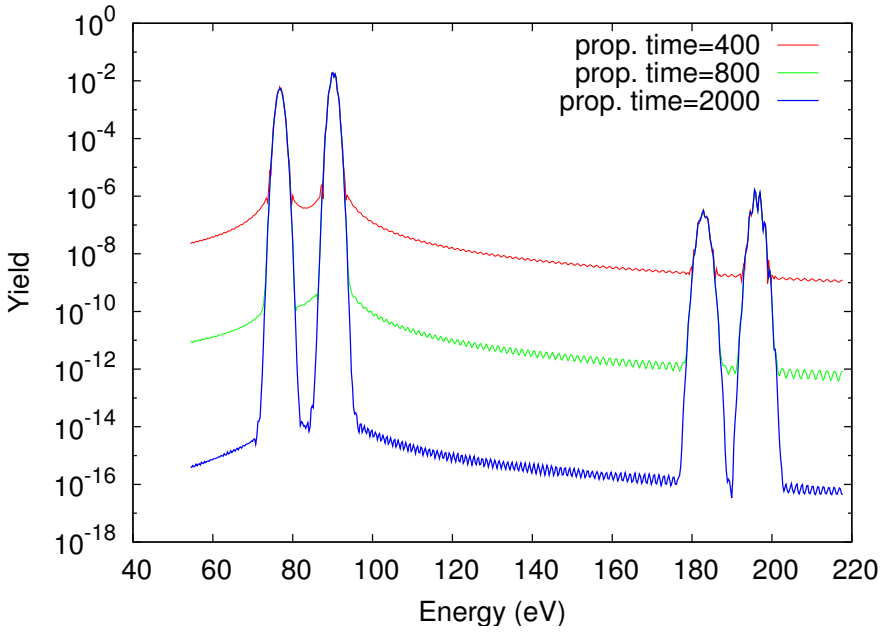

Figure 5.5: The argon photoelectron spectrum calculated via t-surff is shown for different propagation times (in a.u.). The pulse parameters are the same as in Figs. 5.1 to 5.3. The computational parameter specifications are: $r_{\max} = 250$ a.u., $r_{\mathrm{CAP}} = 230$ a.u., $\eta = 1\times10^{-3}$, and $r_c = 180$ a.u. The oscillations decrease by orders of magnitude for longer propagation. © 2014 APS

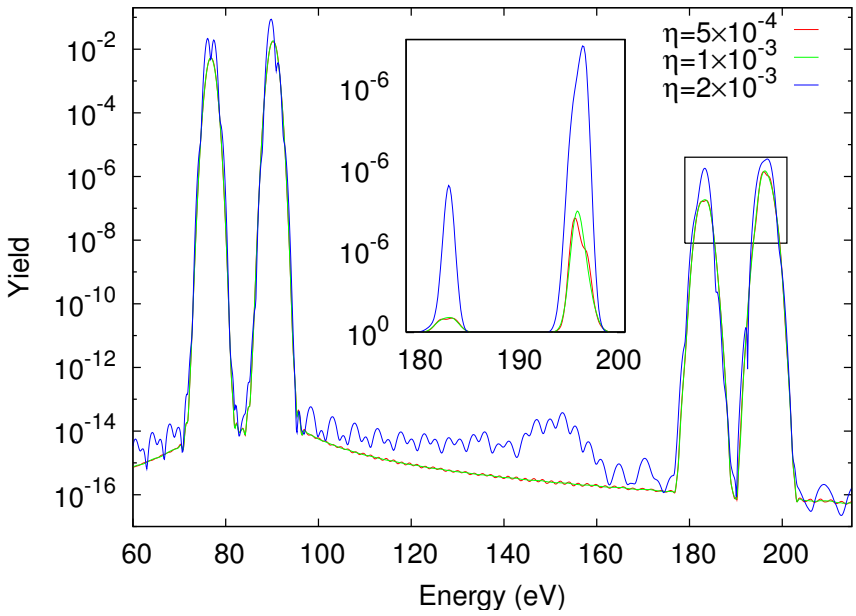

Figure 5.6: The argon photoelectron spectrum along the polarization axis of the field, calculated with t-surff, is shown for a pulse with 105 eV photon energy, 9×10^{13} Wcm^{-2} intensity and 1.2 fs duration for different CAP strengths. The radial grid size is $r_{\max} = 150$ a.u., the CAP radius is $r_{\mathrm{CAP}} = 120$ a.u., and $r_c = 100$ a.u. The oscillations are due to reflections from the end of the radial grid and/or the CAP. © 2014 APS

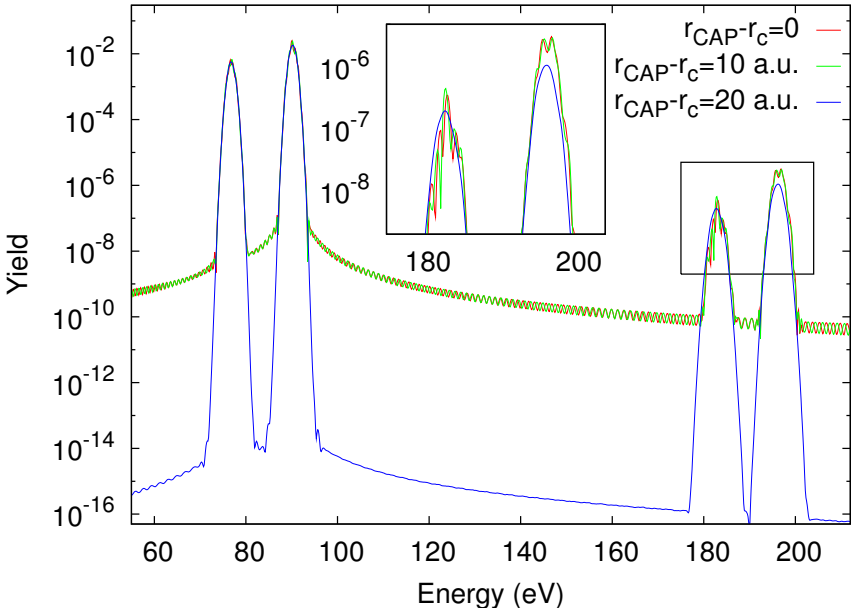

Figure 5.7: The argon photoelectron spectrum for the same pulse as in Figs. 5.1 to 5.3 and Figs. 5.5 to 5.6 is shown along the polarization direction. The numerical parameters are $r_{\max} = 250$ a.u., $\eta = 1 \times 10^{-3}$, $r_{\mathrm{CAP}} = 220$ a.u., and the propagation time is 1000 a.u. The distance $r_{\max} - r_{\mathrm{CAP}}$ is varied in the range from 0 to 20 a.u. © 2014 APS

The method relies on an optimized CAP for the energy range of interest. However, the CAP cannot guarantee a perfect absorption. Since the optimized CAP strength is energy dependent [181] the t-surff spectrum can be optimized only for a limited energy range. In Fig. 5.6 the energy spectrum for $\theta = 0$ is shown for different CAP strengths η. It is clear that reflections from the CAP as well as from the end of the radial grid leave a trace in the spectrum. A weak CAP cannot fully absorb a fast electron before the end of the radial grid. On the other hand, a strong CAP will reflect the electron. For the kinetic energies of the electrons considered here the optimized CAP parameter lies at a value of about 10^{-3}. Of course, the other parameter that must be optimized is the CAP radius r_{CAP}. It is found that the optimum is an absorption range of $r_{\max} - r_{\mathrm{CAP}} = 30$ a.u. For t-surff also the distance of r_c to r_{CAP} plays a role. In Fig. 5.7 the spectrum is shown for different $r_{\mathrm{CAP}} - r_c$ values. For a distance of $r_{\mathrm{CAP}} - r_c = 20$ a.u. the spectrum becomes less oscillatory and the noise level decreases significantly in comparison to shorter ranges $r_{\mathrm{CAP}} - r_c$.

A direct comparison of the spectrum in the direction $\theta = 0$ obtained by splitting and t-surff, respectively, is shown in Fig. 5.8. The pulse characteristics are the same as for the Figs. 5.1 to 5.3 and 5.5 to 5.7. The radial grid size is $r_{\max} = 250$ a.u. The splitting parameters are $r_c = 200$ a.u., $\Delta = 10$ a.u., $\mathrm{d}t_{spl} = 0.2$ a.u., and the propagation time is 400 a.u. For the surface flux method a CAP strength of 10^{-3}, a CAP radius of $r_{\mathrm{CAP}} = 220$ a.u., a sphere radius of $r_c = 200$ a.u. (according to the optimum found for $r_{\mathrm{CAP}} - r_c = 20$ a.u.) and a propagation time of 1000 a.u. are chosen. The spectra agree quite nicely. The one-photon peaks exhibit a nearly

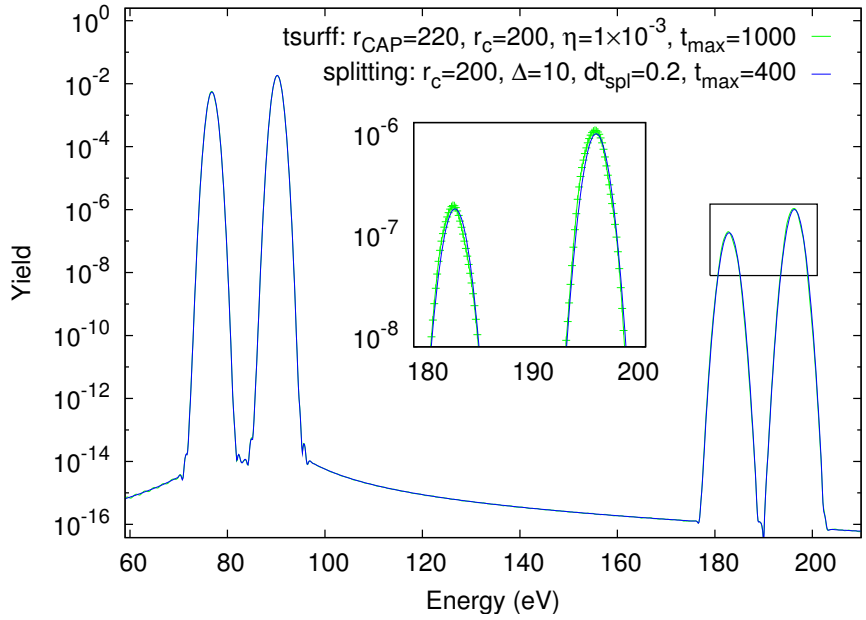

Figure 5.8: The argon photoelectron spectra obtained with the splitting and the t-surff methods for a pulse with 105 eV photon energy, 9×10^{13} Wcm^{-2} intensity and 1.2 fs duration along the polarization direction are compared. The radial grid size is $r_{\max} = 250$ a.u. for both methods. © 2014 APS

perfect agreement. The slight deviation in the two-photon spectrum calculated with t-surff indicates that the CAP could be reoptimized for this energy range. However, for both methods the spectrum has a very low noise level, up to ten orders of magnitude smaller than the physical signal.

Summarizing, the t-surff method is in principle applicable with a CAP, although it requires a good quality absorption over a broad energy range. Qualitatively, the t-surff method reproduces exactly the same results as obtained with the splitting method. In contrast to the splitting less memory capacity is used because only the wave function and its first derivative at one single point need to be stored.

5.2.3 Rabi splitting

In all of the previous examples the channel mixing mentioned in Sec. 5.1.1 was not of particular importance because the photon energy did not match any atomic resonance. In the following we demonstrate exemplarily that our method can also describe cases where two bound states are strongly coupled by a laser field. The influence of the channel coupling will be inferred by comparing the results calculated with and without the mixing described by Eqs. (5.11).

An interesting phenomenon in the strong-field case where the interaction between electrons and holes is important is the Rabi oscillation [175, 176] between bound states and an autoionizing state [194, 195]. It is known that driving a resonance between two resonance states will result in a double-peak structure [196, 197], where

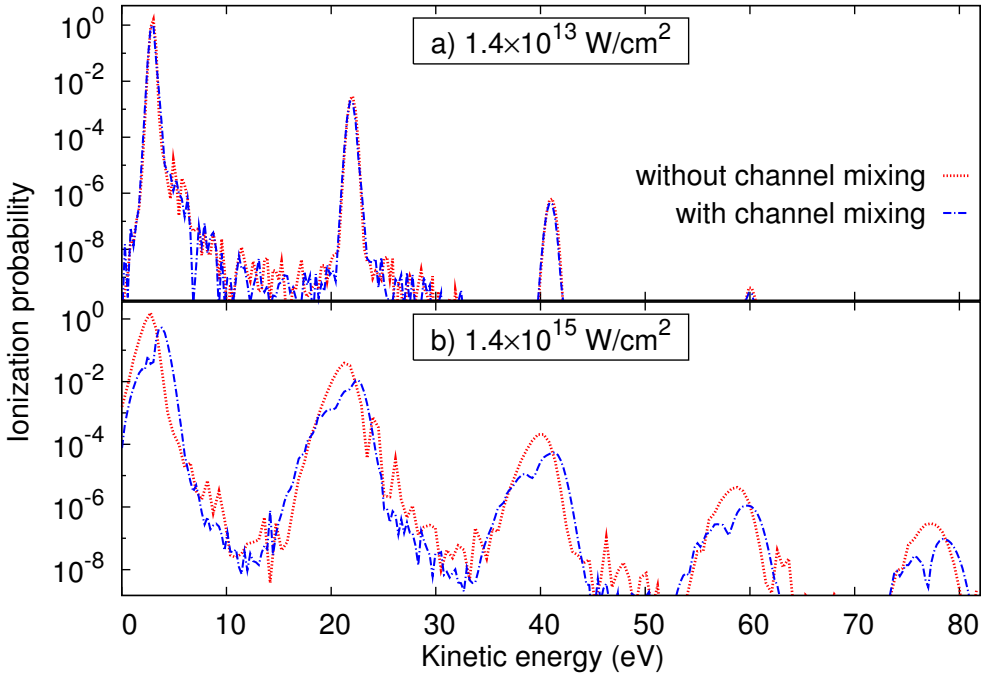

Figure 5.9: Argon photoelectron spectra calculated with the splitting method ($\Delta = 10$ a.u., $\mathrm{d}t_{\mathrm{spl}} = 0.2$ a.u., and $r_c = 80$ a.u.). a) Spectrum calculated for a pulse of 0.7 a.u. photon energy, 4.6 fs duration and an intensity of $1.4 \times 10^{13}\mathrm{Wcm}^{-2}$. The one-photon peak and three ATI peaks are shown. b) Spectrum for the same pulse parameters, except for the intensity, which amounts to $1.4 \times 10^{15}\,\mathrm{Wcm}^{-2}$. The peaks split when the channel coupling is included in the calculation.

the two peaks are separated by the Rabi frequency. This has been studied for instance within a neutral atomic system [198], for negative ions [199] or for coupling within positive ions in the photoionization of a neutral atom [195]. An example of the latter case shall be studied here. The photoelectron distribution is calculated for an argon atom interacting with a laser pulse whose central energy is 0.7 a.u., which corresponds to the energy spacing between the $3s$ and the $3p$ orbitals. When an electron of the $3p$ shell absorbs a photon and is ionized a hole is created in the $3p$ shell. Then, a strong laser field can induce an excitation of a $3s$ electron to the hole in the $3p$ shell. If the laser intensity is high enough the light induces Rabi oscillations of the electronic population between the two shells and the photoelectron distribution is expected to reflect this oscillation. The Rabi frequency depends on the peak electric field strength, $\mathbf{E}_0$, and the dipole matrix element of the two states involved, $\mathbf{d}_{3s-3p}$ is [175]

$$\Omega_{3s-3p} = \mathbf{d}_{3s-3p} \cdot \mathbf{E_0} = \langle \varphi_{3p} | \hat{z} | \varphi_{3s} \rangle E_{z0}, \tag{5.29}$$

where the last equality holds because the light is assumed to be linearly polarized in the z-direction. The transition matrix element between the two orbitals $3s$ and $3p_0$ amounts to 0.86 a.u. Of course, the effect of this oscillation will only be visible in the spectrum if the Rabi splitting is large enough to be resolved compared to the energy width of the photoelectron peaks.

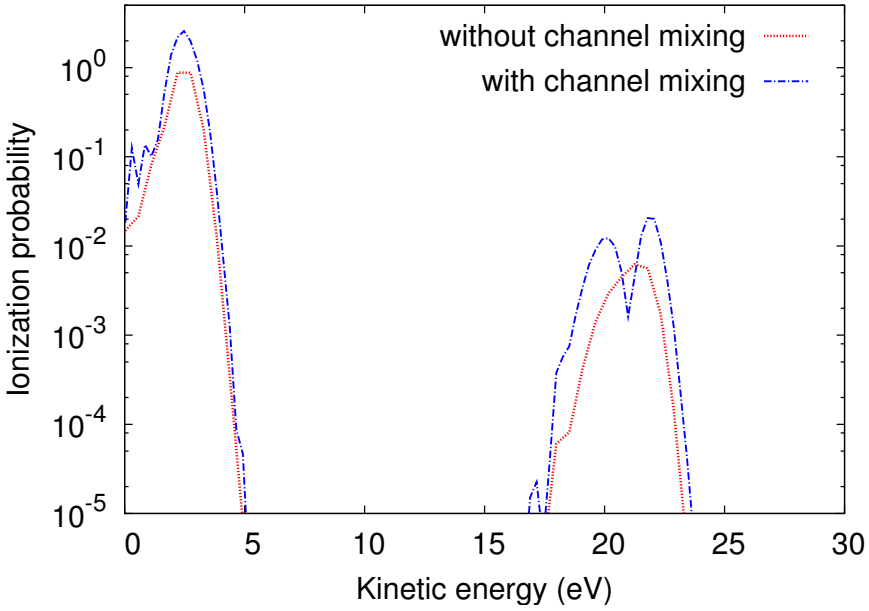

Figure 5.10: Argon photoelectron spectra calculated for the same pulse parameters as in Fig. 5.9 b) with the t-surff method ($r_c = 30$ a.u.). The one-photon peak and the first ATI peak is shown. The splitting is visible when the channel coupling is included in the calculation.

In order to investigate the emergence of the splitting in the photoelectron peaks due to the Rabi oscillation between the $3s$ and $3p$ orbitals two intensity regimes are considered. First results of the investigation are shown in Fig. 5.9. Panel a) shows that for a low peak electric field strength of 0.02 a.u., which corresponds to an intensity of $1.4 \times 10^{13}\,\mathrm{Wcm^{-2}}$, and a pulse duration of 4.8 fs the photoelectron spectrum exhibits the usual one-photon and ATI peaks, separated from one another by 0.7 a.u., the energy of one photon. There is no considerable influence of the channel coupling and the curves calculated with and without including Eqs. (5.11) lie on top of each other. However, increasing the peak-field strength to 0.2 a.u. yielding a peak intensity of $1.4 \times 10^{15}\,\mathrm{Wcm^{-2}}$ alters the spectrum significantly. This is illustrated in Fig. 5.9 b). The Rabi frequency is $\Omega_{3s-3p} = 0.16$ a.u. for these parameters, so that a splitting of the peaks from the weak-field energy position is expected by $\pm\Omega/2 = \pm\,0.08$ a.u.$\approx \pm\,2.2$ eV for the first peak, $\pm\sqrt{2}\Omega/2 = \pm\,0.11$ a.u.$\approx \pm\,3$ eV for the first ATI peak, $\pm\sqrt{3}\Omega/2 = \pm\,0.14$ a.u.$\approx \pm\,3.8$ eV for the second ATI peak, and so forth. Indeed, the higher the order of the peak the broader it is and the more pronounced the splitting becomes on the order of the above-mentioned energies. The peaks are also shifted to slightly smaller energies with respect to the positions in the lower energy case. This can be explained by the AC-Stark shift, because depending on the field strength and the ionization probability of the $3p$ shell the energy position of the doublets shifts toward lower energy [197].

In Fig. 5.10 first results calculated with the t-surff method are presented. The splitting in the high-intensity case of $1.4 \times 10^{15}\,\mathrm{Wcm^{-2}}$ is demonstrated for the two

first peaks. Also here, the splitting can be seen clearly in the first ATI peak. Compared to the splitting method the height of the two Rabi-split peaks is different, both peaks are equally high for t-surff while in the splitting calculation the first peak is lower. However, the agreement between the splitting and the t-surff method is relatively good as far as the positions of the peaks and their width are concerned. Therefore, further studies on the convergence might be necessary in order to obtain the same results for both methods and to investigate the asymmetry in the peaks in more detail. For instance the dependence of the asymmetry on the coupling between the decaying dressed states and the continua [195], which could be influenced by the pulse duration, should be studied.

Nevertheless, in principle, both methods produce the expected strong-field effect of the Rabi splitting in the photoelectron peaks. This shows that our method is applicable in cases where the driving of resonances can change the hole state in the ion which is then also reflected in the photoelectron spectrum.

6 Multiphoton and above-threshold ionization in the XUV energy range

This chapter and the following chapter present the results of our collaboration with the group of Michael Meyer from the European XFEL GmbH. Experimental data were calibrated, results from theory and experiment were compared and a deeper theoretical analysis of the xenon resonance features in the XUV were conducted. In this chapter I present the work on above-threshold ionization (ATI) in argon which was used as a calibration for the xenon measurements presented in Ch. 7.

6.1 Argon: Experiment at FLASH

The experiment which was performed by the group of Michael Meyer in January 2013 at FLASH aimed at measuring sequential and non-sequential multiphoton absorption and, in particular, above-threshold ionization of argon and xenon in the XUV photon energy range [193]. For this reason, and especially in view of the giant dipole resonance in xenon and the two-photon resonance $2p - 4p$ in argon, the three photon energies, 105 eV, 123 eV and 140 eV were chosen. The energy levels of argon are shown schematically in Fig. 6.1 a), the $2p$ shell is accessible with 2 photons, one- and two-photon ionization out of the $3s$ and the $3p$ shells are possible. In Fig. 6.1 b) the possible Auger decay channels illustrated after a hole in the $2p$ shell has been created.

The maximum intensity of the FEL pulses in the experiment mentioned amounted to $10^{14} - 10^{15}$ Wcm^{-2}. For these parameters the ponderomotive potential is (cf. Sec. 1.1)

$$U_p = \frac{I}{4\omega^2} \approx 0.01 \text{ eV} \ll \omega_{\text{photon}}. \tag{6.1}$$

From this expression it becomes obvious that in this case the ponderomotive energy is much smaller than the photon energy. If, additionally, the pulse duration or the duration of the interaction between the light with the system is much longer than the atomic timescale the interaction of the system with the laser pulse can be described by an effective cross section for one-photon processes and by generalized cross sections for higher multiphoton processes [45]; this is often called the perturbative limit. In the present parameter case one-photon processes strongly dominate which means that

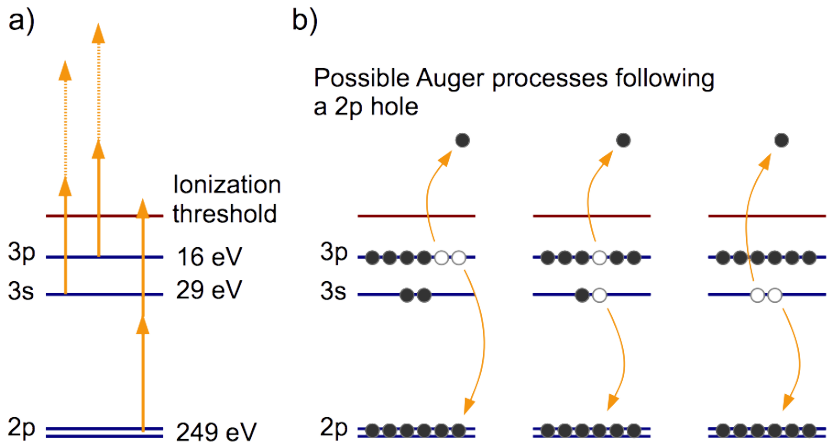

Figure 6.1: a) Argon energy levels schematically depicted. With all three relevant photon energies 105 eV, 123 eV and 140 eV an electron from the $3s$ and the $3p$ level can be ionized (denoted by solid arrows). The $2p$ electrons can be accessed only with two photons. $3s$ and $3p$ electrons can also absorb two photons if the pulse intensity is high enough and undergo above-threshold ionization (denoted by dashed arrows). b) Possible Auger decay channels after $2p$ core hole ionization with two photons.

the absorption cross section can roughly be approximated by the one-photon cross section.

Figure 6.2 shows the depopulation of the relevant shells of argon as a function of the electric field of a Fourier-transform limited pulse for a photon energy of 105 eV and a pulse duration of 12 fs, which is sufficiently long to not span other relevant resonances in argon. The total depopulation (red curve) as a function of the peak electric field can be described almost perfectly by the one-photon depopulation out of the $3p$ channel (blue dotted curve) which is modeled in first order perturbation theory by the one-photon cross section for the $3p$ electrons given by the expression $P(t) = 1 - \exp\left(-\sigma^{(1)}F\right)$, see Sec. 1.1.2. The resulting curve is shown in Fig. 6.2 as a green dashed curve which coincides with the total ionization probability (solid red curve). Therefore, it is possible for this particular problem to use rate equations which involve (generalized) cross sections for calculating the electron yields in ionization. The probability for ionization out of the $3s$ shell is smaller than for the $3p$ shell by almost an order of magnitude. The corresponding above-threshold ionization probabilities are smaller by more than two orders of magnitude for the largest peak electric field shown. The slope of the one-photon ionization curves as a function of the electric field is 2, while it is 4 for the two-photon process ATI. This evidences the applicability of lowest-order perturbation theory, where the probability dependence on the intensity is linear for one-photon ionization and quadratic for two-photon ionization processes. At about 0.1 a.u. of electric field strength the saturation regime is reached, where the significant depletion of the ground state leads to a deviation from this intensity dependence.

Using the splitting method within TDCIS to calculate photoelectron spectra resolved

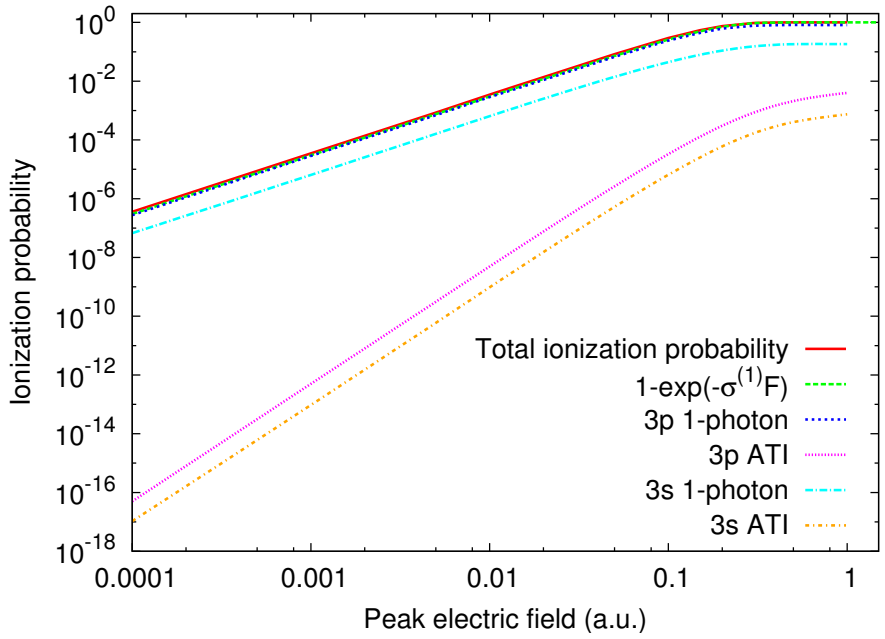

Figure 6.2: Depopulation of argon as a function of peak electric field. The pulse has a duration of 12 fs and a center energy of 105 eV. The probability of ionization is shown for the $3s$ and the $3p$ shell for the cases of one- and two-photon absorption. The two-photon absorption is effectively above-threshold ionization. The total depopulation can be modeled using the one-photon cross section for the $3p$ shell, because this process dominates for the pulse used here and, hence, lowest order perturbation theory can be applied.

in angle *and* energy [1] we are able to produce two-dimensional photoelectron distributions for a pulse with 105 eV photon energy. This is shown exemplarily in Fig. 6.3 for a Fourier-transform limited pulse of 2.6 fs duration and of $10^{15}\,\mathrm{Wcm}^{-2}$ intensity. The pulse duration was chosen according to the bandwidth of the experimental pulses.

The photoelectron distributions reflect the energy position of the photoelectron which amounts to the photon energy subtracted by the corresponding binding energy of the electron in its orbital. In experiment, e.g., with angle-resolved photoemission spectroscopy (ARPES) or velocity map imaging, the number of electrons emitted within a certain energy bandwidth in a certain direction can be measured [46, 109]. The peak energy positions can be read off at the nicely visible one- and two-photon circles (see arrows) from the x- or y-axes. On the right, the top figure shows the one-photon peaks, where the $3s$ electrons are promoted to a p-state exhibiting a $\cos^2\theta$ behavior while the $3p$ electrons are in a state superposition of an s-state and a d-state, reflected in two minima of the angular distribution. Due to the coherent pulse that was used in the calculations the energy width of the peaks corresponds to the Fourier-transform limited energy width for a pulse duration of 2.6 fs. The ATI peaks shown in the bottom figure show a superposition of s- and d-states for the $3s$ electrons and of p- and f-states for the $3p$ electrons resulting in an angular distribution with three minima (one true root and two global minima). The energy

[1] (In fact, this was not the case in the actual experimental setup.)

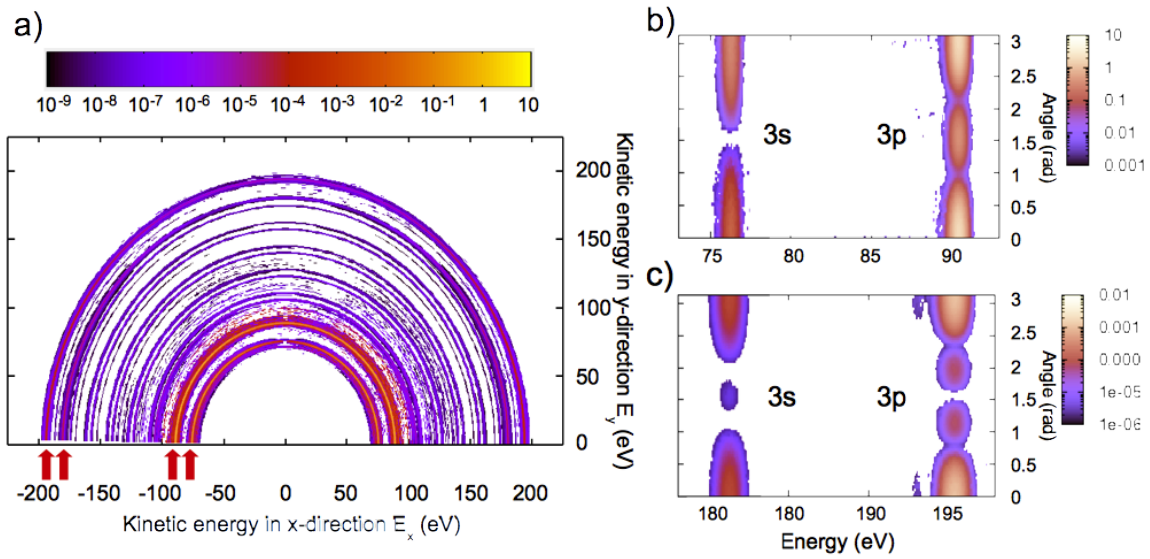

Figure 6.3: a) Angle-integrated PES presented in cartesian coordinates similar to a velocity map image in experiment, the x-axis being the kinetic energy in x direction and the y-axis in y direction. The z axis is defined as the polarization direction of the light. One can distinguish the one-photon peaks and the ATI peaks as circles with the kinetic energy corresponding to the photon energy minus the orbital binding energy, see red arrows. b) Two-dimensional one-photon photoelectron peaks, and c) ATI (bottom) photoelectron peaks of argon for a pulse of 105 eV, a pulse duration of 2.6 fs and an intensity of $10^{15}\,\mathrm{Wcm}^{-2}$, now as a function of the angle θ with respect to the polarization direction (top view on the spectra shown in Fig. 5.4). The angular distribution corresponds to a superposition of spherical harmonics belonging to the angular momentum states arising in ionization.

width of the peaks corresponds to the Fourier-transform limited width multiplied by $\sqrt{2}$ as it should be for two-photon ionization [200]. The fully integrated spectrum, over energy and angle, gives the total ionization probability of argon for the pulse mentioned.

The photoelectron spectra were experimentally recorded using a magnetic bottle spectrometer [4] which collects all electrons from all directions and guides them to the detector. For this reason the angular dependence of the photoelectrons is lost and only the energy dependence is measured. In Fig. 6.4 an angle-integrated photoelectron spectrum measured at 105 eV photon energy is shown (unpublished results). The experimental photoelectron spectra, such as in Fig. 6.4, were recorded for various pulse intensities over several orders of magnitude. Electron yields were obtained by summing over all electrons that are produced by the same process (i.e., by integrating/summing over the corresponding peaks).

This spectrum could in principle be compared to theory if the theoretical $2D$ spectrum is integrated over all angles which corresponds to collecting electrons from all directions. For illustration of the underlying processes a theoretically calculated angle-integrated photoelectron distribution is shown in Fig. 6.5 at a photon energy of 140 eV and at a slightly larger intensity of $10^{15}\,\mathrm{Wcm}^{-2}$. At this photon energy

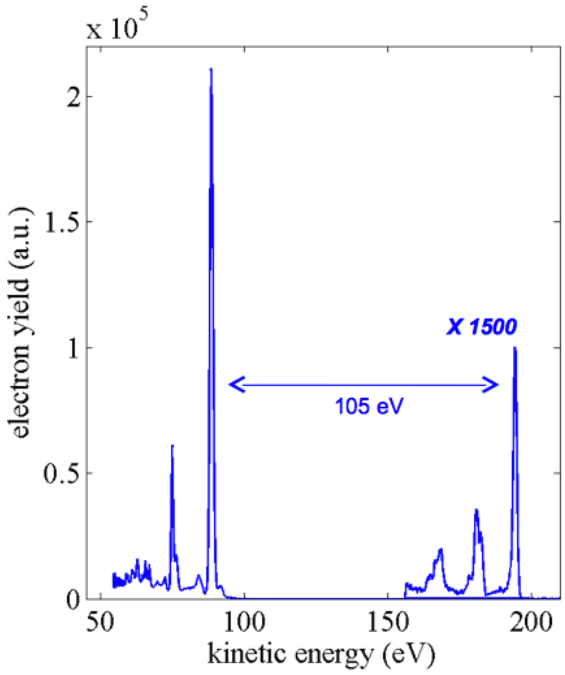

Figure 6.4: Experimental photoelectron spectrum recorded at a photon energy of 105 eV and a peak intensity of $5 \cdot 10^{14}\,\mathrm{Wcm}^{-2}$. One can clearly distinguish the one-photon peaks of the $3s$ and $3p$ shells as well as the ATI peaks that are separated from the one-photon peaks by exactly the energy of one photon. (Courtesy: Tommaso Mazza, unpublished results)

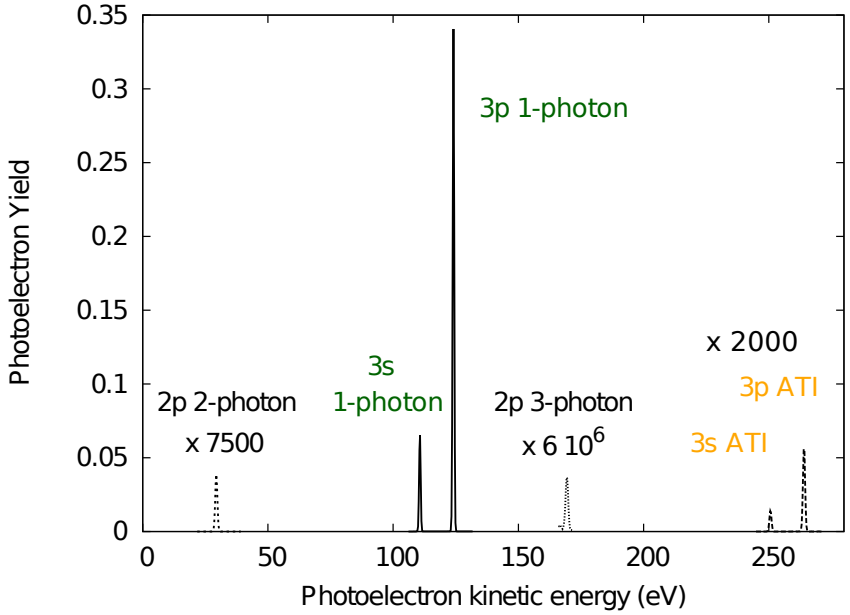

Figure 6.5: Angle-integrated photoelectron distribution of argon at a photon energy of 140 eV as a function of energy, irradiated by a 2.6 fs pulse at an intensity of $10^{15}\mathrm{Wcm}^{-2}$. The dominating part of ionized population stems from the $3p$ and the $3s$ shells, which absorb one photon (solid lines labeled in green). The ATI peaks are shown as well, magnified by the factor 2000 for better visibility (dashed lines labeled in orange). The dotted peak at the lowest kinetic energy which is magnified by the factor 7500 is attributed to the $2p$ shell. By absorbing two photons a $2p$ electron is promoted to the continuum. Finally, a three-photon peak from the $2p$ shell is observed around 170 eV (fine-dotted, magnified by $6 \cdot 10^6$).

one-photon and ATI processes from the $3s$ and $3p$ shells are observed, as well as two-photon ionization out of the $2p$ shell and even three-photon ionization which at this intensity is weaker by 3 orders of magnitude.

6.2 Calculation of cross sections and electron yields

In order to meaningfully compare theoretical calculations of cross sections with experimental electron yield data it is necessary to take into consideration all experimental parameters: the duration and the statistics of the light pulses, the pulse energy and the geometry of the pulse together with the geometry of the optical measurement components. Because of the experimental pulse profile the light intensity varies over the interaction region. Therefore, also the ionization probability depends on the position within the electric field distribution. By volume integration the actual intensity and accordingly the ionization due to the available intensity is taken into account. In the calculation of cross sections Gaussian pulses, i.e., fully coherent pulses were utilized, while in experiment the pulses produced at FLASH exhibit stochastic statistics. For the correct calculation of cross sections within perturbation theory using coherent light for processes induced by stochastic light the cross section must be multiplied by the degree of coherence for stochastic light, which amounts to 2 for a two-photon process.

The cross sections for the one- and two-photon absorption cases for the $2p$, $3s$ and $3p$ shells were calculated by analyzing the angular momentum resolved ion density matrix calculated with TDCIS. As can be seen in Fig. 6.2 the most probable ionization event is a one-photon ionization process out of the $3p$ shell. The two-photon events are suppressed by many orders of magnitude. Therefore, from the perspective of perturbation theory, we can make the approximation that two-photon ionization is the highest order effect that occurs. In this case, the orbital and angular resolved ion density matrix can be used to unambiguously determine the ionization in each channel for one- and two-photon ionization using the dipole selection rules. However, if this approximation cannot be made the cross sections can be obtained by explicitly calculating the photoelectron distribution, by the separation of the different processes by the energy of the photoelectron and by subsequent integration over the angle over the corresponding photoelectron peaks. This yields the ionized population due to the process of interest.

6.2.1 (Generalized) Cross sections

In the framework of perturbation theory ionization cross sections are defined by the ionization probability of the process divided by the fluence corresponding to the process of interest. To provide an example, let us assume that we want to describe the ionization probability of ionizing an electron out of the ground state with a

single photon. As mentioned in Sec. 1.1.2 rate equations can describe the ionization probability in this case. Therefore, the corresponding differential equation for one-photon ionization by a light pulse with flux j_1 has the form

$$\frac{\mathrm{d}N_1}{\mathrm{d}t} = \sigma^{(1)} j_1(t) N_0(t), \tag{6.2}$$

where N_1 denotes the ionized population by one photon, N_0 the population of the ground state, $\sigma^{(1)}$ the one-photon cross section, and $j_1(t)$ the time-dependent flux $j^{(1)}(t) = I(t)/\omega$, where $I(t)$ is the light intensity and ω the photon energy. In other words, the flux is a measure of the number of photons that are available for ionization processes per unit time and area.

An important criterion for the perturbative regime is that the ground state is not depleted, i.e., the field is weak compared to the innneratomic potential and the population of the system remains essentially in its ground state. If the approximation is made that the ground state is far away from being depleted, i.e. $N_0(t) = N_0 = 1$, the equation is simplified and can be integrated

$$N^{(1)} = \sigma^{(1)} \int j_1(t) N_0(t) \mathrm{d}t = \sigma^{(1)} \int j_1(t) \mathrm{d}t, \tag{6.3}$$

where N_0 was set to 1 and $\sigma^{(1)}$ can be pulled out of the integral because it is time independent. Consequently, only the integral over the flux must be carried out. For all our purposes we use a Gaussian pulse with the intensity envelope

$$I(t) = \frac{cE_0^2}{8\pi} \exp\left(-4 \ln 2 t^2/\tau^2\right), \tag{6.4}$$

where c is the speed of light, E_0 is the peak electric field, and τ is the pulse duration (FWHM). Integrating the flux over time we obtain the fluence for one-photon absorption:

$$F^{(1)} = \frac{c\tau}{8\pi\hbar\omega} \sqrt{\frac{\pi}{4 \ln 2}} E_0^2. \tag{6.5}$$

Inserting the fluence into Eq. (6.3) we obtain the expression for the cross section

$$\sigma^{(1)} = \frac{N^{(1)}}{F^{(1)}}, \tag{6.6}$$

so that the units are cm^2 as it should be for a cross section.

So far, we only considered one-photon ionization. The rate equation (6.3) must be complemented by an additional term in the case that the ionized population can also result from population transfer from the ground state by the absorption of two photons. The two-photon ionized population is denoted by $N^{(2)}$. In the following we denote the generalized two-photon cross section by $\sigma^{(2)}$. Thus, the rate equation

reads

$$N^{(1)} = N^{(1)} + N^{(2)} = \sigma^{(1)} \int j_1(t) N_0(t) \mathrm{d}t + \sigma^{(2)} \int j_2 \mathrm{d}t N_0(t) \tag{6.7}$$

$$= \sigma^{(1)} \int j_1(t) \mathrm{d}t + \sigma^{(2)} \int j_1^2 \mathrm{d}t. \tag{6.8}$$

The fluence associated with two-photon absorption, $F^{(2)}$, is given by integrating the flux over time, $F^{(2)} = \int j_1^2 \mathrm{d}t$. For the Gaussian intensity distribution (6.4) we obtain

$$F^{(2)} = \left(\frac{c}{8\pi}\right) \sqrt{\frac{\pi}{8 \ln 2}} \frac{E_0^4}{(\hbar\omega)^2}, \tag{6.9}$$

$$\sigma^{(2)} = \frac{N^{(2)}}{F^{(2)}}, \tag{6.10}$$

and, accordingly, the unit of the fluence $F^{(2)}$ is $\mathrm{cm}^{-4}\mathrm{s}^{-1}$. The unit of the corresponding cross section $\sigma^{(2)}$ is, therefore, $\mathrm{cm}^4\mathrm{s}$. Following this logic, higher order generalized cross sections σ^N, where N is the number of photons needed for the ionization process, have the dimension $\mathrm{cm}^{2N}\mathrm{s}^{N-1}$ [45].

Using TDCIS the depopulations due to one- and two-photon ionization processes, $N^{(1)}$ and $N^{(2)}$, for the $2p$, $3s$ and $3p$ shells are calculated in the perturbative limit, i.e. for pulses that do not deplete the ground state (the total depopulation being significantly less than a percent). The cross sections can be derived using formulae (6.6) and (6.10). These cross sections are used in a rate equation model in order to calculate electron yields for different light intensities. Equivalently, the corresponding peak of the PES can be integrated over the angle and the energy in order to obtain the ionized population.

6.2.2 Electron yields

In order to avoid very small numbers the units of the cross sections are conveniently chosen to be $\mathrm{cm}^{2N}\mathrm{fs}^{N-1}$. The relevant cross sections for the processes of interest in the experiment were

- the one-photon ionization cross section for the $2p$ shell (first index 0) σ_{01},
- the one-photon ionization cross section for the $3s$ shell (first index 1) σ_{11}, and
- the one-photon ionization cross section for the $3p$ shell (first index 2) σ_{21},
- the two-photon cross section for the $2p$ shell σ_{02},
- the two-photon cross section for the $3s$ shell σ_{12}, and
- the two-photon cross section for the $3s$ shell σ_{22}.

As above, the corresponding ionized populations are denoted by P_{ij}, where the index i stands for the shell (0, 1, or 2), out of which the electron originated, and the

second for the ionization process (1 for one-photon, 2 for two-photon). The ground state population is symbolized by P_0. The time dependence of the populations and the flux is omitted for the sake of legibility. Assuming that argon is predominantly in the ground state, the coupled rate equation system for one- and two-photon ionization of argon in the XUV has the following structure:

$$\dot{P}_0 = -\left[(\sigma_{01}+\sigma_{11}+\sigma_{21})j_1 + (\sigma_{02}+\sigma_{12}+\sigma_{22})j_1^2\right] P_0 \tag{6.11a}$$

$$\dot{P}_{01} = \sigma_{01} j_1 P_0 \tag{6.11b}$$

$$\dot{P}_{02} = \sigma_{02} j_1^2 P_0 \tag{6.11c}$$

$$\dot{P}_{11} = \sigma_{11} j_1 P_0 \tag{6.11d}$$

$$\dot{P}_{12} = \sigma_{12} j_1^2 P_0 \tag{6.11e}$$

$$\dot{P}_{21} = \sigma_{21} j_1 P_0 \tag{6.11f}$$

$$\dot{P}_{22} = \sigma_{22} j_1^2 P_0 \tag{6.11g}$$

For consistency, the flux is calculated in photons per cm^2 and per fs. This system is solved for a variety of fluxes spanning the range used in experiment (many orders of magnitude) with the Matlab software [201], using a differential equation solver based on the Runge-Kutta algorithm of order 4 for a sufficiently long time interval of $[-4\tau, 4\tau]$. The resulting electron populations that correspond to each flux must now be employed for integration over the actual interaction volume within the experimental setting. For this purpose, the experimental data were analyzed and the theoretical yields were compared with the experimental yields in order to calibrate the geometric parameters and overall uncertainties in the measurements. In an iterative manner the yields were calculated for a set of possible experimental parameters involved, i.e., focus, Rayleigh length, pulse length and volume integration region along the propagation direction and perpendicular to it. The results were compared to the experimental data sets. It was found that a pulse duration of 80 fs, a focus size of (5 ± 1) μm (FWHM) and a Rayleigh length of 0.4 mm for the measurements result in very good agreement with the slopes for the one- and two-photon ionization yields. The integration range was 0.48 mm with an offset in the propagation direction of 0.13 mm for 105 eV and symmetric around the focus for 140 eV. The pulse geometry did not significantly deviate from the Rayleigh geometry of a Gaussian beam. The measurements at the other photon energies were performed at different intensity and beam parameters.

Now, having calculated the electron yields as a function of intensity the volume integration must be taken into account. Assume that the signal, i.e. the populations, $S(F)$ as a function of fluence is given. Due to the pulse intensity profile in the direction perpendicular to the propagation direction, described by the radial coordinate ρ, and the finite and extended region along the propagation direction z, in which the argon gas and the light pulse interact, the volume integration must be performed along z and ρ. In the following a Gaussian beam profile is assumed. Denoting the integration

volume element by $\mathrm{d}V$ we obtain the expression

$$\int S(F)\mathrm{d}V = \int \rho \, \mathrm{d}\rho \, \mathrm{d}z S(F) = \int \mathrm{d}z \, \mathrm{d}F \, \rho(F,z)\big|J(F,z)\big|S(F), \tag{6.12}$$

where a coordinate transformation $(\rho, z) \to (F, z)$ is performed with the determinant of the Jacobian transformation matrix

$$J(F,z) = \begin{pmatrix} \frac{\partial \rho}{\partial F} & \frac{\partial \rho}{\partial z} \\ \frac{\partial z}{\partial F} & \frac{\partial z}{\partial z} \end{pmatrix}. \tag{6.13}$$

The fluence distribution as a function of ρ and z is given by

$$F(\rho, z) = F_{\mathrm{peak}} \exp[-\rho^2/w(z)^2], \tag{6.14}$$

where $F_{\mathrm{peak}} = \frac{4 \ln 2 N_{\mathrm{ph}}}{\pi w^2(z)}$ is the peak fluence that is taken for each distance from the focus, N_{ph} being the number of photons. The peak fluence is itself a function of z. The function $w(z)$ describes the divergence of the beam, i.e. it determines the spot size at a distance z from the beam waist or focus w_0

$$w(z)^2 = w_0^2 \left[1 + \left(\frac{z}{z_0}\right)^2\right]. \tag{6.15}$$

By inverting Eq. (6.14) it can be seen that this function is invertible bijectively and yields $\rho(F, z)$ when we take the positive (physical) solution. Eq. (6.12) becomes

$$\int S(F)\mathrm{d}V = \int_0^{F_{\mathrm{peak}}} \mathrm{d}F \; S(F) \left\{ \int_{\mathrm{min}}^{z_{\mathrm{max}}} \rho(F,z)|J(F,z)|\mathrm{d}z \right\}, \tag{6.16}$$

where the z-integration limits are given by the experimental gas volume conditions. The z-integration can be performed analytically, the F-integration needs interpolation for the F-grid (which is very cheaply implemented in Matlab).

Equivalently to the Matlab calculations for argon, the XATOM toolkit [139] can be used to solve the rate equation system after inserting the cross sections that were pre-calculated with TDCIS and use the program *vol_int* [2] for volume integration. Figure 6.6 shows the $3p$ one- and two-photon electron yields as a function of pulse energy for a pulse of 80fs duration. As expected the yield decreases with increasing photon energy, the yield curve for 105 eV lies above the 123 eV curve and the photon energy of 140 eV produces the smallest one-photon yield. The same order of the curves with energy holds also for the two-photon yield curves. The slope of the one-photon curves is one, while it is two for the two-photon process, again in accordance with perturbation theory. The saturation regime is only slightly entered at a pulse energy around 10 μJ. Note that XATOM can additionally provide Auger decay rates for the decay channels shown in Fig. 6.1 b), that are not included in the rate equation system

[2] (written by Sang-Kil Son and Zoltan Jurek in our group)

(6.11) because the Auger process leads to doubly ionized argon, a configuration which lies outside the configuration space that is considered within CIS. The $2p$ Auger yield is also shown in purple in Fig. 6.6. It is clear that the Auger yield is of the same order as the two-photon above-threshold ionization, because two photons are necessary to ionize the electron of the $2p$ shell. Consequently, the curve exhibits also a slope of two, cf. Sec. 1.1.2.

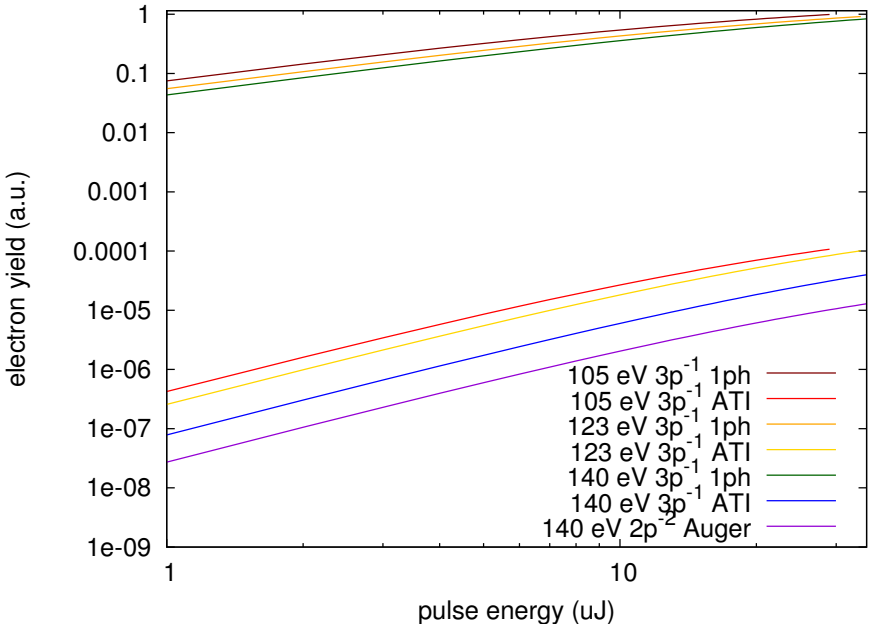

Figure 6.6: Electron yields from one- and two-photon ionization of argon with a pulse of 80 fs duration and photon energies of 105, 123 and 140 eV as a function of pulse energy. Due to the high photon energies the two-photon process is above-threshold ionization. The purple line corresponds to the $2p$ two-photon ionization which leads to subsequent Auger decay.

6.3 Comparison between theory and experiment

Using argon as calibrating system a single overall factor was determined which accounts for the experimental apparatus uncertainty (nozzle parameters, sample density or pressure, transmission of the analyzer, detector gain, deviation from Gaussian beam profile, etc.). These parameters affect the measurements differently over the broad photoelectron energy range that was investigated. In particular, the measurements of the one-photon and the two-photon energy ranges experienced different experimental circumstances. Therefore, upon dividing the experimental ATI data by this factor, which amounts to 2.1, the agreement between the experimental data and the theoretical calculation was very good. The agreement is reflected in the slope as well as the ratio between the one-photon and two-photon electron yields and in the onset of saturation, which is visualized in Fig. 6.7. In this figure the comparison

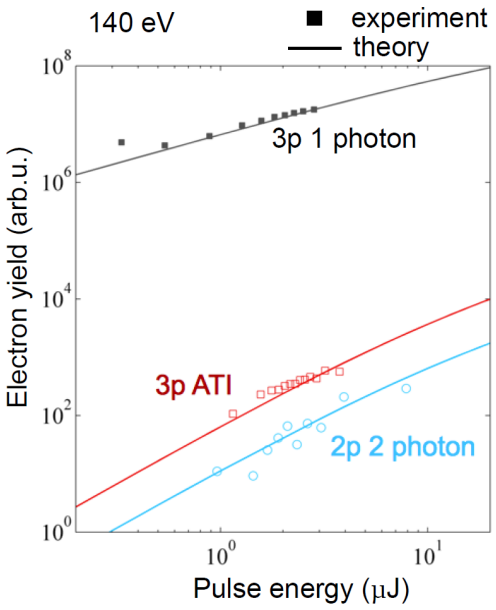

Figure 6.7: Comparison between theory and experiment: Electron yields as a function of pulse energy at a photon energy of 140 eV. The dots denote the experimental data points, the solid lines represent the corresponding theoretical curves. The $3p$ one-photon, ATI and $2p$ Auger yields are shown and are found to agree nicely between theory and experiment.

between theory and experiment is shown for the one- and two-photon electron yields at the photon energy 140 eV; the experimental data are plotted as points (open or full) while the theoretical calculations are drawn as solid lines. Both the theoretical $3p$ one-photon and ATI yields match the experimental data points nicely. At 140 eV photon energy the $2p$ shell can be ionized by two photons and subsequent Auger decay produces electrons with characteristic energies which can be separated from the one- and two-photon yield.

Furthermore, it is interesting to study the interaction of argon with photons of 123 eV energy, because with this energy there is a resonance that can be excited with two photons: The $2p - 4p$ transition can be induced by two-photon resonant excitation at 123 eV. This process was calculated by using a pulse with a very narrow energy bandwidth, in order to avoid excitations of other nearby lying states. The cross section for the resonant two-photon excitation was found to be

$$\sigma^{(2)}_{2p-4p} = 1.8 \cdot 10^{-52}\ \mathrm{cm}^4 s. \tag{6.17}$$

Since argon is a relatively small system which does not exhibit strong electron correlation effects we can rely on the calibration between theory and experiment by fixing this single parameter as described above. The next, exciting example of two-photon ATI will benefit from this calibration and underline the importance of electron correlation effects in a much more complex system, namely xenon. This will be discussed in the following chapter.

7 Xenon above-threshold ionization involving the giant dipole resonance

Nature Communications **6**, 6799, (2015)
Physical Review A **91**, 032503 (2015)

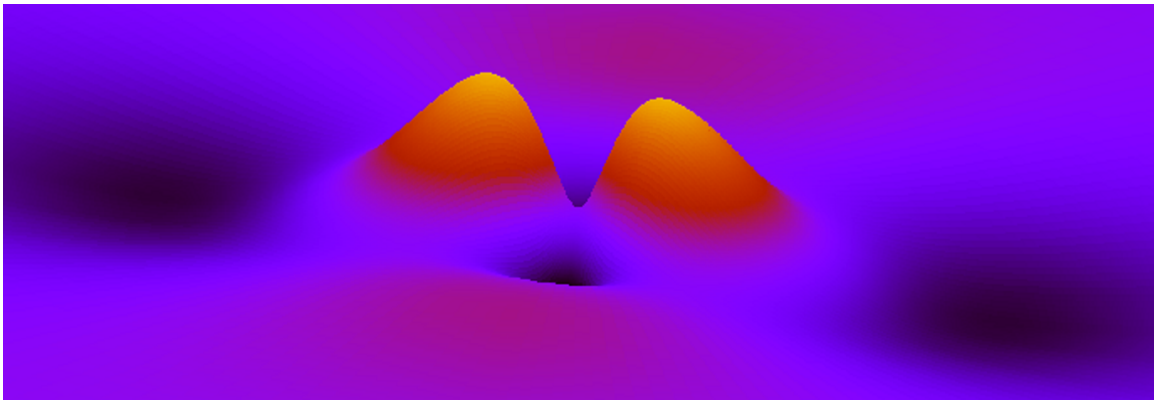

Figure 7.1: Graphical representation of a $4d_0$ electron orbital in atomic xenon; the radial wave function of a $4d$ electron is multiplied by the spherical harmonic $Y_{20}(\Omega)$ and visualized as a function of the cartesian coordinates x and y (axes not shown).

This chapter highlights the results of the collaboration with the group of Dr. Michael Meyer. Combining our theoretical approach with the data of the experiment legitimated our theoretical prediction of hidden resonance substructure in *the* atomic example of collective excitation: the giant dipole resonance in xenon. Our results were only made possible by a high-intensity study at FLASH. The evidence that our findings provide shows, for the first time, the importance of collectiveness in xenon in the nonlinear regime and establishes the existence of two underlying resonances within the range of the giant dipole resonance. Most crucial for our study was the nonlinearity of the effect, namely the two-photon ionization process in xenon as mentioned in the previous chapter. New information about the xenon shell emerged, which was hidden for over 50 years, from the very discovery of the xenon giant dipole resonance [202–204].

7.1 The giant dipole resonance (GDR)

In 1964, while the interest in absorption characteristics of inner shell electrons with high angular momentum was growing, experiments in the XUV photon energy range revealed an "unusual" feature in the photoabsorption cross section of the $4d$ electrons in xenon [202–204] (nuclear charge $Z = 54$, the valence shells following the $4d$ shell of xenon are the $5s$ and $5p$ orbitals). This feature was already at that time attributed to the very nature of the $4d$ shell and received later the name "giant dipole resonance" (GDR). The XUV photoabsorption spectrum of xenon was the topic of numerous studies in the course of the last 50 years, both theoretically and experimentally. It is understood as the interplay of two effects: Qualitatively the phenomenon of this huge absorption resonance can be explained as originating from a shape resonance effect: After absorbing a photon out of the $4d$ shell the electron is promoted predominantly to an f-state. Thus, due to the centrifugal barrier it is trapped temporarily in a resonance state in the electronic continuum near the ionic core [9, 205, 206] until it can tunnel out and leave the ion. At the same time the xenon $4d$ shell is an illustrative example of a many-body system showing collective electronic behavior; its resonating character under XUV radiation is interpreted as the collective response of all ten $4d$ electrons to an external weak-field perturbation[95, 102]. Only when electron correlation effects within the $4d$ shell are included quantitative agreement with experimental data is achieved. This means that the resonant excitation cannot be explained as a purely independent-particle effect.

The giant dipole resonance and its impact on various observables has been studied within TDCIS. One application involving the giant dipole resonance was a detailed investigation of one-photon ionization [207]. In this work the focus lay in particular on many-body effects. It was shown that within the interchannel coupling scheme the experimental one-photon cross-section curve of xenon in the XUV is described quite well, while in the intrachannel case the resonance is much narrower and red-shifted. In Fig. 7.2 the one-photon cross sections are shown for both models. The full TDCIS scheme exactly reproduces the position of the experimentally observed one-photon cross section of xenon in the range of the giant dipole resonance. The height of the peak is underestimated by the interchannel model while the width is overestimated by 18% compared to the experimental cross section. This proves that, qualitatively, the TDCIS theory captures the main features of the many-body effect that renders the one-photon cross section curve broader and shifts it to higher energies.

A second application [208] proved that the many-body correlation effects leading to the giant resonance have also a huge impact on the high-harmonic spectrum [208, 209], i.e., a highly nonlinear phenomenon is greatly influenced by the interchannel coupling: when including the interchannel matrix elements the yield of the HHG spectrum of xenon is enhanced compared to the intrachannel scenario. The study demonstrates that the enhancement stems from the two-body interchannel interaction when the initially ionized $5p$ photoelectron returns to the ion: it can exchange energy with all $4d$ orbitals and promote one of them into a $5p$ vacancy. Thus, this effect can be fully

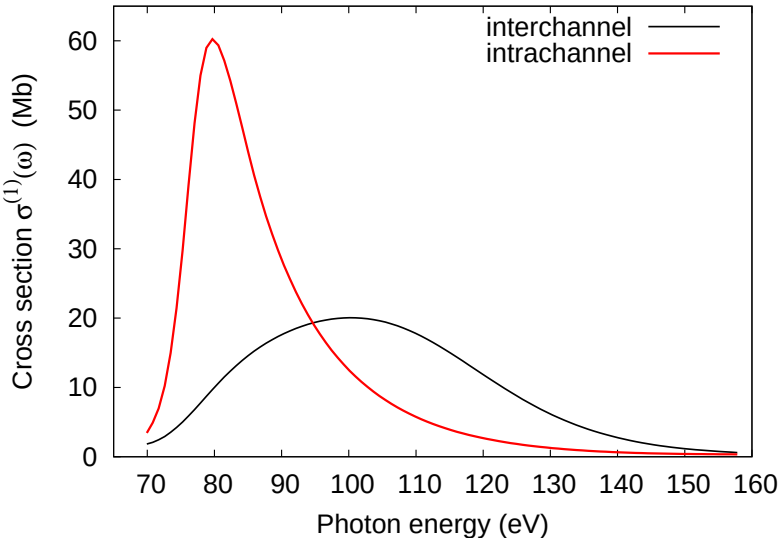

Figure 7.2: One-photon photoabsorption cross section calculated with TDCIS using the two models. The black line shows the interchannel and the red curve the intrachannel calculation.

explained when taking into account the same type of correlations that leads to the one-photon cross section curve.

In the following, we will go beyond the linear-response regime and legitimate the predictability of our theoretical approach further by comparison with the experimental results that were obtained at FLASH. We will study the giant dipole resonance in the two-photon regime, with the help of a process where the first photon is used to excite the giant dipole resonance and the second photon ionizes the system.

7.2 Sensitivity of nonlinear photoionization to resonance substructure in collective excitation

As stated above, the giant dipole resonance in the photoionization of the 4d shell in xenon, which lies in the XUV energy range, is one of the most important and well-studied example for collective effects in atomic systems. The recent advent of high-brilliance light sources such as XUV and x-ray FELs has opened a door to studies beyond the linear regime in these photon energy regimes. Now, the focus lies on the nonlinear light-matter interaction and the corresponding response of the systems under study. In particular, atomic xenon has been studied in various experiments at FELs in a photon range between 93 eV to 5 keV [210–214]. Theoretical work has been done to model the experimental results [215]. The ionization of xenon under the unprecedented conditions at FELs has been the subject of several investigations [210–216], that have stimulated speculations about the influence of collective effects on the process of multiple ionization[210, 211]. Furthermore, a high-harmonic-generation experiment on xenon [217] evidenced the impact of the $4d$ giant dipole resonance on a

nonlinear optical process [208, 209]. Yet, all these observations can be well understood, as far as collectiveness is concerned, considering the one-photon absorption cross sections of the various charge states of xenon [213, 215, 218], i.e., in terms of the spectral characteristics of its linear response.

However, exploiting the opportunities of new, intense light sources allows the investigation of the collective response mechanisms of many-body systems through their nonlinear interaction with short-wavelength radiation. In the same beam time at FLASH where the results on argon were obtained (described in the previous chapter) xenon was investigated at the same photon energies of 105 eV and 140 eV, which lie exactly in the range of the giant dipole resonance. One major objective of our theory-experiment collaboration was to investigate whether and to what extent collective behavior, i.e. many-body effects, plays a role in the nonlinear response regime in the case where the photon energy is greater than the electron binding energies. As shown in the present chapter, nonlinear spectroscopy provides the possibility of unveiling substructures in the spectrum of collective excitations that cannot be resolved with linear spectroscopy. Already in the 1970's a theoretical calculation of the dielectric function of xenon in the range of the giant dipole resonance revealed two energy poles [219]. However, in this investigation the results were not interpreted as resonance states and these calculations were not further pursued. Our analysis of nonlinear xenon ionization, i.e. the process of ATI, re-discovered two energy poles, identified them as resonance states and, for the first time, evidenced that using nonlinear spectroscopy these two underlying resonance states are emerging as clear features in the ATI cross section.

Before the results of the joint work on above-threshold ionization of xenon in the XUV, the theoretical model and the interpretation are presented, I outline the methodology of our approach.

7.2.1 Methodology

At the photon energies that were employed in the experiment, 105 eV and 140 eV, the processes that can occur in atomic xenon are one- and two-photon ionization of the $4d$, $5s$ and $5p$ shells and subsequently Auger decay following an inner shell vacancy. With a lifetime of 3 fs the $4d$ hole decays via the Auger process [220]). Since the pulse durations employed in the experiment are much longer than 3 fs the Auger yields have to be taken into account (see caption of Figs. 7.5 and 7.6). Technically, since the photon energies exceed the binding energy of the orbitals considered, the observed two-photon process is above-threshold ionization. In Fig. 7.3 a schematic representation of the levels of xenon and the ionization processes is given. Panel a) shows simple one-photon ionization, panel b) the absorption of a second photon, i.e. ATI. In order to compare theoretical results to experimental data we choose electron yields as a function of pulse intensity as observable.

Employing nonlinear electron spectroscopy, namely by two-photon ionization of

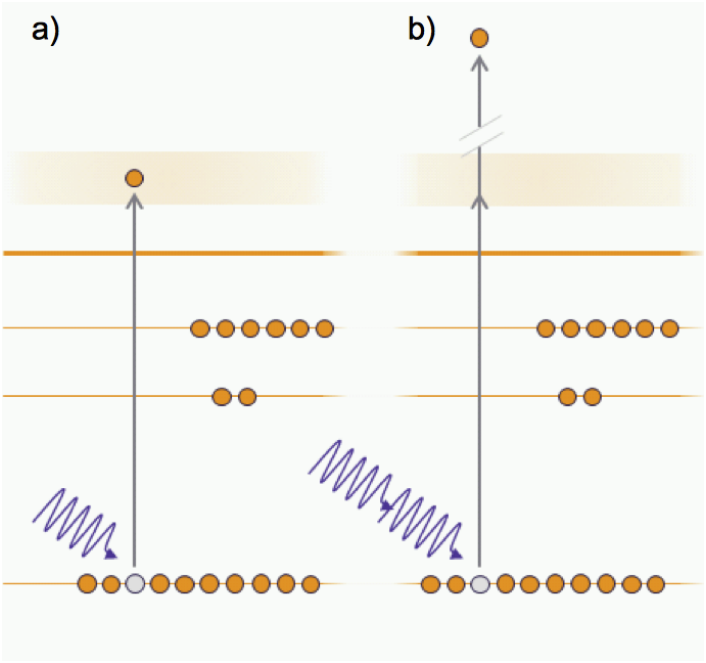

Figure 7.3: Schematic representation of the ionization processes and associated models. a) Single-photon ionization process; b) two-photon, i.e., ATI process. ©2015 Nature Publishing Group

xenon, we demonstrate that the nonlinear process unveils otherwise unresolved aspects of the collective behavior of the system. For this purpose, we analyzed the above-threshold ionization cross section over the whole range of the giant dipole resonance of xenon. Due to the photon-energy selected, the two-photon process occurs through the giant dipole resonance as an intermediate step (Fig. 7.3). We will show in the following that a model assuming a single intermediate state fails to describe the obtained results. Instead, the resonance feature in the predicted energy dependence of the two-photon process and its shape strongly suggest that more than one resonance state underlie the giant dipole resonance. Although these states are unresolved in the linear ionization of xenon, two-photon ionization turns out to be a sensitive process for their observation.

For the theoretical calculation all necessary cross sections are calculated in an *ab initio* manner within TDCIS. These cross sections are introduced into a rate equation system that is similar to the argon case, see Ch. 6. The solutions of the rate equations for various photon fluxes represent the ionization populations which are calculated as a function of pulse intensity. In order to compare with the experimental data, the electron yields are calculated through volume integration of the populations by including the experimental parameters regarding the shape and intensity distribution of the light pulses. The calibration factor which was identified with the help of the argon data presented in Sec. 6.3 enters as the only normalization between theory and experiment and accounts for experimental conditions beyond the simple beam geometry.

First-principles calculation of cross sections

First, an overview of the theoretical method is given. The full N-electron Schrödinger equation, see Eqs. (2.2) and (2.8), is solved numerically within TDCIS and the depopulations in the $4d$ shell due to one- and two-photon absorption are calculated by analyzing the ion density matrix elements and by distinguishing the depopulations corresponding to the angular momenta of the final states [129]. The cross sections for one- and two-photon absorption are calculated via the population in the corresponding hole channels. As long as perturbation theory is valid and higher order processes are negligible, these depopulations are distinguishable due to the different angular momenta of the ejected electron according to the dipole selection rules. All contributions from the $4d_0$, $4d_{\pm1}$, and $4d_{\pm2}$ subshells are added.

As mentioned in Chapters 1 and 2 a particular strength in theoretical modeling is the ability to switch on and off certain parts of the model and study the impact of the corresponding feature. In the present case it is crucial that we can include and distinguish certain electronic correlation effects that are mediated by Coulomb interaction. In particular, for the description of a collective response the system cannot be written as a single particle-hole state, but instead a superposition of particle-hole states is needed. The "full" or "interchannel" model[1] includes the coupling among the holes in the $4d$, $5s$ and $5p$ orbitals and the electron, see Figs. 7.4 b) and 2.2 b). The corresponding Coulomb matrix elements between the particle–hole excitations $|\Phi_i^a\rangle$, $|\Phi_j^b\rangle$, cf. Sec. 2.3,

$$\langle \Phi_i^a | \hat{V}_{\mathrm{e-e}} | \Phi_j^b \rangle, \tag{7.1}$$

are included for all different index pairs (i, j) within the space of active orbitals ($4d$, $5s$, and $5p$), which means that $\langle \Phi_i^a | \hat{V}_{\mathrm{e-e}} | \Phi_j^b \rangle \neq 0$, for all $i = j$ *and* $i \neq j$; a, b are taking values for all virtual orbitals. In this way, superpositions of particle-hole states, i.e. collective states, may be described. In contrast, in the case of the "reduced" or "intrachannel" model[1] the elements with $i \neq j$ are set to zero: therefore, $\langle \Phi_i^a | \hat{V}_{\mathrm{e-e}} | \Phi_j^b \rangle = 0$. Keeping only the elements $\langle \Phi_i^a | \hat{V}_{\mathrm{e-e}} | \Phi_i^b \rangle \neq 0$ results thus in the description of coupling only with the very $4d$ orbital from which the electron was ionized, see Figs. 7.4 a) and 2.2 a).

Summarizing our theoretical model, it captures many-body processes beyond linear response theory quite naturally, allowing the selective inclusion of those electronic correlation effects that are responsible for collectiveness. As mentioned above for a system characterized by collective behavior, the wave function is given by a coherent superposition of particle-hole states [221], due to the strong particle-hole interaction. Experimental results are compared with the full model, which describes the collective response of the system by accounting for the electron-hole interaction in all channels open to ionization, see Fig. 7.4 b), and the reduced model, which confines this interaction to the hole from which the electron was excited, see Fig. 7.4 a).

[1] Both terms will be used on equal footing throughout this chapter.

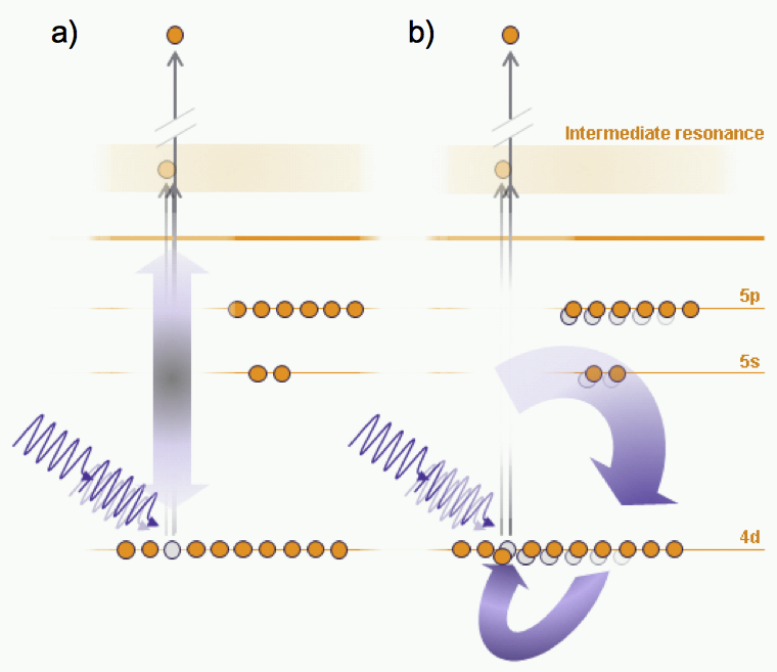

Figure 7.4: Schematic representation of the ionization processes and associated models. a) one- and two- photon processes according to the reduced model, only including interaction of the emitted electron with the hole from which it is excited; b) one- and two-photon processes according to the full model, accounting for electron-hole interaction in all channels open to ionization.

Rate equations for theoretical yield calculation

The theoretical yields are obtained from the numerical solution of the following equations which are valid for the electron yield from the neutral target whose population is denoted by N_0:

$$\begin{aligned} \dot{N}_0(t) &= -\left[y_{1ph}(t) + y_{2ph}(t)\right], \\ y_{1ph}(t) &= \sigma^{(1)} \cdot j(t) \cdot N_0(t), \\ y_{2ph}(t) &= \sigma^{(2)} \cdot j(t)^2 \cdot N_0(t). \end{aligned} \tag{7.2}$$

This system of rate equations is solved assuming a Gaussian pulse with 80 fs (FWHM) duration. The one-photon cross section $\sigma^{(1)}$ and the two-photon cross sections $\sigma^{(2)}$ entering the system of equations (7.2) are obtained both for the full and the reduced model, cf. Fig. 7.4. As described in the previous chapter, Ch. 6, the rate equation solutions (Y_{1ph}, Y_{2ph}) are calculated over the very broad range of 9 orders of magnitude of laser intensities that enter the equations by the flux $j(t)$ (cf. the rate equation system 6.11):

$$\begin{aligned} Y_{1ph} &= \int \mathrm{d}t \; y_{1ph}(t) \\ Y_{2ph} &= \int \mathrm{d}t \; y_{2ph}(t). \end{aligned} \tag{7.3}$$

Thereby the yields for the one- and two-photon ionization are obtained as a function of flux. These results are numerically integrated over the volume of acceptance of the electron analyzer in order to account for the spatial distribution of the FEL fluence.

In the following it is demonstrated how the nonlinear interaction of a many-body system with intense XUV radiation can be used as an effective probe for characterizing otherwise unresolved features of its collective response. The excellent agreement between experiment and theory strongly supports the prediction that two distinct poles underlie the giant dipole resonance.

Experiment and theory approach to nonlinear photoionization

Photoelectron spectroscopy permits the disentanglement of photoemission processes from different orders of interaction. Our first-principles calculations, on the other hand, can interpret the effect of electron correlations in these different processes. In experiment the relative yields of one-photon and two-photon ionization of the $4d$ shell of xenon were measured by electron spectroscopy, cf. Fig. 7.3 a) and 7.3 b). They are compared to the theoretical yields that are obtained from the rate equation solution. Analyzing the experimental data together with Dr. Mazza and employing the calibration factor which was introduced in Ch. 6 the comparison for both scenarios, intrachannel and interchannel coupling, was performed.

Electron spectroscopy of one- and two-photon ionization

For completeness and for a better understanding of the experimental data regarding the energies involved in this xenon experiment, I present briefly some experimental details, that can also be found in our publication in greater detail Ref. [4].

The experiments were performed at the BL2 beamline of FLASH [222, 223]. FEL pulses at photon energies of 105 eV and 140 eV were focused down to a few microns in front of the aperture of a magnetic bottle electron spectrometer. As already mentioned in Ch. 6, the spectrometer was used to measure the kinetic energy of the electrons that are produced by one-photon and two-photon absorption processes in an effusive jet of xenon atoms. Electron spectra [Fig.(7.5)] were collected under different intensity conditions. The spectra include features caused by one-photon direct emission from the $5p$, $5s$ and $4d$ shells as well as from NOO Auger decay [224]. At higher kinetic energies, the two-photon ionization from the $4d$ shell is observed in a spectral feature which resembles in shape the $4d$ (one-photon) emission lines and is separated from them by exactly the energy of one photon.

The relative yields from the $4d$ one- and two-photon ionization processes are obtained by integrating the spectra over the corresponding kinetic energies regions, see Tab. 7.1. They are shown as a function of the FEL intensity in Fig. 7.5. At low intensities ($I < 10^{13}$ W cm^{-2}), the one- and two-photon ionization yields show a linear and quadratic dependence, respectively. This confirms that the processes observed in the experiment can be described within perturbation theory, cf. Ch. 6, expression 6.1

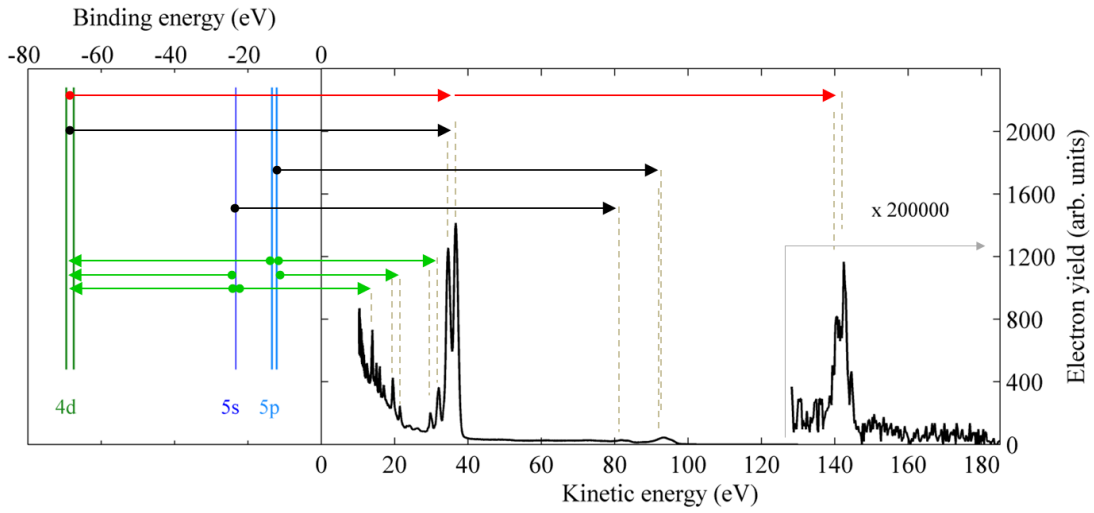

Figure 7.5: Electronic level scheme and emission spectrum. Electron spectrum from XUV ionized xenon atoms, recorded at $h\nu = 105$ eV with a FEL irradiance of $(6 \pm 2) \cdot 10^{12}$ W cm^{-2}, is shown along with the energy level scheme for the xenon orbitals involved in the ionization processes. The spectrum includes features coming from electron emission caused by different processes represented by arrows: one-photon direct emission (black), Auger emission (green) and two-photon direct emission (red). In the lower kinetic energy (KE) region (KE $<$ 50 eV) the spectrum is dominated by the contribution from the 4*d* (one-photon) photoemission and by the subsequent Auger decays involving the 5*s* and the 5*p* shells. The small features at KE between 80 and 100 eV arise from the one-photon photoemission from 5*s* and 5*p* shells. The high energy feature is assigned to the two-photon photoemission from the 4d shell. ©2015 Nature Publishing Group

	one-photon	two-photon
105 eV	33 – 39 eV	136 – 146 eV
140 eV	68 – 74 eV	206 – 216 eV

Table 7.1: Kinetic energy regions for the one- and two-photon ionized electron peaks from the 4*d* shell electrons in xenon for 105 eV and 140 eV.

and Fig. 6.2. At higher intensities, the depletion of the neutral target induced by the enhanced one-photon ionization leads to a pronounced saturation effect.

The SASE FEL pulses had a duration of 80 ± 20 fs and up to 40μJ (at 105 eV) and 15 μJ (at 140 eV) energy per pulse. The bandwidth was about 1% at both photon energies. The FEL pulses were focused onto the sample to produce a tight focusing of $5 \pm 1\mu$m FWHM which was determined in our comparison with the theoretical solutions of the rate equations. In addition, a very effective filtering ($>$ 4 orders of magnitude) of any possible higher harmonic contamination (estimated $<$ 0.3%) that might be present in the FEL beam [222] was performed. The one-photon and two-photon signals were collected for different FEL intensities under different MBES settings as well as different conditions for the sample density. Two-photon electrons were collected under higher sample density conditions and applying a retarding field

at the entrance of the MBES rejecting slow electrons to avoid detector saturation induced by the one-photon signal. The intensity-independent normalization factors defining the relative yields (sample density, transmission of the analyzer, detector gain) are calibrated by comparing the experimental and theoretical results obtained for the one-photon and two-photon ionization from the 3p orbital of argon, which is a much less complex system exhibiting negligible correlation effects, thereby providing a robust calibration reference (cf. Ch. 6).

The experimental intensity domains are not identical for the one-photon and the two-photon yields that were collected in subsequent measurements due to consistent variations of the SASE FEL intensity during the shifts. For the 105 eV case, where electron yields are more severely affected by saturation effects at high intensities, the experiment was performed under different focusing conditions to allow the investigation over a broader intensity range. All the experimental parameters concerning the beam geometry and the pulse intensity distribution were taken into account when integrating the signal over the interaction volume as described in the previous Chapter 6.

7.2.2 Comparison between experimental and theoretical results

Combining the experimental results of electron spectroscopy with our theoretical analysis allows to draw conclusions about the nature of the underlying processes. The impact of collectiveness on the observable of the one- and two-photon cross sections as well as of their mutual ratio can be distinguished by turning on and off electron correlations through the matrix elements given in Eq. (7.1) . The experimental yields are compared to the results of the calculations performed for the full and the reduced model, respectively, obtained from the solutions of the rate equations (7.3). The results are shown in Fig. 7.6, on the left for 105 eV and on the right for 140 eV photon energy. The comparison between experimental points and rate equation solutions employs our single normalization factor for all datasets (one-photon and two-photon yields at 105 eV and 140 eV), cf. Sec. 6.3.

This comparison clearly shows that the full model (solid lines) reproduces the intensity dependence of the experimental yields, whereas the reduced model (dashed lines) fails to do so. This means that the inclusion of Coulomb coupling between all possible electron-hole states, which is responsible for the collective electronic response of the system, is an essential ingredient for the correct description of the two-photon ionization process. The excellent agreement is evident in the ratio between the one-photon and two-photon ionization yields at both photon energies over the whole intensity range as well as in the onset of the saturation due to neutral target depletion. The two points of photon energy measured in experiment are situated at different positions within the giant dipole resonance range: one is nearly at the peak position, the other at the tail. Importantly, there is no common scaling factor such that the results from the reduced model could fit the experimental data at both energies. This can be observed in Fig. 7.6 in the different ratios of the two model curves. Especially

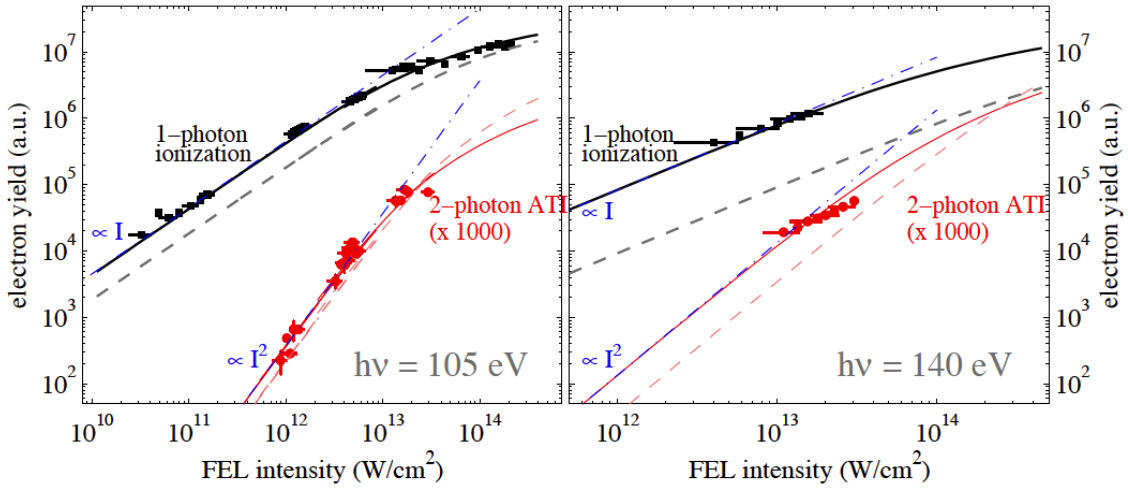

Figure 7.6: Intensity dependence of one-photon and two-photon photoemission yields. Experimental electron yields as a function of FEL intensity are extracted by integrating the electron spectra recorded at 105 eV (left panel) / 140 eV (right panel) photon energy in the 33−39 eV / 68−74 eV (one-photon 4*d*, plotted in black squares) and 136−146 eV / 206−216 eV (two-photon 4*d*, plotted in red circles) kinetic energy ranges. At 105 eV photon energy the one-photon 4*d* electron yield is extracted by subtracting the partially overlapping Auger electron spectrum; the contribution of the latter is estimated from the literature [224] using the two Auger peaks at 30 and 32 eV kinetic energy as a normalization reference. The vertical error bars in the experimental two-photon yields represent the statistical error. Horizontal error bars include uncertainty in the pulse energy, focal spot size and pulse duration measurements. The slopes indicated with blue dash-dotted lines highlight the linear and quadratic dependence of the one-photon and two-photon yields, respectively, in the low-intensity region. The experimental yields are compared with theoretical yields based on the full (solid lines) and the reduced (dashed lines) models for both one-photon (bold lines) and two-photon (thin lines) yields. ©2015 Nature Publishing Group

at 140 eV the experimental results are described by the full model, which gives a much larger cross section than the intrachannel model. This alone had led us already to the conclusion that the curve must be broader than initially assumed.

The main conclusion of this investigation is: Interchannel coupling must be taken into account in the nonlinear regime in order to correctly describe the experimental results at both photon energies.

7.2.3 Theoretical analysis of the ATI cross section

Having validated our full model by the comparison with experimental yields at the two distinct photon energies, the influence of collective effects on the one- and two-photon ionization cross section is investigated over a wide photon energy range (see Fig. 7.7). These cross sections are shown both for the reduced (dashed lines) and the full model (solid lines). The scales are chosen such that the peak heights coincide for the reduced-model curve. As already mentioned above, the broadening of the inter-

channel one-photon cross section (black solid line) with respect to the intrachannel case (black dashed line) can be understood by the inclusion of the coupling among different electron-hole states, a fact which is present in the literature [95] and which is now reproduced by our interchannel calculations with TDCIS [207]. One observes that the two-photon cross section for the reduced model is red-shifted and narrower than the one-photon curve. This is indicated by the red arrow spanning the FWHM and for reasons that are explained below this behavior would also be a naive guess for the two-photon cross section. On the other hand, as a mostly unexpected and counter-intuitive result, the full model predicts a significantly broader two-photon cross section curve than for the one-photon case, demonstrated by the red arrow which only spans half the FWHM. Moreover, the shape of the curve is peculiar, it does *not* resemble a simple Lorentzian curve as can be seen in the inset of Fig. 7.7 which magnifies the interchannel ATI cross-section curve. The interchannel result is very surprising.

In order to explain the origin of this fundamentally different behavior let us employ a simplified model for the two-photon cross section under the assumption that a single intermediate state can be populated resonantly in the two-step ionization process in xenon. By applying it to both the intrachannel and the interchannel scenarios I will show by a "phenomenological proof by contradiction" how the intrachannel result can be explained and why the two models lead to so fundamentally different cross sections.

If perturbation theory can be applied (see Sec. 6.1 for the conditions) and the photon energy lies is the vicinity of a single, isolated one-photon resonance, which can be considered as the intermediate state, the two-photon cross section can be factorized into two one-photon cross sections. In general, the cross section for the transition between the initial bound state and the final continuum state is obtained as the modulus of the transition matrix element squared. In standard perturbation theory, where the interaction of the atom with the light field described by $\hat{H}_{\mathrm{int}}$ can be treated as a perturbation, the transition matrix element between the initial and final states for two-photon absorption is given by:

$$M_{F\leftarrow I} = \frac{\langle F|\hat{H}_{\mathrm{int}}|M_{\mathrm{res}}\rangle\langle M_{\mathrm{res}}|\hat{H}_{\mathrm{int}}|I\rangle}{E - E_{\mathrm{res}} + \frac{i}{2}\Gamma_{M_{\mathrm{res}}} + E_I}, \tag{7.4}$$

where $\Gamma_{M_{\mathrm{res}}}$ is the decay width of the resonance state M_{res}, and E is the photon energy.

For a free-free transition the photoabsorption probability decreases monotonically with photon energy. Let us assume for the sake of simplicity that the transition matrix element from the intermediate state to the continuum follows (for not too small photon energy values) a simple $E^{-13/4}$ dependence. As Bethe and Salpeter show in Sec. 70 of their text book [8] the energy dependence $E^{-l-7/2}$ results for the photoabsorption cross section in the Born approximation (plane wave approximation without any screening effect). Then, if it is assumed that the giant dipole resonance

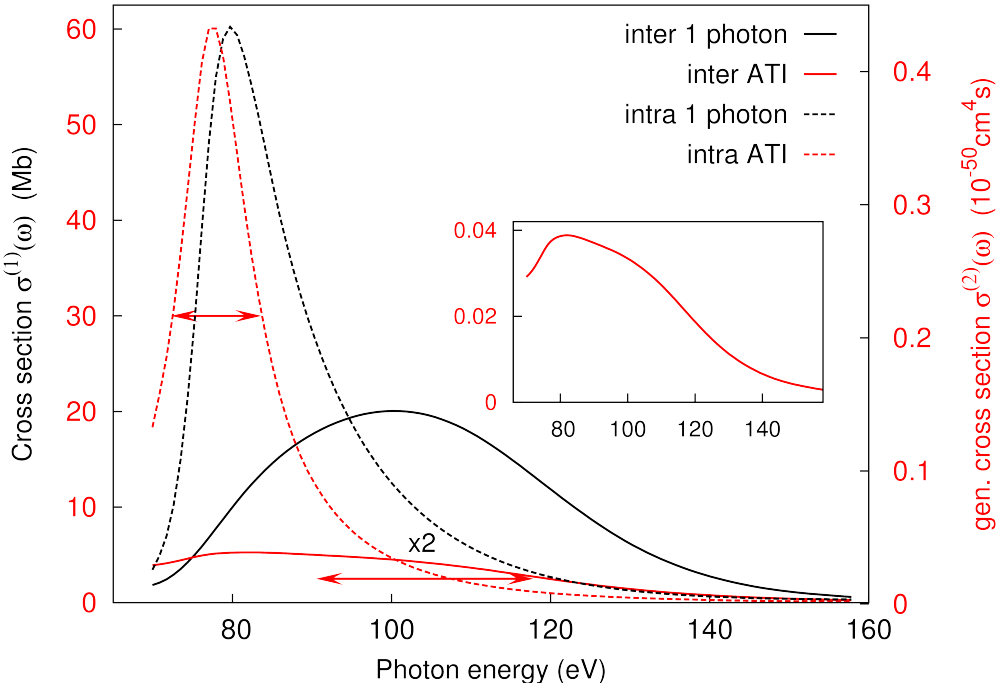

Figure 7.7: One- and two-photon cross sections for the full (solid lines) and reduced model (dashed lines). The full-model ATI cross section exhibits a fundamentally different behavior than the reduced-model curve: it is much broader than the one-photon cross section, see the arrow spanning the half FWHM. The inset demonstrates the peculiar shape of the ATI curve for the interchannel case.

enters as a single intermediate resonance state the cross section has the following form

$$\sigma^{(2)} = \left| \frac{\langle F|\hat{H}_{\text{int}}|\text{GDR}\rangle\langle\text{GDR}|\hat{H}_{\text{int}}|I\rangle}{E - E_{\text{GDR}} + \frac{i}{2}\Gamma_{\text{GDR}} + E_I} \right|^2 . \tag{7.5}$$

Therefore, since the GDR exhibits mostly f-character (angular momentum $l = 3$) the exponent of the assumed energy dependence becomes $-13/2$ for the cross section. This means that for a single, isolated intermediate state, the two-photon cross section is obtained by multiplying the one-photon ionization cross section by the energy-dependent factor. In that case, the two-photon cross section $\sigma^{(2)}$ factorizes into two one-photon cross sections – one photon for exciting the giant dipole resonance from the ground state and one photon for the transition from the resonance to the final continuum state. According to this two-step picture with a single intermediate state one expects a narrower two-photon peak that is shifted to lower energy, since the one-photon cross section for exciting an electron from the intermediate state into the continuum decreases monotonically with increasing energy.

This two-step picture is applied to the two-photon cross sections within the reduced and the full model. The result for the reduced model is shown in Fig. 7.8 a) (blue curve). The one-photon ionization cross section (black curve) multiplied by $1/E^{13/2}$ is shifted to smaller energies compared to the one-photon curve and exhibits also the

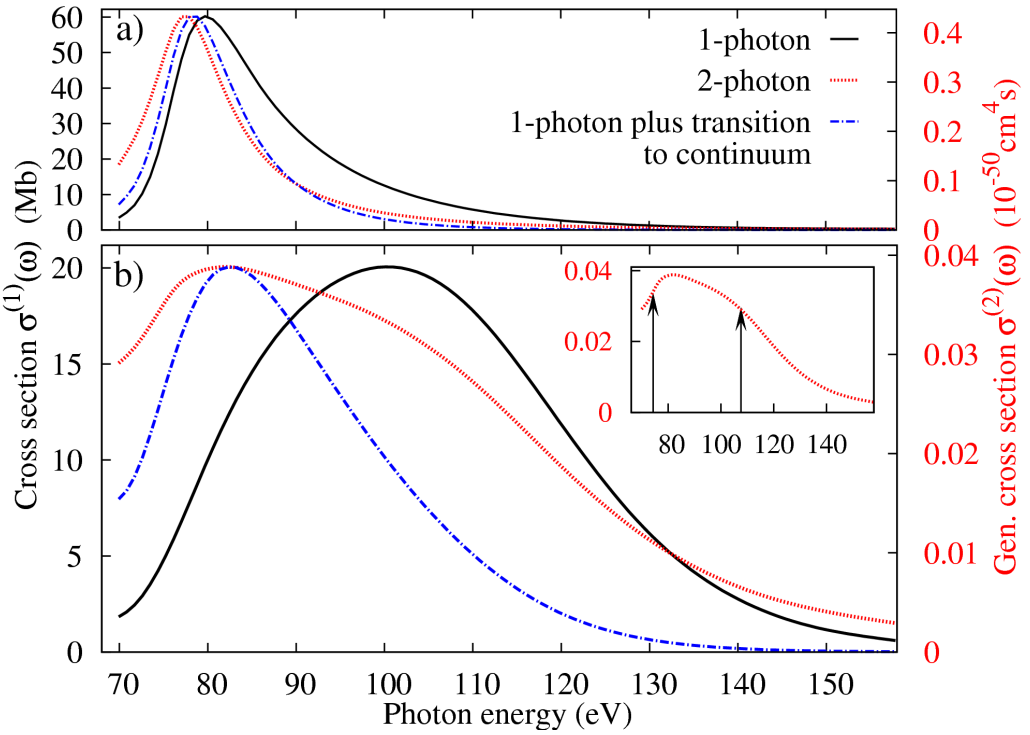

Figure 7.8: Photon-energy dependence of the calculated cross sections. Photon energy dependence of the one-photon (solid black line) and two-photon (dotted red line) cross sections calculated with the reduced model (panel a) and the full model (panel b). The scales on the left and right axes are chosen such that the maxima of the curves appear at the same height as the one-photon cross section peak. The dash-dotted blue lines represent the result for the two-photon cross section within the two-step model with one single intermediate resonance state. In the case of the reduced model this approach captures the main features of the two-photon cross section, while for the full model it breaks down. The inset shows the full model two-photon cross section with two arrows indicating the energy position of the two underlying resonances. They were further analyzed and calculated within the TDCIS model [5]. This will be discussed in Sec. 7.3.

smaller width of the two-photon cross section peak (red curve). This means that for the reduced model the behavior of the two-photon cross section can be qualitatively understood in terms of a sequential process involving a single intermediate state. If there are more than one intermediate state, all states must have nearly the same resonance energy and overlap strongly with comparable widths.

However, in the full model this simple approximation breaks down. As shown in Fig. 7.8 b) the resulting curve for the two-photon absorption cross section within this simplified model (blue curve) is indeed shifted to a smaller energy. But the width is also decreased in strong contrast to the calculated two-photon cross section curve in the full model, which leads to a broadened red curve. Furthermore, the dashed blue curve underestimates the experimental cross section especially at 140 eV by a considerable factor. This demonstrates that this simple model does not capture the physics of the full model if only a single resonance is taken into account as the intermediate state. The picture of a sequential process involving a single intermediate

state does not hold: surprisingly, the two-photon cross section curve is much broader than the one-photon cross section curve and exhibits a knee-type structure.

The fact that the two-photon cross section curve is significantly broader than the one-photon cross section together with its shape provides evidence for the concept of more than one resonance underlying the giant resonance [225, 226]. In this case there must be a sum over all intermediate resonance states in the cross section expression (7.5)

$$\sigma^{(2)} = \sum_{M_{\mathrm{res}}} \left| \frac{\langle F|\hat{H}_{\mathrm{int}}|M_{\mathrm{res}}\rangle\langle M_{\mathrm{res}}|\hat{H}_{\mathrm{int}}|I\rangle}{E - E_{M_{\mathrm{res}}} + \frac{i}{2}\Gamma_{M_{\mathrm{res}}} + E_I} \right|^2 . \tag{7.6}$$

Furthermore, interference terms between overlapping resonances arise, whose relative phase can broaden and change the shape of the cross section curve. Indeed, as mentioned above, there was a hint that there are two energy poles of the dielectric functions in the range of the giant dipole resonance [219], but the one-photon cross section is not a sensitive observable for this fact. Clearly, the two-photon cross section represents a more sensitive observable for testing this hypothesis of two resonances. Motivated by these findings we performed a detailed characterization of the resonance energies within TDCIS [5]. This will be discussed in the next section, Sec. 7.3.

The substructure, which emerges in the nonlinear process due to the cross terms in the cross section expression (7.6), manifests the existence of more than one resonance state underlying the giant dipole resonance. These states give rise to interference terms resulting in a broadening of the two-photon absorption cross section curve. Indeed, the experimental results cannot be explained, simultaneously at 105 and 140 eV, by the two-step picture with a single intermediate state (dash-dotted blue curve). In particular, at 140 eV the cross section measured experimentally is approximately 12 times larger than predicted by the single intermediate state model, while at 105 eV it is larger by a factor of 2.2. As already briefly mentioned, there is no common scaling factor that would adjust the theoretical results to the experimental results at both energies simultaneously. For this reason, the comparison with the experimental electron yields at two distinct photon energies, one near the peak and one at the tail of the xenon GDR, fully legitimates the theoretical model and the prediction of the two underlying resonances.

Summarizing, it was shown that the nonlinear response of an electronic system to intense XUV radiation can be used to unveil information about the collective behavior in many-body systems. The theoretical xenon two-photon cross section exhibits a knee-type structure which is not visible in the one-photon cross section. Here, for the first time, the agreement of a theoretical model with experimental results beyond the linear regime legitimates the prediction of two resonance states underlying the giant dipole resonance. Our study demonstrates, employing xenon as a model system, how the nonlinear interaction regime can be utilized to investigate collective electronic behavior. This stands only at the beginning of the way towards a deeper understanding of the collective response of many-body systems.

7.3 Theoretical characterization of the underlying resonances within the CIS scheme

The ATI cross section of the previous section provided the first hint to the fact that there exist two underlying resonances (which was long known, but forgotten or overlooked because the linear regime is not sensitive to the substructure) and that TDCIS is capable of properly reproducing these resonances. These findings stimulated the characterization of these resonances. As mentioned above, calculations in the 70's hinted at two energy poles in the range of the giant dipole resonance [219, 227]. Wendin studied the dielectric function of xenon in the range of the GDR using the random-phase approximation with exchange (RPAE) and identified two energy poles as the roots of the denominator of the dielectric function. Also in a later work [228] two energies were found, but one of them is incompatible with experimental observations of the cross section. However, these findings were not interpreted as resonance states. Since the experimental observable in the linear-response regime could not provide the necessary resolution to uncover the existence and positions of these resonances the underlying structure of the xenon GDR remained hidden.

In the remainder of this chapter I will present the results on the characterization of the underlying resonances that were obtained within the CIS framework. In order to investigate the resonances in detail we employed two methods which yield similar results: The first method makes use of the ARPACK software package [150, 151], which I implemented into TDCIS (see Chapter 4), to diagonalize the many-electron Hamiltonian using the smooth exterior complex scaling (SES). The second method, which will not be explained here but can be found in Ref. [5], involves a Gabor analysis of the wave-packet dynamics. The results of both methods are consistent with the broad shape and the form of the ATI cross section curve. They lead us once more to the conclusion that due to the strong entanglement between the excited electron and the ionic core hole the resonance wave functions cannot be written as a single particle-hole state: we are dealing with a collective excitation.

In the following I briefly describe the exterior complex scaling (ECS) method for the diagonalization of the Hamiltonian and the results obtained from the analysis of the resonance features. A straightforward approach to obtain the eigenstates of a system is to diagonalize the full N-electron Hamiltonian. However, resonance states, also known as Gamow vectors [183] or Siegert states [184], are exponentially divergent in the asymptotic region, which renders it difficult to access them by a Hermitian Hamiltonian. In order to overcome this obstacle several standard techniques such as exterior complex scaling [180] and complex absorbing potentials (CAP) [181, 186], as well as their equivalence [182], have been developed over the last decades. Thereby the Hamiltonian becomes non-Hermitian and the associated resonance wave functions are transformed into square-integrable functions. The SES consists of an analytic continuation of the radial electron coordinate r into the complex plane, $r \to \rho$, along

the path [185]

$$\rho(r) = r + (\mathrm{e}^{i\theta} - 1)\left[r + \ln\left(\frac{1 + \mathrm{e}^{(r_0 - r)/\lambda}}{1 + \mathrm{e}^{r_0/\lambda}}\right)\right]. \tag{7.7}$$

This mapping rotates the radial coordinate for $r > r_0$ smoothly into the complex plane by the angle θ. With this method the resonance states can be clearly distinguished as isolated poles above the rotated continua in the complex-valued spectrum. The eigenenergies are obtained as the real part and the decay width of a state from the imaginary part of the eigenenergies [185]:

$$E_n = \mathrm{Re}(E_n) - i\Gamma/2, \tag{7.8}$$

where $\mathrm{Re}(E_n)$, $\Gamma \in \mathbb{R}^+$. This is further analyzed in Subsec. 4.4.1 and Ref. [5]. The diagonalization of the Hamiltonian is performed using the iterative Arnoldi algorithm within the ARPACK library. The resonances are found by the requirement to possess a certain minimum overlap with the ground state coupled by a dipole step because for our purposes only those resonances are interesting that are excited by one photon (details can be found in Ref. [5]).

First, the resonances are analyzed in the effective one-particle model: In the intrachannel case, i.e. the reduced model of the previous section, three resonances are found, which form a group around an energy with a real part of $\approx 77\,\mathrm{eV}$ and an imaginary part of $\approx -5.4\,\mathrm{eV}$, which amounts to a lifetime of about 60 as. These three resonances correspond to the three $4d_{\pm m}$, $|m| = 0, 1, 2$, channels. The real part of the resonance group can also be recognized in the peak position and enhanced magnitude in the one-photon cross section calculated within the reduced model, cf. the black-dashed curve in Fig. 7.7. The fact that the three channels lead to slightly different resonances is due to the different, nonspherical ionic potentials that the electrons in the three $4d_{\pm m}$ orbitals experience.

On the other hand, activating the interchannel coupling reveals two underlying resonance states, whose real parts lie at 74.3 and 107.6 eV, respectively. The corresponding decay widths are $\approx$25 eV and $\approx$60 eV, i.e., the lifetimes amount to $\approx$ 26 as and $\approx$ 11 as. This means, that many-body correlations lead to resonances that cannot be attributed to single ionization pathways. This is consistent with our finding in Sec. 7.2.3 regarding the interference of two overlapping resonances. Also, the wave function of the excited electron shows a prominent f-wave character for both resonances so that the xenon GDR is dominated by $4d \to \epsilon f$ transitions. This legitimates our assumption in the simplified theoretical model of the two-photon cross sections in Sec. 7.2.3.

In Fig. 7.9 the two-photon cross section is shown over the range of the GDR, the resonance energy positions within the full model are indicated by arrows. The resonance positions are consistent with the substructure that is apparent in the two-photon cross section curve. In the same figure the positions of the energy poles found by Wendin [219] are indicated for comparison by blue dashed lines. The positions of the first resonance energy coincide perfectly, while the second resonance energy within TDCIS

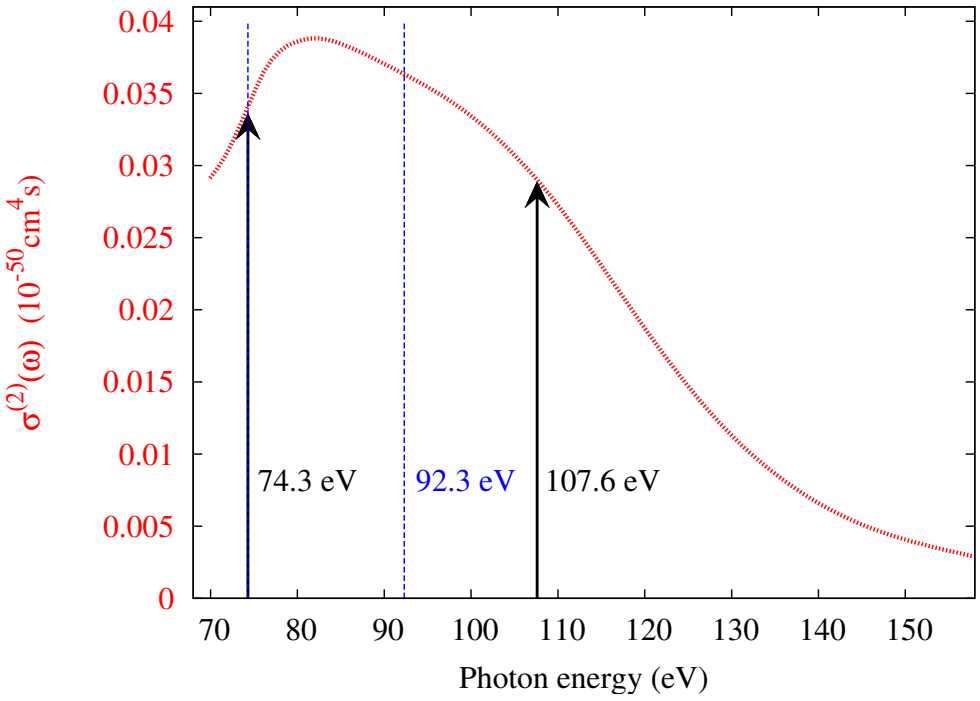

Figure 7.9: The two-photon absorption cross section $\sigma^{(2)}$ of xenon produced with the full model is shown in the range of the giant dipole resonance (cf. Sec. 7.2). The shape of the curve contains an overlapping knee-type structure: The curve accommodates two resonances. The energy positions of the underlying resonances are indicated by black arrows for the CIS model, and with blue dashed lines for Wendin's results [219]. The first resonance energy is the same for both calculations, while the second energy differs considerably. ©2015 Nature Publishing Group

is larger by 15 eV when compared to Wendin's calculation. It must be emphasized that the two methods of calculation and the quantities used for obtaining the energy poles are very different. While Wendin uses a one-channel approximation (together with a random phase approximation with exchange) to evaluate the dielectric function matrix elements, here the many-body wave function in the CIS approximation is utilized to extract the eigenstates of the system [2, 129]. Furthermore, there is an approximation involved in Wendin's approach: A collective resonance is found where the many-body dielectric function, a complex-valued function, vanishes simultaneously for the real and the imaginary part. If the damping of the resonance is sufficiently small, the resonance position can be estimated by the root of the real part of the dielectric function [229]. This approximation adopted by Wendin in Ref. [219] cannot be strictly applied for the xenon GDR because of the two rather broad resonances involved. However, it is found that a fitting of the dielectric function with the resonance positions within the CIS scheme yields consistent results.

It should –for the sake of completeness– also be mentioned that ground state correlations are not included in our approach in contrast to Wendin's work. He shows that taking into account ground state correlations can result in a narrower cross section

curve [219]. TDCIS slightly overestimates the width of the one-photon cross section and, therefore, the width of the two-photon cross section might also be overestimated. In principle, ground state correlations would not affect the spacing between the resonances but they could lead to different transition matrix elements. This could result in different interference behavior, which in turn could change the shape of the two-photon cross section. This question which cannot be addressed at this point remains a challenging task and further experimental measurements and theoretical investigations are needed to determine the exact two-photon cross section. However, the agreement between theory and experiment at two different points of the GDR (one near the peak and one at the tail) is very good when more than a single intermediate state are included, which leads to a broadening of the cross section.

8 Quantum optimal control of photoelectron distributions

The aim of the projects described in the previous chapters was to understand the dynamics and the characteristics of the system when irradiated by (strong) laser pulses. In the present chapter we pose a different, one might even say inverse question. We ask: What time dependence must the light field have in order to induce ionization dynamics toward a final state whose photoelectron distribution exhibits certain desired properties?

One of the predetermined features that we impose on the distribution will be directed electron emission, i.e., the control over the direction in which the electrons are emitted. This information is available due to the implementation of photoelectron distributions within TDCIS. Importantly, for our theoretical and computational approach it is not necessary to know the final state itself. Merely, the desired features are reflected in the angle-integrated PES, the energy-integrated PAD, or both. The energy-integrated PAD is given by integrating over energy or, equivalently, momentum, cf. Eq. 5.19,

$$\frac{\mathrm{d}\tilde{\sigma}}{\mathrm{d}\Omega} = \int_0^\infty \frac{\mathrm{d}^2\tilde{\sigma}(\mathbf{p})}{\mathrm{d}p\mathrm{d}\Omega}\, p^2 \mathrm{d}p\,. \tag{8.1}$$

Analogously, the angle-integrated PES is obtained upon integration over the solid angle,

$$\frac{\mathrm{d}\tilde{\sigma}}{\mathrm{d}E} = p\int_0^{2\pi}\int_0^{\pi} \frac{\mathrm{d}^2\tilde{\sigma}(\mathbf{p})}{\mathrm{d}p\mathrm{d}\Omega}\, \sin\theta \mathrm{d}\theta\mathrm{d}\varphi \tag{8.2}$$

with $p = \sqrt{2E}$. The optimizations considered below are based on these measurable quantities.

In the following I give an overview of first results for hydrogen from our collaboration with Prof. Dr. Christiane Koch and Esteban Goetz. We extended our work also to the multichannel case of argon. It has been submitted to a peer-reviewed journal. I will briefly present the optimal control theory employed here and the numerical challenges emerging from the demanding iterative control algorithm using TDCIS for the electronic structure information and the explicit time propagation. Then, our results for the various control problems we studied and the interpretation of the optimal fields will be shown.

8.1 Optimal control theory

To allow for the direct optimization of features in the photoelectron spectra, we combine Krotov's monotonically convergent method for quantum optimal control [230] with TDCIS to describe the electron dynamics and the wave function splitting approach to efficiently calculate the photoelectron spectra as described in Ch. 5 for linearly polarized electric fields.

8.1.1 Optimization problem

Two different final time optimization functionals are considered in the following to demonstrate the versatility of the approach:

i) First, the full three-dimensional photoelectron distribution is prescribed and a field that produces (at least approximately) a given angle-integrated PES and energy-integrated photoelectron angular distribution (PAD) is determined. Such a detailed control objective is demanding and corresponds to a difficult control problem.

ii) Next, the relative number of photoelectrons emitted into the upper hemisphere compared to the lower hemisphere is maximized assuming that the polarization axis of the light pulse runs through the poles of the two hemispheres. This implies a condition on the PAD but does not restrict the energy dependence. The corresponding control objective leaves considerable freedom to the optimization algorithm and the control problem becomes much simpler.

Maximizing the relative number of photoelectrons emitted into the upper as opposed to the lower hemisphere corresponds to a maximization of the PAD's asymmetry. Asymmetric photoelectron distributions arising in strong-field ionization were studied previously for near-infrared few-cycle pulses where the effect was attributed to the carrier envelope phase [231, 232]. Here, we pose the question whether it is possible to achieve asymmetry in the PAD for multiphoton ionization in the XUV regime, where a single photon is sufficient to ionize an electron, and we seek to determine the shaped pulse that steers the electrons into one hemisphere. For better control spectral and amplitude constraints are introduced.

Our goal is to find a vector potential $\mathbf{A}(t)$, which represents the control in our case, that steers the system from the Hartree-Fock ground state $|\Psi(t=0)\rangle = |\Phi_0\rangle$ to an unknown final state $|\Psi(T)\rangle$ whose PES or PAD displays certain desired features. Mathematically, such an optimization target is expressed as a functional involving the final time, $J_T[\tilde{\varphi}_{\text{out}}, \tilde{\varphi}_{\text{out}}^\dagger]$. Here, $\tilde{\varphi}_{\text{out}}$ is a wave function that depends exclusively on the wave function of the ionized electron, i.e., it depends on the outer parts of the wave function, which were split from the total wave function at each splitting time step (see Ch. 5).

As a first example, we seek to prescribe the angle-integrated PES and energy-

integrated PAD together. The corresponding final time cost functional is defined as

$$J_T^{(1)}[\tilde{\varphi}_{\text{out}}(T), \tilde{\varphi}_{\text{out}}^{\dagger}(T)] = \lambda_1 \int_0^{\infty} \left[\sigma(\mathbf{p}, T)) - \sigma_0(\mathbf{p})\right]^2 \, \mathrm{d}^3p \quad , \tag{8.3}$$

where $\sigma(\mathbf{p}, T) = \mathrm{d}^2\tilde{\sigma}(\mathbf{p})/\mathrm{d}p\,\mathrm{d}\Omega$ denotes the actual photoelectron distribution, cf. Eq. (5.19) in Ch. 5, $\sigma_0(\mathbf{p})$ stands for the target distribution, and λ_1 is a weight that sets into relation the importance of $J_T^{(1)}[\tilde{\varphi}_{\text{out}}, \tilde{\varphi}_{\text{out}}^{\dagger}]$ compared to additional terms in the total optimization functional, e.g., frequency or amplitude constraints.

As a second alternative, we would like to control the relative number of electrons emitted into the lower and upper hemispheres. This can be expressed via the following final-time functional

$$\begin{aligned} J_T^{(2)}[\tilde{\varphi}_{\text{out}}(T), \tilde{\varphi}_{\text{out}}^{\dagger}(T)] = 2\pi\lambda_2^{(-)} \int_0^{\pi/2} \mathrm{d}\theta \int_0^{+\infty} \left|\tilde{\varphi}_{\text{out}}(\mathbf{p}, T)\right|^2 p^2 \, \mathrm{d}p \\ +2\pi\lambda_2^{(+)} \int_{\pi/2}^{\pi} \mathrm{d}\theta \int_0^{+\infty} \left|\tilde{\varphi}_{\text{out}}(\mathbf{p}, T)\right|^2 p^2 \, \mathrm{d}p \,, \end{aligned} \tag{8.4}$$

where the boundaries of the integrals extend over the corresponding regions. We obtain the probabilities of the photoelectrons emitted into the upper (first term) and lower (second term) hemispheres, respectively, and $\lambda_2^{(-)}$ and $\lambda_2^{(+)}$ are the corresponding weights. There are two different ways to obtain directed emission: By suppressing the emission of the photoelectron into the lower hemisphere, without imposing any specific constraint on the number of electrons emitted into the upper hemisphere, or by maximizing the difference in the number of electrons emitted into the upper and lower hemispheres.

The constraints on the vector potential $\mathbf{A}$ are implemented by an additional term $C[\mathbf{A}]$, such that the functional is of the form

$$J \;=\; J_T[\tilde{\varphi}_{\text{out}}(T), \tilde{\varphi}_{\text{out}}^{\dagger}(T)] + C[\mathbf{A}]. \tag{8.5}$$

Without going into too much detail at this point, the constraints can include the regularity and the finiteness of the vector potential, a limited spectral bandwidth of the pulse and a maximum electric field strength that the field can acquire.

8.1.2 Krotov's method combined with wave-function splitting

The crucial novelty of the approach is the combination of an optimization algorithm that iteratively calls the calculation of the photoelectron distribution, i.e., including the propagation of the N-electron wave function. We utilize Krotov's monotonically convergent optimization algorithm for quantum optimal control. Depending on the target functional and additional constraints (see above), the type of equation of motion can vary [230]. The iterative algorithm consists of a set of coupled equations for the update of the control, which in our case is the vector potential, the forward

propagation of the state and the backward propagation of the so-called co-state. The co-state is determined by the functional derivative of the final-time target functional. This state must be propagated backwards and enters the update equation for the vector potential for the next iteration [230, 233]. The computational challenge when combining Krotov's method with the wave-function splitting approach arises from the fact that the splitting method, which was introduced in Ch. 5 for the absorption and analysis of the wave packet of the outgoing electron, must be performed in the backward direction, thus resulting in a "glueing" procedure when propagating the co-state backwards which will be discussed in detail in the following. In order to achieve stable and more precise backward propagation the Lanczos algorithm is employed for the time propagation of the wave function, see Ch. 3. The update equation for the vector potential has the following form, with k labeling the iteration step,

$$\begin{aligned} \mathbf{A}^{(k+1)}(t) &= \mathbf{A}^{(k)}(t) + \frac{1}{\lambda_a} I^{(k+1)}(t) \\ &\quad - \frac{\lambda_\omega}{\lambda_a} s(t) \mathbf{A}^{(k+1)} \star h(t) + \frac{\lambda_e}{\lambda_a} \ddot{\mathbf{A}}^{(k+1)}(t) \,, \end{aligned} \tag{8.6a}$$

where the λ's are weights. Here, $\mathbf{A}^{(k+1)} \star h(t)$ denotes the convolution of $\mathbf{A}$ and $h(t)$

$$\mathbf{A}^{(k+1)} \star h(t) = \int \mathbf{A}^{(k+1)}(\tau)\, h(t-\tau)\, d\tau \,, \tag{8.6b}$$

with $h(t)$ involving the constraint functions and

$$\begin{aligned} I^{(k+1)}(t) &= s(t)\ \mathrm{Im}\left\{ \left\langle \chi^{(k)}(t) \left| \frac{\partial \hat{H}}{\partial \mathbf{A}} \right| \Psi^{(k+1)}(t) \right\rangle \right\} \\ &= s(t)\ \mathrm{Im}\left\{ \langle \chi^{(k)}(t) | \hat{\mathbf{p}} | \Psi^{(k+1)}(t) \rangle \right\} \,, \end{aligned} \tag{8.6c}$$

where $s(t)$ is a shape function for the vector potential and $|\Psi^{(k+1)}(t)\rangle$ and $|\chi^{(k)}(t)\rangle$ denote the forward propagated state and backward propagated co-state at iterations $k+1$ and k, respectively. In order to evaluate Eqs. (8.6), the adjoint state obtained at the previous iteration, $|\chi^{(k)}(t)\rangle$, must be determined using the old vector potential, $\mathbf{A}^{(k)}(t)$. Its equation of motion is found to be a Schrödinger equation [230]

$$i\frac{\partial}{\partial t}|\chi(t)\rangle = \hat{H}(t)|\chi(t)\rangle \,, \tag{8.7a}$$

with the "initial" condition at the final time T,

$$|\chi(T)\rangle = -\frac{\partial J_T[\tilde{\varphi}_{\mathrm{out}}(T), \tilde{\varphi}^\dagger_{\mathrm{out}}(T)]}{\partial \langle \tilde{\varphi}_{\mathrm{out}}(T)|} \,. \tag{8.7b}$$

The wave function is propagated to the final time $t = T$ to yield the total wave function at the final time $|\Psi(T)\rangle$. However, only contributions of the outer parts, i.e., $|\tilde{\varphi}_{i,\mathrm{out}}(T)\rangle$, enter the functional derivative because, by construction, the photoelectron

distribution depends only on the wave function in the outer region. When starting the iterative optimization procedure with a guess vector potential $\mathbf{A}^{(0)}(t)$, one propagates the initial state $|\Psi_0\rangle$ in the forward direction, i.e., for each channel i one obtains the wave function $|\tilde{\varphi}^{(0)}_{i,\mathrm{out}}(T)\rangle$ at the final time, applying the splitting procedure at each splitting time step.

8.1.3 Computational realization

In the following, $\hat{U}[t', \tau, \mathbf{A}(t)]$ denotes the evolution operator that propagates a given state from time $t = \tau$ to $t = t'$ under the control $\mathbf{A}(t)$. We distinguish the time evolution operators for the inner part, $\hat{U}[t', \tau, \mathbf{A}(t)]$, generated by the full Hamiltonian, Eq. (2.8), and for the outer part, $\hat{U}_V[t', \tau, \mathbf{A}(t)]$, generated by the Volkov Hamiltonian, Eq. (5.5). During the forward propagation the wave-function splitting is applied as described in Ch. 5. At the final time T the total outer part for each channel i consists of the coherent sum over all splitting time contributions and, thus, reads

$$|\tilde{\varphi}^{(k+1)}_{i,\mathrm{out}}(T)\rangle \quad = \quad \sum_{j=1}^{N} |\varphi^{(k+1)}_{i,\mathrm{out}}(T; t_j)\rangle \,. \tag{8.8}$$

Here, N denotes the number of splitting times utilized during propagation, and the last splitting time t_N is chosen such that $t_N \leq T$. The best compromise between size of the spatial grid, time step and duration between two consecutive splitting times is discussed Chapter 5.

Since the outer wave function at the final time is known the functional derivative in Eq. (8.7b) can be evaluated. Since our final time functionals all involve the product $\tilde{\varphi}_{\mathrm{out}}(\mathbf{p}, T) \cdot \tilde{\varphi}^{*}_{\mathrm{out}}(\mathbf{p}, T) = \sigma(\mathbf{p}, T)$, Eq. (8.7b) can be written, at the kth iteration of the optimization, as

$$\chi^{(k)}_{i,\mathrm{out}}(\mathbf{p}, T) = \mu(\mathbf{p})\, \tilde{\varphi}^{(k)}_{i,\mathrm{out}}(\mathbf{p}, T) \,, \tag{8.9}$$

where $\mu(\mathbf{p})$ is a function that depends on the target functional under consideration. According to Eqs. (2.2) and (8.7a) $|\Psi(t)\rangle$ and its adjoint $|\chi(t)\rangle$ obey the same equation of motion. This, together with Eq. (8.9), implies that also $|\tilde{\chi}^{(k)}_{i,\mathrm{out}}(T)\rangle$ is obtained by coherently summing up the contributions from all splitting times,

$$|\tilde{\chi}^{(k)}_{i,\mathrm{out}}(T)\rangle = \sum_{j=1}^{N} |\chi^{(k)}_{i,\mathrm{out}}(T; t_j)\rangle \,. \tag{8.10}$$

Conversely, the adjoint state originating at the splitting time t_j and evaluated at the same time is given by

$$\chi^{(k)}_{i,\mathrm{out}}(\mathbf{p}, t_j; t_j) = \mu(\mathbf{p}) \varphi^{(k)}_{i,\mathrm{out}}(\mathbf{p}, t_j; t_j) \,. \tag{8.11}$$

The next step is to construct the adjoint state $|\chi^{(k)}_i(t)\rangle = |\chi^{(k)}_{i,\mathrm{in}}(t)\rangle + |\chi^{(k)}_{i,\mathrm{out}}(t)\rangle$ at

an arbitrary time t from all $|\chi^{(k)}_{i,\mathrm{out}}(t_j;t_j)\rangle$. According to Eq. (8.10), at the final time T, the total adjoint state is given by a coherent superposition of all outer parts originating at the splitting times t_j. Therefore, it suffices to store $|\varphi^{(k)}_{i,\mathrm{out}}(t_j;t_j)\rangle$ and apply Eq. (8.11) to evaluate $|\chi^{(k)}_{i,\mathrm{out}}(t_j;t_j)\rangle$. Once all outer parts of the adjoint state are evaluated at every splitting time, $|\chi^{(k)}_i(t)\rangle$ is obtained for all times t by backward propagation. In detail, $|\chi^{(k)}_{i,\mathrm{out}}(t_N;t_N)\rangle$ is propagated backwards from t_N to t_{N-1} using the full Hamiltonian $\hat{H}$, Eq. (2.8). The resulting wave function at $t = t_{N-1}$ is $|\chi^{(k)}_{i,\mathrm{in}}(t_{N-1})\rangle$. The outer part is given by Eq. (8.11), and the wave function at $t = t_{N-1}$ is obtained by adding $|\chi^{(k)}_{i,\mathrm{in}}(t_{N-1})\rangle$ and $|\chi^{(k)}_{i,\mathrm{out}}(t_{N-1};t_{N-1})\rangle$,

$$|\chi^{(k)}_i(t_{N-1})\rangle = |\chi^{(k)}_{i,\mathrm{in}}(t_{N-1})\rangle + |\chi^{(k)}_{i,\mathrm{out}}(t_{N-1};t_{N-1})\rangle\,.$$

Then, $|\chi^{(k)}_i(t_{N-1})\rangle$ is propagated backwards from $t = t_{N-1}$ to $t = t_{N-2}$ using the full Hamiltonian, resulting in $|\chi^{(k)}_{i,\mathrm{in}}(t_{N-2})\rangle$, and summation yields the wave function at $t = t_{N-2}$,

$$|\chi^{(k)}_i(t_{N-2})\rangle = |\chi^{(k)}_{i,\mathrm{in}}(t_{N-2})\rangle + |\chi^{(k)}_{i,\mathrm{out}}(t_{N-2};t_{N-2})\rangle\,,$$

with $|\chi^{(k)}_{i,\mathrm{out}}(t_{N-2},t_{N-2})\rangle$ given by Eq. (8.11); and so forth for all splitting times,

$$|\chi^{(k)}_i(t_j)\rangle = |\chi^{(k)}_{i,\mathrm{in}}(t_j)\rangle + |\chi^{(k)}_{i,\mathrm{out}}(t_j;t_j)\rangle\,, \tag{8.12}$$

until $t = t_0$. In this way $|\chi^{(k)}_i(t)\rangle$ at time t is obtained, analogously to $|\varphi(t)\rangle$. This is required to evaluate Krotov's update equation for the control, Eq. (8.6), where the iteration label simply indicates whether the guess, $\mathbf{A}^{(0)}(t)$, the old, $\mathbf{A}^{(k)}(t)$, or the new control, $\mathbf{A}^{(k+1)}(t)$, enter the propagation of $|\chi_i(t)\rangle$ and $|\varphi_i(t)\rangle$, respectively. A possible choice for the shape function $s(t)$, which controls the duration of the pulse and a smooth switching on and off, in Eq. (8.6c) is a Gaussian of the type $s(t) = e^{[(t-t_c)/2\tau_{\mathrm{dur}}]}$, where τ_{dur} refers to the duration of the pulse and t_c to the center of the pulse in time.

From a numerical point of view the parameters chosen for the momentum grid require particular attention for the optimization algorithm to work. This is due to the transformation from the CIS representation to the Volkov basis (CIS–to–p transformation) at each splitting time:

$$\begin{aligned}\varphi_{i,\mathrm{out}}(\mathbf{p},T;t_j) &= \int d^3p' \langle \mathbf{p}^V|\hat{U}_V(T,t_j)|\mathbf{p}'^V\rangle\langle \mathbf{p}'^V|\varphi_{i,\mathrm{out}}(t_j)\rangle \\ &= \frac{2}{\pi} e^{-i\vartheta_V(\mathbf{p})} \sum_a (-i)^{l_a}\beta^a_i(t_j) Y^{l_a}_{m_a}(\Omega_{\mathbf{p}}) \times \int_0^\infty dr\, r u^{n_a}_{l_a}(r) j_{l_a}(pr).\end{aligned} \tag{8.13}$$

Here, $|\mathbf{p}^V\rangle$ denotes the Volkov state with momentum $\mathbf{p}$ and $\vartheta_V = -\frac{i}{2}\int_{t_j}^T \mathrm{d}\tau \left[\vec{p}+\vec{A}(\tau)\right]^2$ is the Volkov phase, cf. Eq. (5.18).

During the backward propagation, correspondingly, the inverse transformation is required, i.e., the p–to–CIS transformation. This is because the inner products in

Eq. (8.6c) involve not only calculation of the overlap between the inner part in the CIS representation and the outer part in the Volkov basis, but it also requires evaluation of the mixed terms, $\langle\chi^{(k)}_{i,\mathrm{in}}(t)|\hat{p}_z|\varphi^{(k+1)}_{i,\mathrm{out}}(t)\rangle$ and $\langle\chi^{(k)}_{i,\mathrm{out}}(t)|\hat{p}_z|\varphi^{(k+1)}_{i,\mathrm{in}}(t)\rangle$. In these expressions, the projection of the momentum on the polarization direction has been evaluated, such that the derivative in Eq. (8.6c), $\partial\hat{H}/\partial\mathbf{A}$ yields the z-component of the momentum, cf. Eq. (2.12). Hence, at every time t, for each channel i and at every iteration step $k+1$ one CIS–to–p transformation and integration over two degrees of freedom has to be performed. This is due to the fact, that the splitting function smoothly splits the wave function, such that the outer part is not exactly zero in the inner region and, correspondingly, the inner part does not vanish over the whole outer region. For this reason, finding the best balance between efficiency and accuracy in the p–to–CIS transformation is essential for the feasibility of the optimization calculations.

The CIS–to–p transformation of the outer part is evaluated using Eq. (8.13). The quality, i.e., the numerical accuracy of the transformation can be verified by applying it once and consecutively applying its inverse: Since the inverse transformation involves integration over $\mathbf{p}$, a significant error is introduced if the density of the momentum grid is insufficient. Because we are dealing with an iterative algorithm, the error, which may be small for a single p–to–CIS transformation, accumulates during the optimization procedure. These errors were found to yield optimized pulses exhibiting unphysical jumps at the splitting times where the accuracy of the p–to–CIS transformation is insufficient. Furthermore, insufficient accuracy destroys the monotonic convergence of the optimization algorithm. The jumps disappear when the number of the momentum grid points is increased and p_{max} is adjusted to the maximum momentum included in the wave-function calculation (corresponding to the cut-off parameter mentioned in Sec. 2.2.2). Since the numerical effort significantly increases with the number of momentum grid points in the evaluation of the inner products on the right-hand side of Eq. (8.6c), a computationally feasible compromise must be found. The momentum grid parameters utilized in the simulations, which allowed for a good compromise between efficiency and accuracy, are given below for each project.

8.2 Applications

In order to test the toolbox the algorithm is applied to three different control objectives. In this thesis, we restrict ourselves to hydrogen. First, the full photoelectron distribution shall be retrieved, then the emission into one hemisphere is minimized, which is defined relatively to the light polarization direction, and, eventually the electron yield in one hemisphere is maximized while being minimized in the other hemisphere.

8.2.1 Optimization of the complete photoelectron distribution

As a first example the complete photoelectron distribution of hydrogen shall be optimized, i.e., a shape of the distribution is predetermined that shall be achieved both for the variable of energy, see thick red curve in Fig. 8.1 a), and for the angle, see red curve in Fig. 8.1 b). A random guess pulse is used to start the iteration. This guess pulse produces a PES and PAD denoted by the black lines in the same Fig. 8.1. One observes that the guess field is chosen in such a way that the agreement with the target distribution is poor.

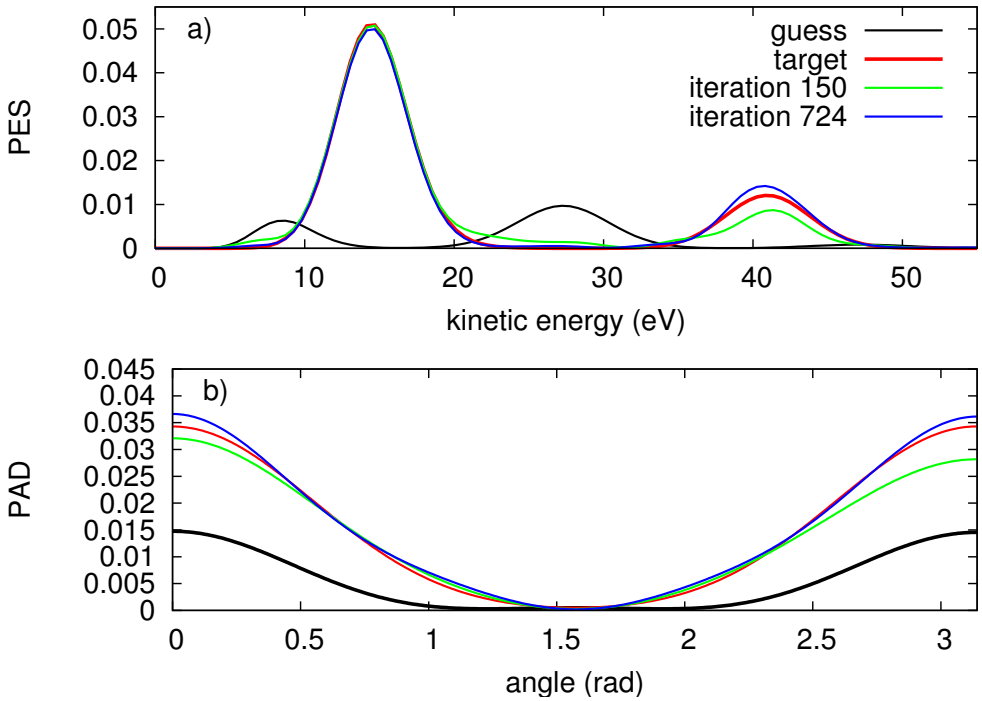

Figure 8.1: Optimal control of the complete photoelectron distribution for a hydrogen atom: a) angle-integrated PES, and b) energy-integrated PAD. As the optimization proceeds iteratively, the actual photoelectron distribution approaches the desired one (red solid line) in both its energy dependence and angular distribution. The photoelectron distribution obtained with the guess field (black lines) differs significantly from the desired distribution.

We start as usual from the Hartree-Fock ground state $|\Phi_0\rangle$. The grid parameters are the grid size $r_{\max} = 200$ a.u., a mapping parameter of $\zeta = 0.5$ [129], and 800 grid points are used. The Volkov basis is represented on an spherical grid in momentum representation $\mathbf{p}$. An evenly spaced grid in the radial coordinate p as well as in the polar coordinate θ is adopted. The energy cutoff as well as the size of the radial component of the spherical momentum grid is $E_{\max} = 6$ a.u. with 300 points. The polar angle extends from 0 to π and is also sampled at 300 points. The splitting radius is set to $r_c = 50$ a.u., the total number of splitting times is $N = 3$ with a smoothing parameter $\Delta = 5.0$ a.u., cf. Ch. 5. The splitting procedure is applied every 30 a.u. of time and a total integration time of 120 a.u. with a propagation

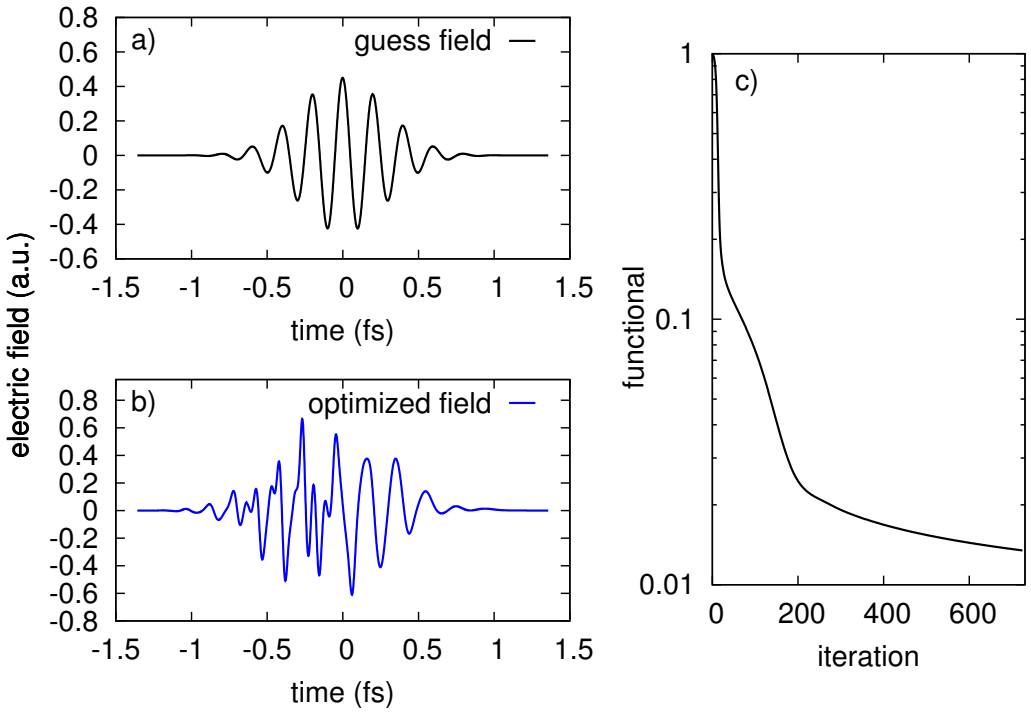

Figure 8.2: Optimization of the full photoelectron distribution. a) Guess field $E_z^{(0)}(t)$ chosen to start the optimization shown in Fig. 8.1. b) Optimized electric field obtained after about 700 iterations. c) Final time cost functional $J_T^{(1)}$, decreasing monotonically as the algorithm proceeds.

time step of $\Delta t = 0.05$ a.u. is utilized for the propagation.

By minimizing the functional defined in Eq. (8.3), we seek a vector potential $A_{z,\mathrm{opt}}(t)$ that generates at every point $\mathbf{p}$ the photoelectron distribution $\sigma_0(\mathbf{p})$, denoted by red lines in Fig. 8.1. Here, no frequency or amplitude restrictions are imposed. In Fig. 8.1 b) the corresponding PADs are shown for various iteration steps. As shown in Fig. 8.2 c), after about 700 iterations the target distribution is realized with an error of less than 2%. The optimization converges monotonically for this two-dimensional target object, illustrated in Fig. 8.1. In Fig. 8.2 b) the optimal electric field is shown, which has a larger amplitude than the initial field, shown in Fig. 8.2 a), and exhibits a high-frequency oscillation.

8.2.2 Minimizing the emission probability into upper hemisphere

As a second application the probability of emission into the upper hemisphere shall be minimized without imposing any specific constraint on the number of electrons emitted into the lower hemisphere. Therefore, the final time cost functional is given by Eq. (8.4) with $\lambda_2^- > 0$ and $\lambda_2^+ = 0$. Again a hydrogen atom is considered in a linearly polarized electric field along the z-axis, using the same numerical parameters as in Sec. 8.2.1.

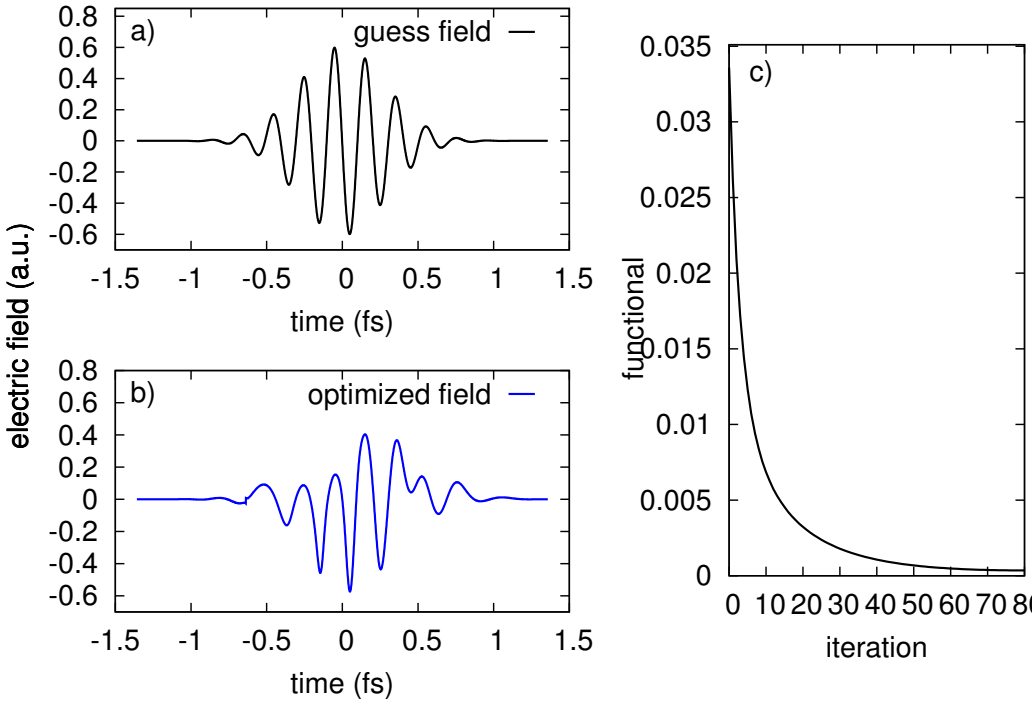

Figure 8.3: Minimization of the probability of emission into the upper hemisphere for hydrogen: (a) Guess and (b) optimized electric field for the optimization shown in Fig. 8.4. Also for this target functional, Eq. (8.4), monotonic convergence of the optimization algorithm is achieved (c).

In contrast to the example discussed in Section 8.2.1, no particular expression for the target PES and PAD is imposed in this case. Only the probability of emission into the upper hemisphere is required to be minimized regardless of the actual shape of the angle-integrated PES or the energy-integrated PAD. The optimization prescription described in Section 8.1.2 is employed. The iteration is initiated with the guess field shown in Fig. 8.3 a), which leads to a symmetric probability of emission for the two hemispheres as illustrated in Fig. 8.4 by the black dashed curve. As the optimization proceeds iteratively, the energy-integrated PAD becomes more and more asymmetric, see Fig. 8.4, favoring emission with angles between $\pi/2$ and π as desired and leading eventually to almost complete extinction of the emission into the upper hemisphere.

The guess and optimized pulses are shown in Fig. 8.3 a) and b). Again, monotonic convergence of the final time cost functional is achieved, cf. Fig. 8.3 c). At the end of the iteration procedure, the probability of emission into the upper hemisphere is two orders of magnitude smaller than the initial configuration. As for the lower hemisphere, the emission probability initially remains almost invariant as the algorithm proceeds iteratively, see Fig. 8.4, while the probability of emission into the upper hemisphere decreases very fast, and monotonically, as expected.

However, for a large number of iterations, the probability of emission into the lower hemisphere starts to decrease as well. After about 150 iterations it reaches an

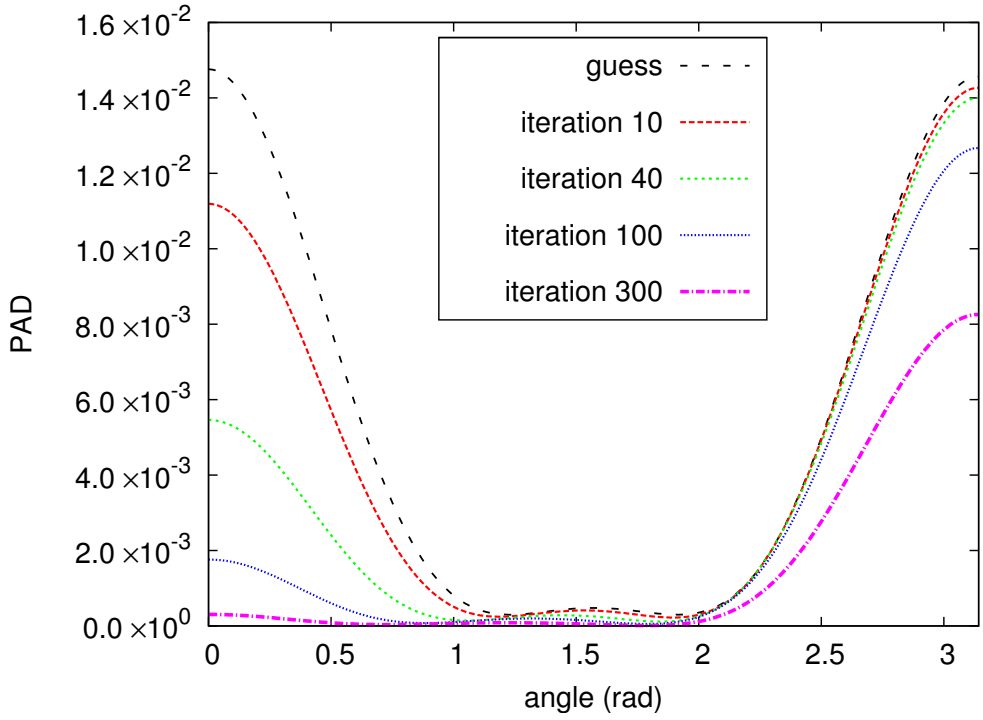

Figure 8.4: Minimizing, for a hydrogen atom, photoelectron emission into the upper hemisphere: Starting from the symmetric guess distribution, shown by the black dashed curve, the probability of emission into the upper hemisphere decreases monotonically as the optimization proceeds iteratively. After 100 iterations the overall ionization probability is decreased together with the ionization into the lower hemisphere, but the probability ratio of ionization into the lower and the upper hemisphere is increased from 1 for the guess field to about 40 for the field shown in Fig. 8.3 b), which leads to the pink dash-dotted PAD.

emission probability of 2.3×10^{-4}. This means that the overall ionization probability is two orders of magnitude smaller than for the guess pulse.

This behavior can be easily explained. Our goal is expressed only in terms of the probability of emission into the upper hemisphere to decrease, and we do not impose any requirement on the ionization probability into the lower hemisphere. Therefore, we do not expect predetermined changes in the probability of emission into the lower hemisphere. More precisely, the optimization does exactly what the functional $J_T^{(2)}$, Eq. (8.4) with $\lambda_2^- > 0$ and $\lambda_2^+ = 0$, targets. In fact, since the target functional depends on the lower hemisphere alone, by construction, the algorithm calculates the corrections to the field according to Eq. (8.6), regardless of how these changes affect the probability of emission into the lower hemisphere.

To keep the probability of emission into the lower hemisphere constant or to maximize it, another optimization functional is required. This is investigated in the following section.

8.2.3 Maximizing the difference in the number of electrons emitted into upper and lower hemisphere

In the last application, the control target of an asymmetric PAD is modified by imposing not only minimization of electron emission into the upper hemisphere, but maximizing emission into the lower hemisphere. In this case, the target can be formulated as maximizing the difference in probability for emission into the upper and the lower hemisphere. It is expressed by the functional in Eq. (8.4) where now both weights, $\lambda_2^{(-)} > 0$ and $\lambda_2^{(+)} < 0$, are non-zero and have different signs, corresponding to maximization and minimization, respectively. Furthermore, the optimized pulse is subject to an additional constraint with two available options: a spectral constraint, and a constraint for the maximum peak electric field-strength.

We consider again a hydrogen atom, interacting with an electric field linearly polarized along the z-axis, using the same numerical parameters as in Sec. 8.2.1. Optimization is carried out with and without restricting the spectral bandwidth of $E_z(t)$. Figure 8.5 a) displays the symmetric energy-integrated PAD, the dashed black curve.

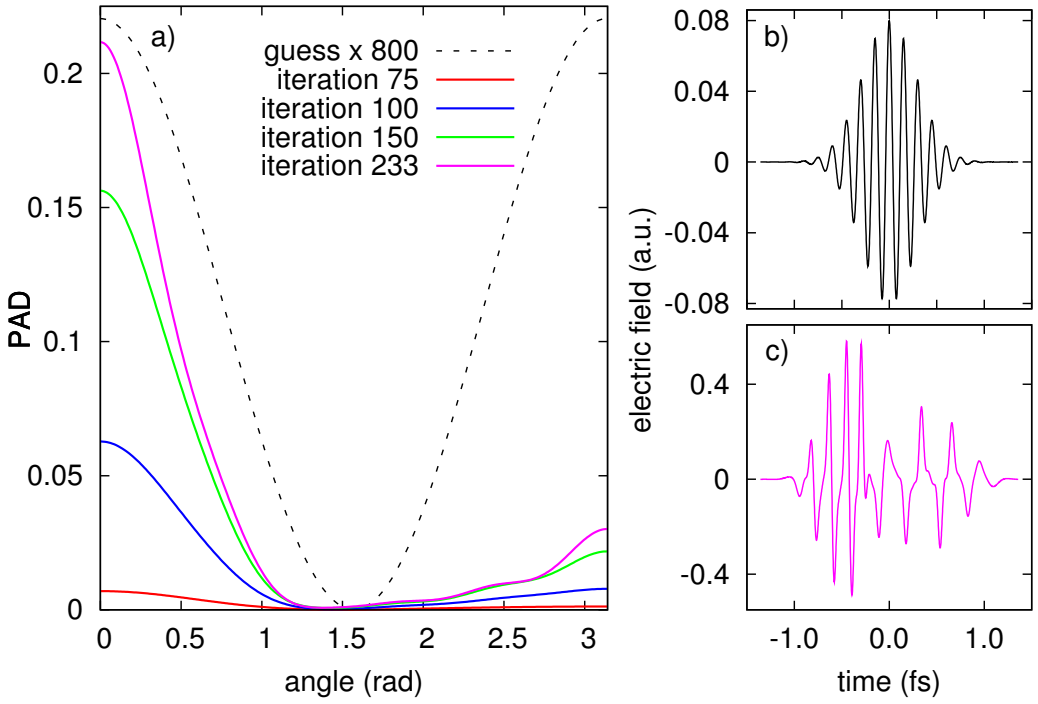

Figure 8.5: Maximization of the difference in emission probability for the lower and the upper hemisphere for hydrogen: a) Energy-integrated PADs are shown for several iterations starting with the initial PAD which is shown magnified by the factor 800 for better visibility (dashed gray line). After 233 iterations the asymmetry is considerably increased. The overall ionization probability is also larger than initially. Although the probability for emission into the lower hemisphere also grows, their difference increases. b) Guess pulse yielding the initial PAD. c) Optimized field obtained with the spectral constraint. Note that the amplitude is significantly larger than for the guess pulse, panel b).

This PAD is obtained with the Gaussian guess field shown in Fig. 8.6 b) with a central frequency of $\omega_0 = 27.2\,\text{eV}$. The admissible frequency components for the optimized field $E_z(t)$ are chosen such that $\left|E_z(\omega)\right|^2$ is vanishingly small for all $|\omega| \geq \omega_{\max}$ with $\omega_{\max} = 5\,\text{a.u.} \approx 136.1\,\text{eV}$. Effectively, a frequency filter is employed filtering out the large frequencies.

As in the previous two examples, the developed optimization approach leads to monotonic convergence of the target functional, Eq. (8.4), with and without spectral constraint. This is illustrated in Fig. 8.6. In Figs. 8.7 a) and b) the spectra of the pulses in the two cases, with and without frequency restriction, are shown. Even though the spectra of the fields optimized with and without spectral constraint are different the speed of convergence is roughly the same, and the maximum values for $J_T^{(2)}$ reached using the two fields are also very similar, cf. Fig. 8.6. This means that the algorithm finds two distinct solutions. This result is encouraging because it implies that the spectral constraint does not restrict the control problem too much. In other words, more than one, and probably many, control solutions exist, and it is just a matter of picking the suitable one with the help of additional constraints. It also implies that most of the frequency components in the spectrum of the field optimized without spectral constraint, and in particular the high frequencies above 140 eV are not essential for this control problem.

This can be further verified by removing a posteriori the undesired spectral components in Fig. 8.7 a) and re-calculating the PAD. The energy-integrated PAD obtained with such a filtered optimized pulse remains asymmetric, and the value of the target

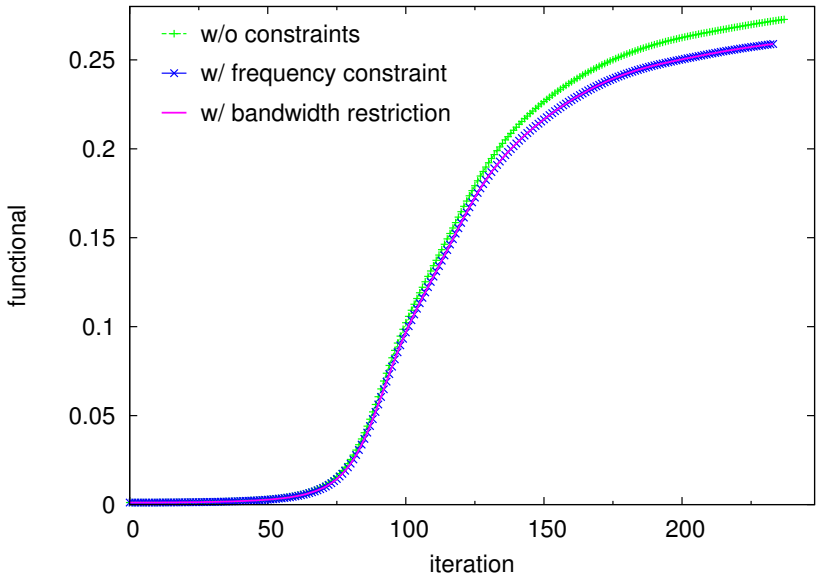

Figure 8.6: Target functional $J_T^{(2)}$, measuring the difference in probability for emission into the upper and the lower hemisphere. It increases monotonically with and without spectral or amplitude constraint. Both types of constraints lead to the same behavior of the functional, which is very similar to the unconstrained case.

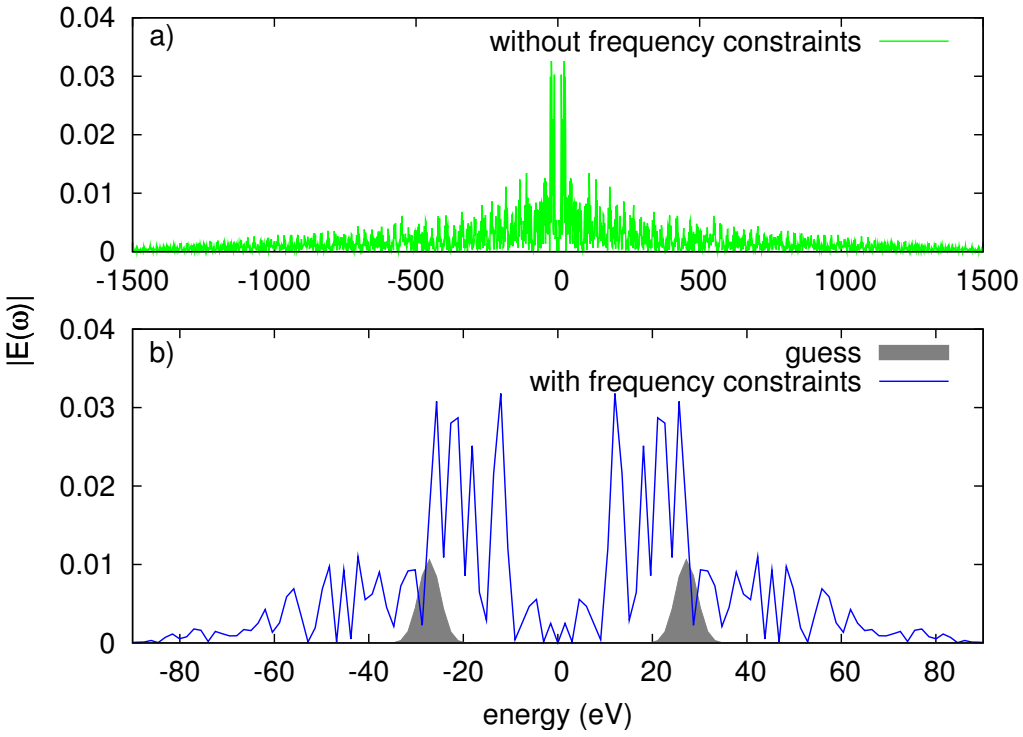

Figure 8.7: Maximization of the anisotropy of emission for hydrogen: Spectrum of the optimized electric field for the optimization shown in Figs. 8.5 and 8.6, a) without, and b) with spectral constraint. The gray-shaded area depicts the spectral content of the initial guess pulse. Beyond 90 eV the frequency components are negligibly small in the frequency-constrained case.

functional $J_T^{(2)}$ is decreased by only about 10%.

The peak amplitude of the optimized field is about one order of magnitude larger than that of the guess field, cf. Fig. 8.5 b) and c). The increase in peak amplitude is connected to the gain in emission probability for the lower hemisphere by almost three orders of magnitude. The optimized pulse thus ionizes much more efficiently than the guess pulse.

Figure 8.8 a) compares the electric fields optimized with and without spectral constraints. Mainly at the peaks a huge difference is observed for the two fields. While the electric field optimized without spectral constraint exhibits very sharp and high peaks in amplitude, going far beyond one atomic unit of field strength, the frequency-constrained optimized field is characterized by reasonable amplitudes and a much smoother shape. The emergence of the high frequency components of the unconstrained field shown in Fig. 8.7 a) now become clear because they are reflected in the rapid changes in electric field strength around the peaks. Note that the difference in amplitude only appears during the first half of the overall pulse duration, see Fig. 8.8 a).

Figure 8.8 b) shows the energy-integrated PAD obtained upon propagation with the two fields. One notes that, although the probability of emission into the lower hemi-

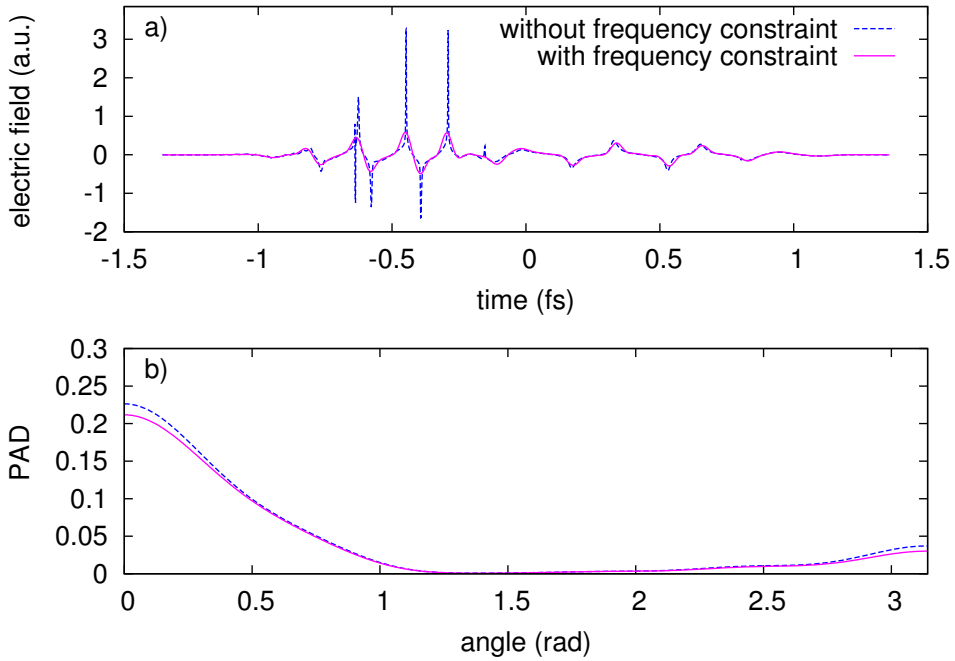

Figure 8.8: Maximization of the difference of photoelectrons emitted into the lower and upper hemispheres for hydrogen: a) Optimized electric fields with ($\lambda_\omega \neq 0$) and without ($\lambda_\omega = 0$) frequency restriction where the pink curve shows the same field as in Fig. 8.5 c). b) Comparison of the energy-integrated PADs with and without frequency restriction.

sphere is larger for the unconstrained than for the constrained field, the same applies to the probability of emission into the upper hemisphere. Therefore, the difference in the number of electrons emitted into upper and lower hemisphere stays eventually relatively close, which explains the similar behavior of the final-time functional observed in Fig. 8.6 a). The electron dynamics generated by the frequency-unconstrained field leads to a slightly larger total probability of emission into both hemispheres, with respect to that obtained with the frequency-constrained field. More precisely, propagation with the unconstrained optimized field results in a total probability of emission of 0.27, i.e., probabilities of 0.23 and 4.3×10^{-2} for emission into the upper and lower hemisphere, respectively. In comparison, a total probability of emission of 0.26 is obtained for the frequency-constrained field, with probabilities of emission into the upper and lower hemispheres of 0.22 and 3.9×10^{-2}, respectively.

The similar behavior in the frequency-restricted and unrestricted cases leads to the conclusion that the spikes observed during the first half of the frequency-unconstrained field do not have considerable impact on the final photoelectron distribution. In fact, this can be easily understood by the short timescale on which the rapid change in intensity occurs. This change happens so fast that the electronic system does not have time to respond to the rapid variations of the field amplitude.

Additionally to the integrated quantities shown above, energy-integrated PAD and angle-integrated PES, the full photoelectron distribution can be investigated. For

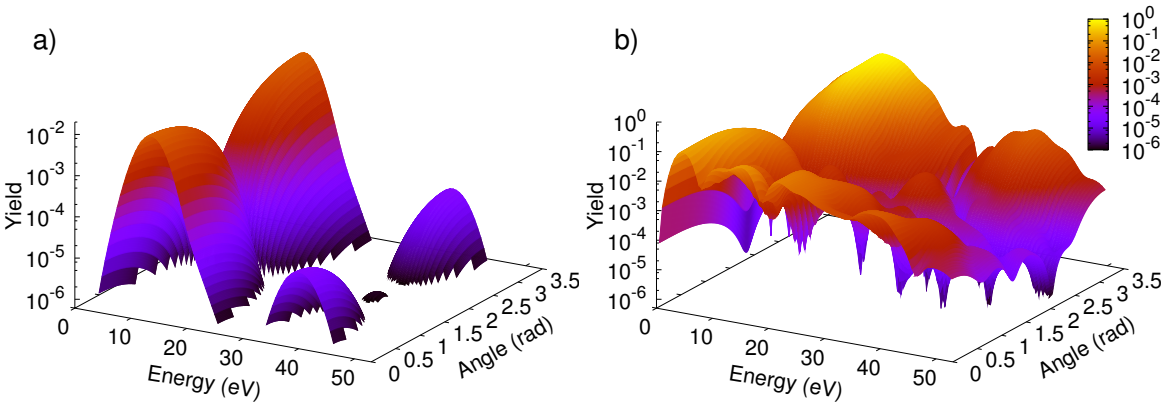

Figure 8.9: Optimization in hydrogen with spectral constraints: a) Initial $2D$ photoelectron distribution obtained with the guess pulse in Fig. 8.5 b). The spectrum corresponds to a usual one-photon and ATI spectrum. b) Highly asymmetric photoelectron distribution obtained with the optimized field in Fig. 8.5 c).

the optimization involving spectral constraints the full $2D$ distributions are shown in Fig. 8.9. In Fig. 8.9 a) the photoelectron distribution is shown for the guess pulse, while in Fig. 8.9 b) the result for the optimized pulse is displayed. One clearly sees in the photoelectron spectrum obtained with the optimized pulse that the energy distribution becomes smeared out, the distinct ATI peaks disappear and there is considerable electron yield at higher kinetic energies. The angular distribution is also altered significantly and does not show the lowest partial wave components of one- and two-photon ionization.

To rationalize how the asymmetry of electron emission is achieved by the optimized field consider the interference of different pathways that lead to the probability of finding an electron with a particular kinetic energy at a certain angle. For asymmetry it is not sufficient to ionize with a combination of different frequencies because this leads to different final energies. In order to achieve asymmetry in the photoelectron distribution it is necessary to add coherently different final states of the outgoing electron with opposite parity at the same kinetic energy. To quantify the contributions from the various orders of photoabsorption, the partial wave decomposition of the angle-integrated PES is analyzed in Fig. 8.10, comparing the results obtained with the guess field to those obtained with the frequency-constrained optimized field. In Fig. 8.10 a) one sees that the initial pulse yields a distribution of the outgoing electron where only partial waves of the same parity exhibit the same energy. In contrast, Fig. 8.10 b) reveals that the desired asymmetry in the energy-integrated PAD is achieved through the mixing of various higher partial waves of opposite parity at the same energy. Furthermore, the optimized field enhances the contribution of states with higher angular momentum that have the same kinetic energy. In particular, the peaks for $l = 5$ are dramatically higher than in the PES obtained with the guess field. Note, that the energy distribution changes from distinct ATI peaks to a quasi-continuous energy spectrum, which can already be inferred from Fig. 8.9.

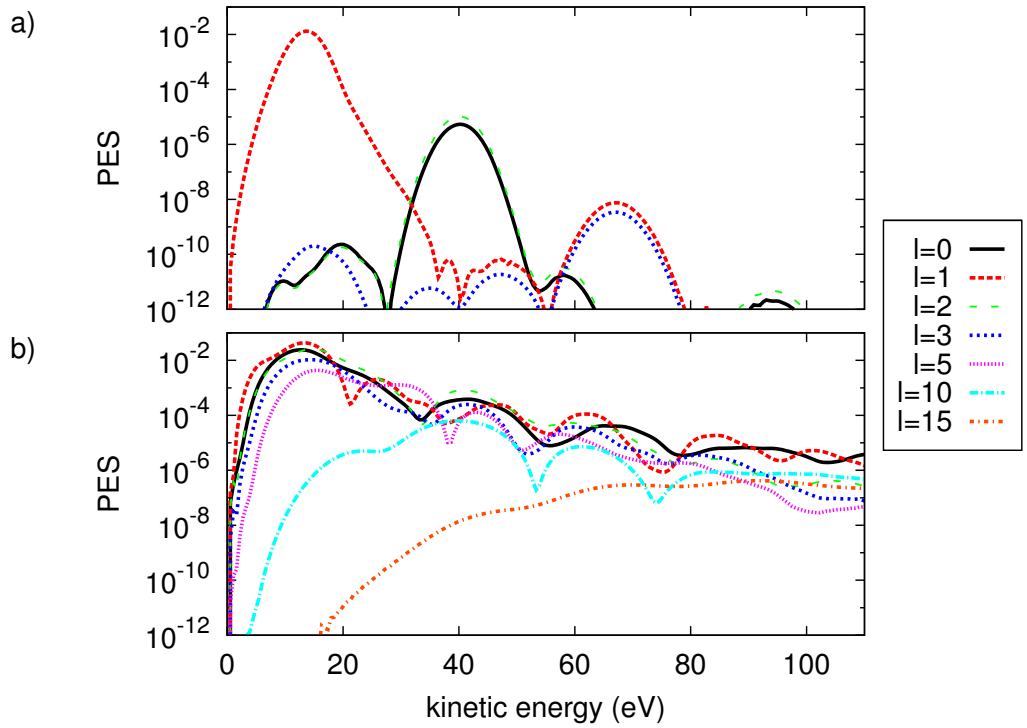

Figure 8.10: Maximizing the anisotropy of photoelectron emission for hydrogen: a) Partial wave contribution to the angle-integrated PES, shown in Fig. 8.5 obtained with the guess field. b) The same for the frequency-constrained optimized field. Additional higher partial wave components in the PES are obtained with the optimized field compared to the PES obtained with the initial field.

Interestingly, especially lower frequencies are mixed with a considerable intensity into the pulse spectrum and, consequently, the main peak is located around the position of the one-photon peak obtained with the guess pulse. All in all, restricting the pulse spectrum to frequencies $|\omega| < 5\,\text{a.u.}$ while permitting low frequency components in the spectrum, cf. Fig. 8.7 b), results in higher order multiphoton ionization leading to comparable and quasi-continuous final energies in the PES. More angular momentum states of opposite parity are mixed in order to achieve asymmetry. For hydrogen, tailored electric fields to achieve asymmetric photoelectron emission have been discussed before in Refs. [232, 234]. While in these publications the carrier-envelope phase dependence was studied for few-cycle pulses in our work we allow for complete freedom, respecting our constraints, in amplitude, frequency and shape.

Summarizing, since the optimization approach requires forward and backward propagation of the state and co-state, respectively, the wave function splitting of the state turns into a wave function "glueing" for the co-state. This was the main conceptual difficulty that had to be overcome. Our work provides the basic prescription to efficiently optimize desired features in the angle-integrated photoelectron distribution, in the energy-integrated photoelectron angular distribution, or both. Both illustrations of our approach, achieving a whole predetermined $2D$ distribution and maximizing the asymmetry of the energy-integrated photoelectron angular distribu-

tion, demonstrate the capabilities of the numerical method. As further applications of our method several investigations are going to be performed for multichannel cases, such as argon and xenon with various optimal control objectives.

9 Above-threshold ionization of light elements in the x-ray regime

Journal of Physics B: Atomic, Molecular and Physics **48**, 124001 (2015),
Special Issue on Frontiers of Free Electron Laser Science Series II

So far, we studied the infrared regime in Ch. 4, we discussed the interaction of intense XUV-laser light with many-electron systems in Chs. 5, 6, investigated xenon in Ch. 7, which exhibits pronounced electron correlations and looked in Ch. 8 at the optimal control problem with PES. We turn now to the x-ray regime and the information that PES can provide in this photon-energy range. After ascertaining that collectivity does not play a decisive role in this photon-energy range we proceed by increasing the intensity of the x-ray pulses that interact with elements that are abundant in organic molecules. The influence of ATI on the ionization probability is then studied as a function of pulse intensity. The question we pose is: How important is ATI in the hard x-ray regime? Hard x-rays are utilized for the purpose of coherent diffractive imaging because due to the small wavelength they can provide high spatial resolution down to a few Ångström.

With higher photon energy the probability for photoabsorption by electrons of the valence shell decreases significantly. In the x-ray regime the absorption probability for electrons in the valence shells at low intensities is negligible compared to visible or XUV light. For instance, already at 1 keV a $2p$ electron in a carbon atom absorbs with a cross section of only 10^{-4} Mb. This amounts to a cross section that is 3 orders of magnitude smaller than for the core electrons [235]. The core electrons are more likely to absorb because they have a larger binding energy. When it comes to very high intensities electrons of the inner shells of atoms might absorb even more than one photon despite of the high photon energy in the hard x-ray regime. Especially for imaging experiments at XFELs this circumstance could be a problem because after diffraction from a sample the real space image needs to be retrieved from the image obtained in momentum-transfer space. For brighter illumination and a higher signal intensity higher pulse intensities are needed, e.g., in order to image the interior of a virus. ATI at such high intensities might be a process that can produce considerable signal in the photon energy regime used in imaging experiments.

Photoelectron spectra (PES) are a most adequate observable for quantifying the impact of ATI. In the present chapter I present the investigation of the multi-photon process of ATI for the light elements hydrogen, carbon, nitrogen and oxygen in the

hard x-ray regime. Numerical challenges are discussed and Hartree-Fock-Slater calculations are compared to TDCIS calculations. Through this comparison the mean-field potential approach is justified in this regime. A theoretical prediction of two-photon above-threshold-ionization cross sections is presented for the mentioned elements. Moreover, we study how the importance of above-threshold ionization varies with intensity. We find that for carbon, at x-ray intensities around $10^{23}\,\mathrm{Wcm}^{-2}$, which might be reached soon at XFELs, two-photon ATI of the K-shell electrons is as probable as one-photon ionization of the L-shell electrons.

9.1 Introduction

The development of XFELs in recent years has allowed the production of ultrashort x-ray pulses at ever increasing intensities. Highly intense hard x rays are of particular interest, e.g., for the purposes of molecular imaging at atomic resolution [236]. Anticipating further developments in the direction of ultrashort x-ray pulses down to a few hundred attoseconds time scale, XFELs will represent the ideal tool for single-molecule imaging via coherent x-ray scattering [140, 237]. Further interesting applications of highly intense and ultrashort pulses include the investigation of electronic dynamics in atoms and (bio-) molecules which typically take place on a time scale between attoseconds and tens of femtoseconds [22, 238].

The Linac Coherent Light Source (LCLS) XFEL has been running since 2009 at the SLAC National Accelerator Laboratory in the United States and was the first XFEL capable of producing hard x-rays [239]. Recently, the SACLA XFEL at the SPring-8 facility in Japan reached intensities of $10^{20}\,\mathrm{Wcm}^{-2}$ at photon energy of 9.9 keV [240]. The European XFEL in Hamburg, Germany, is intended to produce light spanning the range from the carbon K-edge ($\approx 280\,\mathrm{eV}$) to x-rays with photon energies up to 25 keV [241]. By focusing the pulses down to a few nanometers, XFELs can reach intensities that are orders of magnitudes greater than previously achieved. Even though the interaction probability of x-rays with matter is low [242], in this high-intensity regime it is necessary to consider the importance of nonlinear processes affecting electronic dynamics of atomic, molecular or solid-state target systems.

Here, we focus on the nonlinear effect of ATI (cf. Ch. 5). This process has been studied extensively by now, especially in the range of infrared to visible and XUV light [243–245]; however, less work exists for x-ray ATI in the high-intensity regime [246], and mostly on hydrogen or hydrogen-like ions [247–250].

The purpose of this work is to examine the role and the magnitude of ATI in the x-ray regime under the high-intensity conditions that will become available soon at XFELs. To this end, photoelectron spectra are calculated in order to quantify the effect of ATI (cf. Ch. 5). Since we expect correlation effects not to be very relevant at x-ray energies we employ and compare two approaches for the electronic structure: The first-principle calculations of the TDCIS [2, 129, 130] are compared

to calculations treating the atomic potential on the Hartree-Fock-Slater (HFS) level. Our capability of calculating angle-resolved PES is exploited by analyzing the spectra in different directions. For the purposes of molecular imaging the most important elements to consider are those commonly found in organic molecules. For this reason carbon, nitrogen, oxygen and hydrogen are chosen as the focus of this study. The two-photon ATI cross sections for these elements are calculated at the representative and commonly used hard x-ray photon energies of 8, 10 and 12 keV. An investigation is also carried out to see at which intensities ATI makes an important contribution to the overall ionization probability.

The description of light matter interaction in the x-ray regime is challenging both from a numerical and technical point of view because the small frequencies require narrow time sampling and large amounts of data are produced. After briefly describing the challenges faced during the investigation I will present both the two-photon ATI cross sections for light elements and the results of an intensity study for ATI in carbon.

9.2 Method and numerical challenges

The full N-electron Schrödinger equation is solved numerically within TDCIS, where the wave function is expanded in the one-particle–one-hole basis, cf. Ch. 1. The PES are calculated using the splitting method (see Ch. 5, Sec. 5.1.1) with special, converged splitting parameters for the x-ray regime. In order to compute cross sections for open shell atoms, we use here the HFS atomic potential [137]. The HFS potentials for the various elements are calculated using the XATOM code [139].

During the investigation of the interaction of x-rays with atoms a variety of computational and numerical challenges arise. The grid on which the wave function is represented requires a large radius in order to efficiently apply the splitting method to the high-energy wave packets produced. Grid sizes of around 120 Bohr radii were found to be large enough. The number of grid points was chosen at approximately 10 points per de-Broglie wavelength in order to well represent the high-energy parts of the outgoing wave function. Increasing the number of grid points further did not influence the PES. It was found that for the x-ray photon-energy regime choosing a maximum angular momentum of higher than 3 did not significantly affect the PES.

Because of the high photon energy the propagation time step used to propagate the wave function needs to be very small. We found that using Runge-Kutta method to the 4th order about 20 time steps per electric field oscillation are required to prevent significant artifacts from appearing in the PES. As a consequence of the small propagation time step the splitting function had to be applied very frequently. Applying the splitting every 3 time steps is appropriate to remove artifacts due to reflections. However, this causes some practical problems as large amounts of data must be stored. Certain parameters are found to be mostly unimportant for convergence.

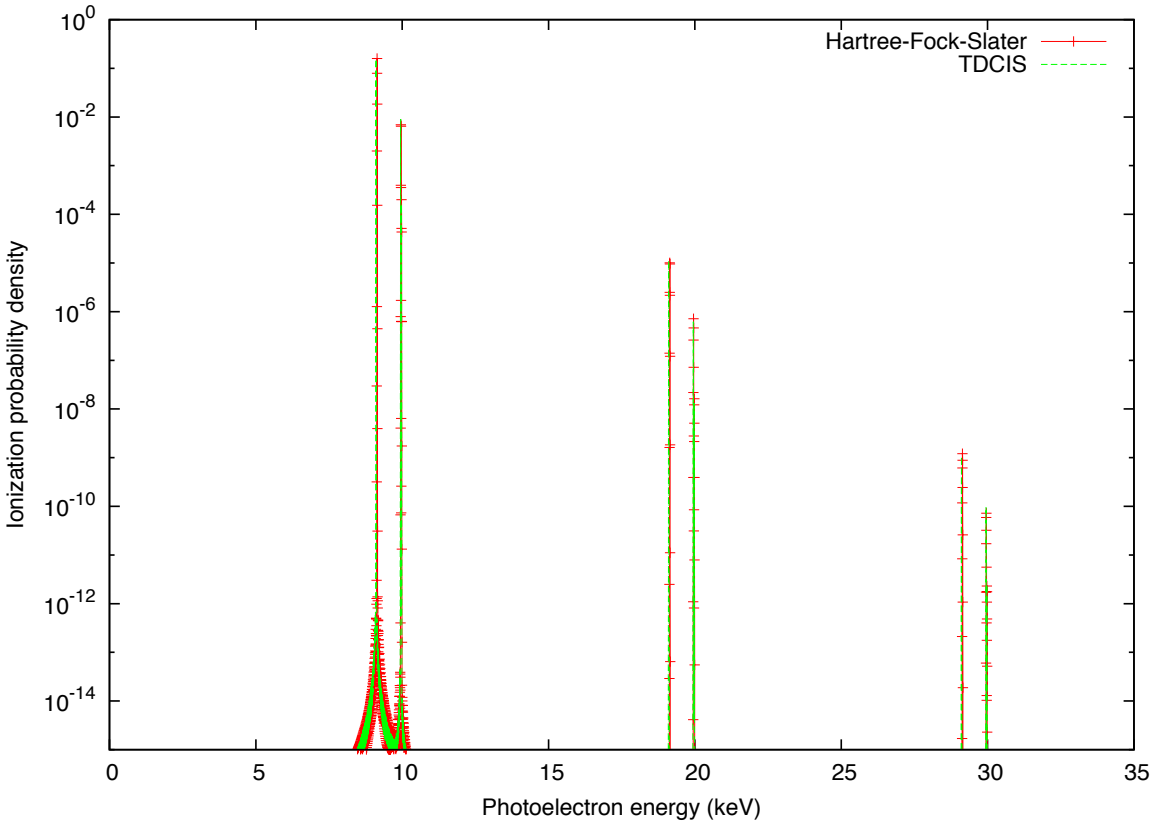

Figure 9.1: Photoelectron spectrum of neon for a Gaussian pulse with 10 keV photon energy, at 10^{21} Wcm^{-2} intensity and 0.48 fs pulse duration, using HFS (green) and TDCIS (red). The one-photon ionization peak and the first two ATI peaks are shown. Each peak consists of two subpeaks, the one at lower energy being associated with ionization from the K shell (cf. Table 9.1), the other one corresponding to L-shell ionization. ©2015 IOP Publishing

Consistently with the study in Ref. [2], the smoothing of the splitting function Δ has little to no effect as long as the wave function close to the nucleus is not disturbed.

Obviously, using the HFS potential significantly reduces the computational time as it removes the necessity to calculate the large number of Coulomb matrix elements, i.e., the exact Coulomb interaction between the electrons. In order to find out if the HFS approach is valid in the x-ray photon-energy range, neon was studied with both methods before applying it to the elements carbon, nitrogen and oxygen, which are more relevant for chemistry and biology than nobel-gas atoms. The binding energies for the K shells for the elements under investigation are summarized in Table 9.1 [242]. For comparison, the energies obtained within our computational model are presented, too. The $L_1 2s$ shells have binding energies below 50 eV. Therefore, on the energy scale we investigate in the present work the energy positions of the peaks arising from the $L_1 2s$ and $L_2 2p$ shells, respectively, reflect essentially the photon energy.

In Fig. 9.1 we present the photoelectron spectrum of neon for a Gaussian pulse of 10 keV photon energy and 0.48 fs pulse duration at an intensity of 10^{21} Wcm^{-2} using the HFS potential (green) and the full TDCIS method (red). Except for the slight

	calculated	X-Ray Data Booklet
Carbon	290.9	284.2
Nitrogen	404.6	409.9
Oxygen	536.9	543.1
Neon	857.1	870.2

Table 9.1: Binding energies of the K shells for carbon, nitrogen, oxygen and neon. The first column shows the binding energies calculated within the HFS approach, the second column reproduces data taken from Ref. [242]. The binding energies of the $L_1 2s$ shells are below 50 eV for all elements considered here.

upward energy shift for HFS the shape and height of the peaks are the same. The noise levels and artifacts present in the spectrum are also unaffected by the method used. The comparison suggests that in the photon energy regime of hard x-rays the HFS approach is well justified for open shell atoms with a similar Z value, namely carbon, nitrogen, and oxygen. Our calculations for neon show that electron correlation effects play a minor role for one- and two-photon absorption in this regime.

9.3 Results and Discussion

We calculated two-photon ATI cross sections for hydrogen and compared them with previous work [247]. They are found to be in very close agreement. Using 10^{20} Wcm^{-2}, a relative difference of 2% was found at the photon energy of 10 keV and 7% at 8 keV. With a slightly larger intensity of 3.5×10^{20} Wcm^{-2} the cross section at 5 keV was found to be 2.02×10^{-65} cm^{4}s, which amounts to a difference of 1% compared to Ref. [247].

Since the method employed here relies on the numerical solution of the Schrödinger equation (2.2), no difficulties arise with sums over intermediate states, which appear in a perturbative treatment [246]. Reference [247] demonstrates that the A^2 interaction, which is not included here, may be neglected in the photon-energy range of current interest. As already indicated in Eq. (2.8) of the theory section 2.2, by the exclusive time dependence of the vector potential in the atom-field coupling term, $\hat{\mathbf{p}} \cdot \mathbf{A}(t)$, all calculations were performed under the assumption of the dipole approximation. However, under the conditions of short-wavelength x-rays this assumption may no longer be valid. Indeed, the influence of nondipole effects especially on angular correlations were studied in detail [250–253]. Zhou and Chu indicate that nondipole effects significantly change the photoelectron angular distribution and that the nondipole ATI spectra are enhanced in the high photon-energy regime [253]. On the other hand, it was shown for the x-ray regime that when including all multipoles the *total* two-photon ATI cross section differs less than an order of magnitude from the cross section calculated in dipole approximation for sufficiently small nuclear charge [250]. Therefore, although our values may underestimate the two-photon ATI

cross section, we expect this underestimation in the integrated spectrum to be much smaller than an order of magnitude (a factor of around $2-3$) [254]. Nevertheless, it would be desirable to possess an approach that includes the treatment of higher-order multipole effects in the radiation-matter interaction. Extending the description beyond the dipole approximation is feasible, however it would break the cylindrical symmetry with respect to the light polarization axis which we exploit in the present implementation of TDCIS. One then needs to describe the coupling of angular momenta with the corresponding magnetic quantum numbers to higher multipole orders which makes the computation more costly.

As far as the relativistic corrections for the ionized electron are concerned we briefly estimate the relative correction for the energy range we are interested in. The first order relativistic correction to the energy consists of the spin-orbit term and the kinetic energy correction $\Delta E_{\text{kin}} = p^4/(8c^2)$, where p is the momentum and c is the speed of light. Since they are both of the same order [174] we examine for simplicity the kinetic energy correction for an electron of 20 keV. Inserting the nonrelativistic momentum $\sqrt{2E}$ this correction amounts to approximately 2% of the nonrelativistic kinetic energy. For this reason, within the precision mentioned above the relativistic correction for the ionized electron can be neglected.

The two-photon ATI cross sections were found in the perturbative limit, i.e., by assuring that the ionization probability is low enough to not deplete the ground state. In the perturbative limit the ionization probability due to two-photon absorption is given by

$$\sigma^{(2)} F^{(2)} = \sigma^{(2)} \int J^2 \mathrm{d}t, \tag{9.1}$$

where $\sigma^{(2)}$ is the two-photon cross section and J is the photon flux in $\mathrm{cm}^{-2}\mathrm{s}^{-1}$; $F^{(2)}$ is the fluence for two-photon absorption. Assuming a Gaussian pulse the electric field has the form

$$E(t) = E_0 \cos(\omega t) e^{-2\ln 2\ t^2/\tau^2}, \tag{9.2}$$

where E_0 is the peak electric field, ω is the central field frequency, and τ is the pulse duration. Then, the fluence $F^{(2)}$ is given by

$$F^{(2)} = \frac{E_0^4}{\omega^2} \sqrt{\frac{\pi}{8\ln 2}} \left(\frac{c}{8\pi}\right)^2 \tau. \tag{9.3}$$

The two-photon K-shell ATI cross sections for hydrogen, carbon, nitrogen, oxygen, and neon at the hard x-ray energies of 8, 10, and 12 keV are presented in Table 9.2. We find the expected increase in the two-photon ATI cross section for higher Z values and a drop with larger photon energy. As mentioned previously, all cross sections were found under the dipole approximation, which is expected to slightly underestimate the cross sections. The two-photon ATI cross section of beryllium was also calculated at 10 keV photon energy to be

$$\sigma^{(2)}_{\mathrm{Be}1s} = 1.25 \times 10^{-63}\ \mathrm{cm}^4\mathrm{s}. \tag{9.4}$$

E (keV)	K-shell two-photon cross sections (cm^4s)				
	Hydrogen	Carbon	Nitrogen	Oxygen	Neon
8	1.44×10^{-66}	1.64×10^{-62}	3.21×10^{-62}	5.62×10^{-62}	1.65×10^{-61}
10	4.69×10^{-67}	4.61×10^{-63}	9.23×10^{-63}	1.70×10^{-62}	3.71×10^{-62}
12	1.72×10^{-67}	1.79×10^{-63}	3.82×10^{-63}	6.94×10^{-63}	1.95×10^{-62}

Table 9.2: Two-photon ATI cross sections for the K shell of the light elements (E is the photon energy). All were calculated from integrating the corresponding photoelectron peaks at 10^{20} Wcm^{-2} intensity and 0.12 fs of pulse duration.

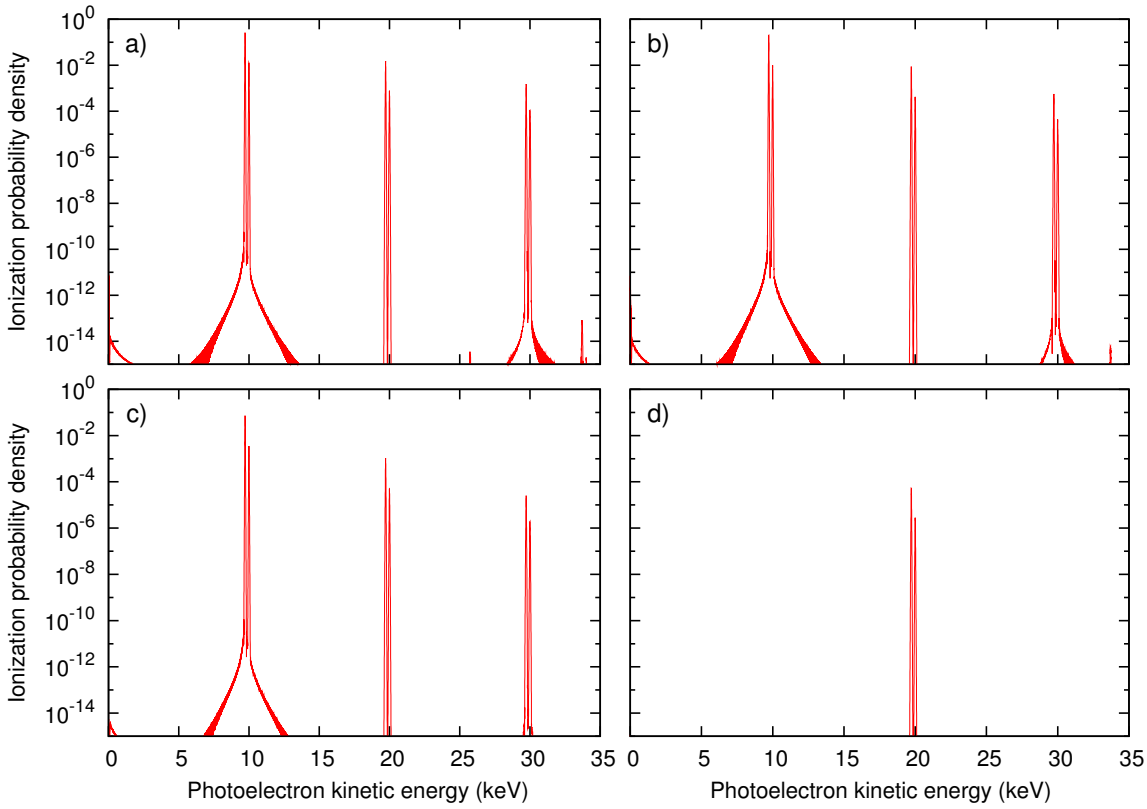

Figure 9.2: Photoelectron spectra of carbon for different angles: a) 0, b) $\pi/6$, c) $\pi/3$, d) $\pi/2$. The spectra are calculated for a pulse centered at 10 keV photon energy, at an intensity of 10^{24} Wcm^{-2} and 0.12 fs pulse duration. Note that the height of the K-shell ATI peak is greater than or comparable to the one-photon L-shell ionization peak. ©2015 IOP Publishing

Because imaging of organic molecules is of particular interest we perform an intensity study on carbon with an incoming photon energy of 10 keV in order to find the regime in which the ionization due to two-photon ATI is of the same order as that for one-photon ionization. As seen in Fig. 9.2, at an intensity of 10^{24} Wcm^{-2} the depopulation due to K-shell ATI in the direction $\theta = 0$ becomes comparable and even higher than valence one-photon ionization. The PES in the directions $\pi/6$, $\pi/3$, and $\pi/2$ are also shown (for better visualization only 15 orders of magnitude are shown).

Note, that a small peak around zero kinetic energy is observed. The emergence

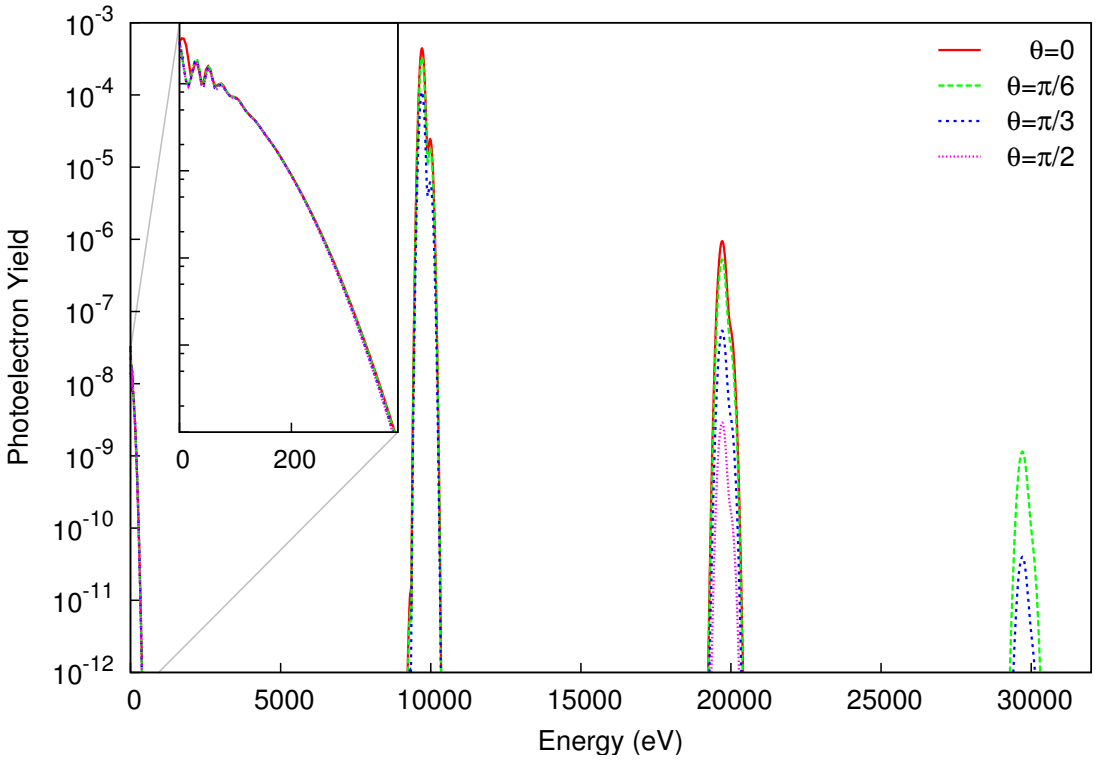

Figure 9.3: Photoelectron yield for carbon, shown for a pulse of 12 as duration and $3.5 \cdot 10^{22}$ Wcm^{-2} intensity with a photon energy of 10 keV after a sufficiently long propagation time. The slow-electron peak (magnified in the inset) as well as the 1-photon peak and the first two ATI peaks are shown for 4 different angles with respect to the polarization direction. The height of the slow-electron peak is comparable to the first ATI peak in the direction of $\pi/2$. ©2015 IOP Publishing

of this peak has been studied in Refs. [255, 256] within the Kramers-Henneberger framework in the case of the negative ion H^- interacting with VUV-XUV radiation in the stabilization regime. It is found that the zeroth peak is of the same order as the 2-photon peak. However, these studies deal with a completely different regime of laser-matter interaction. In the present x-ray ATI study, the height of the peak shown in Fig. 9.2 might be underestimated, because due to our splitting approach the propagation time must be sufficiently large in order to detect all electrons of interest in the splitting region. The results shown in Fig. 9.2 were produced in a calculation where the propagation time was approximately 20 times shorter than necessary to collect all electrons with a kinetic energy on the scale of 1 eV. In order to elucidate this slow-electron peak further, a new calculation was performed, now involving a pulse at 10 keV photon energy, of 12 as duration and $3.5 \cdot 10^{22}$ Wcm^{-2} intensity in order to be able to propagate long enough and to observe the slow-electron peak in its full height. The results are presented in Fig. 9.3. The emergence of the peak can be attributed to the bandwidth of the pulse which spans the binding energy of the valence electrons. This has also been discussed in Ref. [254]. After the absorption of one photon by the valence shell of the atom the emission of a photon can occur and,

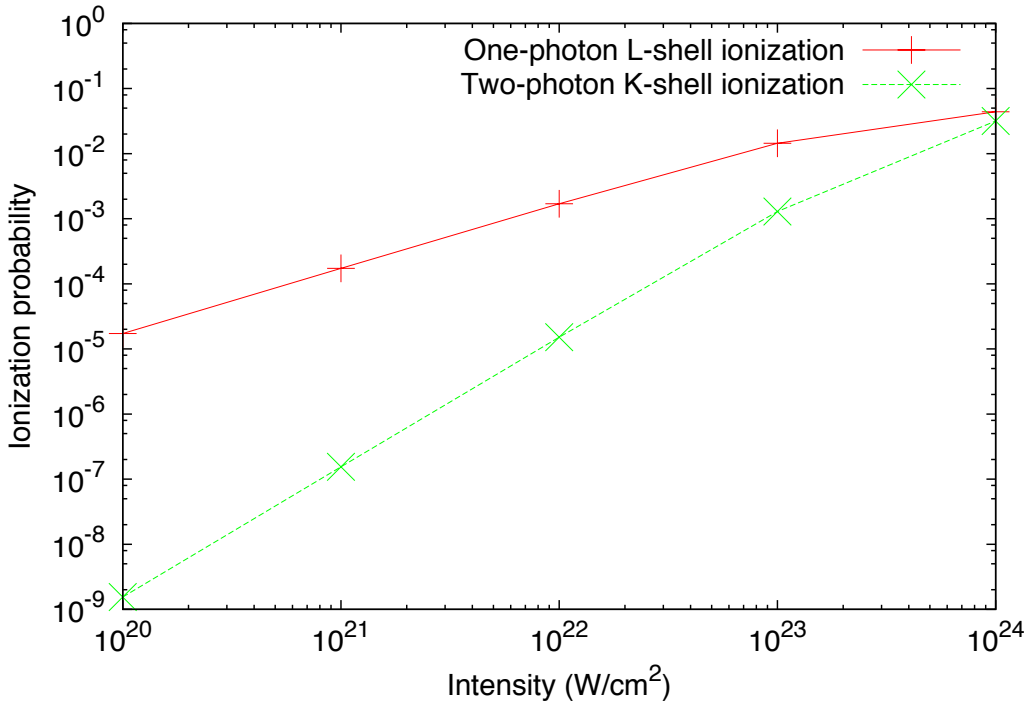

Figure 9.4: Depopulation at different intensities due to two-photon ATI against one-photon valence electron ionization for carbon, at 10 keV photon energy and 0.48 fs pulse duration. The ionization probability was found by integrating the corresponding PES peaks. ©2015 IOP Publishing

thereby, slow electrons are produced.

In Fig. 9.4 the ionization probability of carbon is shown as a function of intensity for the case of one-photon ionization out of the L shell together with two-photon ionization out of the K shell. We see the characteristic quadratic behavior of the ATI peak as a function of the intensity and the linear behavior in the one-photon valence ionization probability. Saturation effects do not play a role until the intensity range near 10^{24} Wcm^{-2} is reached. In fact, one can see that at an intensity between $10^{23} - 10^{24}$ Wcm^{-2} the fully angle- and energy-integrated K-shell ATI peak, i.e., the ionization probability due to ATI out of the K shell, is comparable to the probability to ionize with one photon out of the valence shells.

Summarizing, we have presented a prediction for the two-photon ATI cross sections of the light elements carbon, nitrogen, and oxygen at hard x-ray energies common for current experiments at XFELs. At intensities that one may reach for future hard x-ray experiments, scientists should consider how ATI will affect their results. We conclude that ATI remains a negligible fraction of ionization for intensities at the most recent XFEL experiments with hard x-rays. However, we predict that with photon energies at around 10 keV, when entering the regime of 10^{23} Wcm^{-2} and above, the ionization probability of the core electrons by ATI approaches the same order of magnitude as valence stripping by one-photon ionization for elements with a similar nuclear charge Z as carbon. It is likely that the neglected nondipole effects enhance the ATI spectrum

by less than an order of magnitude. Therefore, our results present a lower limit on the importance of ATI and suggest that ATI be taken into account when entering this high-intensity regime. In particular, we hope that the data presented can be a guide for future experiments investigating imaging and nonlinear x-ray optics.

10 Conclusions and Outlook

Within my doctoral work I studied the ionization of many-electron systems in various photon-energy regimes. I focussed on the nonlinear response regime, i.e., I investigated light-atom interactions where the intensity of the light pulses is sufficiently high to induce multiphoton absorption processes. Such pulses are provided for instance at FELs. In particular, I studied atomic xenon which is known to exhibit strong correlation effects in the electronic shell. I showed for xenon as a model system that nonlinear spectroscopy can be employed as a tool to broaden our knowledge about the collective resonance behavior of atomic systems. We analyzed the spectroscopic data of one- and two-photon absorption of xenon in the XUV which had been obtained by the group of Dr. Michael Meyer at FLASH. With the help of our theoretical model, which captures electron correlation effects in the atomic shell, we uncovered underlying substructure in the XUV giant dipole resonance of xenon. For 50 years this substructure had remained unresolved because linear spectroscopy had so far been used to measure the collective resonance. The nonlinear process enabled us to detect that the giant resonance consists of two resonances instead of a single one.

I extended the TDCIS method in three directions, which are summarized below with their applications in our studies of atomic photoionization from the infrared to the x-ray regime.

The implementation of two methods within TDCIS for the calculation of photoelectron spectra, presented in Ch. 5 provided a practical tool for the characterization of multichannel ionization over a broad range of photon energies. Both methods, the splitting and the t-surff methods, can produce quantitative energy- and angle-resolved spectra within our model. Subshell ionization of any higher order in multiphoton ionization can now be quantified. We have applied and compared these methods in the high-intensity XUV regime. Advantages of the splitting method are the good absorption characteristics through the splitting function and the short propagation time that is needed. A computational disadvantage is the long evaluation time of the radial integrals. The t-surff method needs a longer propagation time. However, the calculation of the photoelectron spectrum in the analysis step is much faster than with the splitting method due to the evaluation at one point. The comparison of the two methods shows that, in principle, the same spectra can be obtained after appropriately optimizing the computational parameters. In principle, it is possible to study processes ranging from the strong-field regime in the infrared range to the x-ray regime by analyzing the photoelectron spectrum, although the infrared strong-field

regime has not yet been a focus of our work.

Second, through the implementation of ARPACK within TDCIS we obtained the eigenstates of the Hamiltonian and further characterized their properties by exploiting the versatility of the iterative Arnoldi algorithm within software package to solve large-scale eigenvalue problems. Depending on the problem, random starting vectors can be used or a defined starting vector can be provided. The range of the spectrum that shall be calculated can be specified, for instance, the eigenvectors with the smallest eigenvalues. The application in the tunneling regime revealed, strictly speaking, that tunneling ionization is a nonadiabatic process and that in the case of few-cycle pulses the dynamics can be described fully by using one single nondiabatic eigenstate.

In a second application of the diagonalization of the many-electron Hamiltonian we verified our discovery of two collective resonances underlying the famous giant dipole resonance in xenon by further characterizing the resonance states. Through the diagonalization we theoretically analyzed their energy positions and lifetimes. Therefore, we could present two results obtained with TDCIS that indicate strongly that the form and the broadening of the two-photon cross section curve can be explained when taking into account the existence of more than one resonance: On the one hand, we found excellent agreement between the experimental results and our full model calculations of the two-photon cross section which exhibits a knee-type structure. On the other hand the calculation of the resonance states reveals two complex resonance energies. These resonances strongly overlap, and, therefore, interfere in the range of the $4d$ giant resonance. In conclusion, experimental measurement techniques in the nonlinear regime are sensitive to the influence of the two underlying resonances of the giant dipole resonance in xenon.

Thirdly, the use of the Lanczos-Arnoldi propagation scheme rendered possible the backward propagation which became more precise by orders of magnitude and more stable. This precision and stability enabled us to study optimal control problems. In this way, we not only calculate the impact an electric field has on the atom and the dynamics it initiates, but we also ask how the field must be tailored in order to achieve special features in ionization, e.g., to produce a certain photoelectron distribution. In combination with the possibility to calculate photoelectron spectra the stable backward propagation allowed for optimizing the anisotropy in the photoangular distribution of the electrons emitted after irradiation by a (strong) pulse centered in the XUV photon-energy range. To this end, we have developed a quantum optimal control toolbox, which combines the Krotov method with TDCIS to target specific features in photoelectron spectra and photoelectron angular distributions that result from the interaction of a closed-shell atom with strong XUV radiation. Constraints on the frequency spectrum and the amplitude of the pulses can be imposed for further control. Considering pure XUV pulses the use of a band-pass filter for the optimized pulse is advisable, which filters out low frequencies. The results from this kind of op-

timization will provide an insight into asymmetries of the photoelectron distributions achieved in the pure multiphoton regime. While hydrogen has already been studied as a test example for our various optimization objectives, further investigations of multichannel systems, such as argon and xenon are envisaged, ongoing or planned.

The applicability of the tools I developed within my doctoral work and presented in the present thesis is by far not exhausted.

One of the most natural applications that due to the shortness of time could not be studied sufficiently is the strong-field ionization in the infrared regime, that means, in the tunneling regime. The calculation of photoelectron spectra is evidently a perfect tool to quantify the influence of electron correlation effects onto the strong-field ATI spectra and study the cut-off and the rescattering process [257]. First preliminary calculations on hydrogen and xenon in the strong-field regime suggest that both the t-surff and the splitting methods yield reasonable results, e.g. can reproduce the semi-classical cut-off at the value of 3.17 U_p. What remains is to perform convergence studies within the parameter space needed for the calculations, and analyze the results.

Moreover, interesting applications arise from the study of the photoelectron spectrum through the fact that information about the coherence, the entanglement of the ionic state, and the photoelectron can be extracted from the properties of the outgoing wave packet. Work in progress includes maximizing or suppressing ionization out of predetermined orbitals in multichannel cases. The investigation of maximizing the coherence in the ionization of xenon is also very promising in view of the decoherence properties on the attosecond time scale studied in Ref. [131]. In combination with the optimal control toolbox we developed in collaboration with Esteban Goetz and Prof. Dr. Christiane Koch this aspect can be analyzed further. With possible extensions and further technical developments in the direction of temporal coherence anticipated for free-electron lasers, such as FERMI or FLASH, coherent control could be possible even at considerably higher intensities.

On a longterm perspective, it would be interesting to lift the restriction to closed-shell atoms in order to extend the range of applicability of TDCIS. Even the extension to a molecular version of TDCIS seems to be feasible which will enable interesting new investigations. In the case of open-shell atoms also ground state correlations can be treated, which are beyond the scope of our capabilities (as mentioned in Ch. 7). Furthermore, going beyond the CIS scheme, namely to the so-called singles-doubles scheme, could be envisaged in order to treat multiple excitations, satellite phenomena and double-ionization processes. On the light-field side one could consider light polarizations that go beyond the linear polarization. As already alluded to in Ch. 9 this would break the cylindrical symmetry about the light polarization axis and would require the mixing of many angular momenta together with their magnetic quantum numbers. When breaking the cylindrical symmetry it is just a small step to generalize the dipole interaction to higher multipole interaction terms. These developments are not trivial at all and computationally very demanding.

But also in its present form the TDCIS framework in combination with the calculation of photoelectron distributions offers various possibilities to investigate correlation phenomena, which are often resolved particularly well in the PAD. For instance, there is work in progress of calculating and analyzing the ATI cross section of xenon in the range of the giant dipole resonance in an angle-resolved manner in order to investigate whether there is a preferred direction where the two underlying resonances are resolved more clearly. If we can identify an angle where the two resonances split and can be distinguished clearly, we could propose direct experimental measurements at this angle in order to find the two resonances. Also, as an outlook for future investigations, it is both experimentally and theoretically feasible to combine multiple photon energies and to study the resonance in deeper detail by exciting the resonance with one XUV photon and by scanning along the range of the giant resonance with the second photon. In view of our results regarding the two different underlying resonances, depending on the energy and the phase of the second photon the results are expected to be very different and possibly to reveal more information on the features of the resonances.

The study of light-induced phenomena, the dynamics and properties of atomic and molecular systems (and matter in general) remains a thrilling subject; we showed that by entering the nonlinear response regime new information can be obtained about the systems under investigation. The study and control of matter with light over its whole energy spectrum will certainly continue to surprise researchers and will establish new routes toward technological applications.

Bibliography

[1] Karamatskou A, Pabst S and Santra R 2013 Adiabaticity and diabaticity in strong-field ionization *Phys. Rev. A* **87** 043422

[2] Karamatskou A, Pabst S, Chen Y J and Santra R 2014 Calculation of photoelectron spectra within the time-dependent configuration-interaction singles scheme *Phys. Rev. A* **89** 033415

[3] Karamatskou A, Pabst S, Chen Y J and Santra R 2015 Erratum: Calculation of photoelectron spectra within the time-dependent configuration-interaction singles scheme [Phys. Rev. A **89** , 033415 (2014)] *Phys. Rev. A* **91** 069907

[4] Mazza T et al. 2015 Sensitivity of nonlinear photoionization to resonance substructure in collective excitation *Nature Communications* **6**(6799)

[5] Chen Y J, Pabst S, Karamatskou A and Santra R 2015 Theoretical characterization of the collective resonance states underlying the xenon giant dipole resonance *Phys. Rev. A* **91** 032503

[6] Tilley M, Karamatskou A and Santra R 2015 Wave-packet propagation based calculation of above-threshold ionization in the x-ray regime *Journal of Physics B: At. Mol. Opt. Phys.* **48** 124001

[7] Goetz R E, Karamatskou A, Santra R and Koch C 2015 Quantum optimal control of photoelectron spectra and angular distributions *to be submitted*

[8] Bethe H A and Salpeter E E 1977 *Quantum Mechanics of one and two electron atoms* (Springer US) 1st edition

[9] Starace A 1982 Theory of Atomic Photoionization Volume 31 1–121 (Springer)

[10] Krause J L, Schafer K J and Kulander K C 1992 Calculation of photoemission from atoms subject to intense laser fields *Phys. Rev. A* **45** 4998–5010

[11] Joachain C, Dörr M and Kylstra N 2000 High-Intensity Laser-Atom Physics Volume 42 of *Advances In Atomic, Molecular, and Optical Physics* 225 – 286 (Academic Press)

[12] Chelkowski S, Bandrauk A D and Apolonski A 2004 Phase-dependent asymmetries in strong-field photoionization by few-cycle laser pulses *Phys. Rev. A* **70** 013815

[13] van der Hart H W and Greene C H 1998 Multichannel photoionization spectroscopy of Ar: Total cross section and threshold photoelectrons *Phys. Rev. A* **58** 2097–2105

[14] Corkum P and Krausz F 2007 Attosecond science *Nature Physics* **3** 381–387

[15] Chapman H N et al. 2006 Femtosecond diffractive imaging with a soft-X-ray free-electron laser *Nature Physics* **2** 839–843

[16] Itatani J, Levesque J, Zeidler D, Niikura H, Pépin H, Kieffer J C, Corkum P B and Villeneuve D M 2004 Tomographic imaging of molecular orbitals *Nature* **432** 867–871

[17] Spanner M, Smirnova O, Corkum P B and Ivanov M Y 2004 Reading diffraction images in strong field ionization of diatomic molecules *J. Phys. B: At. Mol. Phys.* **37** 243–255

[18] Pabst S 2013 Atomic and molecular dynamics triggered by ultrashort light pulses on the atto- to picosecond time scale *The European Physical Journal Special Topics* **221**(1) 1–71

[19] Kanter E P et al. 2011 Unveiling and Driving Hidden Resonances with High-Fluence, High-Intensity X-Ray Pulses *Phys. Rev. Lett.* **107** 233001

[20] Demekhin P V and Cederbaum L S 2012 Coherent intense resonant laser pulses lead to interference in the time domain seen in the spectrum of the emitted particles *Phys. Rev. A* **86** 063412

[21] Midorikawa K 2011 High-Order Harmonic Generation and Attosecond Science *Japanese Journal of Applied Physics* **50**(9R) 090001

[22] Giles J 2002 Attosecond science: The fast show *Nature* **420**(6917) 737–737

[23] Krausz F and Ivanov M 2009 Attosecond physics *Rev. Mod. Phys.* **81** 163–234

[24] Emma P, Bane K, Cornacchia M, Huang Z, Schlarb H, Stupakov G and Walz D 2004 Femtosecond and Subfemtosecond X-Ray Pulses from a Self-Amplified Spontaneous-Emission–Based Free-Electron Laser *Phys. Rev. Lett.* **92** 074801

[25] Baker S, Robinson J S, Haworth C A, Teng H, Smith R A, Chirilă C C, Lein M, Tisch J W G and Marangos J P 2006 Probing Proton Dynamics in Molecules on an Attosecond Time Scale *Science* **312**(5772) 424–427 http://www.sciencemag.org/content/312/5772/424.full.pdf

[26] Wabnitz H et al. 2002 Multiple ionization of atom clusters by intense soft X-rays from a free-electron laser *Nature* **420** 482–485

[27] Young L et al. 2010 Femtosecond electronic response of atoms to ultra-intense X-rays *Nature* **466** 56–61

[28] Moshammer R et al. 2007 Few-Photon Multiple Ionization of Ne and Ar by Strong Free-Electron-Laser Pulses *Phys. Rev. Lett.* **98** 203001

[29] Sytcheva A, Pabst S, Son S K and Santra R 2012 Enhanced nonlinear response of Ne^{8+} to intense ultrafast x rays *Phys. Rev. A* **85** 023414

[30] Drescher M, Hentschel M, Kienberger R, Uiberacker M, Yakovlev V, Scrinzi A, Westerwalbesloh T, Kleineberg U, Heinzmann U and Krausz F 2002 Time-resolved atomic inner-shell spectroscopy *Nature* **419** 803–807

[31] Fukuzawa H et al. 2013 Deep Inner-Shell Multiphoton Ionization by Intense X-Ray Free-Electron Laser Pulses *Phys. Rev. Lett.* **110** 173005

[32] Landau L D and Lifshitz E M 1981 *Quantum Mechanics: Non-Relativistic Theory* (Butterworth-Heinemann) 3rd edition

[33] Keldysh L V 1965 Ionization in the field of a strong electromagnetic wave *Sov. Phys. JETP* **20** 1307–1314

[34] Ammosov M V, Delone N B and Krainov V P 1986 Tunnel ionization of complex atoms and atomic ions by an alternating electromagnetic field *Sov. Phys. JETP* **64** 1191–1194

[35] Bisgaard C Z and Madsen L B 2004 Tunneling ionization of atoms *American Journal of Physics* **72**(2) 249–254

[36] Ivanov M Y, Spanner M and Smirnova O 2005 Anatomy of strong field ionization *J. Mod. Opt.* **52** 165–184

[37] Mainfray G and Manus G 1991 Multiphoton ionization of atoms *Reports on Progress in Physics* **54**(10) 1333–1372

[38] Popov V S 2004 Tunnel and multiphoton ionization of atoms and ions in a strong laser field (Keldysh theory) *Physics-Uspekhi* **47**(9) 855–885

[39] Yamanouchi K 2010 *Lectures on Ultrafast Intense Laser Science 1* (Springer) 1st edition

[40] Mevel E, Breger P, Trainham R, Petite G, Agostini P, Migus A, Chambaret J P and Antonetti A 1993 Atoms in strong optical fields: Evolution from multiphoton to tunnel ionization *Phys. Rev. Lett.* **70** 406–409

[41] Becker A, Plaja L, Moreno P, Nurhuda M and Faisal F H M 2001 Total ionization rates and ion yields of atoms at nonperturbative laser intensities *Phys. Rev. A* **64** 023408

[42] Göppert-Mayer M 1931 Über Elementarakte mit zwei Quantensprüngen *Annalen der Physik* **9** 273–294 http://www.physik.uni-augsburg.de/annalen/history/historic-papers/1931_401_273-294.pdf

[43] Voronov G S and Delone N B 1965 Ionization of the xenon atom by the electric field of ruby laser emission *JETP Letters* **1** 66Ð68

[44] Agostini P, Barjot G, Bonnal J, Mainfray G, Manus C and Morellec J 1968 Multiphoton ionization of hydrogen and rare gases *IEEE Journal of Quantum Electronics* **4** 667–669

[45] Saenz A and Lambropoulos P 1999 Theoretical two-, three- and four-photon ionization cross sections of helium in the XUV range *Journal of Physics B: Atomic, Molecular and Optical Physics* **32**(23) 5629

[46] Hüfner S 1996 *Photoelectron Spectroscopy* (Springer)

[47] Wu G, Hockett P and Stolow A 2011 Time-resolved photoelectron spectroscopy: from wavepackets to observables *Phys. Chem. Chem. Phys.* **13** 18447–18467

[48] Meyer M et al. 2010 Two-Photon Excitation and Relaxation of the 3*d*-4*d* Resonance in Atomic Kr *Phys. Rev. Lett.* **104** 213001

[49] Fabre F, Agostini P, Petite G and Clement M 1981 Angular distribution in above-threshold ionisation of Xe at 0.53 μm *Journal of Physics B: Atomic and Molecular Physics* **14**(21) L677–L681

[50] Becker U and Shirley D A 1990 Threshold Behaviour and Resonances in the Photoionization of Atoms and Molecules *Physica Scripta* **1990**(T31) 56–66

[51] Blaga C I, Catoire F, Colosimo P, Paulus G G, Muller H G, Agostini P and DiMauro L F 2008 Strong-field photoionization revisited *Nature Physics* **5**(013409) 335–338

[52] Agostini P, Fabre F, Mainfray G, Petite G and Rahman N K 1979 Free-Free Transitions Following Six-Photon Ionization of Xenon Atoms *Phys. Rev. Lett.* **42** 1127–1130

[53] Gontier Y, Poirier M and Trahin M 1980 Multiphoton absorptions above the ionisation threshold *Journal of Physics B: Atomic and Molecular Physics* **13**(7) 1381

[54] Schmidt V 1986 Photoionization in rare gases with synchrotron radiation: Some basic aspects for critical tests with theory *Zeitschrift für Physik D Atoms, Molecules and Clusters* **2**(4) 275–283

[55] Schwarz H E 1980 Initial and final state correlations in the photoelectron spectra of In and Tl atoms *Journal of Electron Spectroscopy and Related Phenomena* **21** 257–259

[56] Manson S T and Starace A F 1982 Photoelectron angular distributions: energy dependence for *s* subshells *Rev. Mod. Phys.* **54** 389–405

[57] Reid K L 2003 Photoelectron angular distributions *Annu. Rev. Phys. Chem.* **54**(1) 397–424

[58] Meyer M et al. 2010 Two-Photon Excitation and Relaxation of the 3*d*-4*d* Resonance in Atomic Kr *Phys. Rev. Lett.* **104** 213001

[59] Quan W et al. 2009 Classical Aspects in Above-Threshold Ionization with a Midinfrared Strong Laser Field *Phys. Rev. Lett.* **103** 093001

[60] Wabnitz H et al. 2002 Multiple ionization of atom clusters by intense soft X-rays from a free-electron laser *Nature Physics* **420** 482–485

[61] Kanter E P et al. 2011 Unveiling and Driving Hidden Resonances with High-Fluence, High-Intensity X-Ray Pulses *Phys. Rev. Lett.* **107** 233001

[62] Kitzler M, Milosevic N, Scrinzi A, Krausz F and Brabec T 2002 Quantum Theory of Attosecond XUV Pulse Measurement by Laser Dressed Photoionization *Phys. Rev. Lett.* **88** 173904

[63] Kienberger R et al. 2002 Steering Attosecond Electron Wave Packets with Light *Science* **297** 1144–1148

[64] Itatani J, Quéré F, Yudin G L, Ivanov M Y, Krausz F and Corkum P B 2002 Attosecond Streak Camera *Phys. Rev. Lett.* **88** 173903

[65] Santra R, Kryzhevoi N V and Cederbaum L S 2009 X-Ray Two-Photon Photoelectron Spectroscopy: A Theoretical Study of Inner-Shell Spectra of the Organic Para-Aminophenol Molecule *Phys. Rev. Lett.* **103** 013002

[66] Nikolopoulos L A A, Nakajima T and Lambropoulos P 2003 Direct versus Sequential Double Ionization of Mg with Extreme-Ultraviolet Radiation *Phys. Rev. Lett.* **90** 043003

[67] Boguslavskiy A E, Mikosch J, Gijsbertsen A, Spanner M, Patchkovskii S, Gador N, Vrakking M J J and Stolow A 2012 The Multielectron Ionization Dynamics Underlying Attosecond Strong-Field Spectroscopies *Science* **16** 1336–1340

[68] Shavitt I 1977 The method of configuration interaction in H F S III (Editor), "Methods of Electronic Structure Theory", Volume 3 chapter 6, 189–275 (Springer US)

[69] Kümmel H G 2003 A BIOGRAPHY OF THE COUPLED CLUSTER METHOD *International Journal of Modern Physics B* **17**(28) 5311–5325 http://www.worldscientific.com/doi/pdf/10.1142/S0217979203020442

[70] Amusia M, Chernysheva L and Yarzhemsky V 2012 *Handbook of Theoretical Atomic Physics* (Springer)

[71] Dahlström J M, L'Huillier A and Maquet A 2012 Introduction to attosecond delays in photoionization *Journal of Physics B: Atomic, Molecular and Optical Physics* **45**(18) 183001

[72] Kheifets A S and Ivanov I A 2010 Delay in Atomic Photoionization *Phys. Rev. Lett.* **105** 233002

[73] Burke P G and Taylor K T 1975 R-matrix theory of photoionization. Application to neon and argon *Journal of Physics B: Atomic and Molecular Physics* **8**(16) 2620–2639

[74] Burke P G and Tennyson J 2005 R-matrix theory of electron molecule scattering *Mol. Phys.* **103** 2537–2548

[75] Taylor K T 1977 Photoelectron angular-distribution beta parameters for neon and argon *Journal of Physics B: Atomic and Molecular Physics* **10**(18) L699

[76] Schafer K J and Kulander K C 1990 Energy analysis of time-dependent wave functions: Application to above-threshold ionization *Phys. Rev. A* **42** 5794–5797

[77] Tong X M, Hino K and Toshima N 2006 Phase-dependent atomic ionization in few-cycle intense laser fields *Phys. Rev. A* **74** 031405(R)

[78] Popruzhenko S V and Bauer D 2008 Strong field approximation for systems with Coulomb interaction *Journal of Modern Optics* **55**(16) 2573–2589

[79] Popruzhenko S V, Paulus G G and Bauer D 2008 Coulomb-corrected quantum trajectories in strong-field ionization *Phys. Rev. A* **77** 053409

[80] Burke P G and Burke V M 1997 Time-dependent R-matrix theory of multiphoton processes *Journal of Physics B: Atomic, Molecular and Optical Physics* **30**(11) L383–L391

[81] van der Hart H W, Lysaght M A and Burke P G 2008 Momentum distributions of electrons ejected during ultrashort laser interactions with multielectron atoms described using the *R*-matrix basis sets *Phys. Rev. A* **77** 065401

[82] Lysaght M A, van der Hart H W and Burke P G 2009 Time-dependent *R*-matrix theory for ultrafast atomic processes *Phys. Rev. A* **79** 053411

[83] Moore L, Lysaght M, Nikolopoulos L, Parker J, van der Hart H and Taylor K 2011 The RMT method for many-electron atomic systems in intense short-pulse laser light *J. Mod. Opt.* **58** 1132–1140

[84] Torlina L, Ivanov M, Walters Z B and Smirnova O 2012 Time-dependent analytical *R*-matrix approach for strong-field dynamics. II. Many-electron systems *Phys. Rev. A* **86** 043409

[85] Ngoko Djiokap J M and Starace A F 2011 Evidence of the $2s2p(^1P)$ doubly excited state in the harmonic generation spectrum of helium *Phys. Rev. A* **84** 013404

[86] Tarana M and Greene C H 2012 Femtosecond transparency in the extreme-ultraviolet region *Phys. Rev. A* **85** 013411

[87] Argenti L, Pazourek R, Feist J, Nagele S, Liertzer M, Persson E, Burgdörfer J and Lindroth E 2013 Photoionization of helium by attosecond pulses: Extraction of spectra from correlated wave functions *Phys. Rev. A* **87** 053405

[88] Hochstuhl D and Bonitz M 2012 Time-dependent restricted-active-space configuration-interaction method for the photoionization of many-electron atoms *Phys. Rev. A* **86** 053424

[89] Miyagi H and Madsen L B 2013 Time-dependent restricted-active-space self-consistent-field theory for laser-driven many-electron dynamics *Phys. Rev. A* **87** 062511

[90] Feuerstein B and Thumm U 2003 On the computation of momentum distributions within wavepacket propagation calculations *Journal of Physics B: Atomic, Molecular and Optical Physics* **36**(4) 707–716

[91] Keller A 1995 Asymptotic analysis in time-dependent calculations with divergent coupling *Phys. Rev. A* **52** 1450–1457

[92] Henkel J, Lein M and Engel V 2011 Interference in above-threshold-ionization electron distributions from molecules *Phys. Rev. A* **83** 051401

[93] Tao L and Scrinzi A 2012 Photo-electron momentum spectra from minimal volumes: the time-dependent surface flux method *New Journal of Physics* **14**(1) 013021

[94] Yue L and Madsen L B 2013 Dissociation and dissociative ionization of H_2^+ using the time-dependent surface flux method *Phys. Rev. A* **88** 063420

[95] Amusia M Y and Connerade J P 2000 The theory of collective motion probed by light *Reports on Progress in Physics* **63**(1) 41–70

[96] LaForge A C et al. 2014 Collective Autoionization in Multiply-Excited Systems: A novel ionization process observed in Helium Nanodroplets *Sci. Rep.* **4**(3621)

[97] Borot A, Malvache A, Chen X, Jullien A, Geindre J, Audebert P, Mourou G, Queré F and Lopez-Martens R 2012 Attosecond control of collective electron motion in plasmas *Nature Physics* **8** 416–421

[98] Weber C P, Gedik N, Moore J E, Orenstein J, Stephens J and Awschalom D D 2005 Observation of spin Coulomb drag in a two-dimensional electron gas *Nature* **437** 1330–1333

[99] Sommer A, Ku M, Roati G and Zwierlein M W 2011 Universal spin transport in a strongly interacting Fermi gas *Nature* **472** 201–204

[100] Ernst P T, Götze S, Krauser J S, Pyka K, Lühmann D S, Pfannkuche D and Sengstock K 2010 Probing collective multi-electron dynamics in xenon with high-harmonic spectroscopy *Nature Physics* **6** 56–61

[101] Zhu X, Matsuzaki Y, Amsüss R, Kakuyanagi K, Shimo-Oka T, Mizuochi N, Nemoto K, Semba K, Munro W J and Saito S 2014 Observation of dark states in a superconductor diamond quantum hybrid system *Nature Communications* **5** 3424

[102] Fetter A L and Walecka J D 1980 *Quantum Theory of Many-particle Systems* (McGraw-Hill)

[103] Hau L V 2007 Nonlinear optics: Shocking superfluids *Nature Physics* **3** 13–14

[104] Savel'ev S, Rakhmanov A L, Yampol'skii V A and Nori F 2006 Analogues of nonlinear optics using terahertz Josephson plasma waves in layered superconductors *Nature Physics* **2** 521–525

[105] Fausti D, Tobey R I, Dean N, Kaiser S, Dienst A, Hoffmann M C, Pyon S, Takayama T, Takagi H and Cavalleri A 2011 Light-Induced Superconductivity in a Stripe-Ordered Cuprate *Science* **331**(6014) 189–191

[106] Melentiev P N, Afanasev A E and Balykin V I 2014 Giant optical nonlinearity of plasmonic nanostructures *Quantum Electronics* **44**(6) 547

[107] Kim S, Jin J, Kim Y, Park I, Kim Y and Kim S 2008 High-harmonic generation by resonant plasmon field enhancement *Nature* **453** 757–760

[108] Barnes W L, Dereux A and Ebbesen T W 2003 Surface plasmon subwavelength optics *Nature* **424** 824–830

[109] Becker U and Shirley D A (Editors) 1996 *VUV and Soft X-Ray Photoionization* (Springer US) URL http://dx.doi.org/10.1007/978-1-4613-0315-2

[110] Fano U 1961 Effects of Configuration Interaction on Intensities and Phase Shifts *Phys. Rev.* **124** 1866–1878

[111] Cederbaum L S, Zobeley J and Tarantelli F 1997 Giant Intermolecular Decay and Fragmentation of Clusters *Phys. Rev. Lett.* **79** 4778–4781

[112] Brif C, Chakrabarti R and Rabitz H 2011 *Control of Quantum Phenomena* 1–76 (John Wiley & Sons, Inc.) URL http://dx.doi.org/10.1002/9781118158715.ch1

[113] Meier C and Engel V 1994 Interference Structure in the Photoelectron Spectra Obtained from Multiphoton Ionization of Na_2 with a Strong Femtosecond Laser Pulse *Phys. Rev. Lett.* **73** 3207–3210

[114] Shen Z and Engel V 2002 Target wave-packet control and its detection using time-resolved photoelectron spectroscopy *Chem. Phys. Lett.* **358**(3-4) 344–349

[115] Wollenhaupt M, Engel V and Baumert T 2005 Femtosecond Laser Photoelectron Spectroscopy on Atoms and Small Molecules: Prototype Studies in Quantum Control *Annu. Rev. Phys. Chem.* **56** 25

[116] Gräfe S, Erdmann M and Engel V 2005 Population transfer in the multiphoton excitation of molecules *Phys. Rev. A* **72** 013404

[117] Braun H, Bayer T, Sarpe C, Siemering R, de Vivie-Riedle R, Baumert T and Wollenhaupt M 2014 Coupled electron-nuclear wavepacket dynamics in potassium dimers *J. Phys. B: At. Mol. Opt. Phys.* **47** 124015

[118] Klamroth T 2006 Optimal control of ultrafast laser driven many-electron dynamics in a polyatomic molecule: N-methyl-6-quinolone *J. Chem. Phys.* **124**(14) 144310

[119] Mundt M and Tannor D J 2009 Optimal control of interacting particles: a multi-configuration time-dependent Hartree–Fock approach *New J. Phys.* **11** 105038

[120] Castro A, Werschnik J and Gross E K U 2012 Controlling the Dynamics of Many-Electron Systems from First Principles: A Combination of Optimal Control and Time-Dependent Density-Functional Theory *Phys. Rev. Lett.* **109** 153603

[121] Hellgren M, Räsänen E and Gross E K U 2013 Optimal control of strong-field ionization with time-dependent density-functional theory *Phys. Rev. A* **88** 013414

[122] McCurdy C W and Rescigno T N 1997 Calculating differential cross sections for electron-impact ionization without explicit use of the asymptotic form *Phys. Rev. A* **56** R4369–R4372

[123] Martín F 1999 Ionization and dissociation using B-splines: photoionization of the hydrogen molecule *Journal of Physics B: Atomic, Molecular and Optical Physics* **32**(16) R197

[124] Rescigno T N and McCurdy C W 2000 Numerical grid methods for quantum-mechanical scattering problems *Phys. Rev. A* **62** 032706

[125] Bachau H, Cormier E, Decleva P, Hansen J E and Martín F 2001 Applications of B -splines in atomic and molecular physics *Reports on Progress in Physics* **64**(12) 1815

[126] McCurdy C W and Martín F 2004 Implementation of exterior complex scaling in B-splines to solve atomic and molecular collision problems *Journal of Physics B: Atomic, Molecular and Optical Physics* **37**(4) 917

[127] Greenman L, Koch C P and Whaley K B 2014 Laser pulses for coherent xuv Raman excitation *arXiv:1409.7767* http://arxiv.org/abs/1409.7767

[128] Szabo A and Ostlund N 1996 *Modern Quantum Chemistry* (Dover Publications)

[129] Greenman L, Ho P J, Pabst S, Kamarchik E, Mazziotti D A and Santra R 2010 Implementation of the time-dependent configuration-interaction singles method for atomic strong-field processes *Phys. Rev. A* **82** 023406

[130] Pabst S and Santra R Rev 1144, 2014 XCID program package for multichannel ionization dynamics

[131] Pabst S, Greenman L, Ho P J, Mazziotti D A and Santra R 2011 Decoherence in Attosecond Photoionization *Phys. Rev. Lett.* **106** 053003

[132] Pabst S and Santra R 2013 Strong-Field Many-Body Physics and the Giant Enhancement in the High-Harmonic Spectrum of Xenon *Phys. Rev. Lett.* **111** 233005

[133] Pabst S, Greenman L, Mazziotti D A and Santra R 2012 Impact of multichannel and multipole effects on the Cooper minimum in the high-order-harmonic spectrum of argon *Phys. Rev. A* **85** 023411

[134] Rohringer N, Gordon A and Santra R 2006 Configuration-interaction-based time-dependent orbital approach for *ab initio* treatment of electronic dynamics in a strong optical laser field *Phys. Rev. A* **74** 043420

[135] Pabst S, Sytcheva A, Moulet A, Wirth A, Goulielmakis E and Santra R 2012 Theory of attosecond transient-absorption spectroscopy of krypton for overlapping pump and probe pulses *Phys. Rev. A* **86** 063411

[136] Craig D P and Thirunamachandran T 1998 *Molecular Quantum Electrodynamics* (Dover)

[137] Slater J C 1951 A Simplification of the Hartree-Fock Method *Phys. Rev.* **81** 385–390

[138] Herman F and Skillman S 1963 *Atomic Structure Calculations* (Prentice-Hall)

[139] Son S K and Santra R Rev 1090, 2014 XATOM: an integrated toolkit for x-ray and atomic physics URL http://wavelet.chem.ku.edu/~sangkil/biblio/pdf/Son11f.pdf

[140] Son S K, Young L and Santra R 2011 Impact of hollow-atom formation on coherent x-ray scattering at high intensity *Phys. Rev. A* **83** 033402

[141] Latter R 1955 Atomic Energy Levels for the Thomas-Fermi and Thomas-Fermi-Dirac Potential *Phys. Rev.* **99** 510–519

[142] Feit M, Fleck Jr J A and Steiger A 1982 Solution of the Schrödinger equation by a spectral method *Journal of Computational Physics* **47**(3) 412 – 433

[143] Feit M D and Fleck J A 1983 Solution of the Schrödinger equation by a spectral method II: Vibrational energy levels of triatomic molecules *The Journal of Chemical Physics* **78**(1) 301–308

[144] Tal-Ezer H and Kosloff R 1984 An accurate and efficient scheme for propagating the time dependent Schrödinger equation *The Journal of Chemical Physics* **81**(9) 3967–3971

[145] D H J 2001 *Numerical Methods for Engineers and Scientists* (Dekker) 2nd edition

[146] Golub G H and Loan C F V 1996 *Matrix computations* (The Johns Hopkins University Press) 3rd edition

[147] Leforestier C et al. 1991 A comparison of different propagation schemes for the time dependent Schrödinger equation *J. Comput. Phys.* **94**(1) 59–80

[148] Kosloff R 1994 Propagation Methods for Quantum Molecular Dynamics *Annu. Rev. Phys. Chem.* **45**(1) 145–178

[149] Anderson E et al. 1999 LAPACK Users' Guide http://www.netlib.org/lapack/

[150] Lehoucq R B, Sorensen D C and Yang C 1998 *ARPACK Users' Guide: Solution of Large Scale Eigenvalue Problems with Implicitly Restarted Arnoldi Methods* (SIAM) URL http://www.caam.rice.edu/software/ARPACK

[151] 2012 ARPACK homepage URL http://www.caam.rice.edu/software/ARPACK

[152] Rubbmark J R, Kash M M, Littman M G and Kleppner D 1981 Dynamical effects at avoided level crossings: A study of the Landau-Zener effect using Rydberg atoms *Phys. Rev. A* **23** 3107–3117

[153] Clark W and Greene C H 1999 Adventures of a Rydberg electron in an anisotropic world *Rev. Mod. Phys.* **71** 821–833

[154] Stine J R and Muckerman J T 1976 On the multidimensional surface intersection problem and classical trajectory "surface hopping" *The Journal of Chemical Physics* **65**(10) 3975–3984

[155] Tully J C 1990 Molecular dynamics with electronic transitions *The Journal of Chemical Physics* **93**(2) 1061–1071

[156] Hammes-Schiffer S and Tully J C 1994 Proton transfer in solution: Molecular dynamics with quantum transitions *The Journal of Chemical Physics* **101**(6) 4657–4667

[157] Pechukas P 1969 Time-Dependent Semiclassical Scattering Theory. II. Atomic Collisions *Phys. Rev.* **181** 174–185

[158] Smith F T 1969 Diabatic and Adiabatic Representations for Atomic Collision Problems *Phys. Rev.* **179** 111–123

[159] Miller W H and George T F 1972 Semiclassical Theory of Electronic Transitions in Low Energy Atomic and Molecular Collisions Involving Several Nuclear Degrees of Freedom *The Journal of Chemical Physics* **56**(11) 5637–5652

[160] Bloch I, Dalibard J and Zwerger W 2008 Many-body physics with ultracold gases *Rev. Mod. Phys.* **80** 885–964

[161] Dürr S, Volz T, Marte A and Rempe G 2004 Observation of Molecules Produced from a Bose-Einstein Condensate *Phys. Rev. Lett.* **92** 020406

[162] von Stecher J and Greene C H 2007 Spectrum and Dynamics of the BCS-BEC Crossover from a Few-Body Perspective *Phys. Rev. Lett.* **99** 090402

[163] Potvliege R M, Meše E and Vučić S 2010 Multiphoton ionization and multiphoton resonances in the tunneling regime *Phys. Rev. A* **81** 053402

[164] Zheng J, Qiu E, Yang Y and Lin Q 2012 Nonadiabatic atomic ionization by intense subcycle laser pulses *Phys. Rev. A* **85** 013417

[165] Parker J S, Armstrong G S J, Boca M and Taylor K T 2009 From the UV to the static-field limit: rates and scaling laws of intense-field ionization of helium *Journal of Physics B: Atomic, Molecular and Optical Physics* **42**(13) 134011

[166] Wang X and Eberly J H 2012 Nonadiabatic theory of strong-field atomic effects under elliptical polarization *The Journal of Chemical Physics* **137**(22) 22A542

[167] Yudin G L and Ivanov M Y 2001 Nonadiabatic tunnel ionization: Looking inside a laser cycle *Phys. Rev. A* **64** 013409

[168] Zener C 1932 Non-Adiabatic Crossing of Energy Levels *Proceedings of the Royal Society of London A: Mathematical, Physical and Engineering Sciences* **137**(833) 696–702

[169] Lichten W 1963 Resonant Charge Exchange in Atomic Collisions *Phys. Rev.* **131** 229–238

[170] Baer M 1975 Adiabatic and diabatic representations for atom-molecule collisions: Treatment of the collinear arrangement *Chemical Physics Letters* **35**(1) 112 – 118

[171] Baer M 2002 Introduction to the theory of electronic non-adiabatic coupling terms in molecular systems *Physics Reports* **358**(2) 75 – 142

[172] Thiel A and Köppel H 1999 Proposal and numerical test of a simple diabatization scheme *The Journal of Chemical Physics* **110**(19) 9371–9383

[173] Sadygov R G and Yarkony D R 1998 On the adiabatic to diabatic states transformation in the presence of a conical intersection: A most diabatic basis from the solution to a Poisson's equation. I *The Journal of Chemical Physics* **109**(1) 20–25

[174] Cohen-Tannoudji C, Diu B and Laloë F 1977 *Quantum Mechanics* Volume 2 (Wiley) 1st edition

[175] Friedrich H 1998 *Theoretical Atomic Physics* (Springer) 2nd edition

[176] Sakurai J J 1994 *Modern Quantum Mechanics* (Addison-Wesley) revised edition

[177] Eberly J H and Javanainen J 1988 Above-threshold ionisation *European Journal of Physics* **9**(4) 265–275

[178] Scrinzi A, Geissler M and Brabec T 1999 Ionization Above the Coulomb Barrier *Phys. Rev. Lett.* **83** 706–709

[179] Loudon R 2001 *The Quantum Theory of Light* (Oxford Science Publications) 3rd edition

[180] Moiseyev N 1998 Quantum theory of resonances: calculating energies, widths and cross-sections by complex scaling *Physics Reports* **302** 212 – 293

[181] Riss U V and Meyer H D 1993 Calculation of resonance energies and widths using the complex absorbing potential method *Journal of Physics B: Atomic, Molecular and Optical Physics* **26**(23) 4503–4536

[182] Riss U V and Meyer H D 1998 The transformative complex absorbing potential method: a bridge between complex absorbing potentials and smooth exterior scaling *Journal of Physics B: Atomic, Molecular and Optical Physics* **31**(10) 2279–2304

[183] Bohm A, Gadella M and Mainland G B 1989 Gamow vectors and decaying states *American Journal of Physics* **57**(12) 1103–1108

[184] Siegert A J F 1939 On the Derivation of the Dispersion Formula for Nuclear Reactions *Phys. Rev.* **56** 750–752

[185] Moiseyev N 2011 *Non-Hermitian Quantum Mechanics* (Cambridge University Press) 1st edition

[186] Santra R and Cederbaum L S 2002 Non-Hermitian electronic theory and applications to clusters *Physics Reports* **368**(1) 1 – 117

[187] Kondratjev D A, Beigman I L and Vainshtein L A 2010 Static polarizabilities of helium and alkali atoms, and their isoelectronic ions *Journal of Russian Laser Research* **31**(3) 294–306

[188] Chen M K 1995 Dipole polarizabilities of the 1, 2^1S and 2^3S states of the helium sequence *Journal of Physics B: Atomic, Molecular and Optical Physics* **28**(7) 1349–1355

[189] Pont M, Shakeshaft R and Potvliege R M 1990 Low-frequency theory of multiphoton ionization *Phys. Rev. A* **42** 6969–6972

[190] Scrinzi A 2010 Infinite-range exterior complex scaling as a perfect absorber in time-dependent problems *Phys. Rev. A* **81** 053845

[191] Scrinzi A 2012 t-SURFF: fully differential two-electron photo-emission spectra *New Journal of Physics* **14**(8) 085008

[192] Muga J, Palao J, Navarro B and Egusquiza I 2004 Complex absorbing potentials *Physics Reports* **395**(6) 357–426

[193] Experiment carried out at FLASH by the group of Michael Meyer (European XFEL). Private communication, results to be published.

[194] Knight P, Lauder M and Dalton B 1990 Laser-induced continuum structure *Physics Reports* **190**(1) 1 – 61

[195] Grobe R and Haan S L 1994 Spectral manifestation of core coherence in photoionization *Journal of Physics B: Atomic, Molecular and Optical Physics* **27**(22) L735

[196] Beers B L and Armstrong L 1975 Exact solution of a realistic model for two-photon ionization *Phys. Rev. A* **12** 2447–2454

[197] Knight P L 1978 AC Stark splitting of photoelectron energy spectra in multiphoton ionisation *Journal of Physics B: Atomic and Molecular Physics* **11**(17) L511

[198] Knight P 1977 Saturation and rabi oscillations in resonant multiphoton ionization *Optics Communications* **22**(2) 173 – 177

[199] Grobe R and Eberly J H 1993 Observation of coherence transfer by electron-electron correlation *Phys. Rev. A* **48** 623–627

[200] Carusotto S and Strati C 1973 Incoherent and Coherent Pulses and Multiphoton Absorption Probability *Il Nuovo Cimento* **15B**(2) 159–180

[201] MATLAB and Statistics Toolbox Release 2012b, The MathWorks, Inc., Natick, Massachusetts, United States

[202] Ederer D L 1964 Photoionization of the 4*d* Electrons in Xenon *Phys. Rev. Lett.* **13** 760–762

[203] Codling K and Madden R P 1964 Optically Observed Inner Shell Electron Excitation in Neutral Kr And Xe *Phys. Rev. Lett.* **12** 106–108

[204] Lukirskii A, Brytov I and Zimkina T 1964 Photoionization absorption of He, Kr, Xe, CH_4, and Methylal in the 23.6-250Å region *Opt. Spectrosc. (USSR)* **17** 234–237

[205] Cooper J W 1964 Interaction of Maxima in the Absorption of Soft X Rays *Phys. Rev. Lett.* **13** 762–764

[206] Fano U and Cooper J W 1968 Spectral Distribution of Atomic Oscillator Strengths *Rev. Mod. Phys.* **40** 441–507

[207] Krebs D, Pabst S and Santra R 2014 Introducing many-body physics using atomic spectroscopy *American Journal of Physics* **82**(2) 113–122

[208] Pabst S and Santra R 2013 Strong-Field Many-Body Physics and the Giant Enhancement in the High-Harmonic Spectrum of Xenon *Phys. Rev. Lett.* **111** 233005

[209] Frolov M V, Manakov N L, Sarantseva T S, Emelin M Y, Ryabikin M Y and Starace A F 2009 Analytic Description of the High-Energy Plateau in Harmonic Generation by Atoms: Can the Harmonic Power Increase with Increasing Laser Wavelengths? *Phys. Rev. Lett.* **102** 243901

[210] Sorokin A A, Bobashev S V, Feigl T, Tiedtke K, Wabnitz H and Richter M 2007 Photoelectric Effect at Ultrahigh Intensities *Phys. Rev. Lett.* **99** 213002

[211] Richardson V et al. 2010 Two-Photon Inner-Shell Ionization in the Extreme Ultraviolet *Phys. Rev. Lett.* **105** 013001

[212] Rudek B et al. 2012 Attosecond control of collective electron motion in plasmas *Nature Photonics* **6** 858–865

[213] Fukuzawa H et al. 2013 Deep Inner-Shell Multiphoton Ionization by Intense X-Ray Free-Electron Laser Pulses *Phys. Rev. Lett.* **110** 173005

[214] Gerken N, Klumpp S, Sorokin A A Tiedtke K, Richter M, Bürk V, Mertens K, Juranić P and Martins M 2014 Time-Dependent Multiphoton Ionization of Xenon in the Soft-X-Ray Regime *Phys. Rev. Lett.* **112** 213002

[215] Makris M G, Lambropoulos P and Mihelič A 2009 Theory of Multiphoton Multielectron Ionization of Xenon under Strong 93-eV Radiation *Phys. Rev. Lett.* **102** 033002

[216] Wabnitz H, de Castro A R B, Gürtler P, Laarmann T, Laasch W, Schulz J and Möller T 2005 Multiple Ionization of Rare Gas Atoms Irradiated with Intense VUV Radiation *Phys. Rev. Lett.* **94** 023001

[217] Shiner A D, Schmidt B E, Trallero-Herrero C, Wörner H J, Patchkovskii S, Corkum P B, Kieffer J C, Légaré F and Villeneuve D M 2011 Probing collective multi-electron dynamics in xenon with high-harmonic spectroscopy *Nature Physics* **7** 464–467

[218] Pi L W and Starace A F 2010 Potential barrier effects in two-photon ionization processes *Phys. Rev. A* **82** 053414

[219] Wendin G 1973 Collective effects in atomic photoabsorption spectra. III. Collective resonance in the 4d 10 shell in Xe *Journal of Physics B: Atomic and Molecular Physics* **6**(1) 42

[220] Becker U, Szostak D, Kerkhoff H G, Kupsch M, Langer B, Wehlitz R, Yagishita A and Hayaishi T 1989 Subshell photoionization of Xe between 40 and 1000 eV *Phys. Rev. A* **39** 3902–3911

[221] Povh B, Scholz C, Zetsche F and Rith K 2008 *Particles and Nuclei: An Introduction to the Physical Concepts* (Springer) 6th edition

[222] Tiedtke K et al. 2009 The soft x-ray free-electron laser FLASH at DESY: beamlines, diagnostics and end-stations *New Journal of Physics* **11**(2) 023029

[223] 2015 FLASH DESY homepage URL `http://flash.desy.de/`

[224] Werme L O, Bergmark T and Siegbahn K 1972 The High Resolution $L_{2,3}MM$ and $M_{4,5}NN$ Auger Spectra from Krypton and $M_{4,5}NN$ and $N_{4,5}OO$ Auger Spectra from Xenon *Physica Scripta* **6**(2–3) 141

[225] Danos M and Greiner W 1965 Damping of the Giant Resonance in Heavy Nuclei *Phys. Rev.* **138** B876–B891

[226] Veyssibre A, Beil H, Bergbre R, Carlos P and Leprétre A 1970 Photoneutron cross sections of ^{208}Pb and ^{197}Au *Nucl. Phys. A* **159** 561–576

[227] Wendin G 1971 Collective resonance in the $4d^{10}$ shell in atomic Xe *Physics Letters A* **37**(5) 445–446

[228] Lundqvist S and Mukhopadhyay G 1980 Collective Aspects of Atomic Dynamics *Physica Scripta* **21**(3-4) 503

[229] Amusia M Y, Cherepkov N A, Janev R K and Zivanovic D 1974 On the problem of the existence of collective oscillations in atoms *Journal of Physics B: Atomic and Molecular Physics* **7**(12) 1435

[230] Reich D M, Ndong M and Koch C P 2012 Monotonically convergent optimization in quantum control using Krotov's method *JCP* **136** 104103

[231] Rathje T, Sayler A M, Zeng S, Wustelt P, Figger H, Esry B D and Paulus G G 2013 Coherent Control at Its Most Fundamental: Carrier-Envelope-Phase-Dependent Electron Localization in Photodissociation of a H_2^+ Molecular Ion Beam Target *Phys. Rev. Lett.* **111** 093002

[232] Shvetsov-Shilovski N I, Räsänen E, Paulus G G and Madsen L B 2014 Asymmetric photoelectron momentum distributions due to quantum interference in strong-field ionization by a few-cycle pulse *Phys. Rev. A* **89** 043431

[233] Reich D M, Palao J P and Koch C P 2014 Optimal control under spectral constraints: Enforcing multi-photon absorption pathways *J. Mod. Opt.* **61**(10) 822

[234] Chelkowski S, Bandrauk A D and Apolonski A 2004 Phase-dependent asymmetries in strong-field photoionization by few-cycle laser pulses *Phys. Rev. A* **70** 013815

[235] Yeh J J and Lindau I 1985 Atomic subshell photoionization cross sections and asymmetry parameters: $1 \leq Z \leq 103$ *Atomic Data and Nuclear Data Tables* **32**(1) 1–155

[236] Chapman H N 2009 X-ray imaging beyond the limits *Nat Mater* **8**(4) 299–301

[237] Neutze R, Wouts R, van der Spoel D, Weckert E and Hajdu J 2000 Potential for biomolecular imaging with femtosecond X-ray pulses *Nature* **406** 752–757

[238] Krausz F and Ivanov M 2009 Attosecond physics *Rev. Mod. Phys.* **81** 163–234

[239] Brown R 2009 New Era of Research Begins as World's First Hard X-ray Laser "First Light" http://home.slac.stanford.edu/pressreleases/2009/20090421.htm accessed: 2014-10-01

[240] Mimura H et al. 2014 Generation of 10^20 Wcm^{-2} hard X-ray laser pulses with two-stage reflective focusing system *Nat Commun* **5**

[241] Abela R 2007 The Technical Design Report (TDR) of the European XFEL http://xfel.desy.de/technical_information/tdr/tdr/ edited by M. Altarelli et. al, Accessed: 2014-09-18 and 2015-07-04

[242] Thompson A C and Vaughan D (Editors) 2001 *X-ray Data Booklet* (Lawrence Berkeley National Laboratory, University of California) second edition http://xdb.lbl.gov

[243] Milošević D B, Paulus G G, Bauer D and Becker W 2006 Above-threshold ionization by few-cycle pulses *J. Phys. B: At. Mol. Opt. Phys.* **39** R203

[244] Sekikawa T, Kosuge A, Kanai T and Watanabe S 2004 Nonlinear optics in the extreme ultraviolet *Nature* **432**(7017) 605–608

[245] Nakajima T and Watanabe S 2004 Two-photon above-threshold-ionization cross sections of rare-gas atoms by xuv photons *Phys. Rev. A* **70** 043412

[246] Varma H R, Ciappina M F, Rohringer N and Santra R 2009 Above-threshold ionization in the x-ray regime *Phys. Rev. A* **80** 053424

[247] Florescu V, Budriga O and Bachau H 2011 Two-photon above-threshold ionization of hydrogen over the photon energy range from 15 eV to 50 keV *Phys. Rev. A* **84** 033425

[248] Bachau H, Budriga O, Dondera M and Florescu V 2013 Above-threshold ionization of hydrogen and hydrogen-like ions by X-ray pulses *Central European Journal of Physics* **11**(9) 1091–1098

[249] Karule E and Gailitis A 2010 Above threshold ionization of atomic hydrogen in ns states with up to four excess photons *Journal of Physics B: Atomic, Molecular and Optical Physics* **43**(6) 065601

[250] Florescu V, Budriga O and Bachau H 2012 Two-photon ionization of hydrogen and hydrogenlike ions: Retardation effects on differential and total generalized cross sections *Phys. Rev. A* **86** 033413

[251] Surzhykov A, Koval P and Fritzsche S 2005 Angular correlations in the two-photon decay of hydrogenlike ions: Relativistic Green's-function approach *Phys. Rev. A* **71** 022509

[252] Yerokhin V A, Surzhykov A and Fritzsche S 2014 Relativistic configuration-interaction calculation of $K\alpha$ transition energies in berylliumlike iron *Phys. Rev. A* **90** 022509

[253] Zhou Z and Chu S I 2013 Multiphoton above-threshold ionization in superintense free-electron x-ray laser fields: Beyond the dipole approximation *Phys. Rev. A* **87** 023407

[254] Dondera M and Bachau H 2012 Exploring above-threshold ionization of hydrogen in an intense x-ray laser field through nonperturbative calculations *Phys. Rev. A* **85** 013423

[255] Toyota K, Tolstikhin O I, Morishita T and Watanabe S 2008 Interference substructure of above-threshold ionization peaks in the stabilization regime *Phys. Rev. A* **78** 033432

[256] Toyota K, Tolstikhin O I, Morishita T and Watanabe S 2009 Slow Electrons Generated by Intense High-Frequency Laser Pulses *Phys. Rev. Lett.* **103** 153003

[257] Becker W, Grasbon F, Kopold R, Milošević D, Paulus G and Walther H 2002 Above-Threshold Ionization: From Classical Features to Quantum Effects Volume 48 of *Advances In Atomic, Molecular, and Optical Physics* 35 – 98 (Academic Press)

Acknowledgments

During my time as a PhD student I made the acquaintance of several interesting people, colleagues and friends who in one way or another have contributed to my work.

First of all I am deeply grateful to my supervisor Robin Santra, from whom I learned a lot about theoretical, computational and experimental physics and the connections between them. I had the most valuable chance to benefit from his intuition regarding the microscopic quantum behavior of atoms and also to take part in exciting brainstorming moments and discussions full of enthusiasm with him. I really enjoyed working with him and I am truly indebted to him for his careful reading and his suggestions for corrections in my publication manuscripts.

I would also like to very much thank Stefan Pabst, who introduced me to the huge pre-existing part of the XCID package. Special thanks go to him for always being helpful and an excellent collaborator. With him it was much easier to get started and to extend the programs. I also enjoyed our discussions during Stammtisch or on any other occasion about physics and life in general.

Moreover I am thankful to many other group members who made my life much more pleasant beyond work: Arina Sytcheva who always cared about how I felt and what difficulties I was facing, my office mate Jan Malte Slowik who was always willing to interrupt work for a short chat or discussions, Otfried Geffert who not only helped with computer problems, but who also provided his basement for multicultural and relaxing jam sessions together with Zoltan Jurek, Sang-Kil Son who taught me how to use XATOM, Oriol Vendrell for nice discussions about physics and politics, our very kind and helpful secretary Berit Heiser, Beata Ziaja for organizing our Ladies' Lunch, and actually the whole CFEL Theory Group, it was a great time!

I would like to thank Michael Meyer who was my second supervisor for the nice collaboration on their experiment, and Tommaso Mazza for interesting discussions and information about the experimental reality.

Regarding the organization of our international workshop "Perspectives of ultrafast physics – light-induced dynamics in atoms & molecules" I am obliged to the Körber-Stiftung, to Robin Santra, Klaus Sengstock and Henning Moritz from the SFB 925 for their financial support. I also want to thank Berit Heiser and Christine Berber for their help with organizational matters.

The supervision of my summer student Matthew Tilley was a great experience, I would like to thank him for the nice collaboration within the DAAD RISE program.

The joint work on optimal control problems was not always easy but certainly always enlightening, so I would like to thank Esteban Goetz and Christiane Koch for the interesting collaboration.

Many thanks go also to Daniela Pfannkuche for agreeing to read and review my

thesis.

I thank the people who took the time to proofread my thesis, Miriam Klopotek, Julian Hirscht, Jan Malte Slowik, and Evangelos Karamatskos. Also, I thank all the other people and friends in and around CFEL for the nice time, I enjoyed having coffee, lunch and dinner with you and to share ideas, news and stories.

And, finally, most of all I am grateful to my family, who always stands like a rock, for true support and love.